FUNDAMENTAL AND APPLIED ASPECTS OF CONTACT ELECTRIFICATION

by

Ronald Elsdon
Churchill College, Cambridge

A dissertation submitted for the degree of Doctor of Philosophy
at the University of Cambridge.

September 1975

TO LINDA

CONTENTS

PREFACE

The work described in this dissertation was carried out in the Department of Chemical Engineering, University of Cambridge, between September 1972 and September 1975. It is my own original work except where specifically acknowledged in the text, and includes nothing which is the outcome of work done in collaboration. Neither the present dissertation, not any part thereof, has previously been submitted at any other University.

I should like to express my sincere thanks to Dr. C.J. Shearer, who, before leaving the department, was my supervisor during the first two years of the project, and Dr. R.M. Nedderman my present supervisor, for much helpful advice and encouragement. I am greatly indebted to Mr. F.R.G. Mitchell for designing the electrical instrumentation, and for many fruitful and interesting discussions concerning numerous aspects of the present work.

I should like to thank Mr. K.C. Quinton for the detailed mechanical design of the vacuum chamber apparatus, and Mr. J. Hankin and Mr. J.A. Pryor for constructing the apparatus. I am grateful to Mr. A.E. Disbrey for assembly of the fluidised bed system.

I should like to express my appreciation to the many participants in the Institute of Physics, Static Electrification Group meetings, who have provided much helpful advice.

I am also very grateful to my wife for displaying great patience in translating the first draft of this dissertation into a legible form.

Financial assistance was provided by the Science Research Council, and is gratefully acknowledged.

Churchill College,
Cambridge

R. Elsdon.

September 1975

SUMMARY

Apparatus has been developed, which permits the measurement of electrification produced by rolling or sliding contact between a spherical specimen, and a plane dielectric sample. Measurements of the charge transferred to metal contact spheres, and the two-dimensional dielectric surface charge distribution, have been carried out under controlled conditions. The dissipation processes of air breakdown and bulk condution have been studied. The importance of metal work function , dielectric material, the normal force during contact, the mode of contact, and the time of contact has also been investigated.

Contact electrification and charge dissipation occurring in a vibrated bed have been studied. The variables of interest were the bulk particle resistivity, the amplitude of vibration, and the system electrode geometry. Theoretical models have been developed for the processes occurring, and the models could be used to interpret experimental observations. The relevance of the results to previous particle electrification studies, and to general particle handling situations has been discussed.

Two new applications of particle charging have been examined. The first utilised particle contact electrification occurring naturally in a fluidised bed. By applying a suitable alternating electric field normal to an immersed heater surface, considerable increases in the heat transfer coefficient have been obtained, as a result of the imposed particle movement. The influence on the heat transfer coefficient, of the electric field magnitude and frequency, together with the fluidising air velocity, has been studied.

The second application involved devising a novel means of electrostatic separation, using induction charging applied to the particles on the surface of a vibrated bed. A theoretical model for predicting particle collection rates has been developed, and verified by comparison with experimental observations. An efficient separation has been demonstrated on a combined size/resistivity basis.

CHAPTER 1

INTRODUCTION

When two solid materials are contacted and separated in a gaseous environment, an electric charge frequently remains on the solids. The force due to this charge was noticed as early as the 6th century B.C.[1], and yet the mechanism responsible for the formation of the charge is still incompletely understood. Charge production has been observed for a mercury/polymer contact system[2-4], indicating that friction is not a necessary requirement for charge transfer. Charge production has also been observed, when a small area of one sample of a given material is rubbed by a large area of another sample of the same material.[5-6] This has been termed asymmetric rubbing[6-8], and the charge produced has been ascribed to a temperature difference at the contact junction[7,8]. Thus, two distinct forms of charging are apparent, one is related to the intrinsic behaviour of the contact materials, and the other is related to the distribution of frictional forces during contact.

Electrification arising from the intrinsic material properties has been termed contact electrification[7], whereas electrification arising from the frictional forces has been called triboelectrification[7] or frictional electrification[7]. However the distinction between the application of these terms is not precise, as evidenced by the fact that Peterson[9] suggests calling all electrification by the term contact electrification, whilst O'Neill[10] has termed electrification in which the temperature rise during contact is negligible - triboelectrification. For the purposes of the present study, the term, contact electrification will be used. This is defined as the production of charge when two solid materials are contacted and separated in a gaseous environment, in such a way that the local temperature rise at the contact area, is sufficiently small, to have little effect on the charge separation at the interface. In practice this limits temperature rise to approximately 200°C[7], if an insulator is not to be made semiconducting by the temperature rise. Temperature rises of less than 20°C will have little effect on polymer mechanical properties, for the materials studied in this investigation.

Temperature rises during the present studies, calculated using the method

described by Harper[7] are less than 2°C for the most severe sliding conditions. Temperature rises with rolling contact will be orders of magnitude less than 2°C, thus the charging observed, conforms to the definition of contact electrification.

If two solids are contacted in an electric field, then each will possess a charge if they are separated whilst the electric field is applied[11]. The magnitude of this charge depends on the time of application of the electric field field, both during contact and during separation. This type of electrification known as induction charging[11], is considered in Chapter 6 in relation to an electrostatic separation technique.

1. 1. The importance of dissipation processes.

When materials possessing an electric charge are separated, electron tunnelling due to quantum mechanical effects can occur[7,12]. This ceases with conductors after about 1 nm to 2.5nm of separation[7], and with insulators and semiconductors will sometimes be restricted to much smaller separation distances.[7] Thus the charge observed is modified by this effect. For a given geometrical situation, the charge after tunnelling processes have occurred, is related by a constant term, to the charge existing before tunnelling[12], and therefore the charge after separation can be used to characterise the fundamental charge transfer mechanism. Since the quantity of practical importance, is the charge level remaining after tunnelling ceases, electron tunnelling can be considered as intrinsic to the electrification process.

As the materials are separated further, certain other charge dissipation processes can occur. If the contact material is an electrically isolated conductor, charge rearrangement will ensue, to give an equipotential conductor surface. If the contact material is an insulator or semiconductor, then the possible dissipation processes are gas electrical breakdown, field emission, and conduction through the material bulk and along the surface. Field emission is the spontaneous emission of electrons due to the presence of electric fields. This occurs for electric fields greater than 10^7 V m^{-1}.[13] Gas electrical breakdown processes occur as a result of cumulative ionisation[14-16]. This is due to the acceleration of naturally present ions and electrons in a gas, by a high

electric field, and is discussed in Chapters 2 and 3.

1.2. Practical situations involving contact electrification.

Contact electrification arises naturally in an extremely diverse range of physical situations, which cover many human concerns ranging from large scale industry to domestic activity. There are both useful and hazardous aspects associated with contact electrification.

The most dangerous hazards occur when sufficient charge is accumulated by solid material, to cause electrical discharges of sufficient energy to ignite a flammable gas or vapour, or a dust dispersion[17,18]. This situation can arise with insulating powders and insulating sheet material. Several fires due to this cause, in a diversity of physical situations, have been described in an Institution of Chemical Engineers bulletin[19]. Gibson[17] and Hughes[20] have also described the occurrence of fires due to air breakdown following charge accumulation, and McIntyre[21] has reported dangerous charge accumulations in herbicide storage silos.

Many sources of nuisance arise as a result of contact electrification. Electric discharge occuring during photographic film processing can produce unwanted exposure of the film[22], whilst electrostatic attraction of airborne dust particles to textiles, known as fog-marking[23], presents a considerable problem to the textile industry. Electrical discharge can cause the destruction of metal-oxide-silicon solid state devices, during manufacture[22], and physiological shock caused by electrical discharge is a familiar problem. Tenacious electrostatic attraction of dust particles to industrial handling equipment[1], or in the domestic environment is a further source of nuisance.

Industrical applications of contact electrification have been summarised by Inculet[24], Bright[25] and Corbett[26] and described in more detail in a book by Moore[27]. Applications include, electrostatic coating[24,25,28], electrostatic separation[24,25,27,29-32], xerography[24-27], electrical power generation[24,26], and electrostatic crop spraying[33].

The maximum charge which can be carried by an individual particle, is directly related to the surface area. Thus the force exerted on a particle in an externally applied uniform electric field, which is equal to the product of

particle charge and electric field magnitude, is also directly related to the surface area. Since the gravitational force on the particle is directly proportional to the particle volume, the ratio of electrostatic to gravitational forces is inversely proportional to the particle diameter. Consequently, as the particle size decreases, the importance of electrostatic forces increases. Hence many practical particle handling situations, are much influenced by electrostatic forces, which can arise directly from contact electrification. Utilisation of contact electrification with particulate systems, likewise offers much scope for future development.

In general, the problems and hazards due to contact electrification are widespread, since charging is involved to some degree in almost all material handling operations. However applications of contact electrification are at present quite limited, and are specific to particular situations.

1. 3. Theoretical models describing contact electrification.

The three basic questions which need to be answered, in order to predict the magnitude of contact electrification, between known materials under defined contact conditions, have been stated by Harper[34] as follows. (a) Which charge carries move? (b) Why do they move? (c) Why does the process come to an end?

Harper[7] has analysed charge transfer involving metals and semiconductors in terms of quantum mechanical electron effects. The driving force for the charge transfer process is the difference in Fermi levels between the contact materials. In general the Fermi level corresponds to that energy level which has a probability of 1/2 for being occupied by an electron[35]. For a metal, the Fermi level corresponds to the highest occupied electron energy level at $0^{o}K$[35]. Conditions at room temperature are similar to those at $0^{o}K$ with regard to the Fermi level[35]. The prediction from this analysis[7], is that if both materials are metals, the charge density after contact, at thermodynamic equilibrium, will be directly proportional to the work function difference between the metals. The work function is the minimum energy necessary to remove an electron from the interior, and take it to rest outside the material. The relations derived for semiconductors are more complex and depend on the doping properties. Harper[7] has extended the analysis to insulators, and concludes that for material with

a resistivity greater than $10^{10}\Omega m$, very little charge transfer will occur due to filling of bulk traps at a discrete energy level. This indicates that the theoretical approaches of Van Ostenberg[36] and Mott[37] are in fact incorrect, since they are based on bulk electron transfer.

Several other theories have been proposed for charge transfer involving insulators. These theories are sophistications of the Volta-Helmholtz hypothesis[7]. This attributes charge transfer to the formation of a charge double layer at a solid/solid interface, the effect of sliding acting merely to increase the area of contact. Henry[8] has derived an energy band scheme to describe ionic transfer. Unfortunately the ion energy levels cannot be deduced from known quantities.

Electron transfer theories have been reported by Davies[38], Chowdry[39] and Garton[40], for transfer into the material bulk. Davies[38] assumed that the charge injected into an insulator was not dependent on the concentration of charge carriers in the bulk, and was in fact uniform in depth. On this basis, he predicted that the charge transferred, would be proportional to the effective work function difference between the contact materials.

Chowdry[39] has pointed out inconsistencies in Davies'[38] theory, and has proposed a further theoretical approach, based on either a uniform trap distribution with respect to energy levels, or discrete trapping levels. The former case leads to a prediction that the charge density will be directly proportional to the work function difference between the contact materials, whilst the latter case leads to a prediction that charge will be related quadratically or exponentially to the work function difference, depending on the band bending and the energetic position of the traps. The time required to transfer a charge density of approximately $10^{-4} C\ m^{-2}$ is estimated to be of the order of 120s[39]. Inconsistencies which arise in the theory of Chowdry have been discussed by Wintle[41] and Chowdry[42].

Garton[40] has devised expressions for the charge transferred to an insulator having traps or "self-traps" at a single energy level. The theory is based on a classical approach, and predicts a large increase in charge transfer for a contact potential difference greater than 0.5V, between the contact metal and insulator. The increase is due to the importance of quantum mechanical restrictions

at 0.5V contact potential difference. For contact potential differences less than 0.3V, the predicted charge transfer approaches zero.

Charge transfer associated with surface state charge sites on an insulator, has been considered by Krupp[12]. This analysis applies to electron charge carriers. The surface states may be due to impurities or to the actual insulator material[7]. The surface charge density, following contact between a metal and an insulator at thermodynamic equilibrium is given by[12],

$$\sigma = \frac{ZeD_s(\varphi_m - \varphi_p)}{1 + \frac{ed_cD_s}{\varepsilon_o}}, \qquad 1.1$$

including a modification suggested by Hays[2], to account for the real contact area differing from the apparent contact area, and using the correct dimensions[2]. In equation 1.1 σ is the surface charge density ($C\,m^{-2}$), e is the electronic charge, ε_o is the permittivity of free space, d_c is the separation distance between the metal and the insulator over which charge transfer occur (approximately 4×10^{-10}m), φ_m and φ_p are the metal and polymer work functions respectively (eV), D_s is the density of surface states (unit energy level)$^{-1}$, in the band gap between the valence and conduction bands ($m^{-2}eV^{-1}$). D_s is assumed uniform. Z is the ratio of real to apparent area of contact, (this can have values in the range 1 to 10^{-7} [2,7,43].

If D_s is greater than $10^{18}m^{-2}eV^{-1}$, then equation 1.1 simplifies to

$$\sigma = \frac{Z\varepsilon_o}{d_c}(\varphi_m - \varphi_p). \qquad 1.2$$

If D_s is less than $10^{16}m^{-2}eV^{-1}$, then equation 1.1 simplifies to

$$\sigma = ZeD_s(\varphi_m - \varphi_p). \qquad 1.3$$

In the presence of an applied electric field E, equation 1.1 can be written as[2]

$$\sigma = \frac{ZeD_s(\varphi_m + \int_o^{d_c} E\,dy - \varphi_p)}{1 + \frac{ed_cD_s}{\varepsilon_o}}, \qquad 1.4$$

where y is the distance normal to the metal surface. Simplifications equivalent to equations 1.2 and 1.3 can be derived from equation 1.4. The situation of D_s greater than $10^{18}m^{-2}eV^{-1}$ has been shown to be the probable case for certain

polymers[2].

The theoretical approach of Henry[8] to ionic transfer has also been modified to describe the effect of an applied electric field[7,8]. In this case, as with the surface state electron approach, the prediction is that the relation between the applied field and the charge transferred is linear for an abundance of available ions.

It is apparent that at present there are several theories available to describe charge transfer. The observed diversity of experimental results as discussed in Section 2.1, suggests that none of these theories has universal applicability.

1. 4. Previous experimental work.

Previous experimental work has concentrated either on the fundamental physics of charge generation, or on obtaining empirical information for a particular practical situation.

A summary of previous experimental studies associated with the fundamentals of charge generation, is given in Section 2.1. From this summary, it will be apparent that there is still considerable uncertainty with regard to prediction of the effect on charge transfer of (a) dissipation processes and (b) several independent mechnical variables, for example the force during contact and the mode of contact. The applicability of the charge transfer models discussed in Section 1.3 is also not at present known, and transient charge characteristics are not well understood.

A summary of experimental studies involving particulate systems, is given in Section 4.1. Measurement of a particular variable, such as the potential of a metal probe immersed in a fluidised bed has been carried out. This has been assumed to characterise the electrification behaviour of a particular system, and extrapolation to general material handling processes is not possible.

1. 5. Scope of the present work.

In any practical situation it is the combination of contact electrification and dissipation processes, which determines observed charge levels. Thus, it is essential initially, to obtain independent understanding of the variables affecting the fundamental charge transfer mechanism, and the dissipation processes.

Thus, the first aspect of the present work, involved devising and using experimental apparatus, designed to study contact electrification and dissipation processes at a single well defined contact. This work is described in Chapters 2 and 3.

In practical processing situations, contact electrification is of great importance with regard to particulate material. In order to minimize hazards arising from contact electrification or devise new applications resulting from contact electrification, it is necessary to understand the modifications to individual particle charge behaviour, arising as a result of the presence of a particulate mass. Thus the second part of the study, involved investigating the electrification characteristics of a vibrated particle bed. This study, described in Chapters 4 and 5, was designed to permit conclusions to be drawn, of relevance to general particle handling situation.

The final part of the present work involved devising two new applications associated with particle charging. The first utilised particle contact electrification occuring naturally in a fluidised bed, to improve heat transfer from an immersed heater surface. The second application utilised induction charging applied to a vibrated particle bed, to permit the design of a novel electrostatic separation device. These applications are described in Chapter 6.

CHAPTER 2

FUNDAMENTAL STUDIES OF ELECTRIFICATION AT A SINGLE CONTACT.

PREVIOUS WORK, EXPERIMENTAL APPARATUS, AND CALIBRATION PROCEDURES

The basic requirements for a study of the fundamentals of charge transfer are:- (1) a well-defined contact situation, (2) elimination or measurement of dissipation processes, accompanying charge production. Several previous investigations have been carried out with these ideas in mind as discussed in the following summary.

2. 1. Previous investigations and areas requiring further study.

Harper[7,44], Bredov[45], and Lowell[46] have examined contact electrification between metals of measured work function under well-defined contact conditions. They find that the charge remaining after separation is directly proportional to the work function difference between the materials. This observed behaviour confirms the theory of contact electrification[7] mentioned in Chapter 1, which is based on Fermi level equalisation between metals.

It is reasonable to expect that similar considerations will apply to low resistivity semiconductors[7], and some evidence for the importance of electron transfer with contact electrification of semiconductors has been presented by Krupp[47] and Kasai[48].

The contact electrification behaviour of insulating material, as a function of charge carrier energy distribution, is not well understood. Experimental work performed at atmospheric pressure[49-58] is subject to air breakdown limitations, which complicate interpretation of the results.

2. 1.1. The relation between contact area and charge transferred.

Several studies[50,58,59] indicate, that provided the interfacial temperature rise is small, the effect on charge transfer of relative movement between materials, is simply to increase the area of contact. This is in accord with the Volta-Helmholtz hypothesis[7] mentioned in Chapter 1. However, air discharge processes occurred in the work of Rose[50] and Davies[58], which obscured the dependence of the initial charge transferred on the contact area.

Davies[58] investigated the charged dielectric area produced by contact

between a metal sphere and a dielectric plane for several applied forces. The dependence of the contact area on the normal force was interpreted in terms of the elastic deformation theory of Hertz[60]. The classical theory of Hertz[60], for the contact between a sphere and a plane undergoing elastic deformation, predicts that the area of contact A' is given by,

$$A' = 2.43\left[\frac{FR_p}{Y}\right]^{\frac{2}{3}} , \qquad 2.1$$

where F is the normal force exerted by the sphere on the plane, R_p is the sphere radius, Y is the Young's modulus of the polymer. Equation 2.1 has been derived by assuming the polymer Young's modulus is much less than that of the contact metal, and that Poisson's ratio for the polymer is equal to 0.3[7].

The area measurement technique used by Davies[58], relied upon induction probe measurements (a description of induction probe operation is given in Section 2.5). The area for given contact conditions was determined from the induction probe potential, by assuming a realistic charge density for the surface charge, in order to obtain agreement with the Hertzian[60] area prediction of equation 2.1. The charge density was determined from the smaller area values, and was assumed to remain constant with changing area of contact.

However, in calculating the expected area from equation 2.1, Davies[58] appears to have used incorrect units for the polymer Young's modulus, resulting in an overestimate of the expected area, by approximately two orders of magnitude. If the correct areas are calculated (FIG.1) assuming $Y = 3.25 \times 10^{9} N\ m^{-2}$, then using the probe calibration given implicitly by Davies[58], the necessary surface charge density is found to be $3.76 \times 10^{-4} C\ m^{-2}$. This value can be shown to be consistent with limitation due to air breakdown effects, using the Paschen curve (Section 3.4) and the potential across the air gap[61] for the surface charge density. The measured areas and the Hertzian area prediction are shown in FIG.1. It is apparent that for areas greater than $2.5 \times 10^{-8}\ m^2$, the experimental area diverges markedly from the prediction. This divergence is found to occur when the charged area is a factor of 30 smaller than the probe area used by Davies[58], and Davies'[58] original conclusion that the non-linearity was due to the similarity of probe tip and charged areas is considered

incorrect. It is probable that the Hertzian[60] relation does not describe the real contact area in the case. Confirmation that the Hertz[60] analysis is probably inappropriate can be found in the results of Wåhlin[51,59].

Wåhlin[51,59] measured both the charge transferred, and the track width, for various values of the applied force and contact sphere radius, for sliding contact between metal spheres and Teflon plane surfaces. The conclusion from both of Wåhlin's investigations[51,59], at atmospheric pressure[51] and under vacuum conditions[59], was that the charge transferred per unit length travelled was independent of the radius of curvative of the contact sphere. This behaviour is expected where the force of contact is supported by plastic deformation of the dielectric over the contact area[62,63], or by elastic deformation of a large number of small asperities on the dielectric, in the contact region[59].

In the case of plastic deformation, $A' \times p_m = F$, where p_m is the yield pressure of the material.

Thus, d_w the track width $= \left[\frac{4F}{\pi p_m}\right]^{1/2}$.

Thus, if the charge transferred is directly proportional to the contact area, then the charge $\left[\begin{matrix}\text{unit length} \\ \text{travelled}\end{matrix}\right]^{-1} = \sigma d_w = \sigma \left[\frac{4F}{\pi p_m}\right]^{1/2}$, where σ is the charge $(\text{unit area})^{-1}$.

If the surface charge $(\text{unit area})^{-1}$ remains constant as the force is changed, then the charge $(\text{unit length})^{-1}$ should be proportional to the square root of the applied force. The fact that this dependence was observed by Wåhlin[59], indicates that the charge $(\text{unit area})^{-1}$ is independent of force, and that the charge transferred is directly proportional to the contact area. However, some departure from linearity was observed (FIG.2) for the largest applied force. The charge levels observed, as a function of $(F)^{\frac{1}{3}}$, as would be predicted by elastic deformation theory (equation 2.1), are also shown in FIG.2. It is apparent that within experimental error, a linear relation is found. It is not possible to differentiate between the deformation theories on this basis alone. However, the lack of dependence of charge $(\text{unit length})^{-1}$ on radius of curvature of the contact metal, provides conclusive evidence that Hertzian[60] elastic deformation theory is inapplicable.

The effect of relative movement between the contact materials has been shown to be of great importance for charge separation[10,55]. O'Neill[10] and Kornfel'd[55] report that very little charge transfer resulted from contact of materials alone, whereas relative movement during contact produced greatly increased charge levels. This could be explained as follows[7]. The absence of relative movement results in contact occuring at only a few asperities of small total area. Movement multiplies the number of contact asperities, the real area of contact, and thus the charge transferred.

2. 1.2. Previous studies of variables influencing contact electrification and dissipation processes.

In order to understand the mechanism of charge transfers across an insulator/metal interface, several investigators have studied the effect of an applied electric field[2,3,9,64-68].

Hays[2] and Medley[3] both report an approximately linear dependence to charge on the applied electric field, as expected on the basis of ion or surface state electron transfer theories (Chapter 1). However, interpretation of these results is difficult due to uncertainties as to the particular mechanism responsible for the electric field effect[3]. Induction effects are of overiding importance in some studies[9,66,67], whilst modification of the actual charge transfer mechanism has been postulated to explain further results[68]. Inculet[64,65] observed a maximum and minimum in the charge transfer occuring between a metal and a dielectric, as the field strength was varied. This result is not anticipated on the basis of charge transfer theories proposed to date (Chapter 1).

The effect of temperature on charge transfer is not well understood. Conduction[65] effects were found to increase with increasing ambient temperature, and the ambient pressure has been found to modify temperature effects[10]. The temperature gradient at the contact has been observed to modify the charge magnitude[10,69,70], although no clear pattern of behaviour has emerged.

Attempts to elucidate fundamental mechanisms of charge transfer, have utilised metal/insulator contact, using various metals of different work functions.

Several theories mentioned in Chapter 1, have been proposed, relating electron charge transfer to a particular functional dependence on the work function difference between the contact materials[7,12,36-40]. Each of these theories assumes that one dominant mechanism is responsible for charge transfer. Whilst this situation may prevail in any individual instance, it is certainly not universally true, as shown by the divergence of reported results from different investigations[7,38,59]. In fact, the large variation of measured charge observed, under well-defined and apparently identical conditions[52,71], suggests that more than one mechanism is operative at any one time.

Nevertheless, some studies have been reported[38,52,59,72-80] which indicate one mechanism is dominant under particular conditions.

Several investigators report finding for metal/insulator contact, a linear dependence of the charge transferred on the metal work function[38,52,59,72-75,78]. However, other results indicate a non-linear relation between charge transfer and metal work function[76,81], and in some cases the charge transferred was found to be independent of the metal work function[50,75,77,82].

The linear dependence of charge transfer on work function[38,52,59,72-75,78], supports the theories of Davies[38], Chowdry[39] for a uniform trap distribution, and Krupp[12] for surface state electron transfer. Some results of Davies[83] and Kittaka[81] have been used as confirmation for the theory of discrete trap levels presented by Chowdry[39] which predicts points of inflexion for the charge transferred as the metal work function is changed. Other results given by Davies, have been used to confirm the theory of Garton[40], which predicts essentially zero charging for a substantial range of metal work function values, with sharp increases in the charge levels when the contact material work functions differ by more than 0.5eV.

Several widely divergent theories then can be confirmed by particular experimental results, although no general theory is universally applicable. This reflects the large degree of variability of results. It is not possible at present to ascertain which of the theories mentioned, is most relevant for any practical situation, or indeed, if in fact other variables are involved, which must also be considered.

The fact that further variables may be involved seems probable, particularly when some additional results are considered. Harper[7], found that certain insulators which in subsequent investigations have charged strongly[38,59], gave no charge at all in contact with various metals. This was interpreted as evidence that electron transfer cannot occur with insulators[7].

Evidence for ionic effects has been provided by several investigators using a wide range of materials[55,79,84-89].

In any practical situation involving an insulator, it will probably have undergone surface charging at some point in its past history. This charge will often be neutralised by atmospheric ions,[7,8] and consequently it is to be expected that insulator surfaces will have an ionic coverage under normal conditions, and that contact charging will be affected by this ionic layer.

The lack of reproducibility of experimental observations under well-defined conditions, could be explained by an observation of Hays[90], that atmospheric ozone has a significant effect on the charge characteristics of polymers containing unsaturated material.

Investigations to date then, indicate that both ion and electron transfer may be important in contact electrification. The transient behaviour of material undergoing contact charging is not well understood. There are estimates of the necessary time for charge transfer varying from several minutes[38], to less than tens of milliseconds[59] under different conditions. It is possible that the long time constants are associated with a change in the real contact area.

The only explicit study of iothermal contact electrification bulk conduction, known to the author, which eliminates air breakdown effects and surface conduction, is that carried out by Davies[38]. Further investigations are required in this area, particularly in view of the theoretical mechanisms of conduction which have been developed for corona charged insulators[91-95].

The effect of air pressure on contact electrification has been studied by Medley[96], and Wåhlin[59], for flat polymer sheets. The general behaviour has been established, however detailed behaviour is uncertain, particularly

the applicability of empirical equations developed for air breakdown with conductor systems, and the effect of charge non-uniformity. Studies of contact modes other than the perpendicular case, are extremely limited for situations where dissipation processes have been characterised. Rolling contact has been studied by Davies,[72,73] and sliding contact by Wåhlin[59], and O'Neill[10]. Davies[72,73] only reports studies of metal work function and polymer material, in all cases for contact times of at least several minutes in total.

Wåhlin[59] made no detailed measurements of the charge distribution subsequent to contact, or of the transient characteristics for contact times less than 60ms.

O'Neill[10] studied only the charge on the polymer sheet in the direction of contact movement, and the transient behaviour was not investigated.

2. 1.3. Some fundamental aspects of contact electrification requiring further study.

Bearing these facts in mind, further knowledge is required in the following areas:-

(1) A greater understanding of dissipation processes.

(2) Identification of transient charging behaviour.

(3) Identification of the effect of the mode of contact on charge transfer.

(4) Further study of the effect of metal work function and polymer material on charge transfer during rolling or sliding contact.

(5) Clarification of the relation between charge transferred and the normal force applied during contact, for higher loads than those observed by Wåhlin[59].

In order to study these phenomena, experimental apparatus is necessary which facilitates production of contact electrification under well-defined and known contact conditions, at controlled air pressure levels. A non-destructive charge measurement technique is required, to permit study of dissipation processes. Measurement of charge on both contact members is preferable, allowing a check on the accuracy of the charge measurement methods. Continuous charge measurement is also required, in order to study transient effects. The utilisation of normal commercial materials is desirable, since this permits extrapolation of the results to practical industrial situations. The apparatus described in the following sections was designed to meet these requirements.

2. 2. Vacuum chamber system.

The overall assembly is shown in FIGS. 3 and 4. The assembly consisted of a dural vacuum vessel (A), mounted on a mild steel framework (L), above an Edwards two inch combined vacuum pumping unit, code no. A088-15-000. Two viewing ports were provided in the vacuum vessel (B,C).

Pressure measurement, for the range 3 to 10^{-2} torr was by means of an Edwards Pirani 10 thermal conductivity gauge (η), the sensing head being located adjacent to the rotary pump (Y). Pressures below 10^{-2} torr were measured using an Edwards Penning 8, cold cathode ionisation gauge (K), the gauge head being mounted on the vacuum vessel (I). Pressures above 3 torr were measured using a mercury manometer, which was connected in place of the Pirani 10 head, when required. When controlled pressures above the minimum value were required, an Edwards needle value, series LB, was connected to the two inch spacer (β). Further controlled air leaks were available using an air admittance valve located adjacent to the rotary pump. Atmospheric pressure was measured using a conventional Fortin barometer.

Supported inside the vacuum vessel, the dimensions of which are shown in FIG.5, was a turntable unit, and from the hinged lid, an induction probe, and a sphere support system, as shown in FIG.6. The horizontal lid position was maintained constant using a brass cylindrical spacer on the support hinge (FIG.5). The turntable unit construction is shown in FIGS. 6,7. This consisted of a 228mm diameter dural disc, 19.1mm thick, supported in the horizontal plane. A 0.7mm thick, 17mm wide, gold plated ring was secured to the upper face of the disc, close to the outer edge. On top of this ring, equally spaced around the upper surface, were 4, 12.7mm diameter, 2.5mm thick gold plated discs. The base metal for the ring and discs was brass.

Dielectric specimens could be attached firmly to the table surface using 6BA threaded holes in the dural disc.

The dural disc was supported by a steel shaft, which was held vertically by a tufnol, and a graphite loaded nylon bush, in the gear support unit. The steel shaft and dural disc were electrically isolated. A commutator and carbon brush

slip ring arrangement, mounted as shown in FIG.6, enabled any required potential to be applied to the disc, via an electrical vacuum feedthrough located in the vessel base. The gear unit housing contained a 3:2 Delrin® bevel gear arrangement, which transmitted rotation of the horizontal shaft to the turntable. The turntable and gear unit was moveable in the horizontal plane, being supported by two parallel circular steel runners. The gear unit was clamped to these runners with PTFE pads. This provided a stable and low friction clamping arrangement. Horizontal table movement was obtained from a vertical rotary shaft movement, transmitted through the vessel base via a $\frac{1}{4}$" Edwards rotary vacuum coupling, to a 3:2 Delrin® bevel gear arrangement. This translated rotation of the vertical shaft, to a $\frac{3}{8}$inch Whitworth threaded rod in the horizontal plane, parallel to and supported between, the circular steel runners. A correspondingly tapped brass block was firmly mounted to the gear unit, and rotation of the threaded rod, which passed through the brass block, resulted in horizontal table movement. The table height was constant to 0.001 inch (0.025mm) throughout the transverse movement.

The drive motor was a Fracmo 1500 R.P.M. 12lb in, synchronous motor (FIG.4), with a built in gear reduction to 73.2 R.P.M. This was connected to the Edwards rotary feedthrough, using a Universal connection. The table position was monitored using a variable resistor used as a potential divider, coupled via a 10:1 gear reduction, to the drive shaft outside the vessel (FIG.4). The output from the position monitoring circuit was transmitted to one channel of a 4 channel Honeywell 1706 ultra/violet recorder, the galvanometer of which could respond to an 18Hz oscillation. This was a sufficiently fast response time for present purposes. A series of turntable rotations was performed with a dielectric specimen on the turntable, whilst a sphere was contacted from a known position in the vessel lid. By measuring, with a travelling microscope, the position of the observed track on the disc surface, for several different horizontal table positions, and comparing this with the position sensing output from the ultra/violet recorder, it was possible to calibrate the position sensing device. Micro-switches were positioned as shown in FIGS.6,7, which automatically

switched off the drive motor when they were operated by the gear unit movement. The switching circuit, which also contained a manual direction reversal switch, was designed to operate the micro-switches in the vacuum vessel at 12V, to avoid arcing problems. The total traverse length was 110.8mm, with a constant linear table speed, relative to the surrounding vessel of 2.72mm s^{-1}.

Rotary table movement was provided by a 1500 R.P.M. 1/16hp, synchronous Fracmo motor (FIG.4). Rotation was transmitted from the motor, via a 5:1 reduction toothed belt drive, to a Kopp continuous variable speed gear unit, then, via a Universal coupling to a gearbox constructed in the Department. The gearbox provided a ratio 1:1, or reduction ratios of 5:1, 25:1, and 125:1, as required. The rotation was further transmitted via another Universal coupling, and a support bearing, to a 1:1 toothed belt drive. The connection of the upper wheel of the belt drive to the $\frac{1}{4}$" Edwards rotary vacuum feedthrough, was via a keyway. Rotation inside the vacuum vessel was transmitted from the Edwards coupling, to the horizontal shaft in the turntable gear housing, via a Universal coupling (FIG.6).

The speed of rotation of the horizontal drive shaft, prior to the turntable unit, was monitored using a photocell arrangement, mounted as shown in FIG.4. This consisted of a brass disc, mounted on the rotating shaft, 110mm in diameter with a 5.5mm wide slot, aligned with a static photocell and light source. When disc rotation occurred, movement of the slot produced a light pulse at the photocell. The photocell output pulse was detected using suitable circuitry, and shown on a 1.2 MHz Racal counter timer. By measuring the number of pulses over a known period, the circular table speed was determined for various variable speed settings.

2. 3. Sphere support unit.

2. 3.1. Mechanical construction.

The mechanical sphere support system is shown in FIGS. 8,9. The sphere could be moved accurately in the vertical plane, from outside the vacuum vessel, to within 0.1mm, and was moved initially to the required horizontal position. A 2.0mm diameter silver steel shaft, was secured to each sphere through a hole

located along a diameter. The attachment was by means of soldering for metal spheres, and epoxy resin for the hollow aluminium spheres, sufficient metal/metal contact being maintained to ensure a contact resistance of less than 2 Ω. The dielectric spheres were attached by compression fitting. The silver steel shaft was supported in PTFE bushes which were held in a brass stirrup. The maximum sphere size which could be accomodated was 19.1mm diamter. Two brass discs were held at either end of the silver steel support rod, by steel pins passing through the rod and the discs. The brass discs maintained the sphere horizontal position constant for spheres of diamter less than 19.1mm, and also permitted electrical contact to be made to the sphere, via a spring-loaded carbon brush at one end. The sphere could be clamped rigidly when required at the other end, using a metal clip and a 10BA tapped hole in the brass disc.

The shaft holding the saddle unit, was covered with a PTFE sleeve over the upper part of the length, to reduce horizontal sphere movement to a minimum. The sphere was held in contact with dielectric specimens by the action of a spring in the carrier unit (FIG.9). The total normal force between the sphere and the plane was equal to the weight of the carrier unit, together with the force exerted by the spring. The carrier weight was measured, and the spring was calibrated for force as a function of extension, as follows.

The vessel lid was mounted horizontally, with the sphere carrier shaft positioned in the upward vertical plane. The sphere support saddle was removed and replaced by a flat metal plate of known weight, upon which further weights of known value could be placed. The extension of the spring, relative to the fully compressed position, was measured using a mechanical vernier system, for known applied weight. The relation between spring extension and the number of turns of the control button relative to the end movement point, was measured independently. Both of these relations were linear, and by eliminating the spring extension between the two, the relation between the number of control button turns, and the force was obtained, for three different springs.

When charging experiments were carried out, the number of control button turns required to give contact between the sphere and the dielectric was

observed visually, hence the force during contact could be calculated. The vertical position of the brass support saddle, relative to the support shaft, could be varied, allowing the same force to be exerted for different sphere sizes. The spring calibration, both before and after experimental runs, was found to be identical.

2. 3. 2. Charge measurement.

The charge transferred to the sphere was measured using a Vibron® 33B-2 electrometer, connection being via the carbon brush system, and a vacuum feed-through in the vessel lid. Anti-microphonic coaxial cable, was used where appropriate for electrical connections in the present study, including connection to the sphere. The input capacitance of the electrometer was selected to give a suitable full scale range. The value of this capacitance, together with associated input leads, was determined to an accuracy of 0.5% using a Wayne Kerr B 221 capacitance measuring unit and an AA 221 autobalance adaptor, which utilised an alternating current bridge circuit.

The electrometer leakage current was a maximum of 10^{-15}A. Since the minimum measured charge levels were of the order of 4×10^{-10}C, and maximum measurement times were of the order of 1 hour, the leakage current introduced a maximum measurement error of 1%, and in most cases the error was one hundred times less than this value. The electrometer zero drift of 0.1mV in 12 hours was sufficiently small not to affect measurements.

Measurements of charge at the upper end of the contact velocity range were influenced to a certain degree by the slow response time of the electrometer. A correction was required for this effect, and could be derived from the measured electrometer response to a step change in the input potential. The electrometer output was observed on one channel of the same ultra/violet recorder used for position monitoring. The galvanometer could respond to a 24Hz signal, a sufficiently fast response.

The electrometer response to a step change in the input potential was determined by applying a charge from a storage capacitor. A known capacitor was charged to a given potential from a voltage source through a series

resistance. By a manual switching operation, very rapid transfer of all the charge on the storage capacitor to the electrometer input capacitance was achieved.

In order to ensure total transfer of charge from the storage capacitor to the electrometer, the electrometer capacitance was equal to 210 x storage capacitance. The electrometer response was found to be slightly underdamped (FIG.10) and independent of the input capacitance and range. The electrometer potential after the step charge, agreed well with the expected value, calculated from the charge originally on the storage capacitor. In order to calculate the required correction factor to account for the slow response time of the electrometer, it was assumed that the actual system could be approximately represented by a first order system, with a time constant equal to the time taken by the actual system to reach 63.2% of the final value.

Considering a general first order system, the potential output, V_o from this is related to the potential input V_i, in the Laplace Transform domain by[97],

$$V_o(S_L) = \frac{V_i(S_L)}{\tau_c S_L + 1} \quad . \qquad 2.2$$

$V_i(S_L)$ is the Laplace Transform of the potential applied to the network, and $V_o(S_L)$ is the Laplace Transform of the observed output potential. S_L is the Laplace Transform variable, τ_c is the system time constant (the time to reach 63.2% of the final value).

During transient charge experiments, for which the correction is required, the input to the electrometer can be considered as a ramp change with respect to time.

Thus $V_i(t) = A_1 t$, where A_1 is a constant. The Laplace transform of this is given by[98],

$$V_i(S_L) = \frac{A_1}{S_L^2} \quad . \qquad 2.3$$

Consequently, by substituting for $V_i(S_L)$ from equation 2.3 into equation 2.2 and inversely transforming, $V_o(t)$ can be determined. The inverse transform follows from dividing the expression into partial fractions. The result is given by,

$$V_o(t) = A_1[t - \tau_c(1 - e^{-t/\tau_c})].$$

This defines the output potential for a ramp change in the input potential. When t/τ_c is greater than 3, then,

$$V_o(t) = A_1(t - \tau_c) \text{ to within 5\% .} \qquad 2.4$$

The value of V_o required in the experimental results, is that corresponding to V_i at any time, which is given by $V_i = At$. If t' is set equal to $t + \tau_c$, then $V_o(t')$ is equal from equation 2.4, to $A_1 t$. This indicates that if the electrometer time constant is added to the actual elapsed time, the value of the output potential, unaffected by the electrometer transient characteristics, will be determined. This procedure was easily adopted, using the trace of the output potential from the ultra/violet recorder, during the charging experiments.

The assumption that t/τ_c should be greater than 3 was true in all cases, and in many instances t/τ_c was much greater than 3, resulting in a very small correction factor. The maximum correction required represented at most 25% of the final value, and consequently the initial approximation of a first order system is reasonable.

2. 4. Contact potential measurement.

Contact potential measurement for the metal sphere was carried out by a modification of the Kelvin method[99]. When two conductors are connected together at thermodynamic equilibrium, electron flow occurs until the Fermi level of each is equal[7,100]. This results in a potential difference, the contact potential difference, appearing across the gap between two conductors if their rear faces are connected together. The contact potential difference is numerically equal to the work function difference in eV. If the metal of interest and a reference metal of known work function, form the electrodes of a capacitor, and they are electrically connected through a resistor, then a change of capacitance will cause a current to flow through the resistor. If an external bias potential is included in series in the circuit, and adjusted until any capacitance change produces no potential drop across the resistor, then the contact potential difference, is equal in magnitude, and opposite in polarity to the applied potential[101].

The measurement circuit used is shown in FIG.11. A detailed analysis of this

for vibrated electrodes has been given by Anderson[102] and Macdonald[103], whilst Guptill[104] gives a simplified analysis. Vibrating electrode contact potential measurement systems, have been employed in studies of contact electrification by several investigators[7,10,38,46,52,59,72-74,77].

In the present experimental apparatus, it was possible to utilise the rotating table movement for contact potential measurement, in a similar manner to that described by Kolm[105]. The gold plated ring and four gold plated discs formed the reference surface, and the discs produced a periodic change in capacitance with respect to the test sphere, when the turntable was rotated. The table was positioned so that the discs could be rotated immediately beneath the metal sphere of interest. The observed signal is proportional to the rate of change of capacitance[104], which in turn is proportional to the maximum capacitance. Consequently, by carefully reducing the gap between the sphere and gold discs, the capacitance and hence the measured signal was increased.

The signal was measured using a solid state electrometer device, constructed in the department, with a built-in amplification stage and an input resistance of $5 \times 10^7 \Omega$. The signal was displayed on a Marconi oscilloscope Type TF 2203.

The table circular speed was 94 R.P.M., for all the contact potential determinations. The bias voltage was applied from a 4.5V battery, to the whole electrically isolated section of the turntable unit, and was measured using a range box and galvanometer, having a minimum full scale range of 100mV. The maximum noise level due to stray capacitance effects, was equivalent to 25mV at the input. Measurements to this accurancy were acceptable, since the range of contact potential values was approximately 1V, and contact potentials are sometimes subject to variation of approximately 100mV, due to differences between various samples of the same material[101].

The measured contact potential was independent of the separation distance between the sphere and the gold discs, confirming that stray capacitance effects were negligible. Sensitivity of course decreased with increasing separation distance. The contact potential measured represented an average value over an area of the sphere close to the discs. The change in measured contact potential values, when different parts of the sphere were placed adjacent to the discs,

was below measurement accuracy, indicating that the work function of each sphere was substantially constant over the surface.

In order to determine the metal work function from the measured contact potential, it is necessary to either assume, or measure independently, the work function of the gold reference surface. Early measurements of the work function of gold, indicated a value of 4.7eV , whilst later results gave a value of 5.32 eV[106]. This difference is attributed to a chemisorbed mercury layer in the former experiments, caused by a mercury diffusion pump being used[106]. In general it is rather uncertain as to the actual value which should be used. Since in contact electrification studies, it is the relative value, rather than the absolute value for different metals, that is important, results will simply be expressed as a contact potential relative to gold, rather than a work function.

The gold reference surface was chosen for its stability with time, and its work function is not expected to vary outside measurement accuracy, under the experimental conditions employed in these investigations. Using the technique described, contact potential values of several metals were measured and are shown in Table 1. These values are in reasonable agreement with previous measurements[107]. The contact potential in all cases was found to decrease at the rate of approximately 15mV per hour, during the first two hours of exposure to vacuum conditions. The contact potential of aluminium changed markedly as shown, when the oxide layer was removed by rubbing with very fine abrasive paper. The oxide layer re-formed in a time period of less than two weeks, returning the work function to the original value. The oxide layer effect was much less marked with the other metals. Measured contact potential values during experimental work, were found to lie within $\pm$ 50mV of the values shown.

2. 5. Induction probe unit.

2. 5. 1. Mechanical construction.

The mechanical support system is shown in FIG.12a. Movement of the probe tip was possible from outside the vacuum vessel, with controlled and measured accuracy to 0.001 in (0.0254mm). Rotation of the control button outside the

vessel, which had a tapped interior hole, moved a threaded rod vertically. This was connected by a mechanical lever and pivot, to the probe tip assembly, and produced equivalent vertical movement, of the probe tip assembly. The control button scale was calibrated in 0.001in (0.0254mm) divisions, and the accuracy was confirmed by comparing the scale reading, with the probe tip movement, measured using a mechanical vernier arrangement. The probe could also be adjusted to various angular positions relative to the sphere support unit. The angular position was maintained at 180^{o} throughout the experiments described. The whole probe unit was secured to the vessel lid by means of a tapped brass block, which was screwed tightly to the threaded cylindrical section of the probe unit, protruding through the lid.

The probe tip (FIGS 12b,12c) consisted of a 0.132mm diameter enamelled copper wire (J), which was held in a 0.16mm diameter hole, drilled through the 8mm diameter brass screening electrode (H). This brass cylinder was supported on a threaded PTFE cylinder (N), which in turn was held on an 8BA threaded rod (M). The PTFE and brass cylinders were moved until the probe centre wire was visually level with the brass cylinder surface. The 8BA rod was secured by a nut into a brass block (K). This block was supported in a PTFE block (L), compression fitted to the brass cylinder (F), connected by the lever arrangement (P) to the movement system (Q).

The 8BA rod and part of the brass screening cylinder, were screened further by another brass cylinder (G), which maintained 0.5mm clearance between itself and the inner screening cylinder. This arrangement permitted the centre screening cylinder and probe sensing wire to be accurately lowered visually on to dielectric specimens, and by moving upwards a known amount, controlled separation could be obtained. The inner brass screening cylinder was connected to an anti-microphonic coaxial cable screen, which was connected via an electrical feedthrough in the vessel lid to earth. The centre wire of the probe was connected to the centre core of the coaxial cable and thence via an electrical feedthrough to an electrometer. The vessel itself was earthed, and all other internal metal parts were connected to a common earth point.

The probe tip height could be varied to accomodate different thicknesses of dielectric specimen. The probe tip design is similar to that described by Scruton[108].

2. 5.2. Mode of operation and input capacitance calibration.

Induction probe techniques have been utilised in several previous investigations of contact electrification[10,38,54,72,73,78,109]. Various probe designs[53,110-113], and electrometer circuits[110,114], have been proposed for charge scan measurement, whilst the theoretical relation between uniform surface charge and the probe potential has been derived by several investigators.[61,111,113,115-117]

For the physical situation shown in FIG.13a the relation between probe potential and surface charge density can be derived as follows[117]. FIG.13a shows a specimen of dielectric constant ε_{r2}, thickness L, resting on an earthed base plane. Parallel to, and at a distance g above the dielectric surface, is another conductor , representing the induction probe. The potential of the upper plane is measured using an electrometer of input capacitance C_E, and gain G.

The dielectric is assumed to have a uniform surface charge density σ on the upper surface, and V' is the potential of the upper surface of the dielectric. It is assumed that there is no volume charge distribution.

Charge densities σ_b and σ_p are induced on the lower and upper metal electrodes respectively, due to the dielectric surface charge. Charge densities $-\sigma_a$ and $+\sigma_a$ are on the upper and lower electrodes respectively, due to the potential of the measuring source. Except where otherwise stated, all quantities are expressed in units consistent with the rationalised S.I. system.

Considering cylinder A (FIG.13a), the field between the plates is uniform, and only components perpendicular to the plates exist. From Gauss's Law[118],

$$D_1 = -(\sigma_p - \sigma_a), \qquad 2.5$$

where D is the electric displacement.

The displacement in the conductor is equal to zero, since no steady state electric field component can exist in a conductor. The subscript 1, refers to the air gap region. Considering cylinder B, $D_1 - D_2 = \sigma$, 2.6

where the subscript 2 refers to the dielectric region.

Considering cylinder C,

$$D_1 = \sigma + \sigma_b + \sigma_a \quad . \qquad 2.7$$

The electric field is related to the displacement by[118], $E = \frac{D}{\varepsilon_r \varepsilon_o}$, 2.8

where E is the electric field, ε_o is the permittivity of free space and ε_r is the dielectric constant. In the air space $\varepsilon_{r1} = 1$.

$$E = -\frac{dV}{dy} \quad , \qquad 2.9$$

where y is the distance measured from the lower electrode (FIG.13a).

Integrating 2.9 over the dielectric region, and eliminating D_2 from equation 2.8 gives, $V' = -E_2 L = \frac{-D_2 L}{\varepsilon_o \varepsilon_{r2}}$. 2.10

Similarly, for the air space,

$$V' - V = E_1 g = \frac{D_1 g}{\varepsilon_o} \quad . \qquad 2.11$$

Eliminating V′ from equation 2.10 and equation 2.11 gives,

$$D_2 = \frac{-D_1 g \varepsilon_{r2}}{L} - \frac{V \varepsilon_o \varepsilon_{r2}}{L} \quad . \qquad 2.12$$

Substituting for D_2 from equation 2.12 into equation 2.6 gives,

$$D_1 = -\left[\frac{V \varepsilon_o \varepsilon_{r2}}{L} + \sigma\right]\left[1 + \frac{g \varepsilon_{r2}}{L}\right]^{-1} . \qquad 2.13$$

Thus from equation 2.8 with $\varepsilon_{r1} = 1.0$,

$$E_1 = -\left[\frac{V \varepsilon_{r2}}{L} + \frac{\sigma}{\varepsilon_o}\right]\left[1 + \frac{g \varepsilon_{r2}}{L}\right]^{-1} . \qquad 2.14$$

The charge on the upper plate $Q = A(\sigma_p - \sigma_a) = -AD_1$, from equation 2.5, where A is the area of the upper plate.

Thus using the value of D_1 from equation 2.13 gives

$$Q = \left[\frac{A \varepsilon_o \varepsilon_{r2}}{L + g \varepsilon_{r2}}\right]\left[V - \frac{\sigma L}{\varepsilon_o \varepsilon_{r2}}\right] = C_d(V - V_e) \quad , \qquad 2.15$$

where V_e is the equivalent potential of the surface charge $= \frac{\sigma L}{\varepsilon_o \varepsilon_{r2}}$,

C_d is the capacitance of the unit, $= \frac{A \varepsilon_o \varepsilon_{r2}}{L + g \varepsilon_{r2}}$.

The charge can be changed by changing C_d. The electrode forms a charge source or sink, charging or discharging the detector circuit.

Using the detector circuit shown, consisting of an integration condenser and electrometer, the following charge conservation equation can be derived,

$$dQ + C_E dV = 0 \quad , \qquad 2.16$$

where C_E is the capacitance of the electrometer input. By differentiating 2.15,

$$dQ = C_d dV + V dC_d - V_e dC_d \quad . \qquad 2.17$$

By substituting equation 2.16 into equation 2.17, integrating and rearranging, the following relation between the final potential and the capacitance change can be derived,

$$V_f = V_e \frac{(C_{df} - C_{ds})}{(C_E + C_{df})} + V_s \frac{(C_E + C_{ds})}{(C_E + C_{df})} \quad , \qquad 2.18$$

where V_s and C_{ds} are the initial potential and capacitance, and V_f and C_{df} are the corresponding final values.

The detecting electrometer was constructed in the department according to the circuit diagram shown in FIG.14. The input lead capacitance was of the order of 160pF as measured by a Wayne Kerr capacitance bridge, and the input resistance was $1.5 \times 10^{13} \Omega$. The decay time constant consequently was equal to 2.4×10^3s. This was sufficiently long to ensure that during the maximum scan time of 4 s over charged areas, the error introduced by decay was less than 0.2%. The speed of response of the instrument, which had a response time constant of 1ms, was faster than the associated indicating equipment. This consisted of one channel of the same ultra/violet recorder used for position sensing and sphere charge monitoring. A galvanometer was used in the recorder, which could respond linearly to an alternating frequency at least as high as 80Hz. Since the scanning traverse speed was 2.72 mm s^{-1}, the rise time calculated from the response to an 80Hz signal, corresponds to a distance travelled of 0.017mm. This is much less than the estimated probe resolution as derived later, of 0.5mm. Consequently the response was sufficiently fast so as not to affect the observed charge levels.

When the probe is scanned over a charged area from a point initially very

far from the area, then $C_{ds} = 0$, and C_{df} from equation 2.15 $= \frac{A \varepsilon_o \varepsilon_{r2}}{L + g\varepsilon_{r2}}$.

Using values for a typical dielectric specimen, the maximum observed C_{df} for the present experiments, assuming $\varepsilon_{r2} = 6$, $L = 1.5 \times 10^{-3}$m, $g = 0.127 \times 10^{-3}$m, is found to be 8.2×10^{-16}pF. The surface area assumed for the probe was $3.5 \times 10^{-8} m^2$, which was derived from the calibration results discussed later in this section. It is apparent that C_{df} is less than 0.001% of C_E which was equal to 160pF, and therefore equation 2.18 can be written as

$$V_f = V_e C_{df}/C_E + V_s \quad .$$

If the electrometer gain is equal to G, then the observed output potential $V_j = GV_f = GV_e C_{df}/C_E + GV_s$. The potential increment due to scanning over a charged area, is equal to the potential when the probe is above the charged area, minus the potential when the probe is at infinity and C_{df} is equal to 0. This latter potential is GV_s.

Thus, $V_{mg} = V_j - GV_s = GV_e C_{df}/C_E$,

where V_{mg} is the potential increment with a probe to charge layer separation distance equal to g. Substituting for C_d and V_e from equation 2.15 gives,

$$\sigma = \frac{C_E}{AG}\left[1 + \frac{g\varepsilon_{r2}}{L}\right] V_{mg} \quad . \qquad 2.19$$

By considering the incremental potential change, as the charged area was scanned, any problems due to the small zero drift in the electrometer were eliminated.

The surface charge density can be determined from the measured probe potential, knowing g and L from measurement, and ε_{r2} from standard tabulations, if C_E/AG can be determined. This was achieved by measuring the probe potential for several different known separation distances from a 1.59mm thick dural disc, on the dural turntable, maintained at a known potential. The separation distance between the probe and dural disc, was determined by bringing the probe into contact with the disc, and moving the probe up a known amount. The dural disc was required in order to bring the table height within the probe movement range. Having positioned the probe as required, a step voltage change was applied to the disc from an A.P.T. Electronic Industries Model 509 voltage source. The applied potential was measured using a galvanometer and range box. The

resulting electrometer potential increment was recorded, and this procedure was repeated for several probe to plate separation distances.

The charge induced on the probe

$$Q = -A \varepsilon_o E, \text{ by Gauss's Law, (FIG.13b).}$$

From the line integral of the field, $E = (V_a - V)/g$, where V_a is the potential applied to the disc. Thus, $Q = (A \varepsilon_o/g) . (V - V_a)$. This expression can be differentiated as previously. Substituting into equation 2.16 knowing that $\frac{A \varepsilon_o}{g} \ll C_E$, and including the electrometer gain, then the electrometer potential increment V_m due to a step plate voltage change V_a, is given by

$$V_m = \frac{AGV_a \varepsilon_o}{C_E g} .$$

$$\text{Thus, } \frac{1}{V_m} = \frac{C_E g}{AGV_a \varepsilon_o} . \qquad 2.20$$

A plot of $1/V_m$ determined experimentally, against the measured probe to surface separation distance is shown in FIG.15 for V_a equal to 200V. As predicted from equation 2.20, the experimental points lie on a straight line passing through the origin. This confirms that the screening of the probe connections was adequate. The line would pass through a finite value on the $1/V_m$ axis if screening was inefficient. The value of C_E/AG determined from the slope of the line drawn through the experimental results, and equation 2.20, is $7.77 \times 10^{-4} F\ m^{-2}$.

The electrometer gain was determined independently by applying a known input signal and measuring the output potential. The gain was found to be 5.76, and since C_E was equal to 160pF, the effective probe diameter, calculated from the value of C_E/AG determined above, was equal to 0.213mm. This is of the same order as the expected value of 0.16mm, the discrepancy is due to tapering of the drilled hole in the brass screening cylinder.

The derivation for equation 2.20 assumed a uniform field in the gap, this was obtained by having a flat parallel screening electrode of area much greater than the exposed probe centre core area and close to the probe potential.

The charge tracks scanned in the experimental observations typically had widths greater than 0.6mm, consequently the above resolution was adequate.

The equations derived up to now have assumed that the surface charge density on the dielectric was uniform. In actual measurements charge tracks of finite widths were studied, and a correction for this is required, when converting observed probe potentials to surface charge densities. Murasaki[119] has analysed the response characteristics of an induction probe, to a single polarity sinusoidal charge distribution. The electric field at the probe surface can be determined by solving Laplace's equation in the air space and the dielectric region between the electrodes, using appropriate boundary conditions. The result is [119],

$$E_{1g} = \frac{\sigma_e\left[1 + \frac{B_g}{B_\infty}\right]}{2\varepsilon_o\left[1 + \frac{\varepsilon_{r2}g}{L}\right]} ,$$

for the electric field at the probe surface a distance g above the peak charge region, corresponding to a charge distribution, $\sigma = \frac{\sigma_e}{2}(1 + \cos px_1)$.

The physical arrangement is as shown in FIG.13a.

$$B_g = (\cosh pg + \varepsilon_{r2}\sinh pg \coth pL)^{-1} , \quad B_\infty = \left[1 + \frac{\varepsilon_{r2}g}{L}\right]^{-1} , \quad p = 2\pi/\lambda ,$$

λ is the spatial wavelength, x_1 is the distance coordinate, and g, L, ε_{r2}, ε_o are as defined previously.

The charge distributions measured in the present experiments were not sinusoidal, but consisted of a single peak, together sometimes with associated reverse peaks (FIG.16a). Consequently the electric field value given by Murasaki[119] is not directly applicable. However, the equation can be modified, to allow determination of the peak charge density from the probe potential, for the single charged peak. The actual distribution contains charges of both signs distributed approximately sinusoidally for one periodic distance. Assuming initially that the charge distribution does not terminate after one periodic distance, this can be described by $\sigma = \frac{\sigma_e}{2}(k + \cos px_1)$, as shown in FIG.16b, where k is a parameter to account for the presence of a bi-polar charge distribution. k is equal to 1.0 for the uni-polar charge distribution considered by Murasaki[119], and k is equal to 0 for a symmetrical bi-polar

charge distribution. An analysis similar to that of Murasaki[119] using this new charge distribution, yields for the field at the probe surface, above the peak charge region,

$$E_{1g} = \frac{\sigma_e \left[k + \frac{B_g}{B_{00}} \right]}{2 \varepsilon_o \left[1 + \frac{\varepsilon_{r2} g}{L} \right]} \quad . \qquad 2.21$$

This equation applies to a bi-polar sinusoidal charge distribution.

Murasaki[119] has shown that the average electric field over the probe surface, is related to the point field by

$$E_{1gAv} = \frac{\sin pR_{pw}}{pR_{pw}} E_{1g} \quad , \qquad 2.22$$

for a square probe tip, where R_{pw} is the probe tip width. As a first approximation the same relation is assumed for a circular probe of radius R_{pp}. For the conditions studied $\sin pR_{pp}/pR_{pp}$ is very close to 1, and this approximation is acceptable.

For the present experiments, V is less than 600mV, L is greater than 1.5mm, and ε_{r2} is less than 6, which gives a maximum value for $\frac{V \varepsilon_{r2}}{L}$ of 2.4×10^3. Since σ is greater than $10^{-6} C\ m^{-2}$, $\frac{\sigma}{\varepsilon_o}$ is greater than 1.13×10^5 and $\frac{V \varepsilon_{r2}}{L}$ can be neglected in equation 2.14. Thus

$$E_1 = \frac{\sigma}{\varepsilon_o \left[1 + \frac{g \varepsilon_{r2}}{L} \right]} \quad . \qquad 2.23$$

By substituting for $\frac{\sigma}{1 + \frac{g \varepsilon_{r2}}{L}}$ from equation 2.23, into equation 2.19, V_{mg} can be determined as a function of the field at the probe surface. Thus

$$V_{mg} = AG \varepsilon_o E_1 / C_E \quad .$$

If the field is non-uniform then for a probe to charge layer separation distance of g, $V_{mg} = AG \varepsilon_o E_{1gAv} / C_E$, and using equation 2.22 with R_{pw} equal to R_{pp} gives,

$$V_{mg} = \frac{AG}{C_E} \varepsilon_o \frac{\sin pR_{pp}}{pR_{pp}} E_{1g} . \qquad 2.24$$

Eliminating E_{1g} from equations 2.21 and 2.24 yields

$$\sigma_e = \frac{C_E}{AG}\cdot\left[1 + \frac{g\,\varepsilon_{r2}}{L}\right]\cdot\frac{pR_{pp}}{\sin pR_{pp}}\cdot\left[\frac{2\,V_{mg}}{k + \frac{B_g}{B_\infty}}\right] . \qquad 2.25$$

The charge density required is the value of σ_r, which from FIG.16b is seen to be $\sigma_r = \frac{\sigma_e}{2}(1 + k)$. 2.26

Thus substituting equation 2.25 into equation 2.26 gives,

$$\sigma_r = \frac{C_E}{AG}\cdot\left(1 + \frac{g\,\varepsilon_{r2}}{L}\right)\cdot\left[\frac{pR_{pp}\quad(1 + k)}{\sin pR_{pp}\left(\frac{B_g}{B_\infty} + k\right)}\right].V_{mg} \quad , \qquad 2.27$$

for the charge density of the peak charge region.

As λ approaches ∞, equation 2.27 becomes equal to equation 2.19 for a uniform charge distribution, as expected. The influence on the probe potential of charge regions distant from the probe, decreases with increasing separation distance, and the finite observed charge widths are much greater than the probe diameter. Thus, it is reasonable to expect that the probe potential corresponding to the peak region of the observed finite charge width (FIG.16a) which resembles part of a sinusoidal distribution, will be similar to the probe potential corresponding to the peak region of a complete sinusoidal charge distribution. Therefore, it is postulated that if k is considered as a general parameter, which describes the deviation of the actual finite charge distribution from the complete sinusoidal case, as well as the change from a uni-polar to a bi-polar charge situation, then equation 2.27 can be applied to the actual measured charge distribution. The distant regions in the complete sinusoidal case will have some influence on the probe potential, and thus the value of k in the finite charge width situation, will not correspond exactly to the geometrical interpretation of FIG.16b, which applies to the complete sinusoidal case. A means of determining an appropriate value of k for the actual measured charge distribution, will be described in Chapter 3.

The curvature of the charge line was considered to be zero for this derivation. This is reasonable, since the minimum charge cicle diameter was 40mm, whilst the probe resolution was 0.5mm, and the non-linearity can be shown to be negligible for these dimensions.

The probe resolution was checked using a printed circuit board, with conductive lines of measured width, etched into the surface. The board itself was made of 1.5mm thick insulating material coated with copper. The etched lines on the upper surface were joined by conducting paint at the edges, and similarly to the reverse metallised side of the board. The board was clamped to the dural disc surface and a high potential applied to it. The dural table was then moved beneath the induction probe, and the output signal recorded as the lines passed beneath the probe. For a probe to surface separation distance of 0.127mm, approximately 0.5mm of linear table traverse was required for the probe potential to reach its maximum value. This was close to the expected value[115] of approximately 1.5 x probe diameter, that is 0.32mm. The discrepancy is due to the probe centre core not being absolutely level with the screening cylinder, and the tapering effect of the drilled hole.

All line widths greater than 0.5mm, gave a constant electrometer output for the peak value, indicating the applicability of the technique to line widths greater than 0.5mm, on dielectric specimens. The resolution distance measured above, enabled a correction to be applied to the spatial wavelengths measured on dielectric materials. This eliminated any errors due to probe tip misalignment.

A number of different series resistors were used at the ultra-violet recorder input, to enable selection of different full scale deflections. These were calibrated by applying a signal from a millivolt box, directly to the resistor, the magnitude having been accurately monitored using a digital voltmeter.

Problems due to microphonics associated with cable movement at the electrometer input, were eliminated in the apparatus, since the probe was maintained in a fixed position, whilst the sample was moved relative to it.

It is apparent that the apparatus described, fulfills all the necessary requirements mentioned in section 2.1, for the experimental investigation. Experimental results obtained with this apparatus are discussed in Chapter 3.

CHAPTER 3

ELECTRIFICATION AT A SINGLE CONTACT. EXPERIMENTAL RESULTS AND DISCUSSION.

An experimental study of the dissipation processes subsequent to charge transfer, and of some of the variables affecting charge transfer, was carried out using the apparatus described in Chapter 2.

3. 1. Experimental techniques and materials studied.

The polymers obtained were commercial samples in most cases. Some specimens of additive free polyethylene (L.D.) and polypropylene, and some specimens of polyethylene terephthalate were kindly supplied by I.C.I. Plastics Division. The range of polymers studied is shown in Table 2 together with certain properties of interest. The spherical contact metal or polymer specimens, were supplied by Insley Industrial Limited. Gold, Silver, Nickel and Tin were electroplated on to brass spheres. A list of materials used, together with associated tolerances is given in Table 3.

Before any charging experiment was carried out, both the dielectric sheet, and the contact sphere were cleaned with a tissue soaked in isopropanal, a fresh tissue being used on every occasion. This cleaning technique is similar to that employed satisfactorily by Davies[72] for polymer specimens. As pointed out by Davies[72], over elaborate cleaning techniques lead to increased variability in the experimentally observed charging behaviour. Harper[7] has discussed the notion of a clean surface. He concluded that all real surfaces should be considered as brought to a standard prepared state, rather than an absolute state of cleanliness. The cleaning technique selected, was considered effective in bringing the materials to a standard prepared state, whilst retaining the natural material charging properties.

In order to ensure that no surface charge was present after cleaning, the dielectric specimens were exposed to an α-particle air ionisation source, which consisted of a 3M static eliminator Type 204. This reduced the surface charge below the detection limit of the induction probe, which was approximately equal to 4×10^{-7} C m^{-2}. Since the charge levels studied in these investigations were in general greater than 10^{-5} C m^{-2}, the discharging process was considered satisfactory.

During charging experiments, turntable rotation was initiated before contact was made. This avoided backlash effects in the gear system, modifying charge levels. Likewise, contact was terminated, before, table rotation was stopped.

The linear velocity values given in the following sections, are the velocities of area elements on the dielectric surface, at the radial position for which contact with the sphere occured. These velocities are calculated from the known circular speed and radial position.

The charge transferred to the contact sphere is frequently expressed as charge (unit circumferential length)$^{-1}$ in the following sections. These values are calculated from the quotient of the sphere charge, and the contact track circumference determined from the known radial contact position.

In all cases a fresh track was used on the dielectric specimens for each test. This avoided any progressive effect of changing surface properties, or changing contact area.

Induction probe measurements were carried out by lowering the probe on to the surface of the dielectric, and then raising the probe to a known height. The charge distribution normal to the charge track, was determined by moving the dielectric radially beneath the probe, at various angular positions. This avoided any effects due to the initial probe/surface contact. The charge distribution along the track length was determined by manually positioning the peak charge region directly beneath the probe, and rotating the turntable.

Preliminary studies showed that the degree to which the PTFE bearings supporting the contact sphere shaft, were tightened, had no effect on observed charge levels, over the tension range used experimentally.

The charge produced at a given contact, was subject to changes of up to 50% over periods of time of the order of days, although during any one set of runs on a particular day, the charge remained constant to within approximately 15%. The radial position over the measurement range of 20mm to 80mm track radius, had no effect on the surface charge density. This was confirmed by induction probe measurements and sphere charge measurements. The degree of slip during rolling contact was constant for all traverse radii used. This was confirmed

by counting the number of sphere revolutions, for identical linear speeds, at the extreme radial positions, over the same time interval. The number of revolutions was equal in each case, confirming that slip was identical in each case.

The width of the contact track was estimated by measurement with a travelling microscope, using a light source inclined at a suitable angle, to show the indentation as a shadow. For polypropylene under a load of 8.2N, this width was of the order of 0.7mm, whilst for a similar load on polyethylene, the track width was 1.2mm, in each case after 6 turntable revolutions. These values are significantly smaller than the observed charge widths given in Table 4, and indicate that diffusion effects or local surface conduction, probably occurred at the charge line edges. It is also possible that charged particles attracted from above the dielectric, contributed to this charge spreading effect. The line widths were calculated from plastic deformation theory (Chapter 2), and assuming increasing deformation after several contacts as discussed by Bowden[63]. The calculated values of 0.88mm for polypropylene and 1.5mm for polyethylene using the Yield Strength values given in Table 2, are close to the measured values.

The decay of charge on polypropylene and polyethylene was found to be negligible over an eight hour period, under a vacuum of 10^{-4} torr.

Similarly over a fifteen minute period at atmospheric pressure, no charge decay was observed. Consequently, within these measurement times, the effect of the variables of interest, on charge transfer, could be investigated without interference from charge decay processes.

Any charge present on the dielectric surface adjacent to the turntable surface, could possibly affect the induction probe measurements. However, calculations of the expected effect indicated this to be negligible, compared with the charge on the upper surface. This was confirmed by comparing charge traces from a dielectric coated on the lower side with conducting paint, with those from an uncoated dielectric. There was no difference in the observed behaviour for these two cases, confirming that charge on the lower surface had a negligible effect on the induction probe potential.

Mechanical parameters associated with lowering the sphere on to the dielectric, were shown to have no effect on the transient charge characteristics. This was confirmed by modifying the sphere support system to allow very rapid lowering of the sphere. Results thus obtained, were identical to those obtained using manual lowering.

3. 2. Induction probe calibration for finite charge widths.

The relation between the induction probe potential (V_{mg}) and the peak surface charge density (σ_r), for a finite bi-polar charge distribution, is given by equation 2.27 for a probe surface to charge layer separation distance g, as

$$\sigma_r = \frac{C_E}{AG} \cdot \left(1 + \frac{g \varepsilon_{r2}}{L}\right) \cdot \frac{(1 + k)\, V_{mg}}{\left(\frac{B_g}{B_\infty} + k\right)} \quad , \qquad 2.27$$

since $\frac{pR_{pp}}{\sin pR_{pp}} \approx 1.0$.

In order to determine σ_r it is necessary to know k and the spatial wavelength λ . The wavelength is defined as the distance shown on FIG.16b for a sinusoidal charge distribution. The equivalent spatial wavelength for a finite charge distribution, modified by the probe resolution (λ' of FIG.16a), was measured on probe potential recordings. By subtracting twice the probe resolution length, determined from the resolution test grid, the defined spatial wavelength was obtained. This enabled calculation of B_g and hence B_g/B_∞ for a particular material.

The value of k was determined as follows. From equation 2.24 the ratio of the electrometer potential V_{mg} at any probe height g, to the potential at 0.127mm probe height, V_{md}, in each case for the peak charge region, is given by $\frac{V_{mg}}{V_{md}} = \frac{E_{1g}}{E_{1d}}$, where E_{1g} is the field normal to the probe surface at a separation distance of g from the dielectric surface and E_{1d} is the field normal to the probe surface at a separation distance of 0.127mm, from the dielectric surface.

Thus, from equation 2.21

$$\frac{V_{mg}}{V_{md}} = \frac{E_{1g}}{E_{1d}} = \left(1 + \frac{\varepsilon_{r2} \times 0.127}{L}\right).\left(k + \frac{B_g}{B_\infty}\right).\left[\frac{B_\infty}{k + \frac{B_d}{B_\infty}}\right] , \qquad 3.1$$

where B_d is the value of B_g, for g = d = 0.127mm, and B_g and B_∞ are as defined in Chapter 2.

V_{mg} was measured experimentally for various probe heights including 0.127mm, and several materials, enabling determination of $\frac{V_{mg}}{V_{md}}$ as a function of the probe height. During the measurement time, the charge decay due to conduction effects was negligible. Various values of k were chosen for each set of experimental data and substituted into equation 3.1, until the optimum agreement with experimental results for the lowest probe heights was obtained. All subsequent measurements were taken in the region of lowest probe heights. FIG.17 shows results for the materials and conditions listed in Table 4, whilst the charge distributions for these materials are shown in FIG.18. Agreement between experiment and curve-fitted theory is good for the parameters shown in Table 4. This indicates that the assumed similarity between the effect on the probe of the finite and sinusoidal charge distributions in the peak region is reasonable. The values of k obtained, are purely curve fitting parameters, and they account for the variation of the actual charge distribution from the unipolar infinite sinusoidal situation. Thus, these values can be substituted into equation 2.27, to enable determination of the peak charge density from the probe potential. The general pattern of behaviour is as expected, an increase in k from material B to material C, corresponds to the decrease in positive peak heights.

The values of the peak charge density calculated from equation 2.27 are shown in FIG.18, where C_E/AG is equal to 7.77×10^{-4} F m^{-2}. The positive peak heights shown in FIG.18 for materials B and C respectively, represent extreme values observed in practice. Consequently the corresponding k values can be considered as limiting cases for any measurements. The average k value is 0.36, and from equation 2.18 it is apparent that the maximum error in estimation of σ_r using the average k value is 3%. Consequently for later measurements, this average k value was considered sufficiently accurate. Similar considerations apply to material A, polypropylene, in this case the positive peak heights are inter-

mediate between those of materials B and C, the k value being correspondingly intermediate.

The charge transferred to the contact sphere was monitored during these experiments, the charge (unit circumferential length)$^{-1}$ is shown in Table 5 for each material. The charge (unit circumferential length)$^{-1}$ is related to the surface charge density by

$$\frac{Q}{x} = \sigma \cdot b \quad , \qquad 3.2$$

where x is the length travelled, σ is the uniform charge density over the track width calculated from the radial charge scan (FIG.16a), allowing for the probe resolution.

The actual charge density distribution can be considered approximately, to consist of a triangular shape of height σ_r, and base length b, which in turn is equivalent to a uniform strip of height $\frac{\sigma_r}{2}$ and base length b.

Thus, from equation 3.2, $\frac{Q}{x} = \frac{\sigma_r \cdot b}{2}$.

Values of charge (unit circumferential length)$^{-1}$ calculated from this expression are also shown in Table 5. By charge continuity, these values should be equal in magnitude, and opposite in sign to the corresponding quantity calculated from the sphere charge. This is seen from Table 5 to be approximately true in all cases, any discrepancy can be accounted for by the charge density non-uniformity around the charge track, and the area approximation. This confirms that the probe calibration technique is applicable to distributions of a similar shape to those described.

The greatest error in using this calibration technique will arise when calculating absolute charge density from the probe potential. The maximum possible error is 33% in estimating the charge density from equation 2.27, if incorrect values of k are employed. In the following sections, where absolute charge density values are given, the comparison between various values is of interest and any small systematic calibration error is not of great importance. The principal use of the calibration technique, is in Section 3.4 in relation to the effect of gas pressure on charge levels. In this case the relative

electric field values at different heights above the surface are of importance. The equations in Section 3.4 involving the parameters obtained from the present calibration, are of an identical form to equation 3.1, from which these parameters were derived. Consequently the calibration parameters derived, are accurately applicable to the equations used in Section 3.4.

3. 3. The effect of the ionisation pressure measurement gauge on observed charge levels.

Measurement of the lowest pressures in the vacuum vessel, was achieved by means of a Penning cold cathode ionisation gauge as mentioned in Chapter 2. Whilst the gauge was switched on, a continuous negative current was detected by the electrometer connected to the metal sphere. This indicated that a stream of negative particles was produced in the vacuum vessel by the gauge head. These particles were probably either electrons due to thermionic emission, or negative oxygen ions formed by electron attachment[120]. Although the dural turntable provided some measure of screening for the dielectric sheet from the gauge head (FIG.6), it seemed probable that the gauge could modify observed charge levels. This was indeed found to be the case.

The effect of the dielectric surface charge layer on these charged particles, will depend on the electric field distribution above the dielectric. A similar geometric situation has been analysed by Kao[121]. If the distance to an electrode above the surface is much greater than the dielectric thickness, then electric field reversal occurs at the edges of the charge distribution, due to the effect of image charges in the base electrode.

This situation applies when the induction probe is far removed from the dielectric surface. This was the case in practice, except for small areas under the probe during scan measurements. Consequently the negative particles produced by the ionisation gauge, would be attracted to these electric field reversal regions when there was a negative surface charge, and could have contributed to the observed broadening of the negative charge peaks (FIG.18). The electric field due to the charge itself, possibly could either attract some positive ions from the vacuum space, which were probably present due to the ionisation gauge operation, or cause field emission from the surface. Both of

these effects would predominate at the edge of the charged area[122], and would cause positively charged regions.

In practice, positively charged areas at both edges are always observed at pressures below $2.\times 10^{-4}$ torr, for measured peak field strengths at the probe surface, greater than approximately $6.41 \times 10^{6} V\ m^{-1}$ for a 0.127mm probe height (FIG.18). This effect has been confirmed by a large number of experiments with polypropylene, polyethylene and polytetrafluoroethylene, and occurs even when the ionisation gauge is switched off. If the charge density is close to the limiting value, below which no positive peaks occur, as defined by the electric field strength above, then switching on the ionisation gauge was found to initiate formation of positively charged regions in times less than 30s. Gas pressure of the order of 10^{-2}torr, resulted in increased magnitude of the positively charged areas. The positively charged peaks, at pressures below 10^{-2} torr, increased as the initial negative charge density increased. Both electron emission from the surface, and positive ion capture, could be responsible for the positive peaks, and the relative importance of these mechanisms cannot be established from the observations.

The observed behaviour with positively charged surface layers was different. For charge widths similar to those in FIG.18, small negative reverse peaks appeared at the charge layer edges, when the gauge was switched on. The positive peak height was reduced considerably, over a period of time of the order of minutes, after the gauge was switched on. When wider charged areas were observed, caused by initial surface conduction and diffusion effects, actuation of the ionisation gauage caused charge spreading (FIG.19). In this case the effects due to image charges must have been swamped by those due to the intense actual charge electric field, at the edges of the distribution[122]. This would have attracted the negative particles from the vacuum space, resulting in a charge double layer on the insulator surface. Since the central regions of the positive charge layer, are the greatest distance from the negative layer, they are at the highest potential, and conduction will occur preferentially from central areas. This leads to effective charge spreading, with depletion of the

central sections, as observed in practice.

When the induction probe was held over the charged region, no decay effects were observed, due to the screening effect of the probe.

These observations with positive surface charges could account for the spontaneous decay of positive charge observed by O'Neill[10] on polymer surfaces. This was unexplained, and could have been due to switching on the ionisation pressure measurement gauge.

No reference has been made to this effect by previous investigators, and it is quite possible that some previous charge measurements, have been unintentionally modified by ionisation gauge pressure measurements.

In order to avoid any disturbance to the measured values by the ionisation gauge during the present experiments, the gauge was switched off during all charge measurements. Gas pressure was checked before and after each experimental run.

3. 4. The effect of gas pressure on observed charge levels.

3. 4. 1. Theoretical considerations.

When the electric field above a charged area of material reaches a critical value, determined by the system geometry, gas concentration, number of free electrons initially present in the gas, gas molecular species, and electrode material, then cumulative ionisation resulting in an avalanche effect will occur. For the case of conducting electrodes and a uniform electric field, the critical potential to initiate avalanche ionisation, and hence a spark, as a function of gas pressure (P) and electrode separation distance (c), is given empirically by the so-called Paschen curve[14,16,123]. The critical potential passes through a minimum as (cP) is increased, from below 1 torr mm.

The minimum, which occurs at a value of (cP) equal to 5.67 torr mm for air[16] at 20°C, is anticipated on the basis of Townsend's theory of gas breakdown[15]. This theory attributes the avalanche effect, to the cumulative ionisation resulting, when the naturally present initial electrons,(due to cosmic rays, ultra-violet rays and radioactivity) are accelerated by the electric field, and collide with gas molecules inelastically. When (cP) is greater than the value at the minimum (cP)MIN, the number of collisions made by an electron in crossing

the electrode gap is greater than at (cP)MIN, but the energy gained between collisions and hence the possibility of ionisation is much lower, unless the potential is raised. For (cP) values less than (cP)MIN the reverse applies[15].

The relation between the critical potential V_c, and (cP), for (cP) greater than (cP)MIN, is given by Meek[16], for a number of electrode materials. There is no observed dependence of the critical potential, on electrode material for several metals in air.

For the case of a highly non-uniform electric field, cumulative ionisation is restricted to the region of greatest electrical stress, and the gas discharge process is known as corona discharge. In this case a stable ionisation situation arises, rather than a spark which occurs with uniform electric fields. When the electrode system consists of a wire of circular cross section, surrounded by an outer electrode of arbitrary shape, the corona starting electric field E_{1c}, for air, is given empirically by[120]

$$E_{1c} = 3.22 \times 10^6 \delta' + 8.46 \times 10^4 \ \delta'^{\frac{1}{2}} (R_{po})^{-\frac{1}{2}} \quad , \quad 3.3$$

where δ' the relative gas density is equal to $\frac{298P}{\vartheta 760}$, R_{po} is the inner wire radius, ϑ is the temperature (^oK), and P is the gas pressure in torr.

The pressure dependence of the charge density on insulating surfaces is less well understood, partly because of the complex electric field non-uniformity above the surface, resulting from the charge non-uniformity, both before and during air breakdown[4,56,124-126]. The other principle complication is that during charging of an insulator by contact and separation, no single discharge length can be defined, since a continuous range of lengths is available for discharge, from zero to the final separation distance. The effective observed discharge length, is the greatest separation distance for which avalanche ionisation occurs, as the surfaces are separated.

Medley[96], O'Neill[10] and Wåhlin[59] report behaviour broadly similar to the Paschen curve, for the charge transferred to a metallic electrode during sliding contact with a polymer. The charge was found to pass through a zero value as the pressure was reduced from 760 torr. The Paschen curve predicts a minimum charge value. No detailed examination of the final charge levels was

carried out. Peterson[9,127] detected a charge minimum, for an insulating particle undergoing rolling contact with a metal cylinder, as the pressure was reduced from atmospheric.

The relation between the induction probe potential in the present experiments, and the normal electric field at the probe surface is defined by equation 2.24 as

$$V_{mg} = AG \varepsilon_o E_{1g} / C_E \quad , \qquad 2.24$$

since $\frac{\sin pR_{pp}}{pR_{pp}} \approx 1$ for the present experiments.

The functional dependence of the surface charge density on gas pressure, determines the dependence of E_{1g} and hence V_{mg} on pressure. On the assumption that discharge occurs over a polymer surface to metal sphere separation distance c, the value of the surface charge density $\sigma_{c'}$ after breakdown is given by equations 2.21 and 2.26 with E_{1g} equal to E_{1c}, the critical air breakdown electric field.

$$\text{Thus} \quad \sigma_{c'} = \left[\frac{(1 + k) \varepsilon_o E_{1c}}{k + \frac{B_c}{B_\infty}} \right] \cdot \left(1 + \frac{\varepsilon_{r2} c}{L} \right) \quad , \qquad 3.4$$

where B_c is the value of B_g with g equal to c. The sphere curvature is assumed to be small over the discharge lengths considered. This is approximately true for the discharge lengths estimated later in this section. The electric field is considered as approximately equal to that which would exist if the sphere were replaced by a plane positioned at the discharge length.

When the surface charge density is monitored with the induction probe, the relation between the electric field normal to the probe surface and the surface charge density $\sigma_{c'}$, is given by equations 2.21 and 2.26,

$$E_{1g} = \frac{\sigma_{c'} \left(k + \frac{B_g}{B_\infty} \right)}{(1 + k) \varepsilon_o \left(1 + \frac{\varepsilon_{r2} g}{L} \right)} \quad . \qquad 3.5$$

By eliminating $\sigma_{c'}$ between equations 3.4 and 3.5, E_{1g} as a function of E_{1c} is determined. Substitution of this value into equation 2.24 yields for the probe potential

$$V_{mg} = \frac{AG\,\varepsilon_o E_{1c}\left(k + \frac{B_g}{B_\infty}\right)\left(1 + \frac{\varepsilon_{r2}c}{L}\right)}{C_E\left(k + \frac{B_c}{B_\infty}\right)\left(1 + \frac{\varepsilon_{r2}g}{L}\right)} \quad . \qquad 3.6$$

If the critical breakdown electric field E_{1c}, is known as a function of pressure, then V_{mg} can be determined as a function of pressure. For the case of corona breakdown, E_{1c} from equation 3.3 can be substituted into equation 3.6 to give

$$V_{mg} = \frac{AG\varepsilon_o\left(k + \frac{B_g}{B_\infty}\right)\left(1 + \frac{\varepsilon_{r2}c}{L}\right)\left(\frac{3.22 \times 10^6 P}{760} + \frac{8.46 \times 10^4 (P)^{\frac{1}{2}}}{R_{po}^{\frac{1}{2}}(760)^{\frac{1}{2}}}\right)}{C_E\left(k + \frac{B_c}{B_\infty}\right)\left(1 + \frac{\varepsilon_{r2}g}{L}\right)} \quad , \qquad 3.7$$

at 25°C.

In order to apply the Paschen curve to equation 3.6, it is necessary to know E_{1c} as a function of V_c. The relation betweeneV_c and E_{1c} can be derived using the approach described by Murasaki[119]. It is found that for the values of c determined in the present experiments, which will be discussed later in this section, the electric field can be considered uniform over the air gap and $E_{1c} = V_c/c$. Thus substitution of this expression into equation 3.6 yields the following expression for the probe potential

$$V_{mg} = \frac{AG\,\varepsilon_o(k + B_g/B_\infty)\left(1 + \frac{\varepsilon_{r2}c}{L}\right)V_c}{C_E\left(k + \frac{B_c}{B_\infty}\right)\left(1 + \frac{\varepsilon_{r2}g}{L}\right)c} \quad . \qquad 3.8$$

The Paschen curve is strictly only applicable for a uniform electric field situation. However, it is of interest as a possible means of approximately predicting limiting charge levels in practical situations, for dielectric material having non-uniform surface charge distributions.

3. 4.2. Experimental results and discussion.

The observed charge levels expressed as peak induction probe electrometer potentials, as a function of gas pressure, for three different specimens, are shown in FIG.20. The contact parameters and materials involved are described in Table 6. Discharge, reducing the charge level to a value below the measurement sensitivity of 4×10^{-7} C m^{-2}, occurred over a significant pressure range

as shown in FIG.20, in which each point represents the mean value of five radial scan measurements. This is in contrast to the much larger minimum value predicted by the Paschen curve as will be shown later in this section. The corona discharge equation predicts very low charge levels as observed, however, this equation does not of course apply to the region of increasing charge for pressures below 0.3 torr.

The charge transferred to the contact sphere (unit circumferential length)$^{-1}$ as a function of gas pressure, after six turntable revolutions and after one turntable revolution is shown in FIG.21 and FIG.22 respectively. FIG. 22 is directly comparable with previous results[59,96], and is in agreement with regard to the expected pressure range, for the zero charge values. Likewise the constant charge levels observed below 10^{-3} torr are in agreement with previous results,[59,96] and the charge levels at atmospheric pressure are of a similar magnitude to previous results[59,96]. It is thought that the charge maximum observed near atmospheric pressure (FIG.22), reflects differences in charge uniformity near atmospheric pressure.

A new phenomenom is apparent from the results of FIG.21. The sphere charge passes through a maximum as the pressure is increased from the lowest values, before the charge reaches the expected zero value. The explanation for this behaviour is apparent when the mean free path of gas molecules, in the minimum range is considered. The mean free path L_m, is given by Moore[128] as

$$L_m = (2^{1/2} \pi N d_m^{\,2})^{-1}, \qquad 3.9$$

where N is the molecular concentration, d_m is the molecular diameter, for Nitrogen[128] $d_m = 3.16 \times 10^{-10}$ m.

The charge maximum occurs at a pressure in the region of 0.1 torr. For this pressure, L_m from equation 3.9 is equal to 0.76mm. The longest path length between unscreened parts of the contact sphere, and charged areas immediately adjacent to the contact region is approximately 15mm, which is $20L_m$. For cumulative ionisation to occur it is necessary that the field should exist over many times the mean free path length[8]. The precise number of required path lengths is unknown, however the order of magnitude expected is in the region of

100 to 1000[8]. The available path length to the sphere is less than this value, and consequently cumulative ionisation will occur when the contact sphere is far removed from a particular charged area element. Most ions of the same sign as the surface charge, produced during the breakdown process, will migrate to conductors other than the contact sphere, under the influence of the surface charge electric field. Ions of opposite sign to the surface charge are attracted to the surface and neutralise the charge, until the field above the surface is below the critical breakdown level. This neutralisation process provides areas for further charge transfer during subsequent turntable revolutions. The charge transferred to the sphere after several turntable revolutions, in this case is greater than when the charge transfer process is limited by the electric field due to the charge remaining on the dielectric surface, as occurs for pressures below 10^{-2} torr.

As the gas pressure is increased, the mean free path decreases and gradually a greater proportion of ions of the same sign as the surface charge migrate to the contact sphere. This provides a current of opposite sign to the contact charge separation current, and results in a decrease in the net charge transferred to the sphere. As the pressure is increased from below 10^{-2} torr, the two effects firstly become exactly equal, and no net charge is observed. Eventually the neutralisation current decreases as the air breakdown strength increases, leading to an observed net charge.

The effect of the gas molecule mean free path approaching the available discharge length, has also been observed by Peterson[127]. The charge remaining on an insulating particle, rolling in a metal cylinder, was found to be significantly greater, if a probe was positioned 4 mm. above the particle, for the pressure range 0.02 torr to 0.1 torr, than if no probe were present. The probe limited the available discharge length, and caused an apparent increase in the critical air breakdown strength.

Radial and circular charge scans for various gas pressures, using polypropylene dielectric, sample E, are shown in FIG.23 and FIG.24 respectively. For pressures below that corresponding to the zero measured charge level, it is

apparent that either ions of opposite sign to the surface charge are attracted to the peak field regions at the edges of the charged areas, or field emission is occurring. The discharge occurs at these low pressures, over discharge lengths which are sufficiently long, to allow field intensification[121] at the edge of the charged area to occur. For short discharge lengths when the conductor above the dielectric is much closer to the dielectric surface than the base plane, field intensification at the charge layer edges will be less severe[121]. The observed behaviour at low pressures is consistent with the attraction of individual charged particles or field emission, rather than the occurrence of spark type discharges. Once the pressure corresponding to the zero measured charge level is exceeded, local discharges become much more numerous (FIG.24) and edge effects are no longer evident (FIG.23). The discharge occurs over short path lengths at these pressures. The geometry of the conductors for these path lengths, ensures that the peak field region is over the peak charge region, and consequently discharge effects are evident in this peak charge region (FIG.23), not at the edges of the charged area.

The occurrence of many discharge pulses (FIG.24) is in agreement with the observations of Bertein[124], who used powder developed images to study discharge effects, and Mambetov[129] who used photomultiplier measurements of light pulses emitted during discharge, to examine discharge effects. Sasaki[54] reports charge non-uniformity similar to FIG.24 at atmospheric pressure, for a contact force greater than 10gm, following contact between dielectric or metal rollers with dielectric sheets.

Circular charge scans at atmospheric pressure for the other materials listed in Table 6 are shown in FIG.25. The polypropylene sample D behaves in a similar manner to sample E, however polyethylene shows evidence of greater charge non-uniformity arising from discharge effects. The radial charge scans and circular charge scans at lower pressures are substantially the same for all the samples studied. The fact that numerous discharge peaks are observed, indicates that spark type discharges occur, probably alongside corona discharge.

The induction probe electrometer potential is shown in FIG.26 as a function of

pressure, for values above the pressure corresponding to the zero measured charge level. Also shown in this diagram are predictions from equation 3.7 for corona breakdown with R_{po} equal to half the charge line width, and equation 3.8 for the Paschen curve, using values for V_c given by Meek[16]. B_g/B_∞ was assumed to be 0.604 corresponding to the earlier derived value for polypropylene (Table 4), whilst k was taken as 0.5 since no reverse peaks at the edges of the charge region were evident in this pressure range. Using a value of $\frac{B_g}{B_\infty}$ equal to 0.72 derived for polyethylene (Table 4), results in a maximum decrease in the predicted potential of 4% relative to the prediction for polypropylene. This is less than the experimental data scatter, consequently only the polypropylene predictions are shown. The charge levels are substantially independent of the dielectric material (FIG.26), which is as expected since the dielectric constants of polypropylene and polyethylene are nearly equal (Table 2). Both the Paschen curve and the corona relation, overestimate the breakdown electric field, if a constant discharge length is assumed as shown. This result is in agreement with Peterson[127], who found that the Paschen curve was an overestimate for the breakdown potential, when examining charge on an insulating particle. By assuming that the discharge length is equal to 0.3mm for pressures up to 260torr, and thereafter decreases as shown in FIG.27, the corona prediction closely approaches the observed values, as shown in FIG.26. Likewise the Paschen curve prediction is closer to observation, when the discharge length is chosen to minimise the probe potential predicted by equation 3.8. The discharge lengths required are shown in FIG.27. The deviation of observed charge levels from those predicted by the Paschen curve, is a reflection of the difference in the discharge behaviour of insulating and conducting material. This difference is probably associated with the electric field non-uniformity during discharge of insulating material, and a difference in the electron emission characterisitics of insulators compared with conductors.

The discharge lengths in FIG.27 are seen to decrease with increasing pressure. This is expected, since at a constant temperature, the gas molecule mean free

path is inversely proportional to pressure, and a minimum number of mean free paths lengths is required for cumulative ionisation[8]. The values required by the Paschen curve and the corona relation, deviate most markedly at low pressures, when the discharge lengths are the longest, and the electric field uniformity required for the Paschen curve is least likely to be observed.

The time required for charge neutralisation[15], can be shown to be of the order of 10^{-4} s, which is sufficiently small to ensure that table movement has little effect on neutralisation for the velocities studied.

The critical electric field values observed in this section for atmospheric pressure, will apply to practical situations involving localised charged areas on dielectric surfaces. The electric field distribution for any practical situation must of course be calculated independently. The Paschen curve provides an order of magnitude assessment of the charge level remaining after discharge effects, but will not provide an accurate prediction. The corona discharge conductor relationship, provides a more accurate charge level assessment, provided the charge dimensions are known.

Although no measurements were carried out for pressures above atmospheric, it is apparent by extrapolation from FIG.27, that air breakdown processes will still be of importance for pressures several times atmospheric. This suggests that the postulate of Cole[43], who assumed air breakdown effects to be negligible, for pneumatic transport at three atmospheres pressure, is not necessarily correct.

In fact, it is probable that charge levels obtained under practical conditions, will invariably be limited by air breakdown processes. It is this factor which is instrumental in providing the possibility of attainment, and utilisation, of well-defined charge levels under practical conditions.

3. 5. Decay of contact charge.

3. 5.1. Theoretical considerations.

The decay of surface charge, deposited by corona discharge on insulating surfaces, has been analysed by several investigators[91-95,130,131]. The potential of the initially more highly charged surfaces, was found experimentally

to reduce to a value below that of the initially less highly charged surfaces, after a certain time interval[130]. This behaviour has been termed the "cross-over" effect[131]. The conduction effects subsequent to charge transfer, obey the same defining equations for corona and contact charging, although the charge injection parameters and mobility parameters, may be different in each case.

Wintle[91] has presented an analysis of the decay of surface charge initially present to a depth α on an insulator surface. This analysis applies to the geometrical situation shown in FIG.28a, for which it is assumed that the electric field above the dielectric is zero.

The initial electric field distribution in the insulator is given by,

$$E_2 = E_{2s}y \text{ for } y < \alpha, \quad E_2 = E_{2s} \text{ for } y > \alpha ,$$

where $E_{2s} = \dfrac{n_s e \alpha}{\varepsilon_{r2} \varepsilon_o}$, n_s is the initial concentration of injected charge carriers, e is the magnitude of the elementary charge.

The assumptions made are as follows. (1) Total charge injection is instantaneous. (2) Thermally generated carriers, deep trapping with no subsequent charge release during the period of interest, and diffusion effects can be neglected. Consideration of Poisson's equation, the continuity equation, the conduction equation, and the displacement current, yields for the subsequent behaviour,

$$E_2 = \frac{E_{2s}y}{(\alpha + E_{2s}\mu t)}, \quad n = \frac{n_s \alpha}{(\alpha + E_{2s}\mu t)}, \quad \text{for } y < \alpha + E_{2s}\mu t , \qquad 3.10$$

and $E_2 = E_{2s}$, $n = 0$, for $y > \alpha + E_{2s}\mu t$, 3.11

where μ is the charge carrier mobility.

The induction probe potential when positioned over a volume charge distribution, has been given by Wintle[116] as,

$$V_{mg} = \frac{\int_o^L dy \int_o^y en(y')dy'}{\varepsilon_{r2} \varepsilon_o \left(1 + \dfrac{C_E}{C_d}\right)}, \qquad 3.12$$

where C_E is the measuring electrometer input capacitance,

C_d is the capacitance of the surface charge defined in equation 2.15. This applies to a geometrical situation corresponding to FIG.28b.

The ratio of C_E/C_d was shown in Chapter 2 to be greater than 1000 during measurement under the present experimental conditions, consequently $1 + C_E/C_d$ is equal to C_E/C_d within 0.001%. Substitution of the required value of carrier concentration from equation 3.10 or equation 3.11 into equation 3.12, enables equation 3.12 to be integrated. Performing the integration, and including the necessary electrometer gain, results in the following expressions for the probe potential,

$$V_{mg} = V_{mgs}\left[1 - \left(\frac{\alpha + E_{2s}\mu t}{2L}\right)\right], \text{ for } t < \frac{(L-\alpha)}{E_{2s}\mu}, \qquad 3.13$$

$$V_{mg} = \frac{V_{mgs}L}{2(\alpha + E_{2s}\mu t)}, \text{ for } t > \frac{(L-\alpha)}{E_{2s}\mu}, \qquad 3.14$$

where the probe potential at $t = 0$ is given by,

$$V_{mgs} = \frac{GAn_s e\alpha L}{C_E(\varepsilon_{r2}g + L)} = \frac{E_{2s}LC_dG}{C_E}.$$

$$\text{Thus, } \frac{1}{V_{mg}} = \frac{2\alpha}{V_{mgs}L} + \frac{2C_E\mu t}{C_dGL^2}, \text{ for } t > \frac{(L-\alpha)}{E_{2s}\mu}. \qquad 3.15$$

The time taken by the leading edge of the charge layer to reach the base plane, the transmit time t_L, is equal to $\frac{(L-\alpha)}{E_{2s}\mu}$. These relations for the case of the initial penetration depth α equal to 0, have also been derived by Batra[93] for surface charge decay on photoconducting insulators, using the concept of flow lines. Equations 3.13 and 3.14 predict that the probe potential will fall linearly, reaching half the initial value when $t = t_L$, and henceforth will decay in inverse proportionality with time, independent of the initial charge level.

An alternative explanation of the observed charge decay has been advanced by Van Turnhout[117], who considers decay to be due to a combination of ohmic conduction and dipole polarisation. This results in a prediction, that the observed decay will be the sum of two exponential terms. Results given by Ramer[132] for charge decay on fabrics at atmospheric pressure, support this prediction. However the measurement technique used by Ramer[132] did not produce the well-defined geometrical situation assumed by Van Turnhout. Also, further

possible complications due to air ionisation effects, and surface conduction, render interpretation of these results in terms of the theory, very difficult. Similar problems arise, when theoretical interpreation is attempted of the decay of highly non-uniform charge levels measured by Murasaki[109].

Davies[38] has investigated contact charge decay on glass and polyethylene, under the well defined geometry considered by Wintle[91]. A theoretical treatment is given[38], which is valid if the charge layer remains close to the dielectric surface. The relation between surface charge and time after contact, is given by Davies[38] as

$$\frac{1}{\sigma} = \frac{1}{\sigma_s} + \frac{t\,\mu}{2\,\varepsilon_o\,\varepsilon_{r2}L}, \qquad 3.16$$

where σ is the surface charge density at time t, σ_s is the initial surface charge density. This applies to the case of a negligible concentration of thermally generated carriers.

Using the value of C_d from equation 2.15, and the relation between surface charge density and probe potential from equation 2.19, equation 3.16 can be expressed as

$$\frac{1}{V_{mg}} = \frac{C_E\,\varepsilon_o\,\varepsilon_{r2}}{GC_dL\,\sigma_s} + \frac{\mu C_E t}{2GC_dL^2}. \qquad 3.17$$

The induction probe potential, was observed by Davies[38] for some specimens, to be hyperbolically related to time, as predicted theoretically (Equation 3.17) when the intrinsic carrier density is negligible. A transit time was not identified in these studies.

3. 5.2. Experimental results and discussion.

With the intention of determining a theoretical approach relevant to contact charge decay, charge decay on Nylon 66 and Viton® synthetic rubber, was examined in the present experiments. These two materials were suitable for study, using the apparatus described in Chapter 2, since decay times were convenient for measurement purposes. The technique employed, was initially to charge the dielectric materials, using rolling contact with a metal sphere. The charge decay was then observed, by moving the dielectric beneath the induction probe at known time intervals after termination of charging. To

ensure that the field above the dielectric was zero, the charged area, was in general maintained at a sufficient distance from the probe tip, to reduce the field above the surface to negligible proportions. During scanning measurements, this requirement was of course no longer fulfilled, and the presence of the probe reduced the conduction rate. However, since the proportion of time spent by the charged area beneath the probe tip screening, was less than 2% of the total measurement time, any error due to this factor was negligible.

The electrometer potential spatial distribution during a scanning measurement, is shown in FIG.29 for two samples of Nylon 66 and two samples of Viton®. Sample G (Table 7) was given a surface wash immediately before the charging experiment, causing increased charge spreading due to enhanced surface conductivity. The contact line width was estimated, by independently measuring the indentation, to be 3.2mm for Viton® and 0.7mm for Nylon 66. The charge widths of FIG.29 are significantly greater than the contact line widths, and the specimen thicknesses which limit the area over which volume charge distributions influence the probe. Thus charge spreading occurred, which indicates the presence of surface conduction or diffusion effects. No further charge spreading along the surface was observed for measurement times between 45s and 3600 s, indicating that surface charge spreading occurred very rapidly after termination of contact.

The charge decay situation measured subsequently, corresponds to that of a surface charge layer moving through the dielectric, under the action of its own field, as discussed by Wintle[91] and Davies[38]. The charge layer widths for Nylon 66 and Viton® are greater than the values considered in section 3.2. Consequently the error introduced by considering the charge distribution to be approximately uniform and B_g/B_∞ equal to 1.0 is small, and this assumption is made. Electric field non-uniformity will exist in the dielectric however, and may modify equations 3.10 to 3.17. Since the observed behaviour with Nylon 66 samples G and H is very similar, and the charge line widths are very different, it is reasonable to assume that the field non-uniformity does not have a significant influence on the decay behaviour. Some error is introduced into the

mobility calculation discussed later, by assuming B_g/B_∞ is equal to 1.0 for sample H. A maximum error of 7% for the calculated electric field will result, which is perfectly satisfactory when order of magnitude values are required.

The electrometer potential corresponding to the peak charge density, is shown as a function of time after contact in FIG.30a, for two samples of Nylon 66, and FIG.30b for two samples of Viton®. The linear dependence of potential on time, predicted by equation 3.13, before reaching the transit time, is only observed for Nylon 66 sample H. Equation 3.14 predicts that the measured potential should vary inversely with time, when t is much greater than $\frac{\alpha}{E_{2s}\mu}$, and that the extrapolated plot of the measured potential against the inverse of time to infinite time, should pass through the origin. If, deep trapping of charge carriers in the insulator bulk[92], with no subsequent release during the period of interest, or partial charge injection[92] were occurring, the linear section would extrapolate to a finite potential value for 1/t equal to zero[92].

The measured peak potential is shown plotted against the inverse of time in FIG.31a for Nylon 66, and FIG. 31b for Viton®. The linear section observed for the largest time values is in agreement with the prediction from equation 3.14. The potential is zero when extrapolated to 1/t equal to zero, consequently neither incomplete injection nor deep trapping are significant, and the prediction of equation 3.14 is correct.

Equations 3.15 and 3.17 predict that the reciprocal of the measured potential should be linearly related to time. Equation 3.15 applies to values of time greater than the transit time, and equation 3.17 applies to time values after charge deposition. Field dependent mobility[92], concentration dependent mobility[92], and the presence of a significant concentration of thermally generated carriers[38,92], all result in the prediction of a non-linear relation between the inverse of probe potential and time[38,92]. It is apparent from equation 3.15, that extrapolation of the experimental straight line, for the plot of the inverse of the measured potential against time, to t equal to 0, allows determination of the initial charge penetration depth α.

The reciprocal of the measured peak potential is plotted against time in FIG.32a for Nylon 66 and FIG.32b for Viton®. FIGS. 32a and 32b confirm the hyperbolic behaviour predicted by equations 3.15 and 3.17. It is not possible from FIGS. 32a and 32b to distinguish the transit time. This is expected due to the form of the predicted behaviour before the transit time, from equation 3.13. The observation of a hyperbolic relation, indicates that field dependent mobility[92], concentration dependent mobility[92], and thermally generated carriers[38,92] are unimportant in the specimens studied.

The initial penetration depth α can be calculated from the intercept of the lines in FIG.32, using equation 3.15, and the value of V_{mgs} from FIG.30 by extrapolation to t equal to 0. Values calculated using this method are shown in Table 7. These values are larger than those found in Mylar[133] and Teflon[134], using capacitance techniques. The independent observation that the charge transferred (unit circumferential length)$^{-1}$, remained approximately constant for Nylon 66, regardless of the number of turntable revolutions, indicates that the surface charge must have initially, rapidly dissipated into the polymer or across the surface. This is consistent with the large penetration depths calculated, and the initial surface charge spreading observed (FIG.29). The charge (unit circumferential length)$^{-1}$ for Viton® decreased with an increasing number of turntable revolutions. This is presumably because the much larger contact area in this case ensures that the electric field due to the initial contact charge, is sufficiently strong to influence subsequent charge levels, even though charge movement into the bulk and across the surface has occurred.

The value of the carrier mobility can be calculated from the slope of the lines in FIG.32, using equation 3.15 or equation 3.17. Likewise the carrier mobility can be calculated from the transit time expression, knowing the previously determined value of α, and the value of V_{mgs} from FIG.30 by extrapolation to t equal to 0. The transit time is taken as the time at which the measured probe potential, has decayed to half the value for t equal to zero.

Since potential measurements were not made for t equal to 0, mobility calculations from the transit time are subject to much greater errors,

than calculations from the line slopes in FIG. 32, which do not require measurements at t equal to 0. The results of the mobility calculations are shown in Table 7. Agreement between the mobility calculated from the transit time, and that from equation 3.15 is good. This is expected, since both methods of calculation are based on the same theoretical approach. The values of mobility from equation 3.17 are however four times longer than those calculated using equation 3.15. The discrepancy is due to the fact that equation 3.17 is derived on the assumption that the charge remains close to the upper surface of the dielectric. For this to be the case, charge decay would have to occur by ohmic conduction. This has already been shown not to be the situation. In fact, the surface charge migrates under its own field to the base plane, and does not remain near the upper surface of the dielectric. Consequently the mobility calculated from equation 3.15 is considered more realistic, since this equation is based on the assumption that the charge is distributed throughout the dielectric.

The mobilities calculated, vary with the initial surface potential. This is not anticipated on the basis of equation 3.15, and is contrary to the observation of Batra[93] for photoconducting insulators. The initial potential in the present experiments, was established by contact electrification, which was subject to change, due to the effect of unknown variables. Nylon 66 sample G was given a surface wash very soon before the contact charge application, and this is responsible for the difference in charge levels compared with sample H. The specimens of Viton® were tested several days apart, unknown variables altering the contact charge levels. In these cases the mobilities of charge carriers were also observed to change. Apparently the charge carrier mobility is functionally related to the contact charge magnitude. An increase in the mobility is accompanied by a decrease in the initial contact charge level (Table 7). The possibility that there is a functional relationship between material conductivity and initial contact charge levels has recently also been indicated by Williams[57].

The intial penetration depth α is less for samples of higher initial surface

charge density (Table 7). This is contrary to the observation quoted by Wintle for corona charged specimens[91]. No "cross-over" effect was observed with contact charged specimens (FIG.30). Thus, the corona deposition mechanism is apparently responsible for the "cross-over" effect. This is further confirmed by the observation that the sign of contact charge has no effect on the decay mechanism (FIG.32), whereas the sign of corona deposited charge affects the decay process[135]. Likewise, the dependence of corona charge decay on the gaseous atmosphere during corona[135], suggests that the corona deposition mechanism is important. Batra[93] has shown that corona charge injected instantaneously into a photoconductor, obeys the theory of Wintle[91], and it is probable that the corona deposition mechanism with other insulators, influences the injection and trapping processes.

No evidence was found to suggest that the charge decay in the present experiments could be represented by the sum of two exponentials, and the theory of Van Turnhout[117] is considered inapplicable.

Arridge[136] has examined charge diffusion along the surface of nylon fibres at atmospheric pressure, and for various relative humidities. The measured diffusion coefficient can be expressed as a mobility using the Einstein relation,[136] $\mu = \frac{e\,\mathcal{D}}{k_\beta \vartheta}$, where ϑ is the temperature, $\mathcal{D}$ is the diffusion coefficient in the surface aqueous layers, and k_β is Boltzmann's constant.

By extrapolation of the results given by Arridge[136], the diffusion coefficient in the surface aqueous layers at 20% relative humidity is 10^{-9} $m^2 s^{-1}$, consequently the mobility at $20^{o}C$ calculated from the Einstein relation is 4×10^{-8} $m^2 V^{-1}$ s^{-1}. This value, a factor of approximately 4000 greater than the mobilities found in the present experiments under vacuum conditions, is attributed to diffusion in surface aqueous adsorbed layers. This illustrates the overriding importance of surface diffusion in certain other circumstances, and charge decay experiments performed under ambient conditions are subject to this effect, as shown by Sasaki[53]. Lock[137] however reports that ambient conditions had little effect on charge decay on polyethylene, a high resistance material. Thus, surface diffusion effects do not always dominate under ambient

conditions.

When the induction probe was held over the surface charge layer, in the present experiments, the initial charge decay rate was found to decrease. This is as expected, since close proximity of the probe results in a decreased electric field in the dielectric, and the assumption of zero field above the surface of the dielectric no longer applies. This effect confirms that charge decay is due to charge movement in an electric field, and not to charge movement in a concentration gradient (diffusion). Further confirmation is provided by the observation, that lateral charge spreading was not observed during the measurements, after the initial charge spreading prior to the first measurement. Charge spreading would have been expected if diffusion effects were important.

The charge decay rate was also observed after several turntable revolutions during the charging cycle. After the initial rapid decay rate the probe potential decay was found to follow an equation of the form $V_{mg} = \frac{H}{t^a}$, where $a < 1.0$, and H and a are constants. The experimental results are shown in FIG.33 where the potential and time are plotted on logarithmic coordinates. The value of the exponent a, is 0.69 for nylon, and 0.73 for Viton®. This departure from the value of a equal to 1.0, which was found for one turntable revolution, is due to the situation after several turntable revolutions resembling a case of discrete partial injection. The decay rate is expected to have a complex dependence on the circular speed and number of turntable revolutions.

The mobility values calculated in the present experimental work can be compared with resistivity values. By definition, resistivity $r = (ne\mu)^{-1}$. Thus for two materials A and B, $\frac{r_A}{r_B} = \frac{n_B \mu_B}{n_A \mu_A}$.

It is postulated that during resistivity measurements of insulating polymers, the concentration of charge carriers is dependent upon the injection process and not the intrinsic carriers in the material. The work of Yahagi[138] concerning conduction in polyethylene indicates that this postulate is reasonable. The values of n will be equal for two identical measurement situations, involving different dielectric materials. Consequently $\frac{r_A}{r_B} = \frac{\mu_B}{\mu_A}$. 3.18

Wintle[91] has quoted a mobility value for polyethylene of approximately $10^{-15} m^2 V^{-1} s^{-1}$ at room temperature, whilst the resisitivity of polyethylene is approximately $10^{15} \Omega m$. The resistivity of Nylon 66 is in the range of $10^{11} - 10^{14} \Omega m$ (Table 2), whilst that of Viton® is of the order of $2 \times 10^{11} \Omega m$ (Table 2). The measured mobilities from Table 7 for Nylon 66 and Viton® are approximately $10^{-11} m^2 V^{-1} s^{-1}$. Consequently the postulated relation 3.18 can be satisfied.

This confirms the conclusion of Jonscher[139] and Davies[38], that high resistivities of polymers are caused by extremely low carrier mobilities, rather than small absolute numbers of carriers. The reasons for this low carrier mobility are still not entirely clear, although Jonscher[139] considers that the low transition probability for hopping between the localised sites in the material is responsible. The conduction process has been shown to be consistent with electron hopping models by Davies[140], who found the temperature dependence of mobility, to exhibit thermal activation characteristics. The charge carriers are trapped at both grain boundaries[140], and terminal vinyl groups[137,141], and iodine impregnation[141], or oxidation[137] reduces trapping and increases mobility. Thermal activation characteristics have also been discussed by Seanor[142].

3. 6. The effect of metal work function and the mode of contact on observed charge levels.

The charge transferred (unit circumferential length)$^{-1}$, to metal spheres of various work function values, after one turntable revolution, is shown in FIG.34 for polypropylene dielectric, and FIG.35 for polyethylene (L.D.) dielectric. Results for both rolling and sliding contact are shown. Induction effects due to the remaining dielectric surface charge, introduced a systematic error of less than 5%. The metals used were Aluminium, Brass and Stainless Steel, besides which Gold, Silver, Nickel and Tin were used, electroplated on to brass. Contact potential was measured using the method described in Chapter 2.

From these results, it is apparent that there is no systematic effect of work function. PMMA and Nylon 66 exhibited similar characteristics, in that no

effect of work function was observed.

It has been suggested, that for contact forces of the order of 40gm, oxide layers may have a significant effect on charge transfer[143]. In order to assess the importance of oxide layers in the present studies, charge transfer from oxidised and oxide free aluminium surfaces was examined. The contact potential of aluminium relative to gold, changed from 0.63V to 1.15V when the oxide layer was removed with very fine abrasive paper. No corresponding change in the charge transfer characteristics, with respect to polypropylene was observed. This confirms the previous results, in that no effect of work function was observed.

The fact that contact electrification is independent of metal work function is contrary to the observations of several workers,[10,38,52,59,72-74,78] but agrees with some previous studies.[50,75,77,82] Previous results have been discussed in Section 2.1. Some previous workers[38,59] report using average values for the charge transferred, following a number of observations, when investigating the effect of work function. This approach assumes that fluctuations in charge levels over a time interval, are of a random nature. The present experimental studies indicated the occurrence of some non-random fluctuations due to unknown variables, and it is considered inappropriate in this instance to calculate the average charge levels. These non-random fluctuations apply to time periods of the order of days.

The reason for the discrepancy between the present findings and those of other workers[10,38,52,59,72-74,78] is not clear. Three possible explanations are as follows.

(a) If the polymer effective work function is separated by a large energy gap from the metal work function, then the metal work function would have little effect on the charge levels, even if electron transfer were occurring[12,38]. Thus, if the polymers used in the present studies, possessed different energy structures compared with those employed previously, so as to cause a large work function difference between metal and polymer, then the present observations are in accordance with expectation.

(b) The charge levels in the present study could be sufficiently high to initiate field emission. This would limit all charge levels to the same value regardless of metal work function. The electric fields observed in the present studies are of the same order of magnitude as the 10^7 Vm^{-1} value at which point field emission is initiated[13].

(c) The mechanism responsible for charge transfer in the present studies could be different from that in previous work, where the metal work function had an effect on charge transfer. Thus ionic charge transfer may be dominant in the present investigation, whereas electron transfer was possibly of primary importance in some previous studies.

It is not possible to decide which of these explanations is applicable, on the basis of the results available.

O'Neill[10] reports finding a large degree of scatter in the observed charge levels with highly resistive polymers, as was found in the present studies (FIGS.34,35). This was attributed in part to the non-uniformity of the surface charge characteristics[10]. FIG.36 shows a typical circular charge scan for the polypropylene dielectric, from which it is apparent that the charge is in fact fairly uniform in its distribution. The oscillations of large period are due to non-uniform dielectric thickness, which changed the probe to dielectric surface separation distance. The degree of uniformity shown in FIG.36, is typical for the materials studied, and the non-uniformity does not appear to be sufficient to explain the scatter of experimental data, although non-uniformity will make a significant contribution to experimental data scatter.

Charge levels with sliding contact are in general between 20% and 100% higher than the values with rolling contact. The observed surface wear was significantly greater with sliding contact. The difference in charge levels could be due to:- (a) material transfer effects, (b) a greater real contact area with sliding as opposed to rolling, or (c) a difference in the charging characteristics of the bulk and the surface of the polymer. Effect (c) would arise due to abrasion occurring during sliding. This would expose the polymer region below the surface to contact with the metal. If the charge characteristics of

this region are different from those of the surface, then a modification of observed charge levels compared with rolling contact, would result.

The general pattern of behaviour with respect to different metals, is the same for both modes of contact. Since the frictional force during sliding and rolling contact, will probably differ by a factor of two to three orders of magnitude[7,63] for the same normal force, it is apparent that the charge transfer characteristics are not directly correlated with the frictional characteristics. This is in agreement with an observation of Ramer[132], that charge transfer between sliding insulating fabrics, is not correlated with the coefficient of friction.

3. 7. The polarity of charge transferred for a dielectric/metal contact, and the effect of additives in the dielectric.

The polarity of charge acquired by various polymer sheet materials, after rolling or sliding contact with several metal spheres, is shown in Table 8. Table 8 also shows which of these polymers have a polar structure.

The charge signs are in agreement with several previous investigations[10,50,59,85], although Davies[72] reports charge sign reversal with a change in metal work function. Seanor[144] indicates that some of the polymers in Table 8, have work function values in between those of the metals used, which would produce charge sign reversal with changes in metal work function.

It is apparent that the polymer has a significant influence on the contact charge sign. The theory of Garton[40], which has been presented on the basis that polymers all behave identically with respect to metals, appears to be inapplicable as presented, and different work function values for the different polymers would be required. The polar polymers shown in Table 8 charged positively whilst the non-polar polymers charged negatively.

The polar polymers all contain the functional group $-\overset{O}{\overset{\|}{C}}-$ (Table 2). The carbon oxygen double bond has a highly asymmetric charge distribution[145]. The strongly electronegative oxygen atom retains a significant negative charge. Nucleophilic addition could take place to the carbon/oxygen double bond, from aqueous solvents which may contact the polymer at some point in its history.

This could leave ionic groups on the surface to participate in charge exchange processes. Likewise, the hydrogen atoms on the α carbon atoms, are particularly susceptible to attack and may participate in charge exchange processes, either directly, or indirectly having reacted chemically to form a mobile ionic group. The polar behaviour of the polymer, may be the explanation of Coehn's Law[146], which states that when two insulators are contacted, the material with the higher dielectric constant is charged positively. This has been shown not to be universally applicable[7]. However, several polymers do conform to the predicted behaviour[147], and previous explanations of the law have been based on ionic image charge attraction[147].

An alternative explanation is that the charge characteristics are in fact correlated with the polar behaviour of the material, rather than the dielectric constant. Since a high dipole moment corresponds to a high dielectric constant, but the reverse is not necessarily true, the polar behaviour could account for both the agreement with Coehn's Law[146], and the discrepancies. However, it appears that the chemical structure of the polar group is important, since PVC which is polar, but does not possess the $-\overset{O}{\overset{\|}{C}}-$ functional group, charges negatively with respect to most metals[72,73].

A qualitative interpretation of Coehn's Law[146] in terms of material work function for electron transfer has been given by Ruppel[148]. It is not possible to distinguish between the various interpretations at present.

The charge transfer characteristics between three additive free polyethylene (L.D.) samples, polymerised in different ways, and metals,were found to be very similar to the those of commercial material containing additives. This similarity of behaviour was also observed with additive free and commercial polypropylene, and indicates that, in these cases, the basic polymer chemical structure, determined the charge transfer characteristics, rather than the presence of additives, or polymerisation characteristics of the polymers.

3. 8. Contact electrification of two dielectric materials.

Sliding a dielectric sphere over a dielectric sheet was found to produce very low charge levels, an order of magnitude less than with rolling contact. With

sliding contact the electric field due to the initially formed charge on the sphere, reduces to negligible proportions further charge transfer, as the contact path length is increased. When the sphere is allowed to rotate, any charged element on the sphere surface, experiences a field directed towards the sphere support during part of the sphere rotation. Consequently charge leakage occurs to the support, and a net charge is observed, as shown in Table 9, for several dielectric combinations. From these results, and those of Table 8 it is possible to order the materials in a Triboelectric series as shown in Table 10.

Since the magnitude of the charge levels is dependent on the contact area and sphere conductivity, direct numerical comparison of values is only possible for contacts having identical values of these parameters. The sign of charge transferred is consistent with polar materials charging positively as discussed in Section 3.7. From numerical comparison of the charge transferred to the Viton® sphere which defines identical area values for different dielectric sheets, it is apparent that the polymer sheet material in contact, has a significant influence on observed charge levels.

The observation that charging occurs between samples of the same material, indicates that different specimens of the same material may have different contact electrification characteristics. This could either reflect differences in the bulk structure, or the surface properties. Due to this disparity between different specimens of the same material, it would appear unlikely that a theory based on electron energy structure, which assumes constant parameters for any given material, would have wide practical applicability. However, since in practical situations charge levels are invariably limited by air breakdown effects, the only charge parameter which can be influenced by material properties for a given contact area, is the charge polarity. Thus a knowledge of the geometrical situation, together with the air discharge limitations, and the sign of charge produced on a given polymer, furnishes a complete description of practical charging characteristics in many circumstances.

The theoretical models[12,38,39] furnished to date are useful, in that by also establishing experimentally, effective dielectric work functions[38,72,73,144],

some indication of the expected polarity of charge transfer with particular materials under practical conditions can be obtained. However, the observed variability of charging characteristics for different samples of the same material, places severe limitations on the applicability of the theoretical models. The observation of Section 3.7 that polar polymers charge positively with respect to metals, whilst non-polar polymers charge negatively, permits an immediate prediction of the expected charge sign with respect to metals, if the polymer chemical structure is known. Greater accuracy in prediction of the sign of charge for a given pair of materials in practical conditions, requires a degree of uniformity with respect to charging characteristics, which may not always exist in practice.

3. 9. Contact electrification as a function of the normal contact force.

The charge (unit circumferential length)$^{-1}$, transferred to a gold sphere in contact with a polypropylene dielectric, is shown as a function of the square root of the normal force in FIG.37. The linear relationship observed is in agreement with the results of Wåhlin[59] for normal forces below 1.5N, and sliding contact. The linear relationship indicates that the charge transferred is directly proportional to the real area of contact, since this is directly proportional to the square root of the normal force, for plastic deformation, or elastic deformation of a large number of small asperities (Section 2.1). The present results indicate extension of the linear region to much larger contact forces than those observed by Wåhlin[59]. The surface charge density during the present experiments was constant to within 5%, as determined by measurements using the induction probe. The non-linear behaviour observed by Wåhlin[59] for a contact force of 3N is presumably due to extraneous material transfer effects.

The observed linear dependence of charge transferred, on the square root of the normal force, indicates that effects such as hysteresis energy dissipation processes, which are partly responsible for rolling friction[63], and frictional forces due to plastic deformation[63], are not important for charge transfer. These effects would produce non-linearity in the charge transferred

$(F)^{\frac{1}{2}}$ relation. These findings are in agreement with one of the conclusions of Section 3.6, that frictional effects are not of overriding importance for charge transfer processes. Further confirmation that elastic deformation was not of principal importance, was provided by the observation that no change in the charge transferred was found, when the contact sphere diameter was changed from 19.1mm to 12.7mm for the otherwise identical contact conditions of FIG.37, and a contact force of 10N for both spheres.

3. 10. The effect of the time of contact on contact electrification.

A typical example of the charge transferred to a metal sphere in contact with a polyethylene (L.D.) dielectric specimen, as a function of the contact path length, is shown in FIG.38a. A typical result for a Nylon 66 dielectric specimen is shown in FIG.38b. The behaviour with polyethylene is consistent with increasing contact area during repeated traversals, as described by Bowden[63] for plastic deformation. The charge deposited, reduces subsequent charge transfer to a very small level after several turntable revolutions, since only a small amount of charge spreading occurs. The charge on Nylon 66, on the other hand, undergoes rapid diffusion or surface conduction immediately following deposition, as mentioned in Section 3.5. Thus charge transfer is much less influenced by the charge already deposited, than is the case with polyethylene. (FIG.38).

The charge (unit circumferential length)$^{-1}$ transferred to the contact sphere after one turntable revolution, as a function of the reciprocal of the linear velocity, is shown in FIG.39a for Nylon 66 and polyethylene (L.D.). The time of contact (t_b) is related to the linear velocity by, $t_b = \frac{d_w}{\frac{dx}{dt}}$, where d_w is diameter of the approximately circular contact region between the sphere and the dielectric (which is equal to the contact track width), and (dx/dt) is the linear velocity. Thus the abcissa in FIG.39a is directly proportional to the time of contact. Each point in FIG.39a represents the average of four measurements for polyethylene, and two measurements for Nylon 66. The maximum deviation is also indicated on the diagram. Allowance was made for the slow

response of the electrometer when the charge levels were calculated, as described in Chapter 2, for all results in the present section.

The charge transferred can be represented by an equation of the form

$$q = q_f(1 - e^{-t_b/\tau_b}), \qquad 3.19$$

where q is the charge (unit circumferential length)$^{-1}$, q_f is the charge (unit circumferential length)$^{-1}$ at $t = \infty$, τ_b is a charging time constant, t_b is the time during which any particular area element of the polymer surface is in contact with the metal sphere.

The time constant is dependent upon (a) mechanical transient contact area behaviour, (b) conduction effects, (c) charge transfer transient effects. Conduction effects are anticipated in two principal forms, (1) as the time of contact decreases, the time for charge spreading to the observed charge widths decreases, and the charge injected may thus decrease, due to an increase in the opposing electric field. (2) As the linear velocity increases, the time for conduction to occur back to the contact sphere, from nearby charged areas, effectively decreases and the net contact charge transfer increases[96,149].

The time for the charge spreading process to occur is unknown, since high field conductivity and diffusion effects may influence this quantity.

An approximate estimate of conduction transient effects back to the sphere can be obtained from the charge decay time constant[150] $\varepsilon_{r2}\varepsilon_o r$. This is between 4.4 s and 4.4 x 10^3 s for Nylon 66, and orders of magnitude greater for polyethylene, using the bulk resistivity and dielectric constant values given in Table 2. Once the contact sphere is further from any element of the charged area than the base plane, the electric field will be principally directed into the base plane. The time taken to travel this length of 3mm. at the slowest linear velocity, is 5.83s. This is much less than the expected decay time constant values for polyethylene and Nylon 66. Consequently charge decay back to the contact sphere, will probably not be important.

Since polymers are visco-elastic, the area of contact is dependent upon the time after loading[63]. Related effects are observed in complex time dependent frictional behaviour, at speeds above 200mm s^{-1} during sliding contact[151].

This could reflect complex time dependent real contact area behaviour, which may also be expected with rolling contact.

Amorphous polymers have a viscosity in the region of 10^7 N s m^{-2} [152] at room temperature. The surface deformation time can be estimated very approximately from the quotient of polymer viscosity and the modulus of elasticity. Using the modulus of elasticity values of Table 2, this yields a time of 56ms for polyethylene and 6.5ms for Nylon 66. The contact region during motion is not a precise circle[153], however, for the high viscosity materials studied, the assumption of a circular contact area is reasonable. The measured contact track widths for polyethylene and Nylon 66 are 1.2mm and 0.7mm respectively, and the contact track width is equivalent to the instantateous contact circle diameter. Hence, using the surface deformation times calculated above, the critical linear velocity reciprocal at which point area effects should become important, is 47s mm^{-1} for polyethylene, and 9s mm^{-1} for Nylon 66. The value calculated for polyethylene, coincides approximately with the velocity reciprocal for which charge levels start to decrease on polyethylene (FIG.39a). However the value for Nylon 66 is much less than the critical value shown in FIG.39a. This suggests that the viscoelastic behaviour is not responsible for the decrease in charge levels, but owing to the highly approximate nature of the calculations, this conclusion is only tentative.

Thus the only one of the mechanisms which appears likely to affect the charge injection process, is the intial charge spreading. A further possibility is that the actual charge transfer process determines the observed transient characteristics. There is no means of distinguishing the relevant mechanism using the present results. Indeed the initial charge spreading could be responsible for determining the total charge transferred, and could therefore be considered as a basic part of the transfer mechanism. Thus, the transient characteristics appear to be associated with the basic charge transfer mechanism. The time constant for charge transfer, the time to transfer 63.2% of the final charge, is equal to 8.1ms for polyethylene and 9ms for Nylon 66 from FIG.39a. These values are calculated assuming the previous contact circle

diameters. The time constant for Nylon 66 would lead to an injection time, much less than the transit time discussed in Section 3.5, and is consistent with the conclusion drawn in Section 3.5, that charge injection is effectively instantaneous with respect to the transit time.

Some previous studies have shown that contact time has little influence on charge transfer, down to values of 60ms[59], 36ms[154], 6ms[155]. The first two results are consistent with the present observations, and the discrepancy with regard to the third is probably due to a different charging technique of corona charging, which was employed. Sasaki[54] and Javadi[156] report noticing a decrease in the charge transferred with decreasing contact time, for contact times down to approximately 12ms, in accord with the present results. Jewell-Thomas[157] and Wagner[82] found a maximum in the charge transferred to a rolling dielectric sphere in contact with a metal. Although conduction effects obscured the time constant, the charge reduction for short contact times is consistent with the present results. Results from the contact of monofilaments are contradictory. Levy[158] reports a decrease in charge transfer with decreasing contact time, and Hersh[159] reports either no effect of contact time, or an increase in charge transfer with decreasing contact time, depending on the material. Temperature effects probably modified these results. The present results could account for the observation of Nanevicz[160], that the charge transferred to a projectile fired through an ice fog, increased with increasing residence time from 1ms to 3ms. All results except those of Wåhlin[59] and Wagner[82] were carried out at atmospheric pressure, and air breakdown processes may consequently have influenced the observations.

The effect of contact time on the ratio of charge transferred after one turntable revolution to that transferred after several turntable revolutions, was also studied in the present experiments. FIG.39b shows this ratio for Nylon 66 and polyethylene (L.D.), and the same number of observations as FIG.39a. The results for Nylon 66 are consistent with the rapid initial charge conduction /diffusion effect, resulting in charge transfer occurring under essentially identical conditions, for every revolution. With polyethylene (L.D.) little

charge spreading occurs, and the total charge transferred reaches a limit before twelve turntable revolutions. Thus the ratio of FIG.39b closely resembles FIG.39a.

Time constant values of the order of 10ms, found for the present experiments, are much less than the values anticipated from electron transfer theories considering the polymer bulk (Chapter 1). Several minutes are required for charge equilibrium unless the energy barrier for charge transfer is very small. Thus, it appears probable, that either electron transfer to surface states on the polymer is occurring, or ionic transfer is dominant.

CHAPTER 4

A THEORETICAL CONSIDERATION OF CONTACT ELECTRIFICATION AND CHARGE DISSIPATION OCCURRING IN A VIBRATED BED

4. 1. Introduction.

Studies of particulate electrification in the past have often concentrated on specific particle handling situations. Electrification associated with pneumatic transport has been the subject of several studies[43,161-164]. An increase in the solids loading ratio and the gas flow rate have been found to lead to increases in (a) the current flow to earth from an isolated section of pipeline[43,161], (b) the potential[162] of and the current flow to earth[163] from, a metal probe located in the pipeline and (c) the charge per unit mass of powder collected after pneumatic transport[164]. The observed functional dependence of the equivalent charging current in each case, was different, but the general trends were similar.

The potential of a metal probe immersed in a fluidised bed has been studied by several workers[165-168]. The potential was found to increase to a limiting value with time, after fluidisation was started. Increasing the fluidising air velocity[166-168], decreasing the fluidising air relative humidity[166] to 30% relative humidity, and increasing the bulk particle resistivity,[166,168] all resulted in an increase in the probe potential. Ciborowski[167] however observed a maximum probe potential as the air humidity was increased. The position of this maximum was dependent upon the material being studied, and occurred at 70% relative humidity for vinyl polyacetate and 15-20% relative humidity for sand, in each case at 20°C.

Studies of particle flow along inclined metal chutes[157,169] indicate that charge transfer is always dependent on the time of contact, whilst velocity during contact, and the mode of contact affect charge levels with certain materials.

In all these cases, conduction, induction and air dissipation processes, as well as contact charging, can affect the observations. Induction and dissipation

processes have not been considered explicitly in the studies mentioned (43,157,161-169), consequently the results are not applicable to general particle handling situations.

In many practical particle handling situations the bulk voidage is sufficiently low to permit continuous contact paths to exist through the material. Typical cases are:- fluidised beds, vibrated beds, particle drying equipment, powder flow along chutes and movement inside hoppers and bunkers. Air breakdown processes (Chapter 3) impose an ultimate limiting value on the charge density, whilst conduction effects may limit the charge density to levels below the breakdown value. Since interparticle charging effects will tend to produce a net charge of zero, for a given particle mass, the principle net charge generation processes, during particle handling, are linked to contact and separation of the particles with boundary surfaces.

Some understanding of the electrification behaviour of general particle systems, with continuous contact paths, can be obtained using a suitable simulation experiment. This experiment must utilise well defined contact and separation with a boundary surface, in order to define the charge generation process. Continuous contact paths must be maintained to ensure that conduction effects closely resemble those encountered in practical situations. Ideally, the charge measurement system, should allow interpretation of the importance of dissipation processes. With these ideas in mind, the system chosen as a simulation of bulk handling processes, was a vibrated particle bed.

Sinusoidal vertical motion imposed on a platform, which supports a vessel containing granular material, will cause the particle mass to lift from the vessel base when the acceleration reaches a critical value. For beds of large particles, where air percolation effects do not greatly modify the bed behaviour, the critical acceleration is equal in magnitude, and opposite in direction to the gravitational acceleration[170]. Circulation patterns develop in the bed at this point, and the bed viscosity decreases markedly[170]. The bed is said to be vibrofluidised in this state[171]. For 210-355 μm diameter particles, the bed voidage decreases by less than 15%[170] at 50Hz and a

platform acceleration of $7g_a$, where g_a is the acceleration due to gravity. The particle bulk undergoes repeated contact and separation with the vessel base, during vibration, and continuous contact paths are preserved. Electrification occurs due to the impact, and can be measured.

The bed support vessel, used in the present experiments, consisted of a metal base, and perspex walls. This enabled measurement of the alternating current induced in the base by the moving charged particle bulk. In order to study conduction effects, a plane metal perforated electrode was inserted into the bed, parallel to the base. This caused further charging, and defined a one dimensional conduction path. By connection to a suitable electrometer, a net conduction current could be measured. The immersed electrode perforations were chosen to be sufficiently large to allow the screen to have a minimum modifying influence on the bed displacement behaviour. Charge generation and dissipation, were studied as a function of vibration amplitude and system geometry. The particle bulk resistivity is of great importance in determining the observed behaviour, and the effect of this variable was also studied.

The relation between the measured quantities, and the charge generation and dissipation processes, is derived in the remainder of this chapter for various bulk resistivity regimes.

4. 2. The induced potential due to a moving charged particle mass.

The physical arrangement and electrical circuit shown in FIG.40 are considered. This circuit assumes that the measuring instrument input capacitance is much smaller than the effective capacitance of the charge layer[172]. The capacitive reactance of the measuring instrument input is assumed to be much greater than the measuring instrument input resistance[172]. These assumptions will be shown to be valid in Chapter 5. Similar situations with different charge distributions and geometrical considerations, have been analysed by Sessler[173] for electret microphones, and Van Turnhout[117] for charge measuring instruments.

The physical situation considered is that of a vibrated powder bed, moving

vertically between a base plate, and a parallel upper electrode.

By charge conservation,

$$dQ_3 + i_3 dt = 0, \qquad 4.1$$

where Q_3, the charge on the base plate = $A_b \sigma_3$,

A_b is the effective area of the base plate which has a surface charge density σ_3. A_b is assumed to be equal to the lower bed surface area A_b.

i_3 is the current flowing through the electrometer resistor R, in time dt.

$$i_3 = V_3/R \ , \qquad 4.2$$

where V_3 is the potential of the base plate.

Thus from equations 4.1 and 4.2 $V_3 = -R \dfrac{dQ_3}{dt}$. 4.3

By Gauss's Law, $Q_3 = A_b \varepsilon_o E_3$, 4.4

where E_3 is the electric field in the air gap region below the lower bed surface. E_3 is given in Appendix 1 by equation A.1.8. Eliminating E_3 from equations A.1.8 and 4.4 gives,

$$Q_3 = \left[\frac{A_b \varepsilon_o}{g_1 + \dfrac{L_1}{\varepsilon_{r4}} + g_2}\right]\left[\frac{-\rho_c L_1}{\varepsilon_o}\left(\frac{L_1}{2\varepsilon_{r4}} + g_1\right) - \frac{\sigma_c}{\varepsilon_o}\left(\frac{L_1}{\varepsilon_{r4}} + g_1\right) + V_3\right] \ , \qquad 4.5$$

where g_1 is the air gap between the upper bed surface and the upper electrode, g_2 is the air gap between the lower bed surface and the base plate, L_1 is the particle bed depth, ε_{r4} is the dielectric constant of the particle bed, σ_c is the uniform surface charge density on the lower bed surface, ρ_c is the uniform volume charge density in the particle bed.

Equation 4.5 is based on the assumption that the particle bed has a uniform volume charge density (ρ_c) and a uniform surface charge density (σ_c). The application to particular charge distributions will be considered in Chapter 5.

Equation 4.5 can be written as

$$Q_3 = C_h(V_3 - V_h) \ , \qquad 4.6$$

where C_h is equal to $A_b \varepsilon_o \left(g_1 + \dfrac{L_1}{\varepsilon_{r4}} + g_2\right)^{-1}$, the capacitance of the unit, 4.7a

and V_h is equal to $\dfrac{\rho_c L_1}{\varepsilon_o}\left(\dfrac{L_1}{2\varepsilon_{r4}} + g_1\right) + \dfrac{\sigma_c}{\varepsilon_o}\left(\dfrac{L_1}{\varepsilon_{r4}} + g_1\right)$, 4.7b

the equivalent potential of the charge distribution. Differentiating equation 4.6, combining with equation 4.3 and rearranging yields,

$$\frac{dV_3}{dt} + V_3\left(\frac{1}{C_h}\cdot\frac{dC_h}{dt} + \frac{1}{RC_h}\right) = \frac{V_h}{C_h}\cdot\frac{dC_h}{dt} \quad . \qquad 4.8$$

The particle bed is assumed to move so that the lower air gap changes with time, during one cycle, as shown in FIG.41, according to,

$$g_2 = g_{2o} \sin\frac{\omega t}{2\beta} \ , \text{ for } 0<t<\frac{2\pi\beta}{\omega} \ ,$$

$$g_2 = 0, \text{ for } \frac{2\pi\beta}{\omega} < t < \frac{2\pi}{\omega} \ ,$$

where g_{2o} is the maximum gap width, ω is the angular frequency, β is the fraction of the cycle spent by the bed in flight.

This is close to the observed behaviour as described in Chapter 5.

From equation 4.7a,

$$\frac{dC_h}{dt} = \frac{-C_h\, g_{2o}\, \omega \cos(\omega t/2\beta)}{2\beta\left(g_1 + \frac{L_1}{\varepsilon_{r4}} + g_2\right)} \quad . \qquad 4.9$$

Using an integrating factor $e^{\left(1 + \frac{t}{RC_h}\right)}$, equation 4.8 can be solved for $0<t<\frac{2\pi\beta}{\omega}$, to give,

$$V_3 = e^{-(1 + t/RC_h)} \int_o^t \frac{V_h}{C_h}\cdot\frac{dC_h}{dt}\cdot e^{\left(1 + \frac{t}{RC_h}\right)}dt + k_2 e^{-(1 + t/RC_h)} \ , \qquad 4.10$$

where k_2 is a constant.

Since $(g_1 + L_1/\varepsilon_{r4})$ is much greater than g_2 (Chapter 5), the small variable part of C_h can be neglected in deriving the integrating factor, and hence equation 4.10. Since t is much greater than RC_h for nearly all measurement times as discussed in Chapter 5, the transient term in equation 4.10 can be neglected. Substituting for dC_h/dt from equation 4.9 into equation 4.10, integrating and rearranging yields,

$$V_3 = \frac{-g_{2o} V_h \cdot\left(\sin\frac{\omega t}{2\beta} + \frac{2\beta}{\omega C_h R}\cos\frac{\omega t}{2\beta}\right)}{\left(g_1 + \frac{L_1}{\varepsilon_{r4}}\right)\left(1 + \left(\frac{2\beta}{\omega C_h R}\right)^2\right)} \quad . \qquad 4.11$$

For the conditions of the present experiments (Chapter 5), $\omega C_h R$ is very much

less than 2β , thus

$$V_3 = -\left[\frac{g_{2o} V_h}{g_1 + \frac{L_1}{\varepsilon_{r4}}}\right]\left(\frac{\omega C_h R}{2\beta}\right) \cdot \cos \frac{\omega t}{2\beta} \quad . \qquad 4.12$$

The measuring instrument output potential as a function of time, predicted from this equation is shown in FIG.52, making due allowance for the inverting characteristics of the measuring instrument (Chapter 5) and assuming unity gain and a negative particle charge. It should be borne in mind throughout this chapter, and Chapter 5, that the predictions for the induced potential due to bed movement, apply only when the bed is in flight. When the bed is at rest relative to the vessel base plate, the induced potential is zero. Thus the anticipated behaviour is that of a series of induced pulses of period T_1 (FIG.52), separated by sections of zero potential. The overall wave has a period T_2(FIG.52).

The electric field at the bed base, can now be determined as a function of V_3, the measured potential. Eliminating Q_3 from equations 4.4 and 4.6 yields,

$$E_3 = \frac{C_h}{A_b \varepsilon_o} (V_3 - V_h) \quad . \qquad 4.13$$

Elimination of V_h from equation 4.13 using equation 4.12, gives for the electric field E_{3m} corresponding to the peak potential V_{3m},

$$E_{3m} = \left[\frac{V_{3m}}{g_1 + \frac{L_1}{\varepsilon_{r4}}}\right]\left[\left(g_1 + \frac{L_1}{\varepsilon_{r4}}\right)^2 \cdot \left(\frac{2\beta}{\omega g_{2o} R A_b \varepsilon_o}\right) + 1\right] \quad . \qquad 4.14$$

Equation 4.14 shows that the relation between the electric field and the observed potential is independent of the charge distribution within the particle bed.

The simplification that $\omega C_h R$ is very much less than 2β, made in deriving equation 4.12, is equivalent to simplifying equation 4.6 as follows. From equation 4.6,

$$\frac{dQ_3}{dt} = C_h \frac{dV_3}{dt} + V_3 \frac{dC_h}{dt} - V_h \frac{dC_h}{dt} \quad .$$

The first term on the right hand side can be neglected since C_h is very small, and the second term can be neglected since V_3 is much less than V_h. Thus, from equation 4.3, $\frac{V_3}{R} = V_h \frac{dC_h}{dt}$, which has the solution using equation 4.9

and assuming g_2 is much less than $(g_1 + L_1/\varepsilon_{r4})$,

$$V_3 = -\left[\frac{g_{2o} V_h}{g_1 + \frac{L_1}{\varepsilon_{r4}}}\right] \cdot \left(\frac{\omega C_h R}{2\beta}\right) \cdot \cos \frac{\omega t}{2\beta} \quad .$$

This is identical to equation 4.12, and indicates that equation 4.6 can be treated by neglecting the terms discussed above.

The assumption is made in deriving equation 4.12, that the charge on the vessel walls has a negligible effect on the induced potential. This is expected to be true, since the wall charged area exposed during vibration is much less than the charged particle area. Confirmation that this assumption is correct was found by examining the induced potential at the screen in the bed. This was found experimentally to be similar in magnitude, and inverted with respect to the induced potential in the base, during the bed flight. This behaviour is expected if induction effects are due to particle charges, but not if they are due to wall charges.

The assumption is made in all the derivations connected with vibrated bed charge production, that the fundamental charge transfer process is not affected by the height through which the bed falls.

The contact of the bed with the vessel falls into two distinct regions. The first is during the actual collision process . The time of this collision process is determined by the velocity of a stress wave through the bed,[170] and is approximately equal to 4.5×10^{-4} s for the present 45mm deep bed[170]. Thus charge transfer during this region will be small, if the time constants found in Chapter 3 are applicable. The second region is that during which the bed is at rest relative to the vessel. The area of contact is determined in this case by the bed weight and system geometry, and is not affected by the height of the bed displacement prior to contact. Thus, since charge transfer

was shown in Chapters 2 and 3 to depend directly on the area of contact, the variation of bed displacement will not affect the charge transferred.

4. 3. The electrification behaviour of insulating particles.

The situation under consideration is the vibrated bed shown in FIG.40, containing insulating material. Conduction currents are neglected in the bed, so that each contact surface can be considered independently. This is reasonable for bulk resistivity greater than approximately $10^{13}\Omega$ m.

The quantity of interest is the particle bed charge as a function of time. After a rapid initial increase, the surface charge on the vessel walls will remain approximately constant. The time constant for the wall transient charge behaviour is determined by the charge transfer time, and the time necessary for all wall areas to be contacted by particles. The charge transfer time is of the order of ms as shown in Chapter 3, and the time for all areas to be contacted is small. Thus the wall charge time constant is much less than the bed charge time constant and is subsequently neglected. The net charge due to interparticle charging is zero, consequently interparticle charging is neglected. All charge is assumed to arise as a result of particle collisions with the base plate, which is held at approximately zero potential. Only one type of particle material is considered to be present in the particle bed.

Particles are brought to the lower bed surface as a result of the mixing action caused by the vibration process. While at the surface, they undergo repeated collision with the base plate, until they are mixed with the bulk of the bed again. The rate of surface renewal for a given vibrated bed is determined by the vibration amplitude and frequency.

The case of a particle undergoing repeated contact with a boundary wall during pneumatic transport has been considered by Cole[43]. This approach can be modified to describe vibrated bed charging. The charging process has been analysed on the basis of the following assumptions[43].

(1) The initially charged particle is assumed to have a charge distribution over its surface, which is equivalent to having the total charge concentrated

at the centre of the spherical particle. This assumption will not be absolutely true in practice, since charge regions will be localised on the particle. However the approximation is reasonable, since the principal field component reducing charge transfer is found to be due to the bulk space charge, and not the individual particle charge.

(2) Charge transfer is assumed to occur due to the establishment of an effective driving potential V_{cp}.

(3) Charge transfer ceases at a critical separation distance d_c, which defines the capacitance at separation as $\varepsilon_o A_c/d_c$.

(4) A_c, the area over which charge transfer occurs during a contact, is assumed to be the area of an equivalent parallel plate capacitor. A_c is approximately equal to $2\pi R_p d_c$, since d_c is assumed to be much smaller than the particle radius R_p (FIG.42). No stipulation is made as to the mechanism governing the formation of V_{cp}. The charge transferred per contact event (contact and separation) is given as[43],

$$\frac{dq_{pt}}{dn_p} = \frac{\varepsilon_o A_c Z}{d_c} (V_{cp} - V_{1p} - V_6), \qquad 4.15a$$

where q_{pt} is now, the particle charge due to collisions with the base plate, n_p is the number of particle collisions with the base plate, Z is a factor to allow for the discrepancy between real and apparent contact area, due to the effect of surface roughness[43]. The range of expected values for particle/boundary surface contacts, is 10^{-3} to 10^{-7} [7,43]. V_{1p} is the induced potential difference between the particle and the base plate due to the particle charge. V_6 is the potential difference caused by the bulk of the particles.

The theoretical approach of Cole[43] can be generalised by removing the constraints of assumptions (3) and (4), to accomodate various charge transfer models[12,38,39]. If equation 4.15a is written as,

$$\frac{dq_{pt}}{dn_p} = C_b(V_{cp} - V_{1p} - V_6), \qquad 4.15b$$

then C_b and V_{cp} can be deduced from the particular charge transfer model chosen. The situation defined by Cole[43] can be derived directly from the surface state

electron transfer model (Chapter 1), with the surface state density greater than $10^{18} m^{-2} eV^{-1}$. The value of V_{cp} is then given by the effective work function difference between the contact materials.

It was shown in Chapters 2 and 3 that no individual model of charge transfer is universally applicable to practical situations. Thus, rather than specifying V_{cp} in terms of a particular charge carrier energy distribution, the analysis will be given in generalised form. The approach of Cole[43] will then be applied since this has the advantage for present purposes, of defining C_b by geometrical considerations, and making no stipulation as to the mechanism governing the formation of V_{cp}.

By considering the image charge produced by the charged particle in the base plate, V_{1p} can be shown to be given by[43],

$$V_{1p} = \frac{q_{pf} d_c}{2\pi R_p^2 \varepsilon_o} \quad , \qquad 4.16$$

where q_{pf} is the total particle charge.

The potential difference between the base plate and a point d_c from the base plate, is found by integrating the field in the particle bulk (Appendix 1). The result is given in equation A.1.12. as $V_6 = N_b q_{pf} M$, A.1.12 where N_b is the number of particles per unit volume.

$$M = \frac{\frac{L_1 d_c}{2} - \frac{d_c^2}{2} + g_1 \varepsilon_{r4} \left(d_c - \frac{d_c^2}{2L_1} \right)}{\varepsilon_o \varepsilon_{r4} \left(1 + \frac{g_1 \varepsilon_{r4}}{L_1} \right)} \quad . \qquad A.1.13$$

Considering initially a particle in the surface layer adjacent to the vessel base plate, undergoing repeated contact with the base plate. By definition $q_{pf} = q_{pt} + q_{at}$, where q_{at} is the initial particle charge before contact of the particle. The particles in the bulk of the bed are assumed to have a uniform charge q_{at}, whilst the particle under consideration has a charge $q_{pt} + q_{at}$. Substitution of these charge expressions, and equations A.1.12 and 4.16 into equation 4.15b yields

$$\frac{dq_{pt}}{dn_p} = \frac{dq_{pt}}{fdt} = (q_1 - K_1 q_{at} - k_1 q_{pt}) \quad . \qquad 4.17$$

Here f, the vibration frequency is equal to dn_p/dt, and q_1 is defined as $C_b V_{cp}$, which using Cole's[43] approach is equal to,

$$2\pi \varepsilon_o R_p Z V_{cp} \quad . \qquad 4.18$$

k_1 is defined as $\frac{C_b d_c}{2\pi R_p^2 \varepsilon_o}$, which using Cole's[43] approach is equal to,

$$\frac{Zd_c}{R_p} \quad . \qquad 4.19$$

K_1 is defined as $\frac{C_b d_c}{2\pi R_p^2 \varepsilon_o} + C_b N_b M$,

which using Cole's[43] approach is equal to,

$$\frac{Zd_c}{R_p} + N_b M 2\pi \varepsilon_o Z R_p \quad . \qquad 4.20$$

Solving equation 4.17 with the boundary condition $q_{pt} = 0$ at $t = 0$, yields for the particle charge at time t,

$$q_{pt} = (q_1 - K_1 q_{at}) \frac{1}{k_1} (1 - e^{-k_1 ft}) \quad . \qquad 4.21$$

This describes the transient charge characteristics of an individual particle whilst in the layer adjacent to the vessel base plate

In order to determine the transient behaviour of the bed as a whole, an effective average charge for each particle in a given surface layer is first calculated. If s is the rate of renewal of surface area (unit total area)$^{-1}$, then the fraction of surface area with age between t and t+dt has been shown to be $se^{-st}dt$, by the surface renewal approach of Danckwerts[174]. If there are C_a particles (unit area)$^{-1}$ then the overall charge (unit area)$^{-1}$ of the lower surface layer, using equation 4.21 is given by,

$$C_a q_{pt} = C_a \int_o^\infty \frac{se}{k_1}^{-st} (q_1 - K_1 q_{at})(1 - e^{-k_1 ft}) dt \quad .$$

$$\text{Thus, } q_{pt} = \frac{1}{k_1 + s'} (q_1 - K_1 q_{at}) \quad , \qquad 4.22$$

where $s' = s/f$.

For the vibrated bed system under consideration s' is much greater than k_1 (Chapter 5), consequently equation 4.22 can be simplified to

$$q_{pt} = (q_1 - K_1 q_{at})/s' \quad . \qquad 4.23$$

If the particles at the surface are considered to have an average residence time of $1/s$, rather than the age distribution given by Danckwerts[174], then the charge per particle after this average surface residence time is given by equation 4.21 as $q_{pt} = (q_1 - K_1 q_{at}).(1 - e^{\frac{-k_1 f}{s}})/k_1$, when s' is much greater than k_1 this simplifies to $q_{pt} = (q_1 - K_1 q_{at})/s'$, which is an identical result to that derived using the age distribution function. Consequently it is valid to regard particles as having an average surface residence time, provided s' is much greater than k_1.

The transient characteristics can now be derived for the whole bed from either equation 4.22 or equation 4.23. Equation 4.22 will be considered. This equation enables the particle bed charging process, to be specified in terms of discrete charge layers. Each layer is brought to the lower bed surface by the mixing process. On average every particle will acquire a charge given by equation 4.22, before being returned to the bulk of the bed. The charge per particle in the bulk of the bed is assumed constant and equal to q_{at} during the charging process of any layer, consistent with the derivation of equation 4.21. As successive layers are brought into contact with the base plate, then the value of q_{at} will increase, but for any given layer in contact, q_{at} can be considered constant during the contact time. The overall bed charge increase due to successive layers contacting the base plate, is given by

$$\frac{dQ_m}{dL_p} = N_s \, q_{pt} \quad , \qquad 4.24$$

where L_p is the number of particle layers, Q_m is the total charge in the bed, N_s is the number of particles in the lower bed surface, adjacent to the base plate.

Elimination of q_{pt} from equations 4.22 and 4.24 gives

$$\frac{dQ_m}{dL_p} = \frac{N_s}{k_1 + s'} (q_1 - K_1 q_{at}) \quad , \qquad 4.25$$

where q_1, k_1 and K_1 are defined in equations 4.18, 4.19 and 4.20 respectively. All the particles in the bed, are assumed to have a charge q_a before vibration. The charge added subsequently, due to vibration is denoted by q_p. By definition,

$$q_p + q_a = q_{pt} + q_{at} \quad , \qquad 4.26$$

and by assumption,

$$Q_m = N_v\, q_{at} + N_s q_{pt} \quad , \qquad 4.27$$

where N_v is the total number of particles in the bed. Differentiation of equation 4.27 gives,

$$\frac{dQ_m}{dL_p} = N_v \frac{dq_{at}}{dL_p} + N_s \frac{dq_{pt}}{dL_p} \quad . \qquad 4.28$$

Differentiation of equation 4.22 yields

$$\frac{dq_{pt}}{dL_p} = \frac{-K_1}{k_1 + s'} \cdot \frac{dq_{at}}{dL_p} \quad .$$

Eliminating $\frac{dq_{pt}}{dL_p}$ from this equation and equation 4.28 gives $\frac{dQ_m}{dL_p} = C_1 \frac{dq_{at}}{dL_p}$, 4.29

where $C_1 = N_v + N_s(C_2 - 1)$,

and $C_2 = \dfrac{k_1 + s' - K_1}{k_1 + s'}$.

$\frac{dQ_m}{dL_p}$ is now eliminated using equations 4.25 and 4.29, giving, after rearrangement,

$$\frac{dq_{at}}{dL_p} + \frac{q_{at} K_1 N_s}{(k_1 + s')C_1} = \frac{q_1 N_s}{(k_1 + s')C_1} \quad .$$

Solving, and applying the boundary condition that q_{at} is equal to q_a when L_p is equal to 1, yields,

$$q_{at} = \frac{q_1}{K_1}\left[1 - e^{\left(\frac{K_1 N_s (1 - L_p)}{(k_1 + s')C_1}\right)}\right] + q_a e^{\left(\frac{K_1 N_s (1 - L_p)}{(k_1 + s')C_1}\right)} \quad . \qquad 4.30$$

Substitution of q_{at} from equation 4.30 and q_{pt} from equation 4.22 into equation 4.26 yields,

$$q_p = \frac{q_1}{k + s'} + \frac{C_2 q_1}{K_1}\left[1 - e^{\left(\frac{K_1 N_s (1 - L_p)}{(k_1 + s')C_1}\right)}\right] + C_2 q_a e^{\left(\frac{K_1 N_s (1 - L_p)}{(k_1 + s')C_1}\right)} - q_a \quad . \qquad 4.31$$

Since $\frac{dL_p}{dt} = s, \quad L_p = st + 1,$ 4.32

using the boundary condition that L_p is equal to 1 when $t = 0$.

Elimination of q_{pt} from equations 4.26 and 4.27, and substitution of the expression for q_p from equation 4.31 and q_{at} from equation 4.30, into the result, together with substitution for L_p from equation 4.32 and simplification, yields for Q_m,

$$Q_m = \left[N_v - \frac{N_s K_1}{k_1 + s'}\right]\left[\frac{q_1}{K_1}\left[1 - e^{\left(\frac{-K_1 N_s ts}{(k_1 + s')N_v - K_1 N_s}\right)}\right] + q_a e^{\left(\frac{-K_1 N_s ts}{(k_1 + s')N_v - K_1 N_s}\right)}\right] + \frac{N_s q_1}{k_1 + s'} . \quad 4.33$$

The time constant for charge acquisition τ_1 is given by

$$\tau_1 = \frac{(k_1 + s')N_v - K_1 N_s s}{K_1 N_s s} . \quad 4.34$$

Equation 4.33 does not consider gas discharge effects. If discharge occurs at a certain value of the bed charge, then the increase of Q_m with time will abruptly terminate, at the time corresponding to the critical charge level. If t is much less than τ_1, equation 4.33 can be simplified to

$$Q_m = \left(N_v - \frac{N_s K_1}{k_1 + s'}\right)\cdot\left(\frac{q_1 t + q_a}{K_1 \tau_1}\right) + \frac{N_s q_1}{k_1 + s'} . \quad 4.35$$

For the conditions of the vibrated bed, s' is much greater than k_1 and K_1 (Chapter 5), thus

$$\tau_1 \approx \frac{N_v}{K_1 N_s f} , \quad 4.36$$

and $$Q_m = q_1 t N_s f + N_v q_a + N_s q_1 / s' . \quad 4.37$$

The values of q_{pt} and q_{at} can also be derived assuming t is much less than τ_1 and s' is much greater than k_1 and K_1. Substitution of q_{at} from equation 4.30 into equation 4.22, followed by this simplification yields for q_{pt},

$$q_{pt} = \frac{q_1}{s'} - \frac{K_1 q_a}{s'} . \quad 4.38$$

Similar simplification of equation 4.30 gives for q_{at}

$$q_{at} = \frac{q_1 t N_s f}{N_v} + q_a . \quad 4.39$$

The potential induced in the base plate by the moving particle bed, is given by equation 4.12. V_h, given in equation 4.7b is expressed in terms of a bulk charge density, ρ_c and a surface charge density σ_c. From equation 4.39 the bulk charge density

$$\rho_c = \frac{N_v q_{at}}{U} = \frac{q_1 t N_s f}{U} + \frac{q_a N_v}{U} , \qquad 4.40$$

where U is the volume of the bed.

The surface charge density can be calculated from equation 4.38

$$\sigma_c = \frac{N_s q_{pt}}{A_{b'}} = \frac{N_s}{A_{b's'}} (q_1 - K_1 q_a) . \qquad 4.41$$

Hence, ρ_c and σ_c can be eliminated from equation 4.7b using equations 4.40 and 4.41. Substitution of the resulting expression into equation 4.12, together with substitution of the capacitance C_h from equation 4.7a, gives for the peak induced potential V_{3m}, assuming a negative particle charge,

$$V_{3m} = \left[\frac{g_{20}\omega A_b R}{\left(g_1 + \frac{L_1}{\varepsilon_{r4}}\right)^2 2\beta}\right]\left[L_1\left(\frac{L_1}{2\varepsilon_{r4}} + g_1\right)\left(\frac{q_1 t N_s f}{U} + \frac{q_a N_v}{U}\right) + \left(\frac{L_1}{\varepsilon_{r4}} + g_1\right)\frac{N_s}{A_{b's'}}(q_1 - K_1 q_a)\right] . \qquad 4.42$$

This equation shows that the observed peak potential should increase linearly with time, whilst vibration is applied. However if air breakdown processes occur, then the bed charge will remain constant, and the potential should remain at a constant value. The anticipated behaviour then, when vibration is applied, is a linear rise in peak potential with time, as the charge in the bed increases. This is followed by a constant peak potential when the bed charge has reached a high enough value to initiate air breakdown processes.

4. 4. The electrification behaviour of conducting particles.

The situation considered is shown in FIG.43, where in this case a direct current measurement is considered. The Vibron® electrometer time constant is sufficiently long so as to register a direct current, as discussed in Chapter 5. The particles considered in this case have a bulk resistivity which is sufficiently low to ensure that charge layers at the base and screen are of much smaller dimensions than the bed as a whole. Some idea of the magnitude

of this resistivity limitation can be obtained by considering the charge layer adjacent to the screen, as shown in FIG.44. Convective particle movement carrying charge away from the screen, is opposed by return conduction currents.

Consideration of the limit of the charge balance over the differential element shown, together with the assumption of a steady state and substitution of the differential form of Gauss's Law[118], allows the resulting equation to be solved to give,

$$\rho_c = \rho_{co} e^{-\left(\frac{y}{r_b v_p \varepsilon_o \varepsilon_{r4}}\right)} , \qquad 4.43$$

where v_p is the particle velocity dy/dt, ρ_{co} is the volume charge density at the screen surface, and ε_{r4} is the effective dielectric constant of the bulk particle bed.

The distance over which the charge density falls to 63.2% of the value at y equal to 0, is given by $r_b v_p \varepsilon_o \varepsilon_{r4}$.

Considering v_p as the velocity due to bulk mixing in the bed, this is of the order of 5mm s^{-1} (Chapter 6). The minimum value of L_1 was 5mm. Consequently the maximum resistivity allowable before the charge boundary layer approaches the bed dimensions, is of the order of $10^{10} \Omega m$.

For materials having a bulk resistivity below this value, the charge boundary layer is much smaller than the electrode separation distance and the electric field in the bulk of the bed due to the boundary charge is uniform.

It is now postulated that charging will occur at the perforated screen due to the cascading action of the particles passing through the screen. This is superimposed on any impact charging occuring at the base plate and screen. The cascade charging is postulated as the driving force for ohmic conduction currents in the bed, and diffusion effects and charge migration are neglected. It is further postulated that the vibration process establishes the cascade charge layer depth, since vibration determines the physical position of the charged particles. The extreme depth of the charge layer is given by the amplitude of vibration. It is further postulated that the charge loss during a vibration cycle is small, in relation to the total charge at the screen, hence

the electric field time dependence is determined solely by the charge layer depth. The charge density is assumed constant in the charge layer, so that a quasi steady state prevails. On the basis of these postulates, an expression can be derived for the expected direct current measured at the screen. The field around the screen is given by Gauss's Law. Considering unit area and a one dimensional situation (FIG.43),

$$E_4 = \int_{L_2 - y}^{L_2} \frac{\rho_c dy}{\varepsilon_{r4}\varepsilon_o} = \frac{\rho_c y}{\varepsilon_{r4}\varepsilon_o} \quad , \qquad 4.44$$

where L_2 is the bed bottom surface to screen separation distance.

Thus, using equation 4.44,

$$V_6 = \int_o^y E_4 d(L_2 - y) = \frac{-\rho_c y^2}{2\varepsilon_{r4}\varepsilon_o} \quad . \qquad 4.45$$

The potential at the edge of the charge layer V_{6e} is given by equation 4.45 as,

$$V_{6e} = \frac{-\rho_c g_3^{\,2} k_3}{2\varepsilon_{r4}\varepsilon_o} \quad , \quad k_3 \leq 1.0, \qquad 4.46$$

where g_3 is the depth of the charge layer, and k_3 is a constant to account for the fact that the charge layer will not be entirely uniform, due to some conduction back to the screen. If g_3 is much less than L_2, as is the case in practice, then L_2 is approximately equal to the screen to base plate separation distance L_3, and the uniform electric field in the bed is equal to V_{6e}/L_3.

Thus the conduction current density j_3 is given by equation 4.46 as

$$j_3 = \frac{V_{6e}}{r_b L_3} = \frac{-\rho_c g_3^{\,2} k_3}{2\varepsilon_{r4}\varepsilon_o r_b L_3} \quad .$$

The current measured by the electrometer is the average value.

Since $g_3 = g_{2o} \cos \frac{\omega t}{2\beta}$, for $0 < t < \frac{2\pi\beta}{\omega}$,

and $g_3 = 0$ for $2\pi\beta/\omega < t < 2\pi/\omega$,

then j_{3Av}, the average current density, is given by

$$j_{3Av} = -\frac{\omega\rho_c k_3 g_{2o}^2}{4\pi\varepsilon_{r4}\varepsilon_o L_3 r_b}\int_o^{2\pi\beta/\omega}\cos^2\frac{\omega t}{2\beta}\,dt.$$

Thus, i_{3Av}, the average current is given by,

$$i_{3A_v} = A_b j_{3Av} = -\frac{A_b}{4L_3 r_b}\,\frac{\rho_c g_{2o}^2 \beta k_3}{\varepsilon_{r4}\,\varepsilon_o} \quad . \qquad 4.47$$

The assumption that the charge layer depth is directly proportional to the amplitude of vibration, requires that the particles cascade through the screen perforations at a sufficient rate to fill the gap caused by the bed movement. The mass rate of flow of particles through a circular orifice has been given by Beverloo[175] as

$$W' = 0.585\ \eta_b (g_a)^{\frac{1}{2}}(D_{po} - k_2 D_p)^{5/2},$$

where $\eta_b = \eta_s(1 - V)$ is the bulk density, V is the voidage (≈ 0.4[170]), η_s is the solid density (2600 kg m^{-3} for glass ballotini), D_{po} is the orifice diameter, which was 2mm, k_2 is a constant related to the material and equal to 1.4 for glass ballotini, D_p is the particle diameter, the average value being 128 μm for glass ballotini.

Thus, 1.4×10^3 particles can flow through the orifice in half a cycle at 48Hz (the frequency studied in Chapter 5), if there is no particle mass below the screen. This quantity is greater than the number required to fill the volume of the air space below the screen, produced as a result of bed movement. Consequently the gap is completely filled in accordance with the assumption that the charge layer depth is directly proportional to the vibrational amplitude. The same result applies to quartz particles, by application of the particle flow equation, using relevant parameters.

CHAPTER 5

AN EXPERIMENTAL INVESTIGATION OF VIBRATED BED CONTACT ELECTRIFICATION AND CHARGE DISSIPATION.

An experimental study of particle electrification in a vibrated bed was carried out. The effects of vibrational amplitude, electrode geometry and particle resistivity were studied.

5. 1. The Vibration System.

The physical arrangement of the vibration system is shown in FIGS. 45a,b. A rectangular perspex vessel (C), was supported on a steel vibration table (Q). The vibration table was supported horizontally by two spring steel leaves (J), each of which was clamped to the table at one end. The other end of each leaf was clamped between dural blocks (I), which were held rigidly to the Dexion® support framework (S). The Dexion® framework was firmly bolted to a massive steel base (H).

The vibrator (O) was a Ling Dynamic Systems, Series 202 Model. For its operation, this utilised the force exerted by a permanent magnet, on a current carrying conductor. The moveable central core of the vibrator, forming the current carrying conductor, was rigidly coupled via a dural bar (P) to the vibrating table. A permanent magnet was mounted in the vibrator housing, which was securely bolted to the massive steel base. Vibration of the central core, was produced by the passage of an alternating current through the core. Two power sources were used. The first was an oscillator/amplifier combination constructed in the department, which could supply a maximum power of 40V A to the vibrator. The alternative power supply, used for lower power requirements, was a Ling Dynamic Systems TPO 20 oscillator/amplifier combination. This could supply maximum power of 20V A. The TPO 20 unit supplied a maximum current of 2.5Ar.m.s., for which natural convection cooling of the vibrator was adequate. The power unit constructed in the department could supply 4.5A r.m.s. to the vibrator. Cool air was blown through the vibrator housing to produce the required cooling rate in this case. Significant power losses occurred through mechanical damping in the support system. Consequently it was necessary to

operate at the resonant frequency of the system. The spring leaf lengths, shown in FIG.45b, were chosen to produce a resonant frequency of 48Hz. The maximum table amplitude of displacement, available at this frequency, was 0.8mm. Operation at the resonant frequency of the system ensured that the table displacement behaviour was closely sinusoidal, corresponding to the principle harmonic. Other harmonics were considerably damped in magnitude.

The displacement of the table was monitored using an ASL Model 1055 Displacement Indicator. This device could accurately monitor capacitance changes at a given junction. The capacitance of the junction, was balanced against a variable condenser in the instrument. Changes in capacitance at the measured junction, produced an out of balance voltage, which was viewed on an oscilloscope. The measuring capacitor, consisted of a parallel disc arrangement as shown in FIGS. 45a,b. One plate (G) was held firmly by epoxy resin to a polyethylene block (K) on the vibrating table. The other plate (F) was aligned above and parallel to the first plate, and held rigidly to the support framework. The instrument bandwidth of 300Hz, was sufficiently large to limit attenuation at 48Hz to a small value. Consequently, position calibration under static conditions, was used to determine the relation between output potential and displacement. Simultaneous measurement of the displacement using a travelling microscope, and the instrument output voltage, enabled calibration of the instrument in terms of displacement, to an accuracy of 5%, down to a displacement of 0.01mm. The equilibrium capacitor plate separation distance was 7mm. This could be accurately reset prior to any experimental test, by adjusting the plate separation distance to produce a zero output voltage, for the known calibration instrument settings. A typical output voltage trace is shown in FIG.46.

Distortion of the vibration table sinusoidal waveform was negligible, since the system was operated near the resonant frequency. The weight of the vibration table and attachments was much greater than the particle bed weight, thus the out of phase bed movement, had little effect on the table displacement behaviour.

The frequency of vibration was monitored using a 1.2MHz Racal counter timer, to an accuracy of $\pm$0.1Hz. The drive frequency from the power supplies remained constant over a period of several hours. This was sufficient for all experiments.

Measurement of the air gap beneath the vibrated bed, was achieved using a capacitance technique described by Gutman[170]. This consisted of measuring the capacitance between a pair of plates, parallel to the perspex vessel walls, and adjacent to the bottom of the bed. During bed displacement measurement, the dural base plate shown in FIG.45, was replaced by a perspex base, shaped so as to allow positioning of the capacitance plates adjacent to the bed bottom. The bed behaves as if it were a single plastic mass with a zero coefficient of restitution[170]. Thus the change from dural to perspex does not alter the displacement characteristics of the bed.

The dimensions and positions of the plates are shown in FIG.47, along with the support vessel dimensions. The field between the measurement plates was uniform due to this configuration, except for edge effects round the plate perimeters. The plates were connected via shielded cables to a transformer bridge, which had been constructed in the department. The measurement circuit is shown in FIG.48. The bridge operated in a similar fashion to the ASL Displacement Indicator, mentioned earlier. The bridge was balanced to give a zero cutput voltage for the static bed situation. The out of balance voltage corresponding to bed movement was then displayed on an oscilloscope. Calibration of the instrument was carried out as described by Gutman[170], and consisted of noting the voltage change as the vessel was filled to a known height with granular material.

Voidage changes in the bulk of the bed could also affect the measured capacitance. However, for the virtual earth plate dimensions used, this effect has been shown to be small[170], particularly at the maximum displacement values of interest.

A typical displacement measurement is shown in FIG.49, from which it is apparent that the air gap thickness approximation used in section 4.2 is

reasonable. A more detailed analysis by Gutman[170] of the bed displacement, also confirms the approximation of Section 4.2.

5. 2. Current and potential measurement.

The direct current produced at the perforated screen in the bed, was monitored using a Vibron® 33B-2 electrometer, with a B33B current and resistance measurement attachment. The equivalent first order time constant of this instrument, was shown in Chapter 2 to be 144ms. This is much greater than the periodic time at 48Hz, of 20.8ms. Consequently the current measured was an average value of any current pulses produced. The electrometer input resistance, was always maintained at a value at least ten times less than the bed resistance between the screen and base.

The induced potential in the base plate was monitored using an instrument constructed in the department (FIG.50). The internal loop gain of the instrument was approximately 10^5 which due to the feedback circuit employed, reduced the effective cable input capacitance from 50pF to 5×10^{-4}pF. The overall gain was 1, and the instrument had the property of inverting the signal. The effective input capacitance was much less than the smallest C_h value of approximately 0.4pF, justifying the assumption made in Chapter 4, that the instrument input capacitance can be neglected. The instrument capacitive reactance, $(\omega \times 5 \times 10^{-16})^{-1}$, was equal to $6.6 \times 10^{12}\Omega$ at 48Hz. This was much greater than the input resistance of $10^7\Omega$, thus fulfilling the other requirement given in Chapter 4 for neglecting the instrument input capacitance. The instrument input resistance was at most equal to 1% of the resistance between the screen and base in the bed. The response time constant of the instrument was less than 1ms, which was sufficiently small to cause negligible attenuation of a signal having a periodic time of 20.8ms.

RC_h was calculated to have a maximum value of 0.1ms for the present experiments. Thus the assumption that the transient term can be neglected in equation 4.10 is reasonable for a signal having a periodic time of 20.8ms. Since $\omega C_h R$ has a maximum value of 3×10^{-2}, the assumption made in deriving equation 4.12, that this should be much less than 2β which has a minimum value of 1.2, is reasonable.

The dural vessel base plate was insulated from the vibration table , using a perspex block as shown in FIG.45. Attachment to the vibration table was by means of nylon screws. Electrical screening was positioned as shown in FIG.45b, to reduce any extraneous signals. The position of this screening was found to have a very small effect on measured potentials in the vessel base plate.

The ambient air temperature was within the range 18°C - 22°C for all experiments, and the ambient relative humidity was within the range 40% - 60% throughout.

All metal parts associated with the apparatus, other than those used in electrical measurements, were earthed to a common point during the experiments.

The perforated screen was connected to earth during measurements at the base electrode, whilst the base was connected to earth during current measurements at the screen electrode.

5. 3. Bulk resistivity measurement.

A concentric cylinder, resistivity measurement cell was constructed as shown in FIG.51. This is similar to the design given by Lawver[176], and the relation between bulk resistivity and measured cell resistance, neglecting end effects, is given by[176],

$$r_b = \frac{2\pi L_b R_b}{\ln(D_{p2}/D_{p1})} \quad , \qquad 5.1$$

where R_b is the measured cell resistance, D_{p1} is the diameter of the inner cylinder, D_{p2} is the inner diameter of the outer cylinder, L_b is the length of either electrode covered with particles.

The resistance between the concentric cylinders was measured using a Vibron® 33B-2 electrometer, and a B33B attachment. The known resistance used in the measuring potential divider network, was adjusted to be less than 1% of the unknown. The applied potential required for the measurement, was supplied by an APT Electronic Industries Model 509 voltage source.

The current flowing in the measurement circuit was directly proportional to the applied potential up to 100V for quartz particles. Apart from a small deviation at low potentials, the same proportionality was observed with

ballotini. This ohmic behaviour, confirmed the validity of the resistivity concept applied to the particulate material.

The resistivity values were determined, after having vibrated the cell during filling, to give a constant bed voidage. This ensured standard material packing for all measurements. The resistivity was calculated from the electrometer potential reading, immediately after stabilisation, following application of the known voltage. This was approximately 5s after application of the known voltage. Prolonged voltage application, caused an apparent increase in the measured cell resistance. The method of measurement chosen, ensured that the resistivity deduced, was closely related to the effective resistivity, experienced by contact charge, present in the material as a result of vibration. The measured value was a complex combination of surface, bulk, and interparticle resistances.

The particulate materials used in the vibration studies, together with measured resistivity values taken immediately after the contact electrification experiments, are shown in Table 11. The bulk dielectric constant values in Table 11, were calculated from the approximate relation, $\varepsilon_{r4} = \varepsilon_r(1 - V) + V$, where ε_r is the dielectric constant of the pure solid material, V is the voidage of the bed, and is approximately equal to 0.4 [170] for the present experiments.

This relation is derived on the assumption that the bed can be treated as a parallel combination of solid and air layers.

The bulk dielectric constant values shown, are accurate to within approximately $\pm$ 20%.

5. 4. The electrification behaviour of insulating particles.

The potential induced in the vessel base plate, as a result of a moving charged particle bed was given in equation 4.12. The predicted proportionality between the measured potential, and the instrument input resistance, was observed experimentaly for both conductive and insulating particles in the vibrated bed. Typical oscilloscope records of the output from the measuring electrometer, are shown in FIGS.53a,b and c. The particulate

material was polypropylene of extremely high resistivity (Table 11) in a bed 45mm deep. The perforated screen was positioned 20mm above the upper bed surface, and the results for three values of $\omega^2 y_o/g_a$ are shown, where y_o is the amplitude of the table displacement. The polypropylene particles were charged negatively. This was verified, by pouring the vessel contents into a Faraday pail connected to the Vibron® 33B-2 electrometer. The Faraday pail was of a similar design to that described as Type 1 by Lawver[177], and consisted of two concentric metal cylinders insulated from one another. The sign of charging observed is consistent with that reported in Chapter 3 for polypropylene charging at a single contact. For negative particle charge, equation 4.12 predicts a positive induced potential immediately following the bed lift-off (FIG.52). The nearly horizontal sections of FIGS. 53a,b and c, correspond to the bed at rest on the base plate. Since the amplifier carried out inversion of the signal, the induced potential is seen to be positive as expected, immediately after bed lift-off. The form of the signal, is close to the cosine behaviour predicted by equation 4.12, (FIG.52) and the signal has the expected frequency. The vertical sections predicted are not precisely observed in FIG 52, due to the finite time required for bed lift-off, and contact.

The predicted induced potential, as a function of time after starting vibration, is given by equation 4.42. This was derived on the assumptions that K_1 and k_1 were much less than s', and that t was much less than τ_1. The value of k_1 from equation 4.19 is $8 \times 10^{-7} Z$, for d_c equal to 10^{-10}m as given by Cole[43], and $8 \times 10^{-6} Z$ for d_c equal to 10^{-9}m as suggested by Krupp[12]. From equation 4.20, with ε_{r4} given in Table 11, g_1 equal to 20mm, and L_1 equal to 45mm, then K_1 is equal to $1.09 \times 10^{-4} Z + k_1$, where Z has a value less than 1. The minimum value of s is shown in Chapter 6 to be of the order of $2s^{-1}$, thus the minimum s' is equal to 4.2×10^{-2}. This confirms the assumption that k_1 and K_1 are much less than s'. For a voidage of 0.4, N_b is equal to 7.3×10^{10}, and N_s is equal to 3.4×10^4, whilst N_v is equal to 6.08×10^6, for a 45mm bed depth. N_s is calculated from N_b assuming the top

layer occupies approximately a volume $A_b D_p$. τ_1 from equation 4.36 is therefore equal to $3.43 \times 10^4/Z$. Since t is less than 3.6×10^3, the assumption that t should be much less than τ_1 is seen to be reasonable. Since these assumptions, made in deriving equation 4.42, are seen to be reasonable, equation 4.42 should describe correctly the induced potential as a function of time after starting vibration.

FIG.54 shows the peak to peak induced potential as a function of time after starting vibration, for a 45mm deep vibrated bed of polypropylene particles, with g_1 equal to 20mm. Each set of results at a given vibrational amplitude was obtained with a fresh sample of material. The initial non-linear behaviour is attributed to the non-uniform nature of the bed charge at the start. Equation 4.42 was derived on the assumption of uniform bed charge. After the initial region, the relation between induced potential and time is seen to be linear as predicted by equation 4.42. A limiting value is reached, which is expected if air breakdown processes occur, as mentioned in Section 4.3.

The relation between the electric field adjacent to the base plate, and the induced potential is given by equation 4.14 which involves no arbitrary constants. Substitution of the measured β value of 0.9, and the final constant value of V_{3m} from FIG.54, into equation 4.14, gives an electric field of 2.34×10^6 V m^{-1} for $\omega^2 y_o/g_a$ equal to 5.28, and an electric field of 3.69×10^6 V m^{-1} for $\omega^2 y_o/g_a$ equal to 6.02. The values of V_{3m} are taken as half the peak to peak voltages. The field values are calculated from equation 4.14 using the measured peak bed displacements of 0.38mm for $\omega^2 y_o/g_a$ equal to 5.28, and 0.465mm for $\omega^2 y_o/g_a$ equal to 6.02. The electric fields predicted from the Paschen curve for air[16], are 5.61×10^6 V m^{-1} for 0.38mm gap width, and 5.26×10^6 V m^{-1} for 0.465mm gap width at atmospheric pressure. The agreement between these electric field values, and the observed values is good, providing further evidence for the presence of gaseous discharge effects. The predicted breakdown field values are greater than the observed values by a factor of 1.4 - 2.4. This ratio is of the same order as the Paschen curve overestimate of the non-uniform field break-

down level, which was found to be 1.9 in Section 3.4, for single contact studies.

The value of the product ZV_{cp} can be estimated from the slope of the linear section of the line in FIG.54, and equation 4.42. For $\omega^2 y_o/g_a$ equal to 5.28, ZV_{vp} is found to be 0.99×10^{-3}V, and for $\omega^2 y_o/g_a$ equal to 6.02, ZV_{cp} is found to be 1.9×10^{-3}V. Since V_{cp} is expected to be of the order of 1V[43], Z is of the order of 10^{-3}. This is much greater than the value of 10^{-7} postulated by Cole[43], and indicates that the real area of contact occupies a greater proportion of the apparent area than suggested by Cole[43]. However the value of Z is close to the value of 10^{-4} suggested by Harper[7].

A direct current component was not observed with the polypropylene particles, when the perforated screen was positioned in the bed and the induced potential had stabilised to a constant value.

Assuming the direct current to be directly proportional to the electric field across the bed divided by the resistivity, then for the resistivity value of Table 11, and the estimated charge density from equation 4.37, the predicted current is very small, of the order of 0.1pA. This value is below the measurement sensitivity of the electrometer and is consistent with the observations.

5. 5. The electrification behaviour of conducting particles.

When particles of bulk resistivity below $10^{10}\Omega$m are vibrated, the charge layers produced by contact electrification, are of sufficiently small width, to produce a uniform field across the bulk of the bed examined in the present studies (Section 4.4). Electrolytic effects can also produce measurable currents. This was observed in a static bed. The electrolytic direct currents, were always less than 10% of those due to contact electrification, and were subtracted from the contract electrification current values measured. Some effects which appear to be related to this static bed behaviour. have been reported by Gibbings[178] for liquid systems.

The direct and induced currents due to vibration with conducting material, were found to stabilise to constant values, in times of less than 1s. This

is in contrast to the behaviour with insulators discussed in Section 5.4, and reflects the lack of volume charge in the conductive case. The reproducibility of the results with conductive materials was within 10% from run to run, which is good for contact electrification work.

Equation 4.47 predicts that the direct current should be inversely proportional to the screen to base separation distance L_3. FIG.55 shows the measured direct current as a function of $1/L_3$ for values of L_3 greater than 20mm, with quartz particles. The plot is linear as expected, however the lines do not extrapolate to the origin. This indicates behaviour is not entirely as predicted by equation 4.47, for large values of L_3. FIG.56b shows the direct current as a function of L_3 for quartz over the whole measured range. A maximum is observed in FIG.56b, indicating some deviation from the predicted behaviour for small values of L_3. Similar behaviour with regard to a maximum was observed for ballotini (FIG.56a). Deviations from the predictions are attributed to, (1) Modification of the particle movement pattern as L_3 is changed. (2) A change in the conduction path uniformity for small L_3 values, due to the screen perforations having a significant effect in reducing the field uniformity. (3) The simplifying assumptions made in deriving equation 4.47, which are not entirely representative of the actual situation.

Equation 4.47 also predicts that the direct current should be proportional to the bed maximum displacement (g_{2o}) squared. The direct current is shown as a function of $(g_{2o})^2$ in FIG.57a for ballotini and FIG.57b for quartz. The anticipated linear dependence was observed for quartz and ballotini over most of the range at all values of L_3. Some non-linearity was observed for the highest vibrational amplitude employed with ballotini. This was attributed to instability in the bed cyclic motion. The non-linearity at the smallest vibrational amplitude, is attributed to a change in the value of β, the fraction of the cycle during which the bed is in flight. Previous work[170] indicates that β will not vary by more than approximately 10% over the rest of the range of vibrational amplitudes, which would have a small effect on

the results. Since β can only be accurately measured to about 8%, no correction was applied for variations in β .

The values of g_{2o} shown, are obtained from a calibration experiment with no screen present in the bed, or with the screen positioned at a value of L_3 greater than 25mm. Values of g_{2o} could not be unambiguously measured for smaller values of L_3, since the presence of the screen affected the capacitance measurement. However errors in estimating g_{2o} for small values of L_3, from values measured with L_3 greater than 25mm, will be small and systematic.

Equation 4.47 predicts that for a negatively charged particle mass, the current flow from the screen should be positive to earth. This was observed for both quartz and ballotini which charged negatively on pouring into a Faraday pail. As expected from charge continuity considerations, an equal and opposite direct current was observed at the base plate, when the Vibron® electrometer was connected to the base plate, and the screen was earthed.

The induced potential in the base plate can be predicted using a similar approach to Chapter 4. Since the charge in the bulk of the bed is small, the induced component is due principally to the charge layers adjacent to the base and screen. Conduction effects and the charge transferred to the screen at each contact are neglected, on the assumption that the charge conducted during a cycle is much less than the total charge at the base and screen. This assumption is reasonable, as discussed later.

The charge adjacent to the lower side of the screen, consists of a surface charge due to impact over part of the area, and a charge distributed in depth, due to particles cascading through the perforations. Thus, the charge adjacent to the lower surface of the screen, σ_{cu} is given by

$$\sigma_{cu} = \int_{L_2-g_3}^{L_2} \rho_{cu}\,dy + \sigma_{c1} \quad ,$$

where y is directed as shown in FIG.43, thus,

$$\sigma_{cu} = \rho_{cu} g_3 k_3 + \sigma_{c1} \quad , \qquad 5.2$$

where σ_{c1} is the surface charge density adjacent to the screen, ρ_{cu} is the volume charge density adjacent to the screen, k_3 is a constant defined in equation 4.46, to account for charge conduction back to the screen, g_3 is the depth of the charge layer adjacent to the screen.

A similar analysis to that described in Chapter 4 can now be carried out, to give the induced potential. An air gap will form in the regions below the screen adjacent to metal sections. To simplify the analysis, the field in this region, immediately below the screen is assumed to be given by $E_5 = V_5/k_4 g_3$, where k_4 is a constant dependent upon vibration conditions and screen geometry, to account for the non-uniformity of the air gap. Using the same method as that outlined in Appendix 1, the electric field in the air gap above the vessel base is found to be,

$$E_3 = \frac{-\frac{\sigma_c}{\varepsilon_o}\left(\frac{L_2}{\varepsilon_{r4}} + k_4 g_3\right) - \frac{\rho_{cu} g_3^2 k_4 k_3}{\varepsilon_o} \frac{-\sigma_{c1} g_3 k_4}{\varepsilon_o} + V_3}{g_2 + \frac{L_2}{\varepsilon_{r4}} + g_3 k_4} \quad . \qquad 5.3$$

Thus, following Section 4.2, the induced charge in the vessel base is given by,

$$Q_3 = \left[\frac{A_b \varepsilon_o}{k_4 g_3 + g_2 + \frac{L_2}{\varepsilon_{r4}}}\right] \cdot \left[\frac{-\sigma_c L_2}{\varepsilon_{r4} \varepsilon_o} \frac{-\rho_{cu} g_3^2 k_3 k_4}{\varepsilon_o} - \frac{k_4 g_3 (\sigma_c + \sigma_{c1})}{\varepsilon_o} + V_3\right] \quad . \qquad 5.4$$

Thus $Q_3 = C_{h1}(-V_{h1} + V_3)$, $\qquad 5.5$

where $V_{h1} = \frac{\sigma_c L_2}{\varepsilon_o \varepsilon_{r4}} + \frac{\rho_{cu} g_3^2 k_3 k_4}{\varepsilon_o} + \frac{k_4 g_3 (\sigma_c + \sigma_{c1})}{\varepsilon_o}$, $\qquad 5.6$

and $C_{h1} = \frac{A_b \varepsilon_o}{k_4 g_3 + g_2 + \frac{L_2}{\varepsilon_{r4}}}$. $\qquad 5.7$

The present experimental arrangement can be analysed to give (Section 4.2),

$$V_3 = RC_{h1}\frac{dV_{h1}}{dt} + RV_{h1}\frac{dC_{h1}}{dt} \quad . \qquad 5.8$$

Thus differentiating equations 5.6 and 5.7, substituting into equation 5.8, simplifying, since g_2 and g_3 are much less than L_2/ε_{r4}, and rearranging yields,

$$V_3 = \frac{-g_{2o}\omega C_{h1} R}{2\beta\varepsilon_o}\left[\sigma_c \cos\left(\frac{\omega t}{2\beta}\right) + k_4\sigma_{c1}\sin\left(\frac{\omega t}{2\beta}\right) + \rho_{cu} g_{2o} k_3 k_4 \sin\left(\frac{\omega t}{\beta}\right)\right] \quad 5.9$$

The induced potential during the bed flight is expected to possess a complex time dependent form, with a period equal to the time of flight of the bed.

FIGS. 53d and e show the induced potential for a bed of ballotini (Table 11) with L_2 equal to 45mm and L_3 equal to 40mm. The period of the variable potential section of the waveform corresponds within measurement accuracy to the bed time of flight. The phase of the induced potential corresponds to a negative particle layer, which existed in the bed. The cyclic behaviour is seen to change from a straightforward sine or cosine wave during bed flight, when the vibrational amplitude is increased. This is consistent with the increased importance of the final term in equation 5.9. This term represents the second harmonic of the induced wave form.

FIGS. 59a, b and c show the induced potential for a bed of quartz particles (Table 11), and the same geometery as for ballotini. The particles were charged negatively and the phase of the induced potential corresponds to this sign of charge.

Conduction back to the screen during a cycle can be estimated from equation 4.43. The maximum particle flow velocity is given by $g_{2o}\omega/2\beta$, due to cascading, and y is equal to g_{2o}. The velocity of the particles due to bulk mixing, is much less than that due to bed movement (Chapter 6) and can be neglected. Thus, at 48Hz, the exponent in equation 4.43 is equal to 0.55 for quartz, and 3.32 for ballotini, with β equal to 0.8, and the resistivity values of Table 11. This indicates that significant non-uniformity of the charge layer may exist for the ballotini, and hence k_3 may be less than 1. However, the electrical resistivity of the particle mass below the screen may be greater than the values given in Table 11, due to increased voidage. This would lead to a decrease in the values of the exponents calculated above.

The peak to peak induced potential as a function of $(g_{2o})^2$ is shown in FIGS. 58a and 58b, for ballotini and quartz respectively. The fact that a

linear dependence is observed over most of the range, indicates that the term involving ρ_{cu} in equation 5.9, is dominant over this region. Deviations from linearity are due to the importance of the bed surface charges in the equation. The observation that even with no screen present in the bed, the peak to peak induced potential is directly proportional to $(g_{2o})^2$ is contrary to expectation from equation 5.9 since ρ_{cu} and σ_{c1} are equal to 0. The reason for the discrepancy is not certain. It is possible that conduction effects on the vessel walls near the base, modify charge levels to give the observed behaviour.

When the screen is introduced into the bed, maintaining L_3 approximately constant, the induced potential increases by approximately 50% from the value with the screen above the bed. This indicates that both the charge layer adjacent to the screen and that adjacent to the base make a significant contribution to the observed potential.

The assumption that the charge conducted during a cycle, is much less than the charge at either boundary surface, can now be checked. Considering ballotini with $\omega^2 y_0/g_a$ equal to 5.93, (g_{2o} is equal to 0.71mm), L_3 equal to 40mm, then the induced potential V_{3m} from FIG.58a is equal to 2.15V. Since g_{2o} is equal to 0.71mm, then from equation 5.9, $(k_4 \sigma_{c1} + \rho_{cu} g_{2o} k_3 k_4)$ is approximately equal to 8.1×10^{-6} C m^{-2}. From FIG.57a, the direct current for the same conditions is equal to 2.9×10^{-8}A. Thus, during one cycle, the change in charge per unit area is given by 3.3×10^{-7} C m^{-2}. This quantity is much less than the permanent charge density, and the assumption that this can be neglected is reasonable. For quartz the conduction charge movement is much smaller, and the assumption is also reasonable.

The ratio of the direct currents for ballotini and quartz, from equation 4.47 for identical vibration conditions and electrode geometry is given by,

$$\frac{i_{3Avb}}{i_{3Avq}} = \frac{r_{bq}\ \rho_{cb}}{r_{bb}\ \rho_{cq}} \cdot \left(\frac{g_{2ob}}{g_{2oq}}\right)^2 \cdot \frac{\beta_b}{\beta_q} \cdot \frac{k_{3b}}{k_{3q}} \quad , \qquad 5.10$$

where the final subscript b refers to ballotini, and q refers to quartz. For given vibration conditions and geometry, the ratio $\frac{\rho_{cb}}{\rho_{cq}}$ is expected to be related to the ratio of the alternating peak to peak potentials, Assuming that the volume charge adjacent to the screen is dominant, from equation 5.9,

$$\frac{\rho_{cb}}{\rho_{cq}} = \frac{V_{3mb}\ \beta_b\ k_{3q}\ (g_{2oq})^2}{V_{3mq}\ \beta_q\ k_{3b}\ (g_{2ob})^2} \quad . \qquad 5.11$$

Thus substituting equation 5.11 into equation 5.10, and putting β_b equal to β_q which is approximately observed in practice,

gives, $\frac{i_{3Avb}}{i_{3Avq}} = \frac{r_{bq} V_{3mb}}{r_{bb} V_{3mq}}$.

Thus, for $\omega^2 y_o/g_a$ equal to 5.93, and L_2 equal to 40mm, using the induced potentials of FIGS. 58a and 58b and the resistivities of Table 11, gives $\frac{i_{3Avb}}{i_{3Avq}} = 22.2$. In calculating this value, V_{3m} is assumed to be equal to half the peak to peak induced potential shown in FIGS. 58a and 58b. The observed ratio from FIGS. 57a and 57b is 56.9. The prediction then, is of the correct order of magnitude, the discrepancy is due to the simplifying assumptions made.

5. 6. The electrification behaviour of particles of intermediate resistivity.

The bulk resistivity of a Diakon® particle mass, was found to be $1.9 \times 10^{12} \Omega$ m (Table 11). This value is intermediate, between the resistivity of conducting and insulating particles discussed in Sections 5.5 and 5.4. Neither the assumptions that, (a) charge layers are much smaller than the bed dimensions, nor (b) the charged particle mass has a uniform volume charge density, are valid in the present case. The charge behaviour is anticipated to reflect some aspects of both the conductive and insulating regimes. The time to establish constant current values was of the order of several minutes, intermediate between the conductive and insulating cases. Initial particle charges were often found to be positive, however, after several minutes of vibration, a constant negative charge developed. The anticipated particle

charge from the rolling and sliding contact results of Chapter 3 for PMMA, is positive. This corresponds to the usual initial charge sign with the particles. Rose[50] has quoted earlier studies in which all dielectric particles investigated charged negatively after impact with a metal surface. Thus the negative charge observed during impact caused by vibration with the present studies, is in agreement with these previous findings. The impact contact mechanism appears to influence the sign of charge transfer. All results shown from the present investigation for Diakon® particles, were obtained when the system had stabilised to constant current and potential values after several minutes of vibration.

The induced potential for different values of $\omega^2 y_o/g_a$ is shown in FIGS. 59d,e and f, for a bed of Diakon® particles. The waveform exhibits some deviation from symmetry, presumably due to the non-uniform bulk charge.

The peak to peak induced potential as a function of the maximum bed displacement is shown in FIG.60. The linear behaviour observed, is predicted by equation 4.12 for a volume and surface charge distribution. This observation corresponds to the behaviour of insulating material. A net direct current was observed however, consistent with conductive material behaviour. The direct current is seen to be linearly related to the bed displacement squared in FIG.61 for all values of L_3 except 5mm, when charge widths would exceed L_3. The linear relation is in accordance with the prediction of equation 4.47 for conductive material. In the present case, the effect of L_3 is of course modified by finite charge layer depths. The direct current is shown as a function of the screen to base separation distance in FIG.62. A maximum is observed, in accordance with observations for conductive material (FIGS. 56a and 56b). As anticipated then, the material of intermediate resistivity exhibits some characteristics of both insulating and conducting particles.

5. 7. The relevance of the vibrated bed studies to previous work, and to general particle handling situations.

Some previous studies of electrification associated with low voidage granular

material, have been concerned with fluidised beds[165-168], as discussed in Section 4.1. Previous authors[165-168] have made no distinction between the various bulk resistivity regimes considered in the present study. Thus the theoretical technique of treating each boundary surface independently, in the case of insulating particles, was not developed. Likewise, the importance of conduction currents from boundary surfaces other than the measurement probe, with conducting material, was not appreciated.

Bafrnec[166] has stated that if a metal probe immersed in a fluidised bed, acquires a charge of the same polarity as the charge on the fluidised particles, then charge transfer by direct contact from the particles to the probe is occurring. This will be the case with insulating particles. However, with conductive particles or those of intermediate resistivity as used by Bafrnec[166], conduction currents from other boundary surfaces, for instance the vessel walls or the distributor plate, can lead to the immersed probe acquiring the same charge polarity as the particles. This was evident in the present vibrated bed studies. Further evidence for the importance of conduction currents, is the observation of Ciborowski[167], that the presence of earthed objects in a fluidised bed, caused a large increase in the potential of an immersed metal probe. This behaviour was observed for particles of the intermediate resistivity range, and is consistent with the occurrence of conduction currents.

When the screen in the vibrated bed studies, was connected to an Anders Electronics Ltd., Electrostatic Voltmeter Model 23, with a full scale range of 2kV, then potentials up to 500V were occasionally recorded, although generally the potential remained below 70V. The vessel base plate was earthed, and the bed consisted of quartz or ballotini particles. The potentials observed were found to be highly non-reproducible. The potentials are smaller by approximately an order of magnitude, compared with those measured at metal probes in fluidised beds.[166-168] The final probe potential with a conductive particle bed, can be considered to be determined by an equilibrium between charging and decay currents[167,168]. A change in the leakage path resistance

will therefore cause a change in the probe potential. Since particles were observed on occasions to adhere to the vessel walls in the present studies, this could have caused a resistance charge, and would account for the variability of the potential values. The lower vibrated bed potentials compared with the fluidised bed potentials, are attributed to a lower leakage path resistance.

Kiselnikov[168] considers that the observed transient probe potential behaviour, for a probe immersed in a fluidised bed of insulating particles, is due to an approach to equilibrium between leakage and charging currents. For highly resistive material, the decay currents are negligible, and the transient behaviour according to Kiselnikov[168] is determined entirely by a so-called effective resitance to charging. This situation corresponds to that analysed in Section 4.3, and the time constant predicted for vibrated bed charging was of the order of 10^7s. The time constant for fluidised bed charging will probably not differ by more than two orders of magnitude from this value. Kiselnikov[168] reports a stable constant charge level in a time of 900s for high resistance material. Thus, the charge is not limited by the opposing electric field due to the bed charge, and some other limiting factor is operational. This is probably the occurrence of air breakdown effects. Thus, the expected transient probe potential should resemble FIG.54 if air breakdown effects are operative, since FIG.54 has been shown to be determined by air breakdown. The results reported by Kiselnikov[168] are indeed similar to FIG.54, and thus the presence of air breakdown seems probable.

Boland[179,180] has studied the current and potential, in a metal probe embedded in the wall of a fluidised bed, as a bubble passes the probe. Typical results are shown in FIG.63. The apparent charge polarity reversal as the bubble passes the probe, is interpreted by Boland[179,180] as evidence that different charging mechanisms occur in the nose and wake of the bubble. There is no reason to anticipate that this should be the case, and it is possible that the observed behaviour is in fact due to induction effects, combined with conduction on the vessel wall in front of the probe.

Increasing the relative humidity from 15%, resulted in a maximum occurring in the peak heights of FIG.63. Ciborowski[167] has reported a maximum in the potential of a probe immersed in a fluidised bed, as the relative humidity is increased. The appearance of maxima could reflect a change in the particle behaviour, from that corresponding to the resistive regime, to that corresponding to the conductive regime, as the relative humidity and hence bulk conductivity is increased.

Dolgopolov[181] has carried out investigations of electrification in a vibrated bed of quartz particles. In this case the total bed charge after vibration was measured using a Faraday pail. Complex behaviour was found in the plot of total bed charge against vibrational frequency, with the principal variation around $\omega^2 y_o/g_a$ equal to 1.0. Similar studies were carried out in the present series of experiments for ballotini and quartz particles. It was found that the particle bed charge, was principally determined by the pouring method into the Faraday pail. This is to be expected since, any charge produced during vibration will quickly flow to the vessel walls, when vibration is terminated, for conductive materials such as quartz. Thus the results of Dolgopolov[181] probably reflect the influence of packing changes, induced by vibration, which modify the material behaviour on pouring. This is further supported by the observation that changing the vibration time, in the measurement range of 60s to 600s, had no effect on observed charge levels,[181] as expected if the observed charge was due to pouring and not to vibration.

The importance of air breakdown effects in limiting charge levels is underlined in the present study. Smy[182] reports that air breakdown processes occur when a pile of dust is dispersed from a plane surface by an air blast. The dust charge was found to be almost independent of flow velocity, particle size and material. These results are consistent with the observations reported in Sections 3.4 and 5.4, and support the view that in practice air breakdown processes will invariably limit charge levels with insulating materials at atmospheric pressure.

It is apparent from the present study that significant charge build up can

occur on isolated conductors, in contact with particulate material of bulk resistivity below $10^9 \Omega$ m. These materials may at first sight appear to be sufficiently conducting to eliminate charge build up. Thus, to avoid any danger from spark discharges in practical handling situations, it is essential to ensure that all conductors are earthed, even if they are in contact with a particle mass of bulk resistivity below $10^9 \Omega$ m.

The present results indicate the possibility of a novel economical vibration monitoring technique. Vibration is of importance in several aspects associated with chemical plant operation, for instance with regard to compressor behaviour. Thus expensive vibration monitoring devices are available. A cell of similar design to the present vibrated bed, could be attached to the item of interest, and the measured induced potential, would show both the frequency, and with prior calibration, the amplitude of vibration. The instrumentation required in this case is inexpensive, a current amplifier of similar design to FIG.50, and an oscilloscope would suffice.

The potential induced by moving charged particles in nearby conductors, could also be utilised as an additional analysis technique for studying fluid/particle systems. For instance an instrument similar to FIG.50 could be employed to detect bubble movement in a fluidised bed, as an alternative to conventional capacitance techniques.

CHAPTER 6

NOVEL APPLICATIONS UTILISING PARTICLE CHARGE

The force exerted by a uniform electric field E, on a particle with a charge q_{pf}, is equal to Eq_{pf}. This fundamental property is utilised in most industrial applications of particle charging[24], and in the two applications of particle charging considered in the present study. These new applications are (a) improved heat transfer in a fluidised bed, using contact electrification as a means of particle charging, and (b) electrostatic separation using induction charging in a vibrated bed system.

6. 1. Improved heat transfer in a fluidised bed - Principle of the technique.

The particles in a fluidised bed are known to be charged[165-168]. Limitations on charge levels are imposed by conduction effects and air discharge, as discussed in Chapter 5.

Thus, the application of suitable electric fields will produce additional particle motion in the bed. Fluidised beds are employed conventionally where high heat transfer coefficients are required[183], for instance in combustion or drying operations. Vigorous particle motion in the bed leads to a low resistance to heat transfer. A further improvement in the heat transfer coefficient would be beneficial in two principal areas. (1) When a given heat transfer coefficient is necessary for a particular process. Since increasing the air flow rate leads to an increase in the heat transfer coefficient, application of a low power requirement technique to increase the heat transfer coefficient, would permit decreasing the air flow rate to the bed, and result in a net power saving. (2) For a situation such as drying, where the time of drying is of economic importance, an increase in the heat transfer coefficient would result in advantageous reduced drying times.

Part of the resistance to heat transfer from an immersed surface in a fluidised bed, is due to a stagnant gas film at the heater surface[184,185]. Heat transfer adjacent to an immersed surface can be considered as heat conduction across a gas boundary layer to the particles[185]. In the limit of very small objects in a fluidised bed, of the same size order as the heater used in

the present investigation, Wicke[185] has shown that the heat transfer coefficient to the immersed object is given by,

$$h = \frac{k_g}{L_g} \quad . \qquad 6.1$$

where h is the heat transfer coefficient, k_g is the gas thermal conductivity, L_g is the thickness of the gas layer through which heat passes by conduction.

Application of an alternating electric field normal to the surface will cause oscillation of the charged fluidised particles through the stagnant gas layer. Due to the fluidisation process the particles will also move parallel to the boundary surface. Thus, the oscillating particle movement will tend to reduce the gas layer thickness (L_g), and increase the heat transfer coefficient.

If the rate of renewal of particles at the surface of the immersed object is slow, then an additional resistance to heat transfer may arise, as a result of an increase in temperature of the surface particle layer[184,186]. The heat transfer coefficient in this case will be smaller than indicated by equation 6.1. Application of an electric field will also decrease this resistance. Since particles of both polarities exist in the bed, as is shown later, application of an electric field will cause movement and collision of particles. This will lead to increased mixing and an increased heat transfer coefficient. The movement and collision process, will tend to cause the bulk particle mass to remain in a fixed position. However, particles adjacent to the immersed surface are free to move under the influence of the electric field. Since the motion of a charged particle in an alternating electric field is of fundamental importance to the heat transfer enhancement process, charged particle movement will now be considered.

6. 2. The motion of a charged particle in an alternating electric field.

The physical situation considered, is that of the motion of a charged particle in the horizontal plane, normal to a vertical boundary surface. The assumption is made that drag forces can be represented by Stokes'[187] Law. This is reasonable for the frequencies, materials and geometry considered, since the particle Reynolds Number is always less than 1, and the drag force is shown later

to have little effect on the particle motion. The electric field E, acting on the particle is assumed to be uniform. The electric field due to the charge on the particle mass is neglected, since this is constant with respect to time, and is independent of the applied electric field.

By Newton's second law for a particle in the gas boundary layer, adjacent to a boundary surface,

$$M_p \frac{d^2x_2}{dt^2} = Eq_{pf} - 3\mu_v D_p \frac{dx_2}{dt} \quad , \qquad 6.2$$

where M_p is the particle mass, μ_v is the air viscosity, x_2 is the distance coordinate measured from, and normal to, the boundary surface, E is given by $E_m \sin \omega t$; ω, q_{pf}, D_p and t are as defined previously.

Equation 6.2 is a second order ordinary differential equation, which can be solved by the standard technique of determining the Particular Integral to give the transient behaviour, and determining the Complementary Function to give the oscillatory behaviour. Neglecting the transient term, the amplitude of the oscillatory term is given by

$$x_{2m} = \frac{q_{pf} E_m}{M_p \left[(\omega^2)^2 + \left(\frac{3\pi\mu_v D_p}{M_p} \right)^2 \right]^{\frac{1}{2}}} \quad . \qquad 6.3$$

For a particle diameter of 240 μm, which was the average size used in the experimental investigations, air viscosity of 1.66×10^{-5} N s m^{-2}, the value at 20°C, and a particle specific gravity of 1.1 which applied to the material used, then $\frac{3\pi\mu_v D_p}{M_p}$ is equal to 4.72 s^{-1}. Thus for the lowest frequency used of 20Hz, $(\omega^2)^2$ is much greater than $\left(\frac{3\pi\mu_v D_p}{M_p} \right)^2$ and equation 6.3 can be simplified to

$$x_{2m} = \frac{q_{pf} E_m}{M_p \omega^2} \quad . \qquad 6.4$$

Thus the maximum total displacement due to the oscillatory term is given by

$$\frac{2q_{pf} E_m}{M_p \omega^2} \quad . \qquad 6.5$$

Equation 6.4 can also be derived directly from equation 6.2 if the Stokes' Law term is neglected. Thus the drag term is not important for the present studies, and any error due to the assumption of Stokes' Law applying is negligible.

6. 3. Experimental apparatus and experimental procedure.

FIG.64 shows a schematic diagram of the apparatus, together with associated electrical equipment. The fluidised bed was supported in a 146.5mm internal diameter perspex column (D), fitted with a gauze gas distributor at the base(E) to ensure uniform gas distribution. The unexpanded bed height was 205mm in all cases, and the top surface of the heater (C) was positioned 20mm below the unexpanded bed height. The air flow rate to the fluidised bed was monitored with a rotameter (B) which was calibrated using a wet gas flowmeter. The air flow rate was adjusted using a manual control value (A) situated in the inlet air line. The particulate material used in the fluidised bed was Diakon®, of 240 μm average particle diameter. The bulk resistivity of this material, during the heat transfer studies, measured using the technique described in Section 5.3, was found to be $1.5 \times 10^{14} \Omega$ m.

The heater assembly is shown in FIG.65. This consisted of a mild steel block, which has a slot milled into it, to support a 25W heater element. Two brass plates coated with epoxy resin, were positioned on opposite sides of the heater support block, parallel to, and at a distance of 11mm from the heater block surface. The heater unit and brass plates were supported by vertical perspex rods. The heater unit was aligned with the central bed axis for all experiments.

The temperature of the heater unit was measured with a copper/constantan thermocouple, soldered to the support block side. A similar thermocouple was placed in the fluidised bed to measure the bed temperature. The output from the thermocouples was indicated on a Bryans Model 21004 chart recorder. The bulk bed temperature at different positions, was found to be constant within measurement accuracy of $\pm 1^{o}$C. Consequently one thermocouple reading was sufficient to establish the bed temperature. The thermocouples were calibrated

against a mercury thermometer, by immersion in an oil bath, at temperatures from 17°C to 95°C, to an accuracy of ± 1°C. The variable direct current supply to the heater unit, was produced by a rectifier/variac circuit. The power supplied to the heater was determined by measuring the voltage and current using an Avometer.

The sinusoidal electric field, was derived by applying a sinusoidal high potential to the brass plates, from an oscillator/amplifier/transformer network. The heater support block was earthed. The epoxy resin coating of the brass plates, ensured that leakage currents and hence the power consumption were of a small value, regardless of the bed bulk electrical resistivity. The root-mean-square potential applied to the brass plates was measured using an Anders Electronics Ltd. Electrostatic Voltmeter, Model 23. Two versions were available, with full scale ranges of 2kV and 10kV. The maximum alternating potential available was 8kV r.m.s. at frequencies from 20Hz to 600Hz. A constant potential of either polarity could also be applied to the brass plates when required from a Brandenburg Model 776 high voltage unit. Potentials up to 15kV were available. Values below 15kV were derived from a resistor potential divider network.

The experimental procedure adopted, was to fluidise the bed at uniform controlled gas velocities. The power supply to the heater unit was then adjusted to the required level, and the system was allowed to stabilise. The point in time at which the heater was in a steady state, could be determined from the recorder output of the transient behaviour. Since the bed thermal capacity was large, and the heater input power was comparatively small, the bed temperature change was slow, and a pseudo steady state situation was assumed.

The required electric field magnitude and frequency was then selected, and applied to the brass plates. The heater temperature was then noted again, when steady state conditions prevailed.

(188)

The heat transfer coefficient for any given conditions was calculated from,

$$h = \frac{X}{A_h \Delta\vartheta} \quad , \qquad 6.6$$

where h is the heat transfer coefficient, A_h is the surface area of the heater support block, $\Delta\vartheta$ is the temperature difference between the heater support block surface, and the bulk of the bed, and X is the power supplied to the heater.

A preliminary experiment had shown that the heat transfer coefficient was independent of the heater input power, and thus one power setting was sufficient to determine the heat transfer coefficient for particular conditions.

During all series of experimental runs, the heat transfer coefficient with no applied electric field was checked regularly. Thus, if, as happened occasionally, the zero electric field heat transfer coefficient varied during a set of experiments at particular fluidising conditions, the experimental data were rejected. This variation in the heat transfer coefficient, is presumably due to changes in the bed bulk charge, affecting the bed fluidisation behaviour.

The ambient temperature was within the range 18°C to 22°C throughout the experiments described in this chapter, and the ambient relative humidity was within the range 40% - 60%.

6. 4. Experimental results and discussion.

Preliminary experiments indicated, that if the particle bed was left for several days without supplying fluidising air, then the effect of an electric field on the heat transfer coefficient was small. During subsequent fluidisation, the effect of an electric field on the heat transfer coefficient was found to increase, reaching a limiting value in a period of the order of two hours. During the same two hour period, the minimum fluidisation velocity was observed to increase by approximately 10%. Both of these effects were attributed to particle charge build up in the bed. All subsequent experiments were carried out when the electric field effect was constant with respect to time after fluidisation.

Variation of the gas flow velocity, caused a change in the heat transfer coefficient, both with and without an applied electric field, as shown in FIG.66, and a change in the heat transfer coefficient increase due to an applied

electric field, as shown in FIG.67. The minimum fluidisation velocity throughout the experiments was approximately 25mm s^{-1}.

In agreement with previous work[184], the heat transfer coefficient without an applied electric field is found to increase with increasing gas flow velocity. The increase in the heat transfer coefficient due to application of an electric field, decreases with increasing gas flow velocity (FIG.67). The effect of mechanical stirring on heat transfer in a fluidised bed, has been shown previously [184] to be virtually independent of gas velocity, in contrast to the effect of an electric field. Mechanical stirring is unaffected by gas velocity, and thus the heat transfer coefficient increase due to mechanical stirring should be independent of gas velocity. However the electric field technique, acts locally on individual particles. Increasing agitation of the particles, due to fluidisation air velocity increases, will tend to cause the agitation due to the applied electric field to be overwhelmed. Thus the heat transfer coefficient increase due to the applied field, will tend to decrease with increasing gas flow velocity.

The heat transfer coefficient as a function of the frequency of the applied alternating potential, is shown in FIG.68a for a gas velocity of 28.2mm s^{-1}, and FIG.68b for a gas velocity of 32.8 mm s^{-1}. For potentials below 4kV r.m.s., the heat transfer coefficient decreases with increasing field frequency from 20Hz. For potentials above 4kV r.m.s., the heat transfer coefficient passes through a broad maximum as the frequency is increased from 20Hz. The heat transfer coefficient for a 4kV r.m.s. applied potential passes through a maximum for a gas velocity of 28.2mm s^{-1}, whilst no maximum is observed for a gas velocity of 32.8mm s^{-1}.

The explanation for this behaviour can be deduced from equation 6.5, and considerations of the critical impressed particle movement length. If particle movement across the gas boundary layer is the principal mechanism which is changed by electric field application, then the optimum electric field parameters would be those for which the amplitude of particle movement is equal to the boundary layer thickness. If the particle does not traverse the whole

boundary layer thickness, then the reduction in the effective gas layer thickness will be below the optimum value. If the particle traverses the boundary layer thickness very quickly and is held at the heater surface for a length of time, then a reduction in the heat transfer coefficient is expected, compared with the case where an insignificant time is spent by the particle at the heater surface. At high frequencies the former effect will become operative, and at low frequencies the latter effect will appear, for a particular magnitude of the electric field. Thus an optimum is expected in the heat transfer coefficient as the frequency is changed. Due to the variation of particle sizes and charge levels, the optimum is expected to be broad, as is observed in practice (FIGS. 68a, 68b). An estimate for the effective gas layer thickness can be derived from equation 6.1, using the measured heat transfer coefficient for zero electric field (FIGS. 68a, 68b), and the thermal conductivity of air ($0.026 W m^{-1} K^{-1}$). Thus the effective boundary layer thickness is of the order of 150μm. If on the other hand, the principal mechanism altered by electric field application is the mixing process, then the optimum impressed particle movement length will be approximately equal to the particle radius. Shorter movement lengths will be ineffective in promoting mixing, whereas greater lengths will cause particle adherence for significant lengths of time to the heater surface, as in the previous case. Thus the optimum distance of travel is of the order of 120-150μm in the case of either mechanism.

The maximum oscillatory displacement of a particle, when unimpeded by any boundary surface, calculated from equation 6.5 is shown in FIG.69. A particle charge of 2.45×10^{-13} C has been assumed, since this ensures that the optimum travel distance of 120μm, corresponds to the observed optimum frequency. (FIGS. 68a, 68b) of approximately 100Hz for 6kV r.m.s. applied potential. The maximum oscillatory displacement is assumed to be equal to the optimum travel distance. The charge value above is reasonable, since the air breakdown charge level for a 240μm diameter particle is 4.8×10^{-12}C, based on a breakdown electric field of 3×10^{6} V m^{-1} (7). This indicates that the theoretical requirements are of the correct order of magnitude.

If the optimum point is taken on the 6kV r.m.s. line of FIG.69, corresponding to 100Hz and 120μm, then it is apparent that for greater electric fields, the optimum distance will correspond to higher electric field frequencies than at 6kV. Due to the breadth of the observed maximum (FIGS. 68a and 68b), it is not possible to accurately determine any movement in the position of the optimum for different electric field values. However, no inconsistencies are apparent in the behaviour. If the electric field in FIG.69 is reduced below 6kV r.m.s., then the optimum distance corresponds to lower frequency values. Eventually no optimum will be observed for low field values, above the minimum frequency employed of 20Hz.

The predicted optimum is at a frequency of 60Hz for a 3kV r.m.s. potential applied to the field plates. However, due to the breadth of the maximum, and the assumptions made in deriving the critical length, it is not surprising that no optimum is observed at this frequency (FIGS. 68a, 68b). The behaviour actually observed (FIGS. 68a, 68b) is a continual decrease in the heat transfer coefficient with increasing frequency. This indicates that the optimum lies below 20Hz which is at a much smaller frequency value than observed for the larger electric fields applied, precisely as expected from FIG.69.

The result of applying a negative constant potential is shown in FIG.70. The heat transfer coefficient reaches a maximum value at an applied potential of -1.7kV, as the potential is decreased. The initial increase is attributed to increased turbulence, caused by different velocities being imported to particles of various sizes and charges. When the potential is decreased below -2kV, particles are probably held firmly to the heater surface, causing a decrease in the heat transfer coefficient. When a positive potential was applied, the heat transfer coefficient decreased for all potential values. This indicates charge asymmetry in the bed.

PMMA was found to charge positively with respect to metals as discussed in Chapter 3 for rolling contact. Diakon® (PMMA) particles were found often to charge positively before lengthy vibration periods, as mentioned in Chapter 5. Thus the particle layer adjacent to the heater support block in the fluidised

bed, will probably carry a predominantly positive charge. Application of a positive potential to the brass plates, would lead to permanent attachment of positive particles to the heater support, and thus a decrease in the heat transfer coefficient. Application of a small negative potential to the field plates would lead to the increased turbulence already mentioned. However, increasing the potential further would cause negatively charged particles present in the bulk of the bed to attach to the heater support block surface. Due to the anticipated larger separation distances from the heater surface, for negative as opposed to positive particles, attachment potentials for negative particles will be higher. Thus, the observed behaviour is consistent with the sign of charging observed in the other studies.

The fact that particles of both polarities were present in the bed, was verified by lowering a plate at a high potential into the bed. Particles were found to adhere to the plate for either polarity. No adherence occurred if the high potential was not applied.

It is of interest to consider whether induction charging of the particles is relevant to the present studies. The charge relaxation time is approximately equal to $\varepsilon_o \varepsilon_r r_b$ [11] for an element of the bed. For Diakon®, of bulk dielectric constant approximately equal to 2.2 and bed bulk resistivity $1.5 \times 10^{14} \Omega m$, the relaxation time is of the order of $3 \times 10^3 s$. Thus for frequencies of upwards from 20Hz, induction effects will be small, since significant induction charging requires electric field application for a time greater than the charge relaxation time.

If field asymmetry, with respect to time, is introduced, by combining both alternating and constant potential values, then further increases in the heat transfer coefficient can be obtained, compared with the value using either separately. The effect of applying a negative constant potential to various alternating potential values, is shown in FIG.71a for a gas velocity of $28.2 mms^{-1}$, and FIG. 71b for a gas velocity of $32.8 mm\ s^{-1}$. The behaviour resembles that for a negative potential alone (FIG.70) and the mechanisms leading to an increase in heat transfer coefficient, due to both constant and

alternating potentials appear to be basically additive. Moreover, the increased particle movement due to the alternating potential, improves the effectiveness of the constant potential in increasing the heat transfer coefficient. Application of a constant positive potential combined with the alternating potential, leads to a decrease in the heat transfer coefficient compared with that for the alternating potential alone. This also is in accord with the observations when applying only a constant positive potential, and further suggests the effects due to constant and alternating potentials are additive.

If reduction of the gas boundary layer thickness, is the principal effect of electric field application, then the optimum anticipated improvement in heat transfer coefficient will be of the order of 100%. This is because in the optimum situation for a symmetric field with respect to time, the particles adjacent to the heater surface, will on average, be positioned half the distance away from the surface, they occupy when no electric field is applied. Thus, from equation 6.1, a decrease in L_g by 50% leads to a 100% increase in the heat transfer coefficient, based on the zero field values. Further small increases may be expected due to additional mixing effects. From FIG.68 , the maximum percentage increase in the heat transfer ccefficient is 140% in accordance with expectation.

It should be noted that Masuda[189] has reported an investigation into the charge production capabilities of various powder systems. It was found that certain powders would charge naturally in a homogeneous state, polyethylene and epoxy resin falling into this category. However, other powders such as nylon and PVF, would not charge if in a homogeneous state. The addition of a small proportion of a different material to the non-active powders, was found to give a product which was charged and responded to electric field variations. Consequently it may be helpful in a practical application of the heat transfer enhancement technique, if boundary surface areas are small, to add small quantities of different materials to the bulk material, and therefore aid contact electrification.

The increase in heat transfer coefficient in the present experiments was achieved with the electric field only active over approximately 65% of the heater support block surface. In a practical situation this percentage could be raised, and proportionately greater heat transfer coefficient increases could be expected, compared with those observed in the present study.

6. 5. Applications of the technique.

It is essential to ensure that danger to personnel is minimal, during practical operation of the heat transfer enhancement technique. This can be achieved by including a high resistance in the high potential circuit, in series with the unit to which the potential is applied. This limits the available current should anyone short circuit the device, and minimises the operational hazard.

Applications could be envisaged in any processing situation, where a particle mass of bulk resistivity greater than approximately $10^{11}\Omega m$, is contacted with a boundary surface, to give heat or mass transfer. The $10^{11}\Omega m$ limitation is necessary, to ensure that particles retain contact charge for a sufficient length of time, to be acted upon by the electric field.

Thus a possible suitable situation for application of the technique, is paper drying or textile drying[183] in a fluidised bed. The process consists of passing a continuous length of paper or textile through the bed, which is maintained at a high temperature. The sheet material is dried by contact with high temperature particles and air, and an increase in the heat transfer coefficient could lead to significant savings in drying time. By positioning two electrodes parallel to, and on opposite sides of the sheet material, and applying an alternating electric field to the electrodes, the heat transfer coefficient could be increased. An increase in the heat transfer coefficient leads to a proportionate decrease in the drying time, if the drying periods of importance are the constant rate period or the first falling rate period[190].

6. 6. Electrostatic Separation - Principle of the technique.

When a potential is applied across a capacitor, each plate carries a surface charge density dependent upon the magnitude of the applied potential and the

system geometry. Due to the electric field between the capacitor plates, and the surface charge density, a force is exerted on each area element of the plates. A critical point can be reached, when the electrostatic forces overcome any restraining forces, and if one capacitor plate consists of discrete conducting units, then movement of these discrete units will result. The units will carry an electric charge, and the mechanism of charging is known as induction charging as mentioned in Chapter 1.

For the purposes of the present separation technique, one capacitor plate was positioned above a vibrated bed surface, whilst the other capacitor plate was the bed surface. The discrete conducting elements were particles in the bed. The charge induced in an isolated conducting particle (q_{pi}) resting on a flat plate, has been given by Felici[191] as,

$$q_{pi} = 1.65 \times 4\pi \varepsilon_o R_p^2 E \ , \qquad 6.7$$

where E is the electric field which would exist if the particle were not present.

The initial removal force acting on the particle, is influenced by the presence of image charge attraction, and has been given by Felici[191] as,

$$F_{Rs} = 1.369 \times 4\pi \varepsilon_o R_p^2 E^2 \ . \qquad 6.8$$

The force acting on the particle when it is far removed from the initial contact plane is given by,

$$F_{Rf} = 1.65 \times 4\pi \varepsilon_o R_p^2 E^2 \ . \qquad 6.9$$

Experimental observations confirming the applicability of these equations have been given by Cho[192] and Krasucki[193]. For a particle behaving as an insulator q_{pi} will be zero. The criterion for conducting or insulating behaviour will be discussed in Section 6.9.

Thus, if the vibrated bed consists of a mixture of conducting and insulating particles, then conducting particles can be removed by electrostatic forces, and a separation based on electrical resistivity is feasible.

The principal restraining force acting on a particle is gravitational, since vibration will tend to overcome adhesional forces. Also adhesional forces for

particles of diameter greater than 100μm will probably be much less than gravitational forces[194]. Thus the ratio of removal to restraining forces is given by $k_5 E^2/R_p \eta_s$ where k_5 is a constant and η_s is the particle density. By suitable selection of the electric field magnitude, this ratio can be made greater than 1 for a particular particle type, and removal of these particles from the bed will occur. The electric field value can also be chosen such that the force ratio is less than 1 for particles of higher density or larger radius, and these particles will not move in the electric field. Consequently, in principle, size and density separation are also possible using the vibrated bed.

The vibrated bed provides a convenient means of renewing particles at the surface, to facilitate continuous collection of one component from a mixture. Some degree of control over the surface renewal rate, can be obtained by variation of the vibrational intensity. Electrostatic separation using a vertical applied electric field, acting upon particles charged by contact electrication as well as induction in a fluidised bed, has been described by Inculet[32]. In this case surface particle renewal is provided by the fluidisation mechanism.

Design of a practical system based on the vibrated bed, would require a means of predicting the particle collection rate for given conditions. The present study consisted of measuring collection rates for a single component bed, and a binary particle mixture. A means of predicting collection rates was developed, and this is compared with experimental observations.

6. 7. Experimental apparatus and experimental procedure.

A schematic diagram of the separation system is shown in FIG.72. A dural deflector plate and collector chute, were firmly attached to the top of the vibrated bed vessel described in Chapter 5. The vessel was fitted with a dural base plate as in the case of current measurements, and attached directly to the vibration table. The vessel base was earthed, and a high potential was applied to the deflector plate and collector system, from a Brandenburg Model 776 high potential unit, fitted with a resistor potential divider network. The applied potentials up to 10kV were measured with an Anders Electronics Ltd.

Electrostatic Voltmeter, Model 23 with a full scale range of 10kV. Higher potential values were known from the resistor values in the divider network.

The collector chute was fitted with a dural cover (FIG.72), which ensured that no particles were lost from the system, before collection in a suitable vessel positioned below the collector chute.

The deflector plate was constructed to give a deflection section at an angle of 48^{o} to the horizontal. This ensured that all particles, regardless of the coefficient of restitution, were moving after impact at the deflector plate, with a velocity directed above the horizontal. It was hoped that this would ensure the collection of most particles travelling to the deflector plate.

The experimental procedure adopted, was to initially fill the bed to the required depth of 76mm, leaving a gap of 23mm below the top of the perspex vessel walls as shown in FIG.72. Vibration of the required amplitude and frequency was then initiated, and finally the electric field was applied for a known time interval, during which all particles arriving at the chute were collected. Vibration of the collection chute ensured that no particles remained on the chute. Vibration was applied after electric field application, for the case where no vibration was applied during electric field application, to ensure that no particles remained on the chute. The particulate materials used, the corresponding measured resistivity values, and the literature density values, are shown in Table 12.

A crude measure of the surface renewal rate for the vibrated bed was obtained as follows. A bed of grey glass ballotini (250-599 μm in diameter), was placed in the support vessel to a depth greater than 30mm. A layer of 300-699 μm diameter red glass ballotini was evenly applied on top of the grey ballotini to a depth of 10mm. Vibration was then initiated at the required amplitude and frequency, and the time from the start of vibration to the appearance of grey ballotini at the bed surface, was measured using a stopwatch. The rate of surface renewal is given by the measured number of surface layers renewed, divided by the total time. The number of surface layers renewed is approxi-equal to the depth of the red ballotini layer divided by the particle diameter.

The rate of surface renewal calculated from the measured time of appearance of the lower ballotini section and assuming an average particle diameter of 500 μm, is shown in FIG.73 plotted against $\omega^2 y_o/g_a$. It is apparent that the rate of surface renewal is linearly related to $\omega^2 y_o/g_a$. The assumption is made that the renewal rate measured for the particles described, is approximately applicable to particles in the diameter range 100-700 μm. This assumption will not be entirely correct, however the measured values should give a reasonable estimate of renewal rates for other particle sizes.

6. 8. Movement of an isolated charged particle in a vertical electric field.

The situation considered is that of a single particle moving between two electrodes in a uniform vertical electric field. The drag forces are assumed to be represented by Stokes' Law[187]. By Newton's second law of motion,

$$M_p \frac{d^2y}{dt^2} = F_{Rf} - M_p g_a - 3\pi\mu_v D_p \frac{dy}{dt} \quad , \qquad 6.10$$

where y is the vertical distance coordinate measured from the lower electrode, F_{Rf} is the force due to the electric field on the particle, and M_p, g_a, μ_v, D_p, t are as defined previously.

Equation 6.10 is a second order ordinary differential equation, which can be solved by standard techniques[98]. Solving, and applying the boundary conditions that dy/dt = 0 and y = 0 when t = 0, gives,

$$y = \left(\frac{F_{Rf} - M_p g_a}{M_p}\right) \tau_d \left[t - \tau_d(1 - e^{-t/\tau_d})\right] \quad , \qquad 6.11$$

where $\tau_d = \dfrac{M_p}{3\pi\mu_v D_p}$ s.

When t/τ_d is much less than 1, equation 6.11 simplifies to,

$$y = \left(\frac{F_{Rf} - M_p g_a}{2M_p}\right) t^2 \quad . \qquad 6.12$$

Equation 6.12 is the solution of equation 6.10 with drag forces neglected.

If the time taken by a particle to travel the distance between the electrodes y_f, is defined as t_f, then t_f from equation 6.12 is given by,

$$t_f = \left(\frac{2M_p y_f}{F_{Rf} - M_p g_a} \right)^{\frac{1}{2}} . \qquad 6.13$$

6. 9. The distinction between conductors and insulators from the viewpoint of induction charging.

For a particle to acquire the charge given by equation 6.7, it is necessary that the particle potential remains equal to that of the electrode on which it is resting, for a sufficient time for charge redistribution to occur and an equilibrium situation to result. If the particle is lifted by the electric field against gravitational forces, then electron tunnelling will ensure that particle and electrode potentials are equal over approximately the initial 2nm of separation[7]. Thus the criterion for a conducting particle, is that charge redistribution much occur in a time less than that taken by the particle to travel the initial 2nm.

The time taken to travel the first 2nm can be estimated from equation 6.13. Since the value of $(F_{Rf} - M_p g_a)$ must lie between zero and the value for complete charging, $(F_{Rf} - M_p g_a)$ is assumed to equal half the value for complete charging. In practice $(F_{Rf} - M_p g_a)$ will vary continuously over some, or all, of the initial region. The value of F_{Rf} for complete charging is calculated from equation 6.8 since image forces will still be important over the 2nm separation distance. Thus the time taken by glass ballotini of 128 μm diameter to travel the first 2nm is 4.5×10^{-6}s for an applied electric field of 3.86×10^5V m^{-1}. 3.86×10^5V m^{-1} is the average electric field at the bed surface, when the maximum available potential of 15kV is applied to the deflector plate. The charge redistribution time is given approximately by $\varepsilon_o \varepsilon_r r$. Therefore the critical resistivity is equal to $7.8 \times 10^4 \Omega$ m for ballotini since ε_r is equal to 6.5

The ratio of particle resistivity to bulk resistivity has been given by Harper[7] as $2d_p/\pi R_p$, where d_p is the diameter of the contact circle between two particles. The value of d_p can be calculated from equation 2.1, which applies to light loads. Assuming that the normal force during contact = $M_p g_a$, and that $Y = 6.55 \times 10^{10}$N m^{-2} for glass, the particle resistivity is found to be $5.31 \times 10^{-4} r_b$. The bulk resistivity is given in Table 12, from which the particle

resistivity can be calculated as $6.5 \times 10^{4} \Omega$ m. Thus the 128 μm ballotini should behave as conductors and charge to the limiting value. Similar considerations applied to the quartz particles of Table 12, indicate that the material is in the insulating range, but close to the critical value. The 104-250 μm diameter iron shot is found to be well into the conducting range, and charging to the theoretical limit is anticipated. The particles in the sample of 300-690 μm diameter ballotini, with a diameter greater than 375 μm, would not move under the influence of the available field, even if conducting, since F_{Rf} is less than $M_p g_a$. All particles in this sample are also well into the insulating range, and little charging is expected.

The increase in induction charging resulting from decreased powder resistivity has also been demonstrated by Sato[67], for photoconductive powders sliding down an inclined metal chute under the influence of an applied electric field.

6. 10. Prediction of the electric field induced particle collection rate, from a vibrated bed.

In order to predict the particle collection rate, three simplifying assumptions are made. Firstly the time taken by a particle to travel the distance from the deflector plate, to the collector chute is neglected. This assumption is reasonable, since the average distance from the bed surface to the deflector, is a factor of 3 greater than the average distance from the deflector plate to the collector chute for the experimental results considered. The verticle particle velocity in the region below the deflector plate, will on average be approximately equal to the horizontal particle velocity after impact, since the coefficient of resitution is expected to be close to 1.0. Thus the time taken by a particle to travel from the deflector to the collector is significantly less than the time taken to travel from the bed surface to the deflector, and is neglected.

The second assumption made, is that the collection of particles can be considered in terms of discrete particle layers. The system is assumed to behave as if a complete layer of particles is removed from the bed surface at a particular time. Finally, it is assumed that only one layer of particles can exist in the

space between the bed surface and the deflector plate (the freeboard) at any instant. This assumption will be discussed after the derivation of the collection rate equation.

On the assumption that the particles in the bed are conducting, the number which can charge to the limit given by equation 6.7 can be calculated. The maximum charge which can exist on the bed surface, is equal in magnitude, and opposite in sign to that existing on the upper electrode. As a first approximation the system can be considered as a parallel plate capacitor. Thus the maximum charge which can exist on the bed surface is given by Gauss's Law as $EA_s \varepsilon_o$, where A_s is the bed upper surface area. The maximum charge which can exist on the top surface particle layer is $f_p A_s E \varepsilon_o$, where f_p is the fraction of the bed surface occupied by particles. Thus the number of particles which can carry the charge given by equation 6.7 is $\frac{f_p E \varepsilon_o A_s}{1.65 \times 4\pi\varepsilon_o R_p^2 E}$. Since the total number of particles in the top layer is equal to $f_p A_s / \pi R_p^2$, then

$$\frac{\text{the number of particles charged to the limiting value of equation 6.7}}{\text{the total number of particles in the bed upper surface layer}} = n_t = 0.15$$

If F_{Rf} is close to $M_p g_a$ then the electric field non-uniformity due to the upper electrode shape, can result in particle removal over only a part of the bed surface. The correction for this effect, is calculated by determining the proportion of the bed surface over which the electric field has a sufficient magnitude to make F_{Rf} greater than $M_p g_a$, and thus produce particle removal. This calculated fraction of the bed surface over which removal can occur is defined as p_f. The collection rate can then be calculated using the average electric field over the active region, and knowing the value of p_f.

Thus, the mass of particles removed in time t_c is given by,

$$W_c = \frac{M_p N_{su} n_t p_f t_c}{t_f} \quad , \qquad 6.14$$

where W_c is the mass of particles collected, N_{su} is the number of particles in the upper surface layer, t_f is the time taken by a particle to travel the

average distance to the deflector under the influence of the average electric field. If F_{Rf} is much greater than $M_p g_a$, then from equations 6.13 and 6.9, t_f is inversely proportional to the applied electric field. Therefore the mass of particles collected in a given time, from equation 6.14 is linearly related to the applied electric field.

The assumption that only one particle layer can exist in the freeboard at any instant, can now be examined. From Gauss's Law and the line integral of the electric field, the electric field in the region above the bed surface, below a moving induction charged particle layer is given by,

$$E_L = \frac{a_f V}{y_f^2} \quad . \qquad 6.15$$

In deriving this equation the system was considered as a parallel plate arrangement, with the upper plate at a potential V and a distance y_f above the bed surface, and the particle layer a distance a_f above the bed surface.

From equation 6.15 it is clear that the electric field acting upon the bed surface, increases as the particle layer approaches the deflector plate. The next layer could therefore lift before the first has left the freeboard, under the action of a reduced electric field. The two effects of lifting before the predicted time, and movement under a reduced electric field, will offset each other to a certain degree, maintaining the actual collection quantity close to that predicted from equation 6.14. These effects will be most evident when F_{Rf} is much greater than $M_p g_a$, and the particle layer can lift for an electric field well below the maximum.

If a particle mixture is initially present in the bed, one component of which is removed by the electric field, then the collection rate may be modified, compared with the case of a single component bed.

If the rate of removal of particles through the freeboard is given by N_{R1} particles s^{-1}, and the rate of renewal of the particles which are collected, at the bed surface is given by N_{R2} particles s^{-1}, then for N_{R2} greater than N_{R1}, the collection rate will be given by N_{R1}. This is equal to $N_{su} n_t p_f / t_f$

from equation 6.14. Particle movement through the freeboard is the rate limiting step. However, if N_{R1} is greater than N_{R2}, then the rate limiting step is the rate of particle renewal at the bed surface N_{R2}, and this determines the collection rate.

$$N_{R2} = sX_c N_{su} p_f \quad , \qquad 6.16$$

where s is the rate of renewal of surface area (unit total area)$^{-1}$, X_c is the volume fraction of the bed occupied by particles which are collected.

If a batch separation process is carried out, X_c will change with time. The change in X_c over the collection time employed in the present experiments, was sufficiently small to be neglected.

If the volume fraction of removeable particles is increased from zero, a linear increase in the collection rate is expected from equation 6.16, terminating at a constant value when N_{R1} is equal to N_{R2}. The renewal rate for which the collection rate becomes constant with increasing X_c, is found by equating N_{R1} and N_{R2} as,

$$s = \frac{n_t}{X_{cc} t_f} \quad , \qquad 6.17$$

where X_{cc} is the value of X_c for which the collection rate becomes constant with increasing X_c.

6. 11. Experimental results and discussion.

Preliminary experiments indicated that the particle bed height had a large effect on the particle collection rate. This confirmed the validity of regarding the electric field as applied between the upper bed surface and the deflector plate. The importance of induction charging as the principal particle charge mechanism, rather than contact electrification, was also established.

The mass of 106-150 μm diameter glass ballotini collected over the initial 30s period after application of an applied electric field, is shown plotted against the applied potential in FIG.74. For potentials above 9kV, F_{Rf} is much greater than $M_p g_a$, and thus it is anticipated from Section 6.10 that the mass collected should be linearly related to the applied electric field, and hence the applied potential. This indeed is seen to be the case (FIG.74). The lower

collection rates for lower $\omega^2 y_o/g_a$ values, are presumably due to the following two factors. (1) Increasing $\omega^2 y_o/g_a$ causes a small increase in the bed height. (2) Increasing $\omega^2 y_o/g_a$ causes a reduction in image and adhesional forces by separating particles.

The bed height decreased slightly during the 30s collection period. This effect was small, resulting in a decrease of less than 20% in the amount collected over the following 30s period.

The mass of particles collected over the initial 30s period, is shown plotted against $\omega^2 y_o/g_a$ in FIG.75, for a 15kV applied potential, and particle beds of 106-150 μm diameter ballotini, 106-150μm diameter quartz, and 104-250 μm diameter iron shot. Also shown in the diagram, is the prediction from equation 6.14 for the mass collected, of 128 μm diameter ballotini and quartz, and 177 μm iron shot. The constant p_f in equation 6.14 was calculated to be 1.0 for quartz and ballotini and 0.54 for iron shot. The average electric field values based on the dimensions of FIG. 72 were used to calculate t_f. The value of N_{su} was determined from N_b, the number of particles (unit volume)$^{-1}$, N_b was calculated assuming a voidage of 0.4[170]. The surface particle layer was assumed to occupy a volume $A_s D_p$.

It is apparent from FIG.75 that prediction and observation are in good agreement for the glass ballotini. For the iron shot, the observed mass collected is less than the predicted value. This is attributed to the assumptions made in determining p_f, and to neglecting the time for particles to travel from the deflector to the collection chute. In view of the assumptions made, agreement between measured and predicted values is good. Quartz has a resistivity above the level at which particles exhibit insulator behaviour (Section 6.9). Thus the particles receive a charge below the value predicted from equation 6.7, and the collection rate is expected to fall below the predicted value, for charging to the upper limit. This indeed was found to be the case (FIG.75).

The assumption made in deriving equation 6.13, that t_f should be much less than τ_d was checked for both ballotini and iron shot. The error in the final

predicted collection rate due to this assumption, was less than 10% for the ballotini and much smaller for the iron shot.

In order to investigate the importance of particle concentration in the bulk of the bed when performing a separation, mixtures of 300-699μm diameter red ballotini, and 106-150μm diameter clear ballotini were prepared at various concentration levels. The bulk resistivity of the two materials when separated is given in Table 12. As discussed in Section 6.9 the red ballotini will behave as insulators. Since F_{Rf} is less than $M_p g_a$ for particles of diameter greater than 375μm, separation based on size is anticipated. Thus a combined size/resistivity separation will result with this particle mixture.

FIG.76 shows the mass of clear ballotini collected over the initial 30s period after 15kV potential application, plotted against the initial volume fraction of clear ballotini in the mixture. For the intermediate volume fractions, a linear relation is observed between the amount collected and the initial volume fraction. Equation 6.16 predicted this linear section and also predicted that the straight line should pass through the origin in FIG.76. The observation that the line does not pass through the origin is thought to be due to the action of smaller particles falling through the interstices between the larger particles. This reduces the concentration of clear ballotini in the surface layer , below that in the bulk. Thus the origin of the straight line is effectively moved along the volume fraction axis of FIG.76, and some non-linearity occurs in the observed behaviour for the smaller volume fractions.

The collection rate reached a constant value with increasing concentration as predicted in Section 6.10. The rate of surface renewal for which this constant value occurs is given by equation 6.17. Using the value of t_f given by equation 6.13, and $n_t = 0.15$, $X_{cc} = 0.61$ from FIG.76 for $\omega^2 y_o/g_a = 3.99$, gives s equal to 4.79 s^{-1} from equation 6.17. For the same value of $\omega^2 y_o/g_a$, the measured surface renewal rate is shown in FIG.73 to be 4.6 s^{-1}. Thus, the measured surface renewal rate agrees closely with the value predicted from the separation collection rate theory. From equation 6.17, for two

different $\omega^2 y_o/g_a$ values, the surface renewal rates for which $N_{R1}=N_{R2}$, should be inversely proportional to the X_{cc} values. For $\omega^2 y_o/g_a$ equal to 3.99 and 3.06, the measured surface renewal rate ratio is 1.32 from FIG.73. The inverse ratio of the X_{cc} values from FIG.76 is 1.32. Thus agreement is good between observation and prediction.

The percentage by weight of the red ballotini collected, is shown plotted against $\omega^2 y_o/g_a$, for an applied potential of 15kV, in FIG.77. It is apparent that the separation process is extremely efficient for all values of $\omega^2 y_o/g_a$. The improved efficiency with increasing $\omega^2 y_o/g_a$ is thought to be a result of the fact that red ballotini were always carried over in association with clear ballotini, presumably due to image charge attraction. Increasing $\omega^2 y_o/g_a$ would reduce association between the particles, and therefore improve the separation efficiency.

For industrial application, several separators in series would permit continuous separation. The bed bulk resistivity must be maintained close to that of the conducting component, to ensure that the electric field acts principally between the bed surface and the deflector plate. This can be achieved by maintaining the conducting component volume fraction in the bed above 0.07 - 0.25[195]. The critical level depends on the relative particle sizes of the different components.[195]

CHAPTER 7.

GENERAL CONCLUSIONS AND SUGGESTIONS FOR FURTHER WORK.

(i) Even under well defined contact conditions, at gas pressures below 10^{-3} torr, metal/insulator contact electrification was found to be subject to a certain lack of reproducibility. In spite of this variability, it was apparent that the chemical nature of the dielectric material had an important influence on the sign and magnitude of contact electrification, although the effect of commercial additives was found to be small. Polar materials were found to charge positively with respect to non-polar materials and metals.

(ii) Previous suggestions that contact electrification between a metal and an insulator material, could be directly correlated with the metal work function, were found to be contrary to the present experimental observations. The present studies provided further confirmation of the notion that relative movement between contact materials serves merely to increase the contact area, and thus the charge transferred. The functional dependence of the charge transferred on the normal force, was consistent with the real contact area being defined by plastic deformation, or elastic deformation of a large number of small asperities over the contact region. Charge transfer was observed not to be directly correlated with frictional forces during contact.

(iii) The magnitude of the time constant for charge transfer, which was found to be of the order of 10ms, indicates that charge transfer is probably not a result of electron transfer from the material bulk, if, as appears likely, transient contact area effects can be neglected.

(iv) Gas pressure was found to influence charge separation in a manner broadly anticipated from Townsend's theory of gas breakdown[15]. The observed charge level on insulating surfaces, passed through a minimum value as the pressure was decreased from atmospheric. The pressure range for the minimum (0.5-20 torr) corresponded approximately with the minimum range in the Paschen curve for conductors. The minimum charge level was below the measuring instrument sensitivity of 4×10^{-7} C m^{-2}, and was much smaller than that expected from the

Paschen curve. The observed dependence of charge density on pressure, for pressures above that corresponding to the minimum charge valve, was close to a prediction from the critical corona electric field, assuming the discharge length decreased with increasing gas pressure. The discharge length was estimated to be of the order of 10^{-4}m at atmospheric pressure. Charge levels for pressures below 10^{-3} torr were a factor of 2.5 - 3.2 greater than at atmospheric pressure.

Even at pressures below 2×10^{-4} torr, charge regions of opposite sign to that initially formed by contact, were observed on occasions adjacent to the initial charged area. These regions were attributed to field emission, or ion capture from the vacuum space.

The good reproducibility of charge levels observed at atmospheric pressure, suggests that attainment and utilisation of well-defined charge levels, under a variety of practical conditions is a realistic possibility.

(v) Bulk conduction processes following contact electrification of Nylon 66 and Viton®, were found to be in accordance with the theoretical predictions given by Wintle[91]. The charge carrier mobility was found to be independent of carrier concentration, charge injection was total, deep trapping with no subsequent release during the time of interest did not occur, and diffusion effects were found to be negligible after the rapid initial phase.

The charge carrier mobility was found to be related to the initial surface potential, suggesting some form of causal relationship between contact electrification and carrier mobility. The observed mobility values of the order of $10^{-11} m^2 V^{-1} s^{-1}$, confirmed a previous conclusion, that the high resistivity of polymers is due to extremely low charge carrier mobility.

(vi) The contact electrification and dissipation characteristics of particulate materials, were greatly influenced by the bulk resistivity. The presence of continuous contact paths, facilitates the appearance of conduction currents. This was observed with a vibrated bed system, and a bulk resistivity below $10^{9} \Omega$ m. Theoretical predictions of the influence of vibrational amplitude and bulk resistivity on the conduction currents were in reasonable agreement with

observation. However, the electrode geometry influenced conduction currents in a manner which was not predicted theoretically.

(vii) The appearance of air breakdown processes, predicted from the vacuum chamber studies, was implicitly observed for insulating particles of bulk resistivity greater than $5 \times 10^{15} \Omega m$ in a vibrated bed. The electric field at which breakdown was considered to occur, could be determined using a theoretical model to interpret charge induction observations. This gave a breakdown electric field of the order of $3 \times 10^{6} V\ m^{-1}$, which was related to the prediction from the Paschen curve, by a similar factor, to that found in the single contact studies relating observation to prediction from the Paschen curve. The transient charge behaviour of the vibrated bed of insulating material, was found to conform to a prediction from a theoretical model, once the charge in the bed had become uniform.

(viii) The possibility of developing an economical vibration monitoring device, arises from the theoretical and experimental studies of electrification in the vibrated powder bed. Likewise, the possibility of using induced charge effects as an analysis technique to study fluid/particle mechanics, arises from these studies.

(ix) In order to reduce hazards arising from contact electrification in a practical particle handling situation, it is essential to ensure that all conductors in contact with the particulate material are earthed. This applies even if the bulk particle resistivity is below $10^{9} \Omega m$. If particles of bulk resistivity greater than $10^{13} \Omega m$ are being handled, then charge can be retained for considerable periods of time. If any possibility of fire exists, due to the occurrence of a spark, then precautions to allow for this eventuality must be taken.

(x) The application of an applied alternating electric field, to cause movement of particles charged naturally by contact electrification in a fluidised bed, was demonstrated as a technique for increasing the heat transfer coefficient at an immersed heater surface. The optimum heat transfer coefficient was found for frequencies in the region of 100Hz, and increases in the heat transfer

coefficient of up to 140% were obtained. A semi-quantitive explanation of the observed behaviour was given, and the application of the technique to paper or textile drying was suggested.

(xi) Induction charging of vibrated bed particles, together with charged particle movement in a vertical applied electric field, was demonstrated as a new electrostatic separation technique. Separation based on particle size, resistivity or density is feasible. The predicted collection behaviour from a single component bed and a binary particle mixture was found to be in good agreement with observation. The effectiveness of the process was demonstrated for a glass ballotini separation, on a combined size/resistivity basis.

Suggestions for further work.

(i) The vacuum chamber apparatus could be usefully employed, to study contact electrification behaviour involving dielectric materials of well-defined composition, to clarify the importance of the polar nature of the material. Extension of the investigations to include other variables such as polymer orientation and surface roughness would also be of interest. The effectiveness of anti-static treatments and charge neutralisation devices could also be usefully studied.

(ii) The vibrated bed investigations, suggest further work could be directed towards assessing the economic and practical utility of the system as a vibration monitoring device, and towards developing charge induction as an analysis technique for fluid/particle systems. The present theoretical considerations would be of use in these cases. Charge measurement in a broader range of particle handling situations would also be of interest, to assess the generality of the theoretical ideas in the present study.

(iii) The heat transfer studies could be extended, to include dielectrophoretic forces in non-uniform electric fields as a possible means of obtaining further increases in the heat transfer coefficient. A study of the importance of particle size, and the influence of higher gas velocities than those investigated, would also be of practical utility.

(iv) The electrostatic separation work, could be usefully complimented by optimising the design of the deflector plate system, using the theoretical ideas in the present study. Construction of a continuous multi-stage unit would also be of interest, permitting determination of the economic advantages of the system for particular separation requirements.

APPENDIX 1

THE ELECTRIC FIELD AND POTENTIAL, DUE TO A CHARGED PARTICLE MASS

The geometrical situation considered is shown in FIG.40. The particle mass is assumed to have a uniform volume charge density ρ_c, and a uniform surface charge density σ_c on the lower surface. The following derivation is similar to that for the induction probe in Section 2.5. Surface charge densities σ_3 and σ_5 are induced on the base and screen respectively, by the particle charge. The base is at a potential V_3 relative to the earthed screen. By Gauss's Law,

$$D_5 = \rho_c L_1 + \sigma_c + \sigma_3 \quad , \qquad \text{A.1.1}$$

$$D_4 = \sigma_3 + \rho_{cy} + \sigma_c \quad , \qquad \text{A.1.2}$$

and $$D_3 = \sigma_3 \quad . \qquad \text{A.1.3}$$

From the line integral of the electric field and the definition of electric displacement, the following relations can be established, where V_4 is the potential of the lower bed surface, and V_5 is the potential of the upper bed surface.

$$\frac{V_5}{g_1} = E_5 = \frac{D_5}{\varepsilon_o} \quad . \qquad \text{A.1.4.}$$

$$V_5 - V_4 = -\int_o^{L_1} E_4 dy = -\int_o^{L_1} \frac{D_4 dy}{\varepsilon_{r4}\varepsilon_o} \quad . \qquad \text{A.1.5}$$

$$\frac{V_4 - V_3}{g_2} = -E_3 = -\frac{D_3}{\varepsilon_o} \quad . \qquad \text{A.1.6.}$$

ε_{r4} is the effective dielectric constant of the bulk particle bed. The surface charge density σ_3 can be eliminated from equations A.1.2 and A.1.3. The resulting expression for D_4 is then substituted into equation A.1.5, which can now be integrated. Elimination of D_3 and V_4 from the result using equation A.1.6 gives,

$$V_5 = -\left(\frac{E_3 L_1}{\varepsilon_{r4}} - V_3 + E_3 g_2 + \frac{\rho_c L_1^2}{2\varepsilon_{r4}\varepsilon_o} + \frac{\sigma_c L_1}{\varepsilon_{r4}\varepsilon_o}\right) \quad . \qquad \text{A.1.7}$$

Elimination of σ_3 from equations A.1.1 and A.1.3, determines E_5 as a function of E_3 using the electric displacement definition.

Equation A.1.4 permits elimination of E_5, and elimination of V_5 from the result and equation A.1.7, together with rearrangement yields,

$$E_3 = \frac{-\frac{\rho_c L_1}{\varepsilon_o}\left(\frac{L_1}{2\varepsilon_{r4}} + g_1\right) - \frac{\sigma_c}{\varepsilon_o}\left(\frac{L_1}{\varepsilon_{r4}} + g_1\right) + V_3}{g_1 + \frac{L_1}{\varepsilon_{r4}} + g_2} \quad . \qquad \text{A.1.8}$$

The potential at a defined distance from the base plate is also required, for the situation where the particle mass is very close to the base and $g_2 \approx 0$, $V_3 \approx V_4$. Since $V_5 = \frac{D_5 g_1}{\varepsilon_o}$, A.1.9

V_5 can be eliminated from equations A.1.5 and A.1.9. Substitution of D_4 from equations A.1.1 and A.1.2 having eliminated σ_3, into the result, together with integration, permits determination of D_5. Using this result together with equations A.1.1 and A.1.2 to eliminate D_5 and σ_3, and the definition of electric displacement yields,

$$E_4 = \frac{1}{\varepsilon_o \varepsilon_{r4}\left(\frac{g_1 \varepsilon_{r4}}{L_1} + 1\right)} \cdot \left[\rho_c \left(\frac{-L_1}{2} + y - g_1 \varepsilon_{r4}\left(1 - \frac{y}{L_1}\right)\right) + \frac{V_3 \varepsilon_{r4} \varepsilon_o}{L_1}\right]. \qquad \text{A.1.10}$$

The potential between the base and a point d_c very close to the base is given by $V_6 = -\int_o^{d_c} E_4 dy$. Thus,

$$V_6 = \frac{\rho_c\left[\frac{L_1 d_c}{2} - \frac{d_c^2}{2} + g_1 \varepsilon_{r4}\left(d_c - \frac{d_c^2}{2L_1}\right)\right] - \frac{V_3 d_c \varepsilon_{r4} \varepsilon_o}{L_1}}{\varepsilon_o \varepsilon_{r4}\left(1 + \frac{g_1 \varepsilon_{r4}}{L_1}\right)} \quad . \qquad \text{A.1.11}$$

Equation A.1.11 can be simplified, since $V_3 d_c \varepsilon_{r4} \varepsilon_o / L_1$ is much smaller than the other terms due to the measuring circuit (Chapter 5), and expressed as

$$V_6 = N_b q_{pf} M \quad , \qquad \text{A.1.12}$$

where N_b is the number of particles per unit volume, q_{pf} is the charge per particle assuming all particles have the same charge,

$$M = \frac{\frac{L_1 d_c}{2} - \frac{d_c^2}{2} + g_1 \varepsilon_{r4}\left(d_c - \frac{d_c^2}{2L_1}\right)}{\varepsilon_o \varepsilon_{r4}\left(1 + \frac{g_1 \varepsilon_{r4}}{L_1}\right)} . \qquad \text{A.1.13}$$

NOMENCLATURE

a Constant in the charge decay equation (Section 3.5.2)

a_1 Radius of the particle charge transfer area during contact (FIG.42) (m)

a_f Bed surface to particle layer separation distance (m)

A Induction probe surface area (m^2)

A Contact area (m^2)

A_1 Constant defined in equation 2.3 ($V\ s^{-1}$)

A_b Effective area of the vibrated bed base plate which has a charge σ_3, (approximately equal to the lower bed surface area). (FIG.40)(m^2)

A_b Area of the lower surface of the vibrated bed (m^2)

A_c Particle charge transfer area (m^2)

A_d Cross-sectional area of a differential element (m^2)

A_h Heater support block surface area (m^2)

A_s Area of the upper surface of the vibrated bed (m^2)

b Actual charge line width (m)

b' Measured charge line width modified by the induction probe resolution (See FIG. 16a) (m)

B_c $(\cosh pc + \varepsilon_{r2} \sinh pc \coth pL)^{-1}$

B_d $(\cosh pd + \varepsilon_{r2} \sinh pd \coth pL)^{-1}$, where d = 0.127mm

B_g $(\cosh pg + \varepsilon_{r2} \sinh pg \coth pL)^{-1}$

B_∞ B_g for $\lambda = \infty$, p = 0, i.e. $(1 + \varepsilon_{r2} g/L)^{-1}$

c Length over which gas discharge occurs (m)

$(cP)MIN$ Value of (cP) for which the minimum surface charge density occurs. (torr mm)

C Capacitance (F)

C_1, C_2 Constants defined in equation 4.29

C_a Number of particles (unit surface area)$^{-1}$ (m^{-2})

C_b Particle charging capacitance (eqn. 4.15b) (F)

C_d Capacitance associated with the induction probe, defined in eqn. 2.15 (F)

C_{ds}, C_{df} Initial and final values respectively of C_d (F)

C_E Electrometer input capacitance (F)

C_h, C_{h1} Capacitances associated with the charged particle bed, defined in equations 4.7a and 5.7 respectively (F)

d Induction probe to dielectric surface separation of 0.127mm

d_c Distance over which charge transfer occurs (m)

d_m Molecular diameter (m)

d_p Contact circle diameter (m)

d_w Contact track width (m)

D Electric displacement ($C\ m^{-2}$)

$\mathfrak{D}$ Diffusion coefficient ($m^2\ s^{-1}$)

D_1 Electric displacement in the air gap ($C\ m^{-2}$)

D_2 Electric displacement in the dielectric ($C\ m^{-2}$)

D_3, D_4, D_5 Electric displacements associated with the vibrated bed (FIG. 40) ($C\ m^{-2}$)

D_p Particle diameter (m)

D_{po} Perforated screen orifice diameter (m)

D_{p1} Resistivity cell inner cylinder diameter (m)

D_{p2} Resistivity cell outer cylinder inner diameter (m)

D_s Density of electron surface states (unit energy of surface levels)$^{-1}$ ($m^{-2} eV^{-1}$)

e Electronic charge ($1.6 \times 10^{-19} C$)

E Electric field ($V\ m^{-1}$)

E_1 Electric field in the air gap ($V\ m^{-1}$)

E_2 Electric field in the dielectric ($V\ m^{-1}$)

E_3, E_4, E_5 Electric fields associated with the vibrated bed (FIG.40)($V\ m^{-1}$)

E_{1c} Electric field at which point gas breakdown occurs ($V\ m^{-1}$)

E_{1d}, E_{1g} Electric fields at the induction probe surface, for probe to dielectric surface separations of d and g respectively ($V\ m^{-1}$)

E_{1gAv} Average value of E_{1g} over the induction probe surface ($V\ m^{-1}$)

E_{2s} Electric field in the dielectric before charge decay (See eqn.3.10)($V\ m^{-1}$)

E_{3m} Value of the electric field at the vibrated bed base plate when the induced potential has the peak value ($V\ m^{-1}$)

E_L Electric field below the charged particle layer in the electrostatic separator ($V\ m^{-1}$)

E_m Peak value of the sinusoidal alternating electric field ($V\ m^{-1}$)

f Vibrational frequency (Hz)

f_p Area fraction of the vibrated bed surface occupied by particles

F Force (N)

F_{Rf} Force acting on an induction charged particle, well removed from either electrode, in an electric field (N)

F_{Rs} Force acting on a conducting particle, placed on an electrode to which an electric field is applied (N)

g Separation distance between the induction probe, and either the dielectric surface or the high potential plane during calibration (m)

g_1 Vibrated bed surface to screen electrode, separation distance (m)

g_2 Air gap width adjacent to the vibrated bed base (m)

g_{2o} Peak value of g_2 (m)

g_{2ob}, g_{2oq} g_{2o} for ballotini and quartz respectively (m)

g_3 Air gap width and charge layer depth, adjacent to the lower surface of the screen in the vibrated bed. (m)

g_a Acceleration due to gravity (9.81m s^{-2})

G Electrometer gain

h Heat transfer coefficient (W $m^{-2}K^{-1}$)

H Constant in the charge decay equation (Section 3.52) (V s^a)

i_3 Electric current from the vibrated bed (A)

i_{3Av} Average value of i_3 (A)

i_{3Avb}, i_{3Avq} i_{3Av} for ballotini and quartz respectively (A)

j_3 Electric current density from the vibrated bed (A m^{-2})

j_{3Av} Average value of j_3 (A m^{-2})

k Constant to account for deviation of the charge distribution, from the infinite sinusoidal case.

k_1 Constant defined in equation 4.19

k_2 Constant in particle flow rate eqn. (Section 4.4)

k_3 Constant used in eqn. 4.46 and subsequently

k_{3b}, k_{3q} k_3 for ballotini and quartz respectively

k_4 Constant used in equation 5.3 and subsequently

k_5 Constant used in Section 6.6 (F m^{-1})

k_g Gas thermal conductivity ($W\ m^{-1}\ K^{-1}$)

k Boltzmann's constant ($1.38 \times 10^{-23}\ J\ K^{-1}$)

K_1 Constant defined in equation 4.20

L Dielectric sheet thickness (m)

L_1 Vibrated bed depth (m)

L_2 Screen electrode to bed bottom separation distance (m)

L_3 Screen to base plate separation distance (m)

L_b Resistivity measurement cell electrode length covered by particles (m)

L_g Gas boundary layer thickness (m)

L_m Gas molecule mean free path (m)

L_p Number of particle layers

M Constant defined in equation A.1.13 ($m^3\ F^{-1}$)

M_p Particle mass (kg)

n Concentration of injected charge carriers (m^{-3})

n_A, n_B n for materials A and B respectively (m^{-3})

n_p Number of collisions by a particle

n_s Initial concentration of injected charge carriers (m^{-3})

n_t Fraction of particles in the vibrated bed upper surface, charged to the induction limit (See eqn. 6.14)

N Molecular concentration (m^{-3})

N_b Number of particles (unit volume)$^{-1}$ (m^{-3})

N_{R1} Rate of particle removal from the bed surface (s^{-1})

N_{R2} Rate of particle renewal at the bed surface (s^{-1})

N_s Number of particles in the lower surface layer of the vibrated bed

N_{su} Number of particles in the upper surface layer of the vibrated bed

N_V Number of particles in the vibrated bed

p $2\pi/\lambda$ (m^{-1})

p_f Proportion of the vibrated bed surface, from which particle removal can occur due to application of a sufficiently large electric field

p_m Yield pressure ($N\ m^{-2}$)

P Gas pressure (torr:- mm mercury)

q Charge (unit circumferential length)$^{-1}$ (C m^{-1})

q_1 Particle charge defined in eqn. 4.18 (C)

q_a Initial particle charge before vibration (C)

q_{at} Charge on any particle in the bulk of the vibrated bed (C)

q_f Charge (unit circumferential length)$^{-1}$ for $t_b = \infty$ (C)

q_p Particle charge in excess of q_a (C)

q_{pf} Total particle charge (C)

q_{pi} Particle charge due to induction (C)

q_{pt} Particle charge in excess of q_{at} (C)

Q Charge (C)

Q_3 Total charge on the vibrated bed base plate (C)

Q_m Overall vibrated bed charge (C)

r Resistivity (Ω m)

r_b Particle bed bulk resistivity (Ω m)

r_{bb}, r_{bq} r_b for ballotini and quartz respectively (Ωm)

r_A, r_B r for materials A and B respectively (Ωm)

R Electrical resistance (Ω)

R_b Resistivity measurement cell electrical resistance (Ω)

R_p Particle radius (m)

R_{po} Wire radius (See eqn. 3.31) (m)

R_{pp} Probe radius (m)

R_{pw} Probe width (m)

s Rate of renewal of surface area (unit total area)$^{-1}$ (s^{-1})

s' s/f

S_L Laplace Transform variable (s^{-1} in eqn. 2.3)

t Time (s)

t' $t + \tau_c$ (s)

t_b Time of contact (s)

t_c Collection time (s)

t_f Time for particle to travel the average distance from the vibrated bed surface to the deflector plate (s)

t_L Transit time (s)

T_1 Periodic time of the variable part of the induced potential (See FIG. 52) (s)

T_2 Periodic time of the overall induced potential waveform (See FIG. 52) (s)

U Vibrated bed volume (m^3)

v_p Particle velocity in the vibrated bed ($m\ s^{-1}$)

V Potential (V)

V' Potential of the upper surface of a dielectric, positioned as in as in FIG. 13a (V)

V_o Potential output (V)

V_{1p} Induced potential between the particle and the base plate due to the particle charge, defined in equation 4.16 (V)

V_3 Vibrated bed base plate potential (V)

V_{3m} Peak value of V_3 (V)

V_{3mb}, V_{3mq} V_{3m} for ballotini and quartz respectively (V)

V_4, V_5 Potentials associated with the vibrated bed (FIG.40) (V)

V_6 Potential in the vibrated bed (V)

V_{6e} Potential at the edge of the screen charge layer (V)

V_a Applied potential during the induction probe calibration (V)

V_{ba} Bias potential (V)

V_c Potential at which point gas breakdown occurs, as defined by the Paschen curve (V)

V_{cp} Potential responsible for charge transfer (V)

V_{cpd} Contact potential difference (V)

V_e Equivalent potential of a surface charge, defined in eqn. 2.15 (V)

V_f Final induction probe potential (V)

V_h, V_{h1} Equivalent potentials of vibrated bed charges, defined in eqns. 4.7b and 5.6 respectively (V)

V_i Potential input (V)

V_j Induction probe electrometer output potential (V)

V_m Increment in V_j due to an applied electric field from a conductor (V)

V_{md}, V_{mg} Increment in V_j, due to induction probe movement parallel to a charged dielectric, separated from the probe by distances d and g respectively (V)

V_{mgs} Initial value of V_{mg} (V)

V_s Initial induction probe potential (V)

W' Flow rate of particles (kg s^{-1})

W_c Mass of particles collected (kg)

x Length along the contact track (m)

x_1 Distance coordinate, parallel to the dielectric surface and normal to the charged line (m)

x_2 Distance coordinate normal to the heater surface (m)

x_{2m} Amplitude of particle oscillatory movement (m)

X Input power supplied to the heater (W)

X_c Bed,volume fraction of particles which are removed by electric field application

X_{cc} Value of X_c at which point the collection rate becomes constant, when X_c is increased from 0

y, y' Vertical distance coordinates (m)

y_o Amplitude of the vibration table displacement (m)

y_f Average distance between the vibrated bed surface and the deflector plate (m)

Y Young's Modulus (Modulus of Elasticity) (N m^{-2})

Z Ratio of real to apparent area of contact

α Initial charge penetration depth (m)

β Fraction of cycle spent by the vibrated bed in flight

β_b, β_q β for ballotini and quartz respectively

δ' Relative gas density defined in equation 3.3

$\Delta\vartheta$ Temperature difference between the heater support block surface, and the bed bulk (^oK)

ε_o Permittivity of free space (8.854×10^{-12} F m^{-1})

ε_r Dielectric constant

ε_{r1} Dielectric constant of the air space (≈ 1)

ε_{r2} Dielectric constant of the insulating sheet

ε_{r4} Bulk vibrated bed dielectric constant

η_s Particle density (kg m^{-3})

η_b Bulk density, $= \eta_s(1 - \nu)$ (kg m^{-3})

ϑ Temperature (^oK)

λ Sinusoidal charge distribution wavelength (See FIG.16b) (m)

λ' Measured charge distribution wavelength modified by the induction probe resolution (See FIG. 16a) (m)

μ Charge carrier mobility ($m^2V^{-1}s^{-1}$)

μ_A, μ_B μ for materials A and B respectively ($m^2V^{-1}s^{-1}$)

μ_v Air viscosity (N s m^{-2})

ν Voidage

ρ_c Volume charge density in the vibrated bed (C m^{-3})

ρ_{co} Volume charge density at the vibrated bed screen (C m^{-3})

ρ_{cb}, ρ_{cq} ρ_c for ballotini and quartz respectively (C m^{-3})

ρ_{cu} Volume charge density adjacent to the vibrated bed screen lower surface (C m^{-3})

σ Surface charge density on an insulator (C m^{-2})

σ_3, σ_5 Surface charge densities associated with the vibrated bed (FIG. 40) (C m^{-2})

σ_a Surface charge density due to the measuring source potential (C m^{-2})

σ_b Induced surface charge density on the base plane (C m^{-2})

σ_c Surface charge density on the vibrated bed lower surface (C m^{-2})

$\sigma_{c'}$ Surface charge density on a dielectric surface after gas breakdown has occurred (C m^{-2})

σ_{c1} Surface charge density adjacent to the lower surface of the vibrated bed screen (C m^{-2})

σ_{cu} Effective total surface charge density adjacent to the lower surface of the vibrated bed screen defined in eqn. 5.2 (C m^{-2})

σ_e Peak to peak surface charge density of a sinusoidal distribution (C m^{-2})

σ_p Induced surface charge density on the induction probe (C m^{-2})

σ_r Effective peak surface charge density (C m^{-2})

σ_s Initial surface charge density (eqn. 3.16) (C m^{-2})

τ_1 Vibrated bed charging time constant defined in eqn. 4.34 (s)

τ_b Time constant for charge transfer (s)

τ_c Effective time constant of Vibron® electrometer (s)

τ_d Time constant defined in equation 6.11 (s)

φ_m, φ_p Metal and polymer work functions respectively (eV)

ω Angular frequency (s^{-1})

REFERENCES.

(1) Napier D.H. — Instn. Chem. Engrs. Symp. Ser. No. 34 Instn. Chem. Engrs., London (1971) p.170.

(2) Hays D.A. Donald D.K. — 1971 Annual Rep., Conf. on Electl. Insulation and Dielectric Phenomena. Nat. Acad. Sci., Washington D.C. (1972) p.74.

(3) Medley J.A. — Br. J. appl. Phys., Suppl. No. 2, (1953) p.S28.

(4) Donald D.K. — J. Electrochem. Soc.: Solid State Sci. 115, (1968) p.270.

(5) Shaw P.E. — Proc. Phys. Soc. 39, (1927) p.449.

(6) Henry P.S.H. — Br. J. appl. Phys., Suppl. No. 2, (1953) p. S31.

(7) Harper W.R. — Contact and Frictional Electrification. Clarendon Press, Oxford (1967).

(8) Henry P.S.H. — J. Textile Inst. 48, (1957) p.5.

(9) Peterson J.W. — J. appl. Phys. 25, No. 4 (1954) p.501.

(10) O'Neill B.C. Foord T.R. — Paper presented at the 4th Conference on Static Electrification. London (May 1975).

(11) Hendricks C.D. — Electrostatics and its Applications. Edited by Moore A.D., Chapter 2 Wiley, New York (1973).

(12) Krupp H. — Inst. Phys. Conf. Ser. No. 11: Static Electrification Inst. Phys., London (1971) p.1.

(13) Cobine J.D. — Electrostatics and its Applications. Edited by Moore A.D., Chapter 19. Wiley, New York (1973).

(14) Brown S.C. — Introduction to Electrical Discharges in Gases. Wiley, New York (1966).

(15) Howatson A.M. — An Introduction to Gas Discharges. Pergamon Press, Oxford (1965).

(16) Meek J.M. Craggs J.D. — Electrical Breakdown of Gases. Clarendon Press, Oxford (1953).

(17) Gibson N. — Proc. 2nd Int. Conf. on Static Electrification. Frankfurt (1973): Dechema Monographien vol. 72 Weinheim: Verlag-Chemie-GmbH, p.321.

(18) Gibson N. Lloyd F.C. — Br. J. appl. Phys. 16, (1965) p.1619.

(19) Instn.Chem.Engrs. — Loss Prevention Bulletin No. 002 (1974). Instn. Chem. Engrs., London.

(20) Hughes J.F. Corbett R.P. Bright A.W. Bailey A.G. — Paper presented at the 4th Conference on Static Electrification, London (May 1975).

(21) McIntyre D.
Gaines A.
Chem. Processing (U.S.A.) 37, (1974) p.1.

(22) Eden H.F.
Electrostatics and its Applications.
Edited by Moore A.D., Chapter 18.
Wiley, New York (1973).

(23) Finlayson D.
J. Textile Inst. 48, (1957) p.55.

(24) Inculet I.I.
Proc. 2nd Int. Conf. on Static Electrification.
Frankfurt (1973): Dechema Monographien vol.72
Weinheim: Verlag-Chemie-GmbH, p.163.

(25) Bright A.W.
Phys. Education 9, (1974) p.381.

(26) Corbett R.P.
Hughes J.F.
Engineering, July 1974.

(27) Moore A.D.
(Editor)
Electrostatics and its Applications.
Wiley, New York (1973).

(28) Bright A.W.
Paper presented at the Organic Finishing of
Metals Conference, Stresa (1974).

(29) Ralston O.C.
Electrostatic Separation of Mixed Granular Solids.
Elsevier Monograph, London (1961).

(30) Lawver J.E.
J. Electrochem. Soc. 116, (1969) p.57C.

(31) Morel R.
Inst. Phys. and Physical Soc., Conf. Ser. No. 4:
Static Electrification.
I.P.P.S., London (1967) p.165.

(32) Inculet I.I.
Bergougnou M.A.
Proc. 10th Int. Miner. Processing Congr.,
London (1973), p.1.

(33) Coffee R.A.
Inst. Phys. Conf. Series No. 11: Static Electrification
Inst. Phys., London (1971) p.22.

(34) Harper W.R.
Inst. Phys. and Physical Soc., Conf. Ser. No. 4:
Static Electrification.
I.P.P.S., London (1967) p.3.

(35) Dekker A.J.
Solid State Physics.
MacMillan, London (1958).

(36) Van Ostenberg D.O.
Montgomery D.J.
Textile Res. J. 28, (1958) p.22.

(37) Mott N.F.
Gurney R.W.
Electronic Processes in Ionic Crystals.
Clarendon Press, Oxford (1940).

(38) Davies D.K.
Inst. Phys. and Physical Soc. Conf. Ser. No. 4:
Static Electrification.
I.P.P.S., London (1967), p.29.

(39) Chowdry A.
Westgate C.R.
J. Phys. D: Appl. Phys. 7, (1974) p.713.

(40) Garton C.G. — J. Phys. D: Appl. Phys. 7, (1974) p.1814.

(41) Wintle H.J. — J. Phys. D: Appl. Phys. 7, (1974) p.L128.

(42) Chowdry A.
Westgage C.R. — J. Phys. D: Appl. Phys. 7, (1974) p.L149.

(43) Cole B.N.
Baum M.R.
Mobbs F.R. — Proc. Instn. Mech. Engrs. 184, Part 3 (1969) p.77.

(44) Harper W.R. — Soc. Chem. Ind. Monograph No. 14, (1961) p.115.

(45) Bredov M.M.
Kshemianskaia I.Z. — Sov. Phys. Tech. Phys. 2, (1957) p.844.

(46) Lowell J. — J. Phys. D: Appl. Phys. 8, (1975) p.53.

(47) Krupp H.
Schnabel W. — J. Adhesion 5, (1973) p.269.

(48) Kasai A.
Nishi J. — Proc. 2nd Int. Conf. on Static Electrification, Frankfurt (1973): Dechema Monographien vol. 72, Weinheim: Verlag-Chemie-GmbH, p.419.

(49) Macky W.A. — Proc. R. Soc. A119, (1928) p.107.

(50) Rose G.S.
Ward S.G. — Br. J. appl. Phys. 8, (1957) p.121.

(51) Wåhlin A.
Bäckström G. — Inst. Phys. Conf. Ser. No.11: Static Electrification. Inst. Phys., London (1971) p.52.

(52) Arridge R.G. — Br. J. appl. Phys. 18, No. 9 (1967) p.1311.

(53) Sasaki K. — Kobunshi Kagaku 25, (1968) p.460.

(54) Sasaki K. — Kobunshi Kagaku 26, (1969) p.21.

(55) Kornfel'd M.I. — Sov. Phys. Solid State 11, No. 6 (1969) p.1306.

(56) Johnson E.G.
Wallner A.J. — J. Colliod and Interface Sci. 32, (1970) p.377.

(57) Williams M.W. — I.E.E.E. 9th Conf. of Ind. Applic. Soc., Pittsburg (1974).

(58) Davies D.K. — J. Phys. D: Appl. Phys. 6, (1973) p.1017.

(59) Wåhlin A.
Bäckström G. — J. appl. Phys. 45, No. 5 (1974) p.2058.

(60) Hertz H. — J. reine angew. Math. 92, (1882) p.156.

(61) Sessler G.M.
West J.E. — Rev. Scient. Instrum. 42, No. 1 (1971) p.15.

(62) Furey M.J. — Ind. Engng. Chem. 61, No. 3 (1969) p.12.

(63) Bowden F.P.
Tabor D.
The Friction and Lubrication of Solids.
Part 1 (1950), Part 2 (1964), Clarendon Press, Oxford.

(64) Inculet I.I.
J. Colloid and Interface Sci. 32, No. 3 (1970) p.395.

(65) Inculet I.I.
Greason W.D.
Inst. Phys. Conf. Ser. No.11: Static Electrification.
Inst. Phys., London (1971) p.23.

(66) Gill E.W.B.
Alfrey G.F.
Nature 163, (1964) p.172.

(67) Sato K.
Jap.J. appl. Phys. 12, No. 6 (1973) p.938.

(68) Cunningham R.G.
Whitmore T.C.
Adv. in Static Electricity, Vol. 1.
Auxilia, Brussels (1970) p.207.

(69) Bowles A.H.
Proc. Physical Soc. 78, (1961) p.958.

(70) McClelland J.A.
Power C.J.
Proc. R. Ir. Acad. 34, (1917) p.40.

(71) Loeb L.B.
Static Electrification.
Springer, Berlin (1958).

(72) Davies D.K.
Br. J. appl. Phys. Ser.2, 2, (1969) p.1533.

(73) Davies D.K.
Adv. in Static Electricity Vol. 1.,
Auxilia, Brussels (1970) p.10.

(74) Cunningham R.G.
Hood H.P.
J. Colloid and Interface Sci. 32, No. 3 (1970)p.373.

(75) Inculet I.I.
Wituschek E.P.
Inst. Phys. and Physical Soc. Conf. Ser. No. 4:
Static Electrification.
I.P.P.S., London (1967) p.37.

(76) Bauser H.
Proc. 2nd Int. Conf. on Static Electrification.
Frankfurt (1973): Dechema Monographien vol. 72
Weinheim: Verlag-Chemie-GmbH. p.11.

(77) Coffee R.A.
Jap. J. appl. Phys. 11, (1972) p.1391.

(78) Graf von Harrach H.
Chapman B.N.
Vacuum 22, No. 11 (1972) p.535.

(79) Robins E.S.
Rose-Innes A.C.
Paper presented at the 4th Conf. on Static
Electrification, London (May 1975).

(80) Carta M.
Ciccu R.
Del Fa C.
Ferrara G.
Ghioni M.
Massacci P.
Proc. 9th Int. Miner. Processing Conf.
Prague (1970) p.47.

(81) Kittaka S.
Murata Y.
16th Conf. Electrostatic Soc. of Japan,
Osaka (1971).

(82) Wagner P.E. — J. appl. Phys. 27, (1956) p.1300.

(83) Davies D.K. — Proc. 1972 Annual Rep., Conf. on Electl. Insulation and Dielectric Phenomena. Natn. Acad. Sci., Washington D.C. (1973) p.1.

(84) Owe Berg T.G. Gaukler T.A. — J. Chem. Engng. Japan 3, (1970) p.217.

(85) Shashoua V.E. — J. Polymer Sci. 33, (1958) p.65.

(86) Shashoua V.E. — J. Polymer Sci. Part A 1, (1963) p.169.

(87) Knoblauch O. — Z Phys. Chem. 39, (1902) p.225.

(88) Shaw P.E. Jex C.S. — Proc. R. Soc. A 118, (1928) p.97.

(89) Medley J.A. — Nature 171, (1953) p.1077.

(90) Hays D.A. — J. Chem. Phys. 61, No. 4 (1974) p.1455.

(91) Wintle H.J. — J. appl. Phys. 41, No. 10 (1970) p.4004.

(92) Wintle H.J. — J. appl. Phys. 43, No. 7 (1972) p.2927.

(93) Batra I.P. Kanazawa K.K. Seki H. — J. appl. Phys. 41, No. 8 (1970) p.3416 .

(94) Kanazawa K.K. Batra I.P. Wintle H.J. — J. appl. Phys. 43, No. 2 (1972) p.719.

(95) Perlman M.M. — Paper presented at 4th Conf. on Static Electrification, London (May 1975).

(96) Medley J.A. — J. Textile Inst. 45, (1954) p.T123.

(97) Pollard A. — Process Control. Heinemann, London (1971) p.31.

(98) Kreyszig E. — Advanced Engineering Mathematics. Wiley International Edition (1967) p.194.

(99) Kelvin Lord — Philosophical Mag. 46, (1898) p.82.

(100) Vick F.A. — Br. J. appl. Phys. Suppl. No. 2, 4, (1953) p.51.

(101) Surplice N.A. D'Arcy R.J. — J. Phys. E: Scient. Instrum. 3, (1970) p.477.

(102) Anderson J.R. Alexander A.E. — Aust. J. appl. Sci. 3, (1952) p.201

(103) Macdonald J.R. Edmondson D.E. — Proc. Instn. Radio Engrs. 49, (1961) p.453.

(104) Guptill E.W., Calkin M.G., Jericho M.H. — Can. J. Phys. 50, (1972) p.2967.

(105) Kolm H.H. — Rev. scient. Instrum. 27, No. 12 (1956) P.1046.

(106) Rivière J.C. — Solid State Surface Science Vol. I. Edited by Green M, Chapter 4. Dekker (1969).

(107) Michaelson H.B. — J. appl. Phys. 21, (1950) p.536.

(108) Scruton B., Blott B.H. — J. Phys. E: Scient. Instrum. 6, No. 5 (1973) p.472.

(109) Murasaki N., Kono N., Matsui M., Mada H. — Inst. Phys. Conf. Ser. No. 11: Static Electrification. Inst. Phys., London (1971) p.44.

(110) Hughes K.A., Secker P.E. — J. Phys. E: Scient. Instrum. 4, No. 3 (1971) p.362.

(111) Foord T.R. — J. Phys. E: Scient. Instrum. 2, (1969) p.411.

(112) Krämer H., Messner D. — Kunststoffe 54, No. 11(1964) p.696.

(113) Davies D.K. — J.Scient. Instrum. 44, (1967) p.521.

(114) Scott W.D. — Rev. scient. Instrum. 43, No. 1 (1972) p.152.

(115) Secker P.E. — J. Electrostatics 1, No. 1 (1975) p.27.

(116) Wintle H.J. — J. Phys. E: Scient. Instrum. 3, (1970) p.334.

(117) Van Turnhout J. — Adv. in Static Electricity, Vol. 1. Auxilia, Brussels (1970) p.56.

(118) Lorrain P., Corson D. — Electromagnetic Fields and Waves. Freeman W.H., San Francisco (1970).

(119) Murasaki K., Kono M., Matsui M., Ohno M. — Electl. Engng. in Japan 90, No. 5 (1970) p. 187.

(120) Robinson M. — Electrostatics and its Applications. Edited by Moore A.D., Chapter 9. Wiley, New York (1973).

(121) Kao C.C. — J. appl. Phys. 44, No. 4 (1973) p.1543.

(122) Neugebauer H.E.J. — Xerography and Related Processes. Edited by Dessauer J.H., Clark H.E., Chapter 8 Focal Press, New York (1965).

(123) Schaffert R.M. — IBM J. Res. Dev. 6, No. 2 (1962) p.192.

(124) Bertein H. — Proc. 2nd Int. Conf. on Static Electrification, Frankfurt (1973): Dechema Monographien vol. 72. Weinheim: Verlag-Chemie-GmbH p.183.

(125) Bertein H. — Inst. Phys. and Physical Soc., Conf. Ser. No. 4: Static Electrification. I.P.P.S., London (1967) p.11.

(126) Donald D.K. — 1968 Annual Rep., Conf. on Electl. Insulation and Dielectric Phenomena, Publ. 1705, Natn. Acad. Sci, Washington D.C. (1969) p.170.

(127) Peterson J.W. — J. appl. Phys. 25, No. 7 (1954) p.907.

(128) Moore W.J. — Physical Chemistry. Fourth Edtn. Longmans, London (1963) p.222.

(129) Mambetov D.M. Knyazeva N.P. — Sov. Phys. Dokl. 15, No. 3 (1970) p.279.

(130) Ieda M. Sawa G. Shinohara U. — Jap. J. appl. Phys. 6, (1967) p.793.

(131) Batra I.P. Kanazawa K.K. — Jap. J. appl. Phys. 11, (1972) p.267.

(132) Ramer E.M. Richards H.R. — Textile Res. J. 38, (1968) p.28.

(133) Cresswell R.A. Perlman M.M. — J. appl. Phys. 41, (1970) p.2365.

(134) Sessler G.M. — J. appl. Phys. 43, (1972) p.408.

(135) Ieda M. Sawa G. Takeuchi R. — Jap. J. appl. Phys. 8, (1969) p.809.

(136) Arridge R.G.C. — Br. J. appl. Phys. 11, (1960) p.202.

(137) Lock P.J. — Proc. 2nd Int. Conf. on Static Electrification. Frankfurt (1973): Dechema Monographien vol. 72. Weinheim: Verlag-Chemie-GmbH.p.29.

(138) Yahagi K. Shinohara H. — Elec. Engng. in Japan 90, (March-April 1970) p.191.

(139) Jonscher A.K. — Proc. 2nd Int. Conf. on Static Electrification. Frankfurt (1973): Dechema Monographien vol. 72. Weinheim: Verlag-Chemie-GmbH. p.29.

(140) Davies D.K. — J. Phys. D: Appl. Phys. 5, (1972).

(141) Davies D.K. Lock P.J. — J. Electrochem.. Soc. 120, No. 2 (1973) p.266.

(142) Seanor D.A. — Electrical Properties of Polymers. Edited by Frisch K.C. and Patsis A. Technomic Pub. Co. (1972) p.1.

(143) O'Neill B.C. — Private Communication.

(144) Seanor D.A. — Electrical Properties of Polymers. Edited by Frisch K.C., Patsis A. Technomic Pub. Co. (1972) p.37.

(145) Morrison R.T. Boyd R.N. — Organic Chemistry. Allyn and Bacon, Boston (1966).

(146) Coehn A. — Ann. Phys. 64, (1898) p.217.

(147) Morris W.T. — Plastics and Polymers 38, (1970) p.41.

(148) Ruppel W. — Proc. 2nd. Int. Conf. on Static Electrification. Frankfurt (1973): Dechema Monographien vol. 72 Weinheim: Verlag-Chemie-GmbH p.321.

(149) Horvath T. Berta I. — Paper presented at the 4th Conference on Static Electrification, London (May 1975).

(150) Montgomery D.J. — Solid State Physics 9, (1959) p.139.

(151) McLaren K.G. Tabor D. — Nature 197, (1963) p.856.

(152) Zichy E.L. — Adv. in Static Electricity Vol. 1. Auxilia, Brussels (1970) p.42.

(153) Halaunbrenner J. — Br. J. appl. Phys. 16, (1965) p.1393.

(154) Hubbard R.W. — Inst. Phys. and Physical Soc., Conf. Series No. 4: Static Electrification. I.P.P.S., London (1967) p.156.

(155) Cunningham R.G. — J. Colloid and Interface Sci. 32, No. 3 (1970) p.401.

(156) Javadi S.H.S. Napier D.H. — Proc. Symp. on Chem. Process Hazards. Inst. Chem. Engrs. Symp. Ser. No. 39a (1974) p.267.

(157) Jewell-Thomas S.R.C. — Ph.D. Thesis, University of London (1957).

(158) Levy J.B. Wakelin J.H. Kauzmann W.J. Dillon J.H. — Textile Res. J. 28, (1958) p.897.

(159) Hersh S.P. Montgomery D.J. — Textile Res. J. 25, (1955) p.279.

(160) Nanevicz J.E. — Inst. Phys. Conf. Series No. 11: Static Electrification Inst. Phys., London (1971) p.248.

(161) Gorshkov V.I. Popov B.G. Verevkin V.N. — Theoretical Foundations Chem. Engng. 2, (1968) p.756.

(162) Taneya S. — Jap. J. appl. Phys. 2, (1963) p.718.

(163) Cheng L.
Soo S.L.
J. appl. Phys. 41, (1970) p.585.

(164) Ramackers L.
Adv. in Static Electricity, Vol. 1., Auxilia, Brussels (1970) p.370.

(165) Končar-Djurdjevic S.
Vukovic D.
Nature 193, (1962) p.58.

(166) Bafrnec M.
Bena J.
Chem.Engng. Sci. 27, (1972) p.1177.

(167) Ciborowski J.
Wlodarski A.
Chem.Engng. Sci. 17, (1962) p.23.

(168) Kiselnikov V.N.
Vyalkov V.V.
Filatov V.M.
Int. Chem.Engng. 7, (1967) p.428.

(169) Cooke B.A.
Ph.D. Thesis, University of London (1954).

(170) Gutman R.G.
Ph.D. Thesis, University of Cambridge (1974).

(171) Chlenov V.
Mikhailov N.
Vibrofluidised Beds.
Izdatel'stvo Nauka, Moscow (1972).

(172) Macdonald J.R.
Edmondson D.E.
Proc. Instn. Radio Engrs. 49, (1961) p.453.

(173) Sessler G.M.
J. Acoustical Soc. Am. 35, No. 9 (1963) p.1354.

(174) Danckwerts P.V.
Ind. Engng. Chem. 43, (1951) p.1460.

(175) Beverloo W.A.
Leniger H.A.
Van de Velde J.
Chem. Engng. Sci. 15, (1961) p.260.

(176) Lawver J.E.
Wright J.L.
AIME - Soc. Min. Engrs. Trans. 244, (1969) p.78.

(177) Lawver J.E.
Wright J.L.
AIME - Soc. Min. Engrs. Trans. 241, (1968) p.445.

(178) Gibbings J.C.
Saluja G.S.
Mackey A.M.
Inst. Phys. Conf. Ser. No. 11: Static Electrification Inst. Phys., London (1971) p.93.

(179) Boland D.
Geldert D.
Powder Technology 5, (1971/1972) p.289.

(180) Boland D.
Al-Salim Q.A.W.
Geldert D.
Chem. Engng. Sci. 24, (1969) p. 1389.

(181) Dolgopolov N.N.
Karagod I.S.
Sov. Phys. Dokl. 16, No. 12 (1972) p.1081.

(182) Smy P.R.
Proc. I.E.E. 120, No. 4 (1973) p.523.

(183) Zenz F.A.
Othmer D.F.
Fluidisation and Fluid Particle Systems.
Reinhold, New York (1960).

(184) Botterill J.S.M.
Williams J.A.
Trans. Instn. Chem. Engrs. 41, (1963) p.217.

(185) Wicke E.
Fetting F.
Chem. Ing. Tech. 26, (1954) p.301.

(186) Mickley H.S.
Fairbanks D.F.
Hawthorn R.D.
Chem Engng. Prog. Symp. Ser. 57, No. 32 (1961) p.51.

(187) Coulson J.M.
Richardson J.F.
Chemical Engineering Vol. 2.
Pergamon Press, Oxford (1968).

(188) Coulson J.M.
Richardson J.F.
Chemical Engineering Vol. 1.
Pergamon Press, Oxford (1965).

(189) Masuda S.
Matsumoto Y.
Proc. 2nd Int. Conf. on Static Electrification.
Frankfurt (1973): Dechema Monographien vol. 72.
Weinheim: Verlag-Chemie-GmbH. p.293.

(190) Perry R.H.
Chilton C.H.
Kirkpatrick S.D.
Chemical Engineer's Handbook, 4th Edition.
McGraw-Hill, New York (1963)p.15-37.

(191) Felici N.J.
Rev. Gen. de l'Electricité 75, (1966) p.1145.

(192) Cho A.Y.H.
J. appl. Phys. 35, No. 9 (1964) p.2561.

(193) Krasucki Z.
Paper presented at 4th Conf. on Static
Electrification, London (May 1975).

(194) Corbett R.P.
Proc. 2nd Int. Conf. on Static Electrification.
Frankfurt (1973): Dechema, Monographien vol. 72.
Weinheim: Verlag-Chemie-GmbH. p.261.

(195) Malliaris A.
Turner D.T.
J. appl. Phys. 42, No. 2 (1971) p. 614.

TABLE 1

THE MEASURED CONTACT POTENTIAL VALUES OF SEVERAL METALS RELATIVE TO GOLD

METAL	CONTACT POTENTIAL RELATIVE TO GOLD(V)
GOLD	0.02
SILVER	0.11
NICKEL	0.24
TIN	0.55
STAINLESS STEEL	0.16
BRASS	0.26
ALUMINIUM (OXIDISED)	0.58
ALUMINIUM (OXIDE-FREE)	1.15

TABLE 2 A SUMMARY OF SOME PROPERTIES OF THE MATERIALS STUDIED IN THE VACUUM CHAMBER APPARATUS (THE VALUES ARE TAKEN FROM MANUFACTURERS HANDBOOKS AND STANDARD TABULATIONS)

MATERIAL	BASIC STRUCTURAL UNIT	ε_r	YOUNG'S MODULUS ($N\,m^{-2} \times 10^{-9}$)	YIELD STRENGTH ($N\,m^{-2} \times 10^{-7}$)	VOLUME RESISTIVITY (Ω m)
POLYPROPYLENE	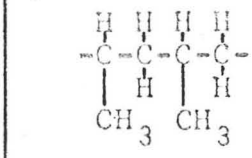	2.22	1.32	3.21	$> 10^{15}$
POLYETHYLENE (LOW DENSITY)	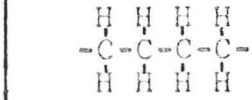	2.25	0.179	1.14	$> 10^{15}$
POLYMETHYLMETHACRYLATE (PMMA)	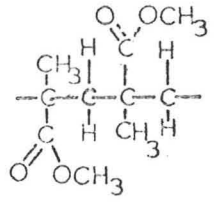	3	2.9	6.55	10^{12}-10^{14}
POLYCARBONATE	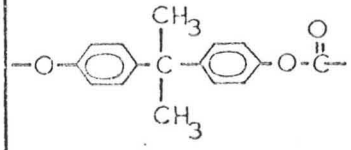	3.02	2.29	6.31	10^{13}
NYLON 66	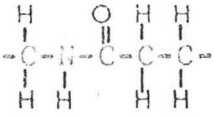	3.6-6	1.55	6.89	10^{11}-10^{14}
POLYTETRAFLUOROETHYLENE (PTFE)	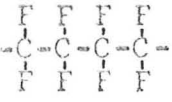	2.05	0.358	2.93	$> 10^{16}$
VITON®	HYDROCARBON CONTAINING FLUORINE	4-10	-	1.38	2×10^{11}
POLYETHYLENETEREPHTHALATE (PETF)	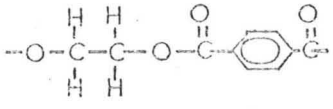	3.2	3.25	4.41	$> 10^{14}$

TABLE 3 THE TOLERANCES OF THE SPHERICAL SPECIMENS

MATERIAL	DIAMETER TOLERANCE (mm)	SPHERICITY (mm)
BRASS	±0.05	0.013
HOLLOW ALUMINIUM (Wall thickness =1mm)	±0.254	0.13
STAINLESS STEEL	±0.025	0.0025
NYLON 66	±0.025	0.013
PTFE	±0.05	0.025
POLYPROPYLENE	±0.05	0.025
VITON®	±0.076	0.076

TABLE 4 THE INDUCTION PROBE CALIBRATION CHARACTERISTICS CALCULATED BY FITTING THE POTENTIAL HEIGHT DEPENDENCE CURVE

(Probe resolution length=0.5mm)

MATERIAL	CODE	L	GAS PRESS. (TORR)	CONTACT METAL (19.1 mm DIAM.)	CONTACT MODE & NORMAL FORCE	LINEAR VELOCITY ($mm\ s^{-1}$)	χ (mm)	$\frac{B_c}{P_\infty}$	k	ε_r
POLYPROPYLENE	A	3	$< 10^{-4}$	BRASS	ROLLING 9.1N	17.48	3.42	.604	.35	2.22
POLYETHYLENE (L.D.)	B	3	$< 10^{-4}$	STAINLESS STEEL	SLIDING 9.8N	17.48	4.56	.72	.22	2.25
POLYETHYLENE (L.D.)	C	3	$< 10^{-4}$	ALUMINIUM	ROLLING 10.0N	87.5	4.56	.72	.5	2.25

TABLE 5 A COMPARISON BETWEEN THE MEASURED CHARGE TRANSFERRED TO A CONTACT SPHERE (UNIT CIRCUMFERENTIAL LENGTH)$^{-1}$, WITH THE CHARGE (UNIT CIRCUMFERENTIAL LENGTH)$^{-1}$ CALCULATED FROM THE INDUCTION PROBE POTENTIAL

MATERIAL	CODE	SPHERE ($C\ mm^{-1} \times 10^{10}$)	INDUCTION PROBE ($C\ mm^{-1} \times 10^{10}$)	CHARGE LINE WIDTH (mm)
POLYPROPYLENE	A	+1.15	-1.06	2.3
POLYETHYLENE (L.D.)	B	+2.4	-2.4	2.7
POLYETHYLENE (L.D.)	C	+0.99	-1.0	3.2

TABLE 6 THE MATERIALS USED FOR THE GAS PRESSURE STUDIES (LINEAR VELOCITY = 17.48mm s^{-1})

DIELECTRIC	CODE	L (mm)	CONTACT METAL (19.1mm DIAMETER)	CONTACT MODE	CONTACT FORCE (N)
POLYPROPYLENE	D	3	STAINLESS STEEL	ROLLING	8.8
POLYPROPYLENE	E	3	ALUMINIUM	ROLLING	9.8
POLYETHYLENE	F	3	ALUMINIUM	ROLLING	9.8

TABLE 7 THE CHARGE CARRIER MOBILITIES CALCULATED FROM THE CHARGE DECAY RESULTS

ε_r WAS ASSUMED=5 FOR NYLON 66 AND VITON®.
g=0.127mm , L=3mm

MATERIAL	SLOPE FROM FIG.32 $(Vs)^{-1}$	μ FROM EQN. 3.15 $(m^2V^{-1}s^{-1})$	V_{mgs} $(Vx10^3)$ (FROM FIG.30)	TRANSIT TIME (t_L) (s)	μ FROM t_L $(m^2V^{-1}s^{-1})$	α (mm)	μ FROM EQN. 3.17 $(m^2V^{-1}s^{-1})$
NYLON66 G	0.2	$1.41\ 10^{-11}$	36	210	$1.19\ 10^{-11}$	1.08	$5.64\ 10^{-11}$
NYLON66 H	0.084	$5.94\ 10^{-12}$	59	420	$4.0\ 10^{-12}$	0.89	$2.38\ 10^{-11}$
VITON® I	0.392	$2.76\ 10^{-11}$	17	195	$2.27\ 10^{-11}$	1.4	$1.11\ 10^{-10}$
VITON® J	0.192	$1.35\ 10^{-11}$	22	270	$1.33\ 10^{-11}$	1.32	$5.4\ 10^{-11}$

TABLE 8 THE POLARITY OF CHARGE TRANSFERRED TO SEVERAL DIELECTRIC MATERIALS AS A RESULT OF CONTACT WITH VARIOUS METALS

DIELECTRIC	POLARITY OF CHARGE ON THE DIELECTRIC	POLAR OR NON-POLAR DIELECTRIC	CONTACT METALS
POLYPROPYLENE	-ve	NON-POLAR	AS SECTION 3.6
POLYETHYLENE (L.D.)	-ve	NON-POLAR	AS SECTION 3.6
PTFE	-ve	NON-POLAR	silver, aluminium
VITON®	-ve	NON-POLAR	aluminium, gold
PETF	+ve	POLAR	gold
POLYCARBONATE	SMALL +ve	POLAR	AS SECTION 3.6
PMMA	+ve	POLAR	AS SECTION 3.6
NYLON 66	+ve	POLAR	AS SECTION 3.6

TABLE 9

THE SPHERE CHARGE (UNIT CIRCUMFERENTIAL LENGTH)$^{-1}$ ($C\,mm^{-1} \times 10^{12}$) AFTER ONE TURNTABLE REVOLUTION, FOR CHARGE TRANSFER BETWEEN TWO DIELECTRIC SPECIMENS

SPHERE DIAMETER-VITON® 12.7mm, OTHERS 19.1mm
GAS PRESSURE $< 10^{-4}$ TORR
NORMAL CONTACT FORCE 10.3N
ROLLING CONTACT, LINEAR VELOCITY 17.48mm s^{-1}

3mm THICK PLANE	POLYPROPYLENE	NYLON66	PTFE	VITON®	SPHERE
POLYPROPYLENE	+0.43	+37.5	-10.0	-187.8	
NYLON 66	-9.5	+17.0	-13.5	-813	
PTFE	+4.07	+53.2	-2.45	-22.2	
VITON®	+28.8	+90.3	+6.6	+160.5	

TABLE 10

A TRIBOELECTRIC SERIES FOR THE MATERIALS IN TABLE 9

POSITIVE	NYLON 66
	METALS
	POLYPROPYLENE
	PTFE
NEGATIVE	VITON®

MATERIAL HIGHER IN THE SERIES CHARGES POSITIVELY WITH RESPECT TO MATERIAL LOWER IN THE SERIES

TABLE 11 PROPERTIES OF THE MATERIALS USED FOR THE VIBRATED BED STUDIES

MATERIAL	PARTICLE SIZE(μm)	MEASURED RESISTIVITY (Ω m)	ε_r FOR THE PARTICLES	ESTIMATED BULK ε_r
GLASS BALLOTINI	106-150	4.2×10^{7}	6.5	4.3
QUARTZ	106-150	3.9×10^{8}	4.0	2.8
DIAKON® (PMMA)	AVERAGE 240	1.9×10^{12}	3.0	2.2
POLYPROPYLENE	AVERAGE 250	5×10^{15}	2.22	1.7

TABLE 12 PROPERTIES OF THE MATERIALS USED FOR THE ELECTROSTATIC SEPARATION STUDIES

MATERIAL	PARTICLE SIZE(μm)	MEASURED RESISTIVITY (Ω m)	DENSITY OF THE PARTICLES ($kg\ m^{-3}$)
GLASS BALLOTINI (CLEAR)	106-150	1.2×10^{8}	2600
GLASS BALLOTINI (DYED RED)	300-699	1.6×10^{11}	2600
QUARTZ	106-150	8×10^{8}	2600
IRON SHOT	104-250	1.6×10^{5}	7500

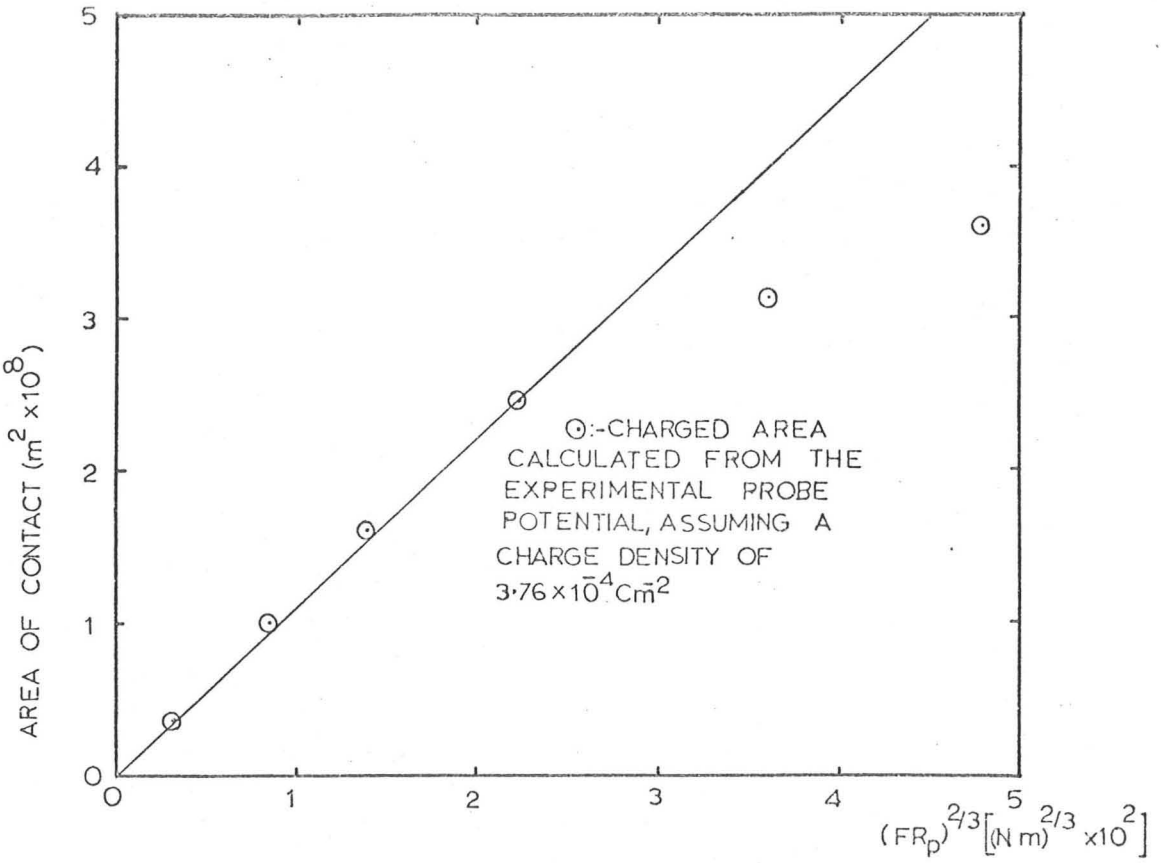

FIG.1 PLOT OF THE CORRECTED RESULTS OF DAVIES[58] FOR THE CALCULATED CHARGED AREA, AGAINST THE PARAMETER $(FR_p)^{2/3}$. THE FULL LINE SHOWS THE CONTACT AREA CALCULATED FROM EQUATION 2.1

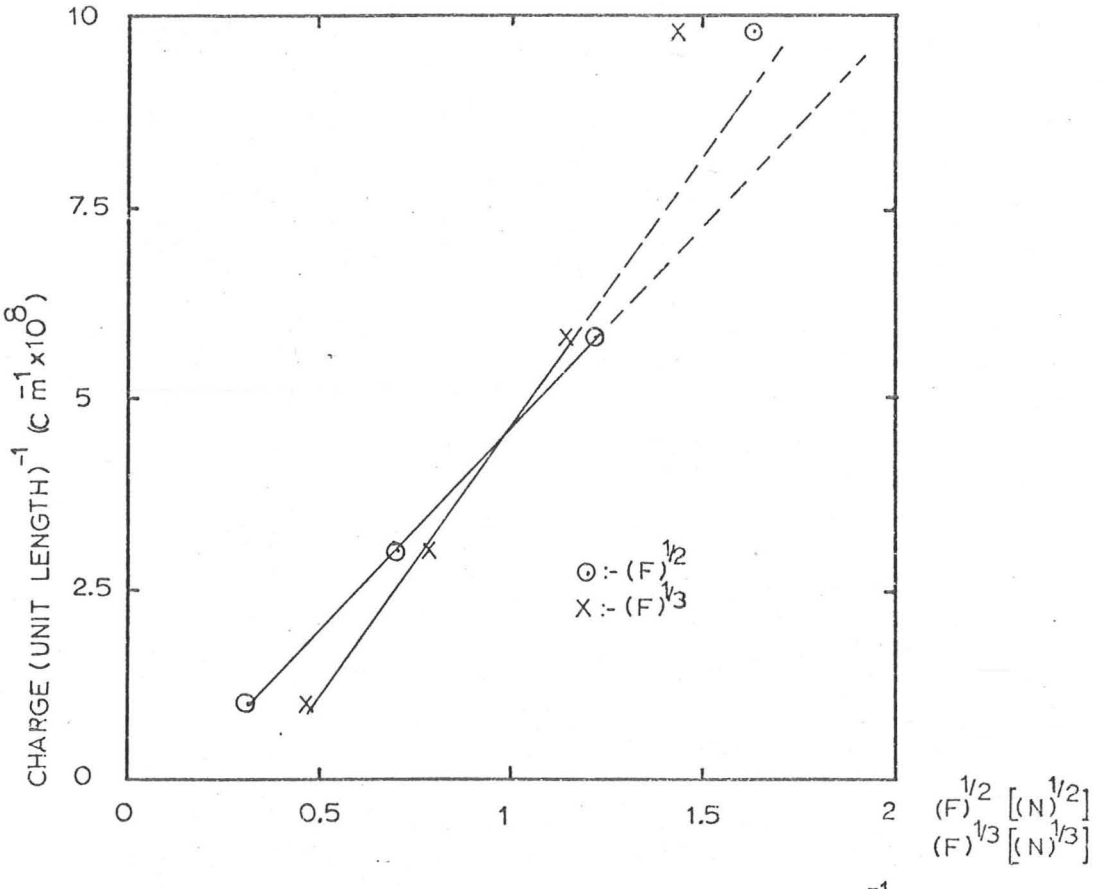

FIG. 2 PLOT OF THE OBSERVED CHARGE (UNIT LENGTH)$^{-1}$ REPORTED BY WÅHLIN[59], AGAINST THE NORMAL FORCE TO THE POWER OF $\frac{1}{2}$ AND $\frac{1}{3}$. THE SIGN OF CHARGE SHOWN CORRESPONDS TO THE CHARGE TRANSFERRED TO THE CONTACT METAL

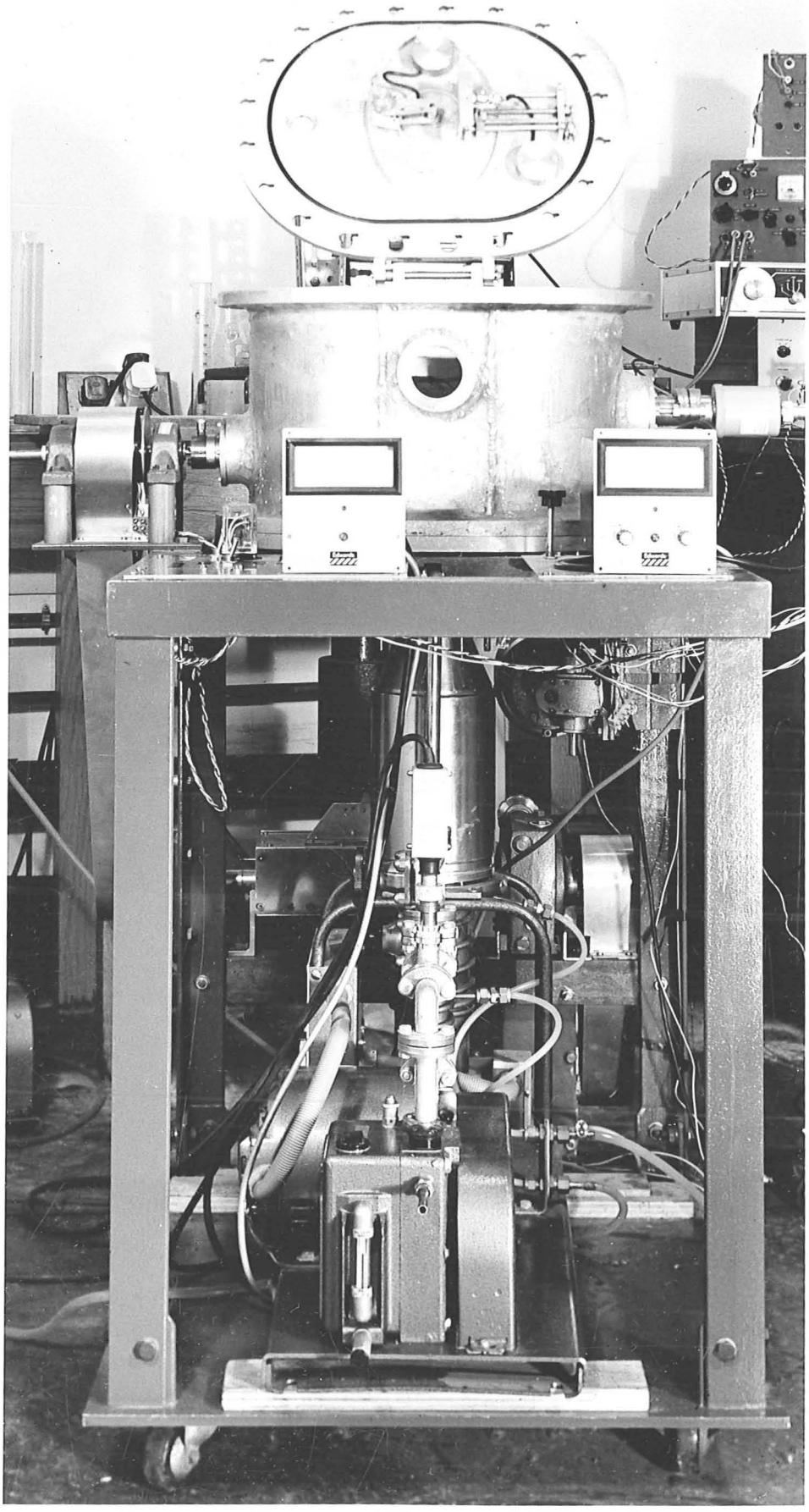

FIG. 3 THE VACUUM VESSEL SYSTEM

KEY FOR FIG.4.

A:- Vacuum Vessel

B:- 25.4mm diam. viewing port

C:- 53mm diam. viewing port

D:- Pivot support system

E:- Induction probe movement control

F:- Induction probe electrical connection

G:- Sphere electrical connection

H:- Sphere movement controls

I:- Penning gauge head

J:- Contact potential variable resistor

K:- Penning gauge indicator

L:- Mild steel support frame

M:- Position sensing resistor

N:- Electrical connection to turntable unit

O:- Horizontal table movement motor

P:- NTM2A liquid nitrogen trap

Q:- Water cooled oil diffusion pump

R:- Variable speed gear unit

S:- "Power Grip" belt drive

T:- Universal coupling

U:- Support wheel

V:- Rotary drive motor

W:- Rotary vacuum pump

X:- Heavy support base plate

Y:- Pirani gauge head

Z:- Gearbox

α:- Quarter swing butterfly valve

β:- 2 inch spacer

γ:- Roller bearings

δ:- Revolution counter

ε:- Control switches for horizontal and rotary movement

ζ:- Relays for horizontal movement control

η:- Pirani gauge indicator

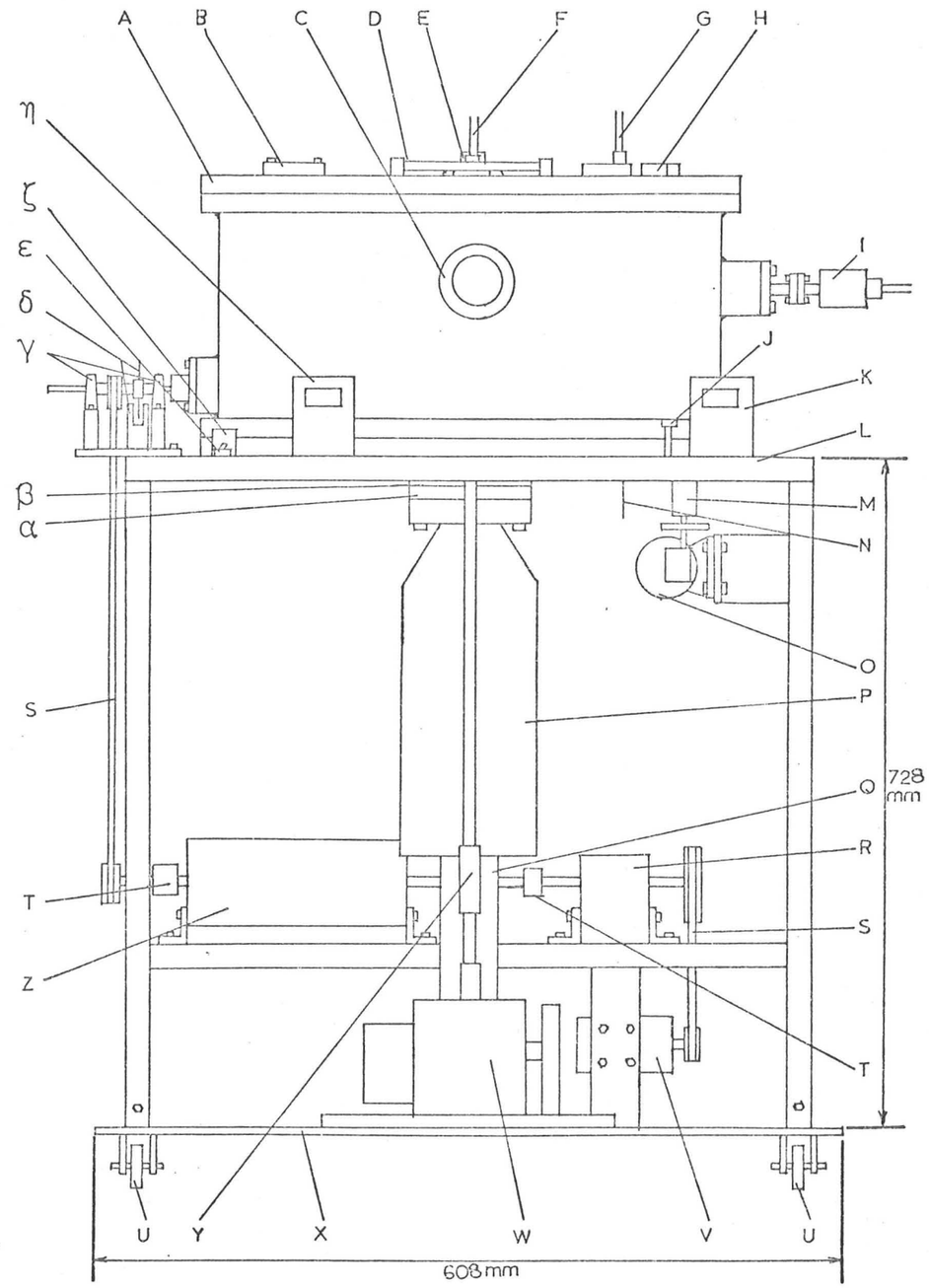

FIG. 4 SCHEMATIC VIEW OF THE VACUUM VESSEL SYSTEM (THE BELT DRIVE COVERS ARE NOT SHOWN)

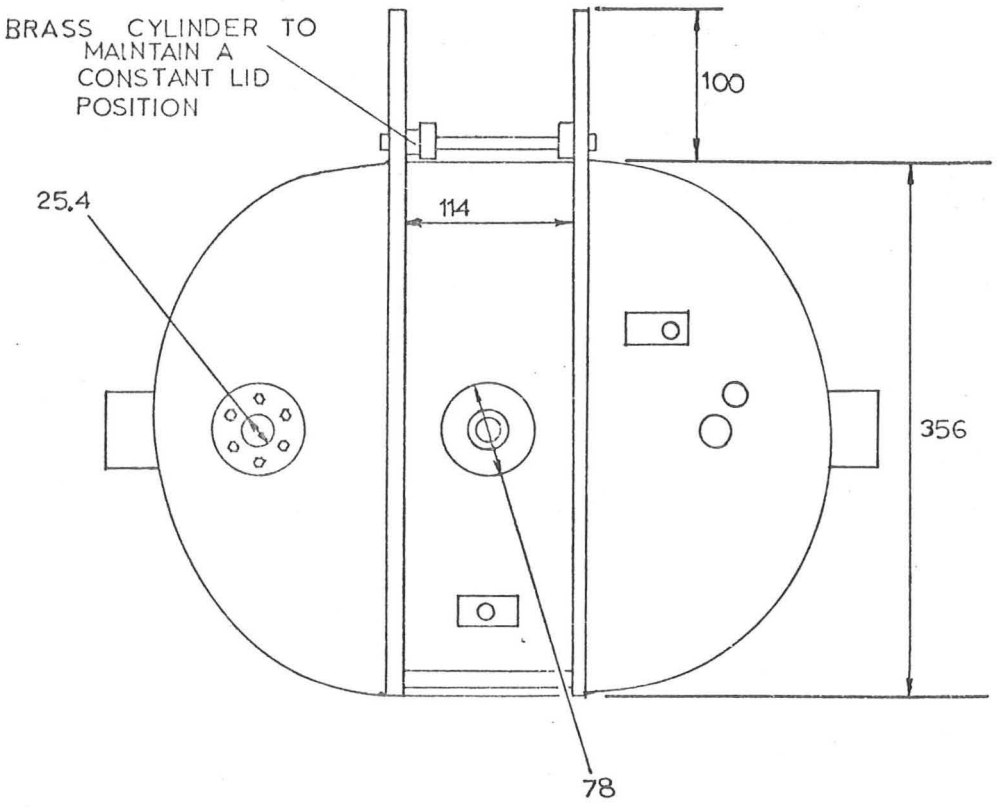

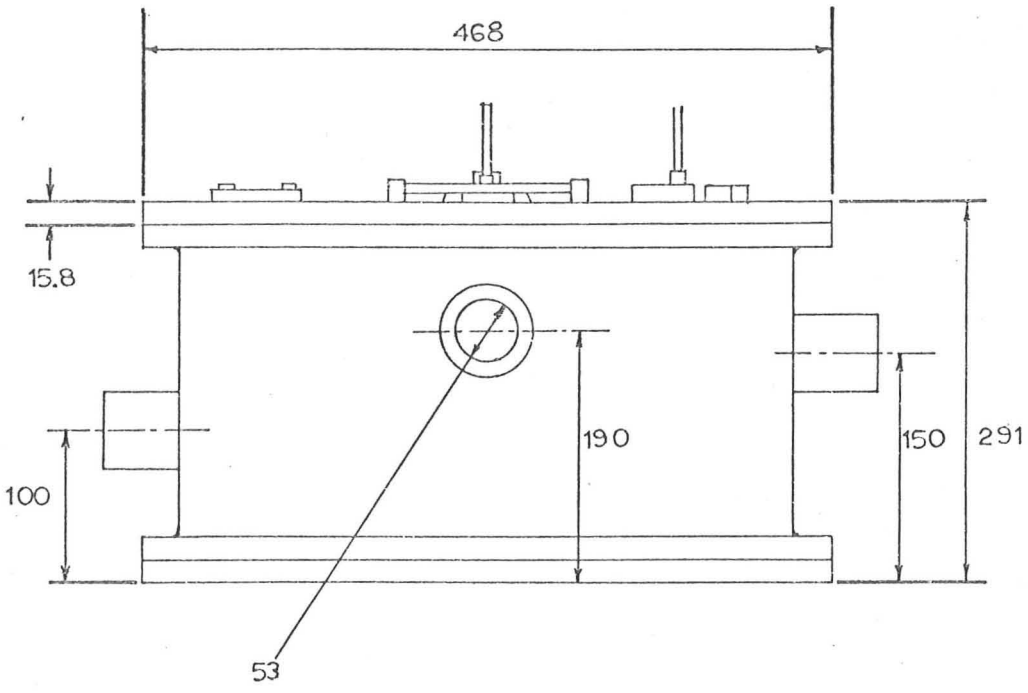

FIG. 5 THE VACUUM VESSEL
(DIMENSIONS IN mm, NOT TO SCALE)

KEY FOR FIGS. 6 and 7.

A:- Induction probe support

B:- Induction probe electrical feedthrough cover

C:- Sphere electrical screening

D:- Sphere support base

E:- Contact sphere

F:- Sphere electrical feedthrough cover

G:- Slip ring support

H:- Carbon brush

I:- Electrical connection from carbon brush to a plug

J:- Gear unit housing

K:- Electrical plug and socket

L:- Support for vertical gear shaft

M:- 3:2 Delrin® bevel gear unit, step up from outside

N:- Table slide base support

O_1:- Graphite loaded nylon bush

O_2:- Tufnol bush

P:- PTFE pads

Q:- Steel support plates

R:- Tufnol block

S:- Steel disc

T:- Steel ball bearing

U:- Universal coupling

V:- 3:2 Delrin® bevel gear unit, step up from outside

W:- Table support shaft

X:- Dural turntable

Y:- Gold plated brass ring

Z:- 4 x 12.7mm diameter gold plated brass discs

α:- Dielectric specimen

β:- Table slide support base attachment screw

γ:- $\frac{3}{8}$in Whitworth threaded drive rod

δ:- 12 - 6BA screws

ε:- Microswitch

ζ:- Electrical feedthrough

η:- Steel guide rod

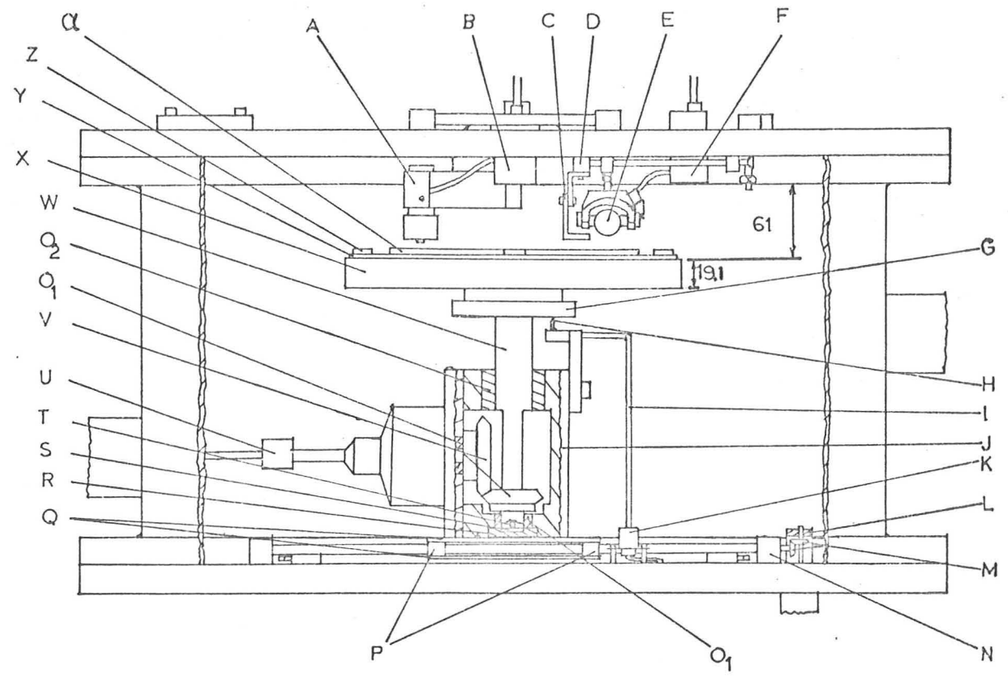

FIG. 6 VACUUM VESSEL INTERIOR
(THE TABLE GEAR SUPPORT SYSTEM IS SHOWN WITH PART OF THE WALL REMOVED, AND THE TABLE IS SHOWN IN THE MIDDLE POSITION.
DIMENSIONS IN mm, NOT TO SCALE)

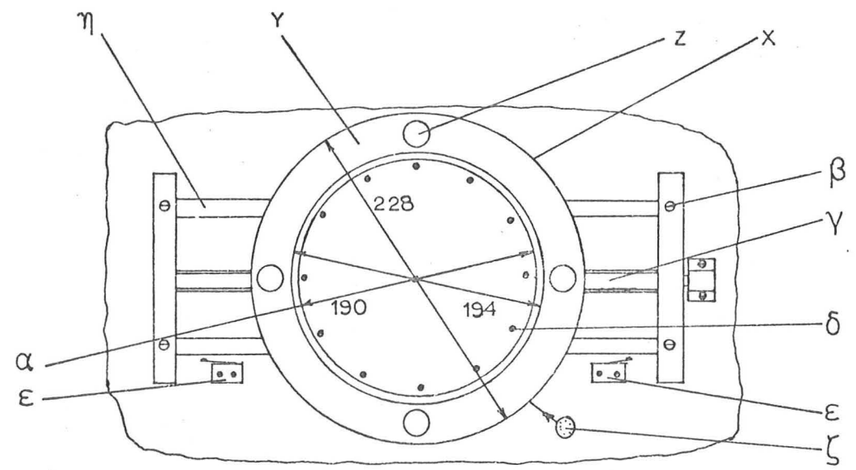

FIG. 7 TOP VIEW OF THE TABLE POSITIONED AS IN FIG. 6, THE TABLE DRIVE SHAFT IS NOT SHOWN
(DIMENSIONS IN mm, NOT TO SCALE)

KEY FOR FIGS. 8 and 9.

A:- Steel guide rod.

B:- Threaded brass rod (2BA).

C:- 1:1 Bevel gear unit.

D:- Brass unit connecting OBA threaded rod to the keyway.

E:- Steel pin through the sphere support shaft.

F:- Brass block with central 2BA tapped hole

G:- OBA threaded rod, with split pin inserted through a hole at one end.

H:- Steel block, with central OBA tapped hole.

I:- PTFE sleeve.

J:- 4BA nut.

K:- 4BA threaded rod.

L:- Brass saddle.

M:- Carbon brush on a spring steel strip.

N:- PTFE bush

O:- Brass disc.

P:- Contact sphere.

Q:- Brass disc with a 10BA tapped hole.

R:- 10BA screw and nut.

S:- Brass strip with a 10BA clearance hole.

T:- PTFE block.

U:- Steel rod with a 4BA tapped hole.

V:- Steel spring.

W:- Dural support block.

X:- Removeable brass block.

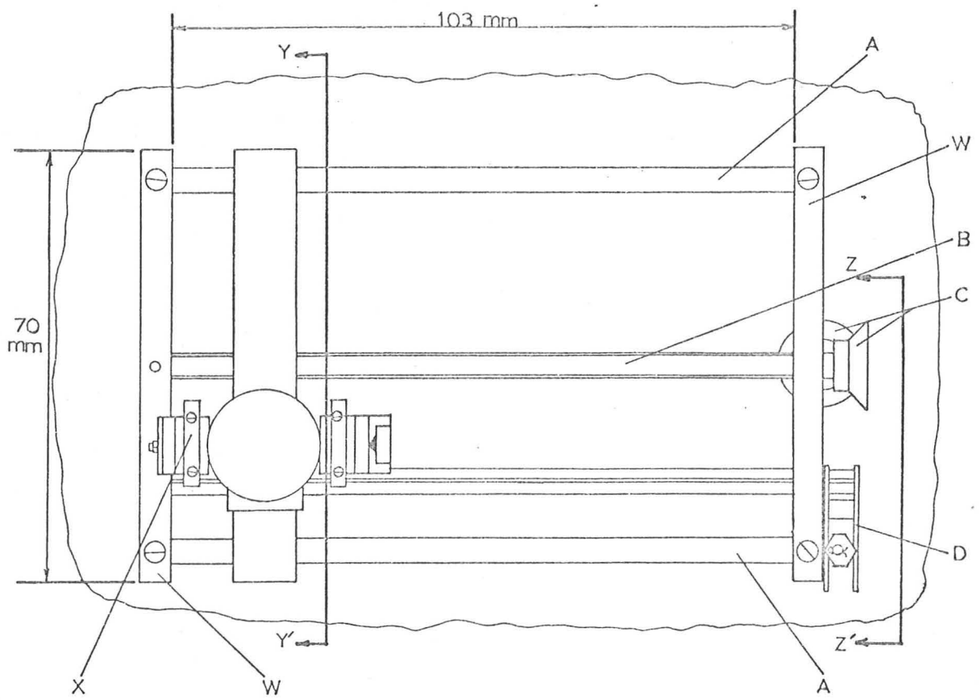

FIG. 8 OVERALL VIEW OF THE SPHERE MECHANICAL SUPPORT (NOT TO SCALE)

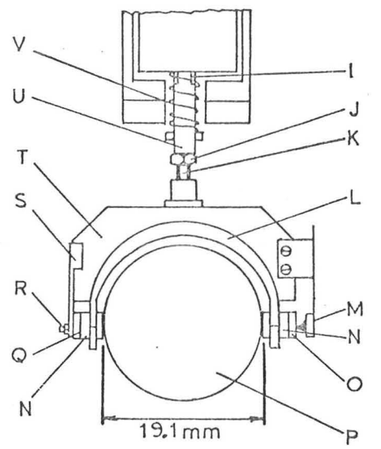

DETAILED VIEW OF THE SPHERE ASSEMBLY

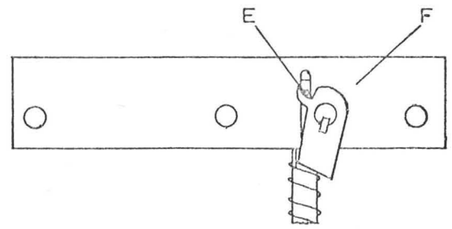

VIEW ALONG YY' IN FIG.8

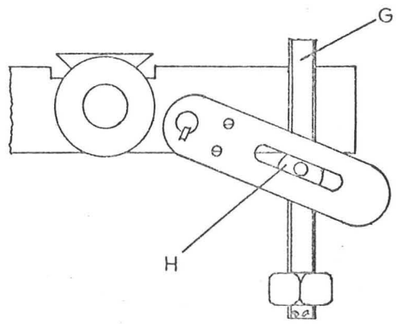

VIEW ALONG ZZ' IN FIG.8

FIG. 9 DETAILED VIEW OF THE SPHERE MECHANICAL SUPPORT (NOT TO SCALE)

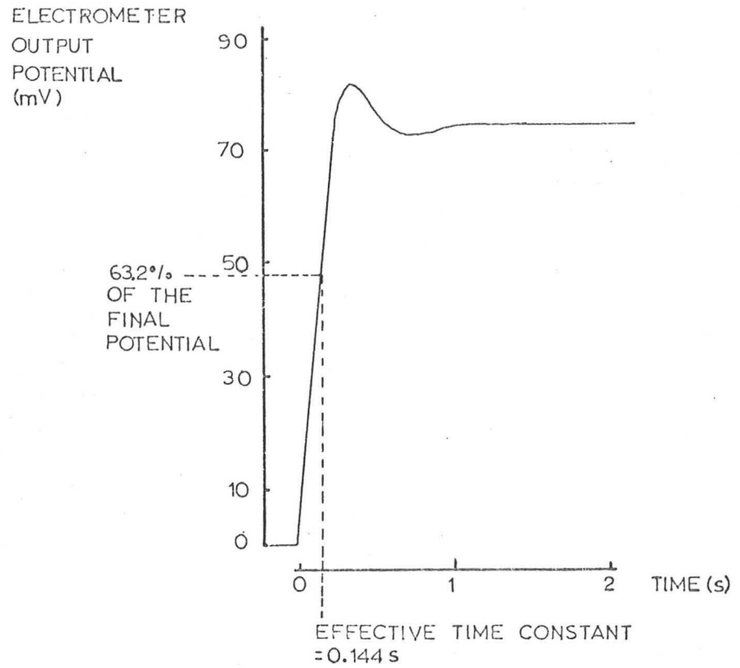

FIG. 10 TRACE OF THE VIBRON® ELECTROMETER OUTPUT POTENTIAL, AS A RESULT OF A STEP CHANGE IN THE INPUT POTENTIAL

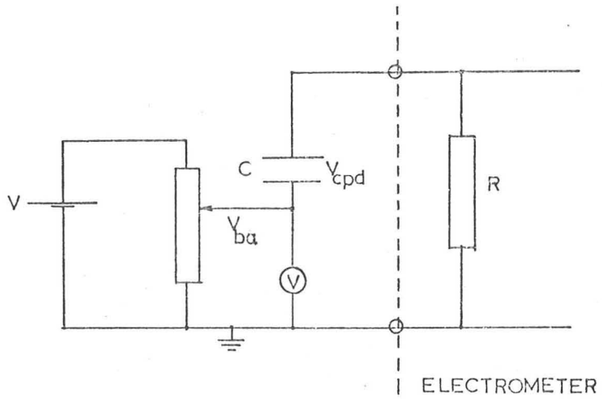

V:- 4.5 V , V_{ba}:- BIAS POTENTIAL, R:- 50 MΩ,

V_{cpd}:- CONTACT POTENTIAL DIFFERENCE

C:- CAPACITANCE OF THE JUNCTION OF INTEREST

FIG. 11 CONTACT POTENTIAL MEASUREMENT CIRCUIT

KEY FOR FIG. 12.

A:- Vacuum vessel lid.

B:- Brass support unit for the probe. Upper section is threaded.

C:- Cover plate.

D:- Spring to maintain contact between the steel member (P) and the pin.

E:- Steel pin.

F:- Brass support cylinder.

G:- Brass screening cylinder.

H:- Brass screening cylinder.

I:- Enamel wire covering.

J:- Probe centre wire.

K:- Brass block, 8BA tapped hole in the centre.

L:- PTFE block.

M:- 8BA threaded rod.

N:- PTFE block. 8BA threaded hole in the centre.

O:- Tension springs.

P:- Steel plate.

Q:- Steel rod. A slot was cut in the lower section. The section above the vessel lid was threaded to contact the control button.

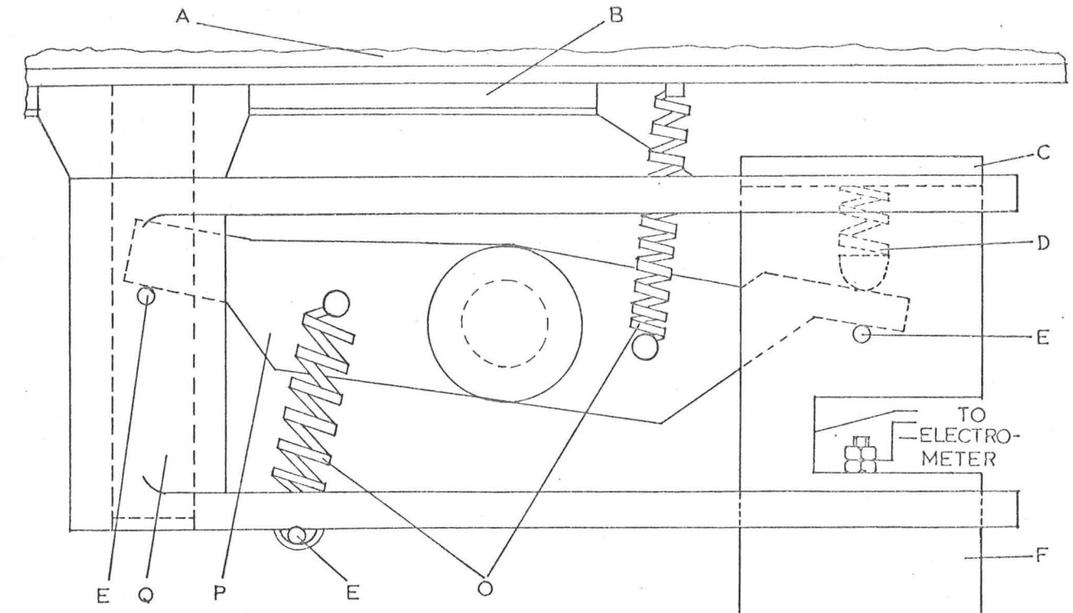

a. MECHANICAL SUPPORT (THE ELECTROMETER CONNECTION SCREENING IS NOT SHOWN)

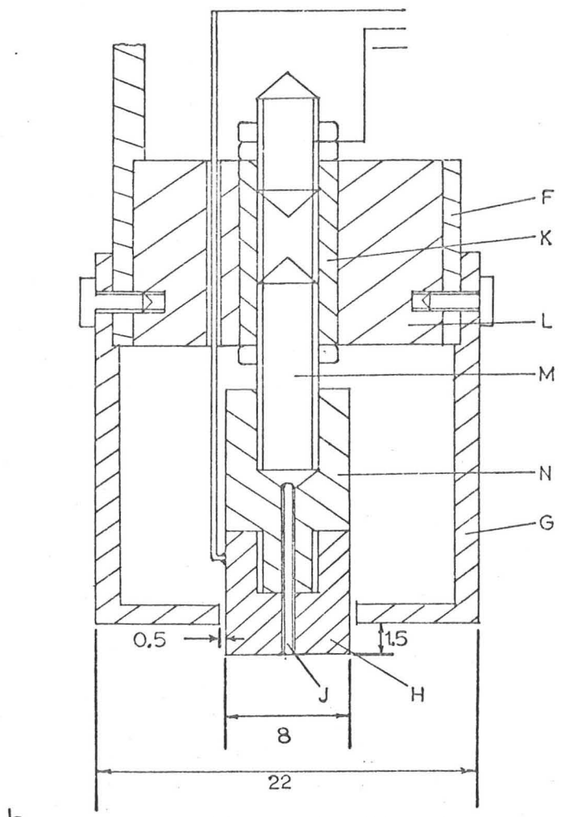

b. SECTIONAL VIEW OF THE PROBE TIP SCREENING

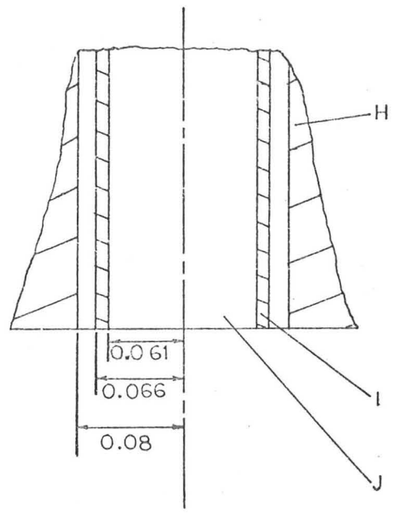

C. SECTIONAL VIEW OF THE PROBE TIP

FIG. 12 INDUCTION PROBE UNIT (DIMENSIONS IN mm, NOT TO SCALE)

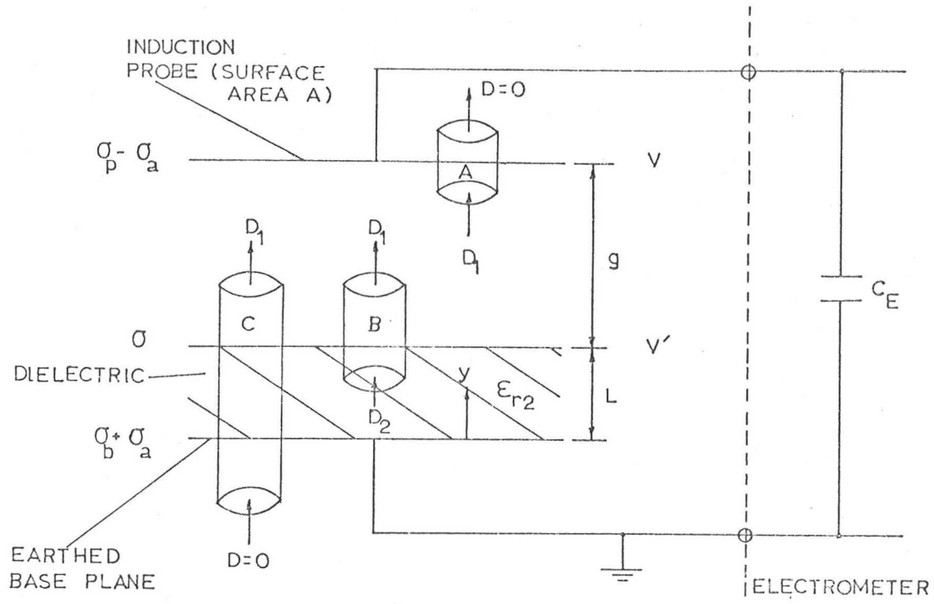

a. MEASUREMENT OF SURFACE CHARGE DENSITY ON A DIELECTRIC SHEET USING AN INDUCTION PROBE

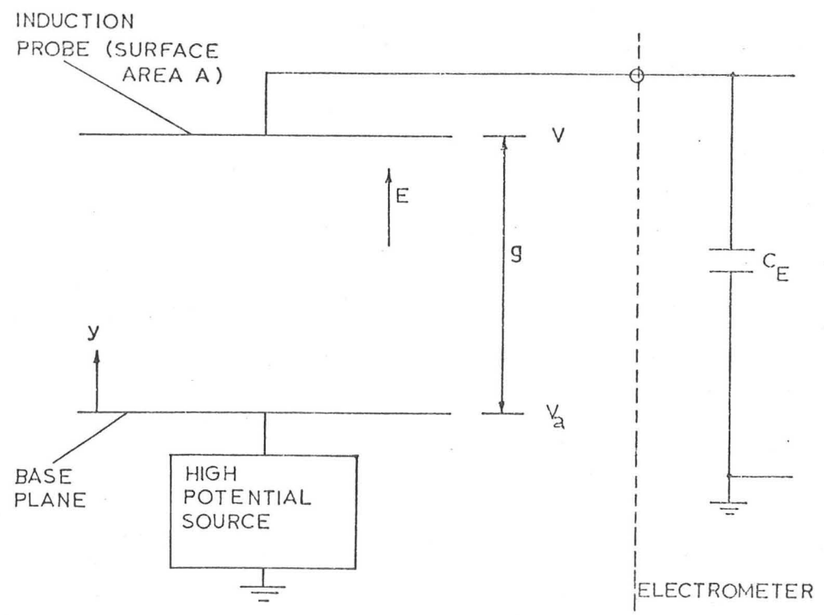

b. INDUCTION PROBE CALIBRATION SYSTEM

FIG. 13 APPLICATION AND CALIBRATION OF THE INDUCTION PROBE

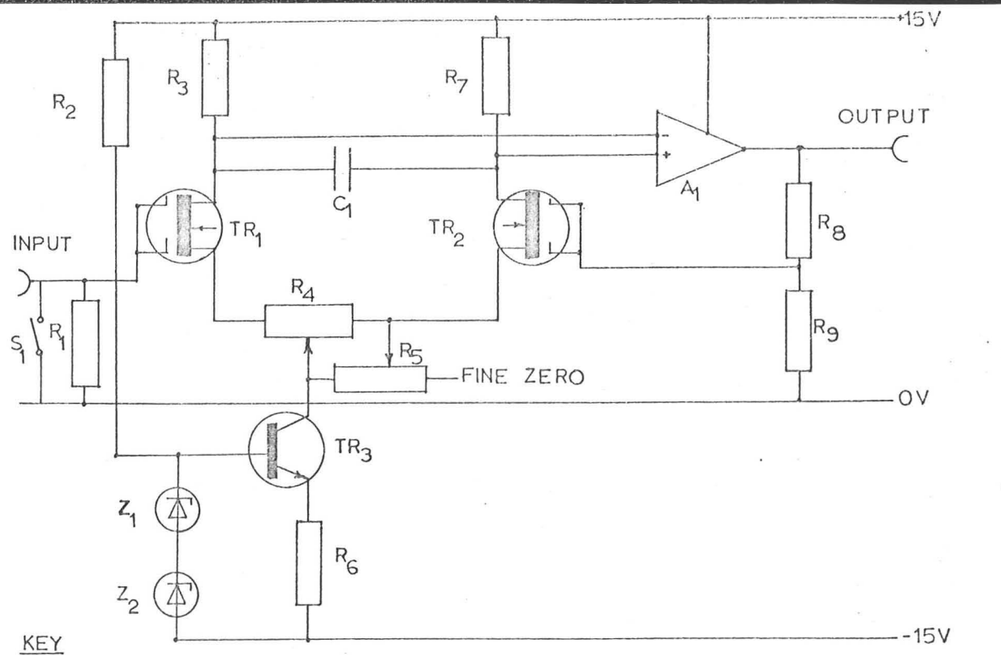

KEY

R_1:-15TΩ R_3:-10kΩ R_5:-10kΩ R_7:-10kΩ R_9:-1kΩ TR_1:-BFS28 TR_3:-BC107
R_2:-3.3kΩ R_4:-1kΩ R_6:-12kΩ R_8:-4.7kΩ C_1:-0.1μF TR_2:-BFS28 Z_1, Z_2:-6.2V ZENER DIODES

A_1:-SN 72301 S_1:-MANUAL SWITCH

FIG. 14 CIRCUIT DIAGRAM OF THE CHARGE SCAN ELECTROMETER (THE AMPLIFIER COMPENSATION NETWORK IS NOT SHOWN)

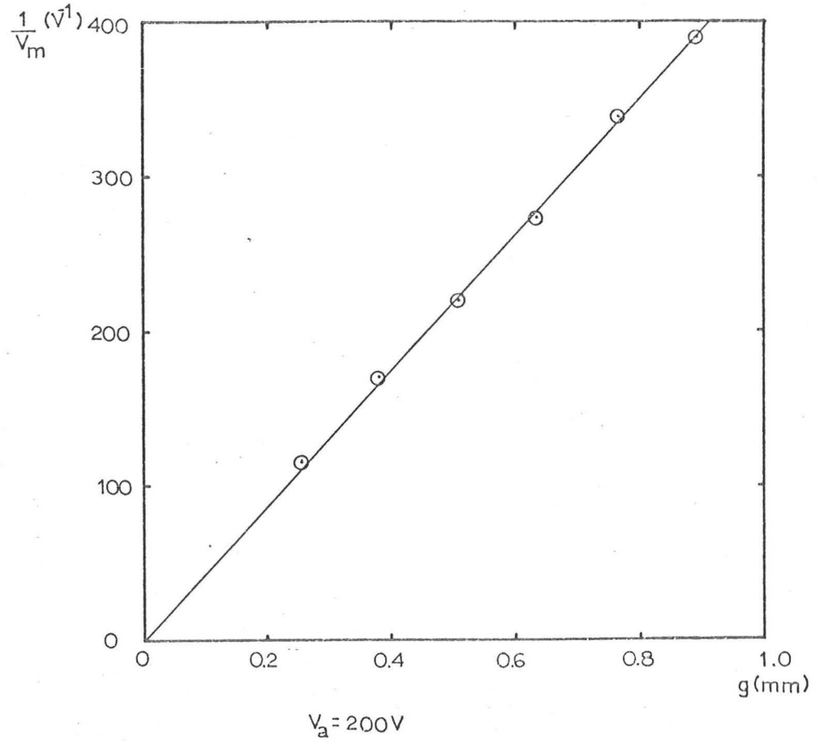

FIG. 15 CALIBRATION OF THE INDUCTION PROBE

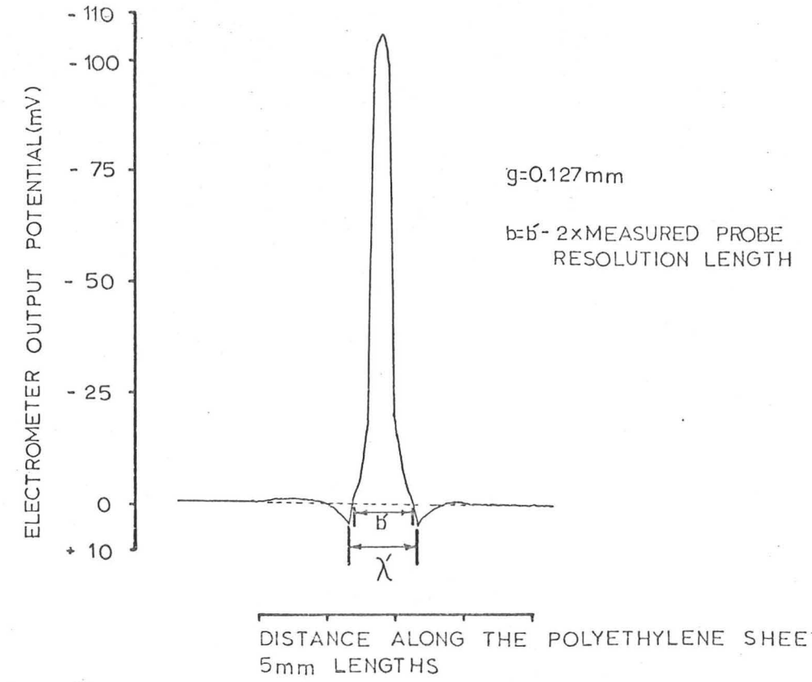

a. ELECTROMETER OUTPUT POTENTIAL AS A 3mm THICK POLYETHYLENE SHEET WAS MOVED BENEATH THE INDUCTION PROBE. THE CHARGED REGION WAS CAUSED BY ROLLING CONTACT WITH A 19.1mm DIAMETER NICKEL PLATED SPHERE, A NORMAL CONTACT FORCE OF 9.7N, AND GAS PRESSURE BELOW 10^{-4} TORR

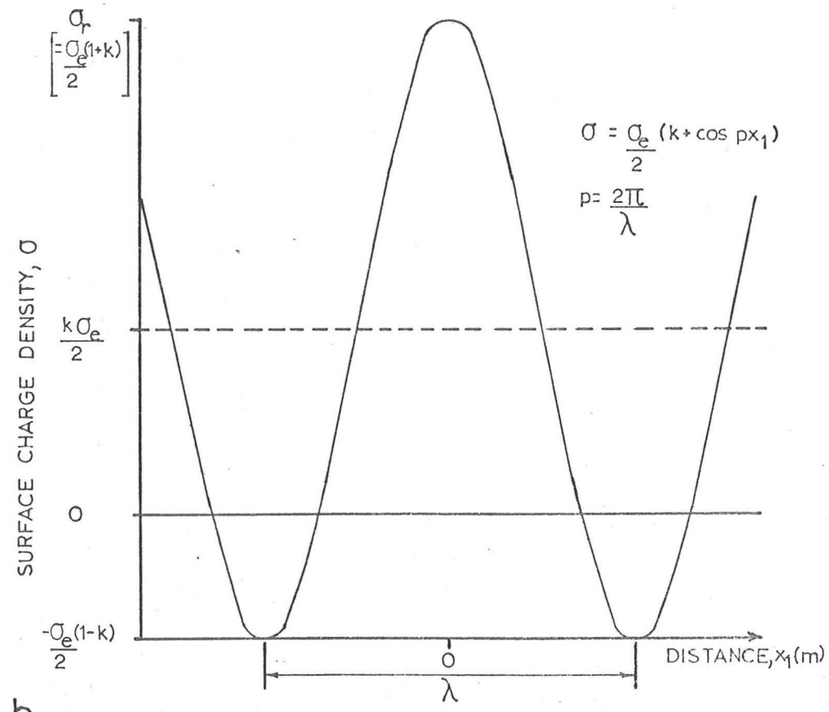

b. CHARGE DISTRIBUTION ASSUMED IN ORDER TO EXTEND THE THEORETICAL APPROACH OF MURASAKI[119] TO INCLUDE BOTH SIGNS OF CHARGE

FIG. 16

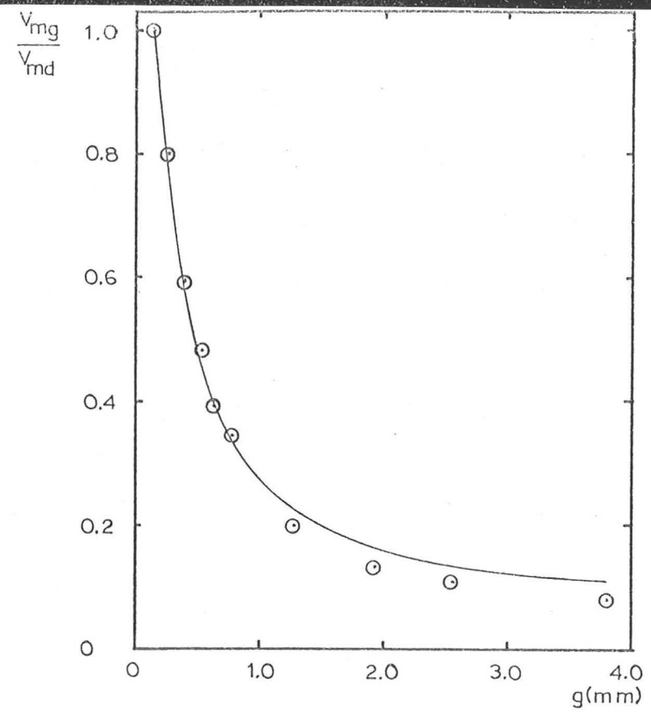

—⊙—3mm THICK
POLYPROPYLENE A

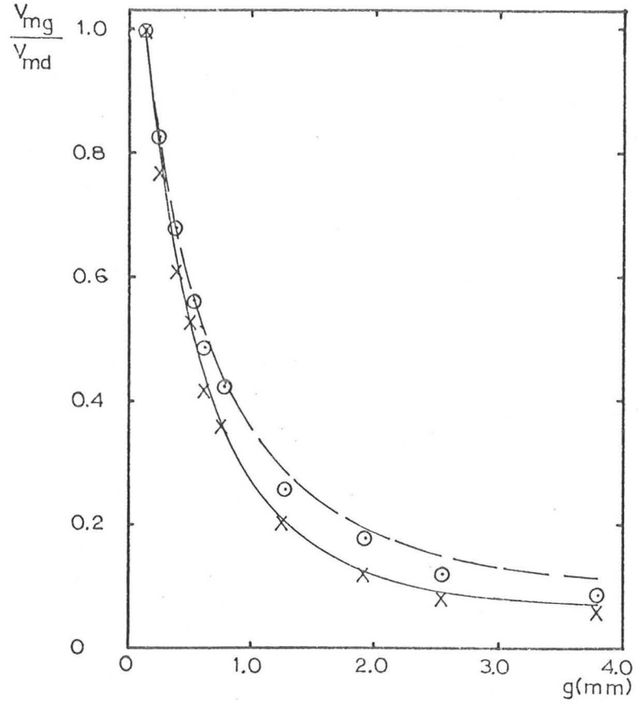

—X—3mm THICK
POLYETHYLENE B

—⊙—3mm THICK
POLYETHYLENE C

FIG. 17 CALIBRATION OF THE INDUCTION PROBE FOR FINITE CHARGE WIDTHS. THE SOLID AND BROKEN LINES SHOW THE CURVE-FITTED THEORETICAL CALCULATIONS. THE POINTS ARE EXPERIMENTAL VALUES. THE CODE LETTERS REFER TO TABLE 4.

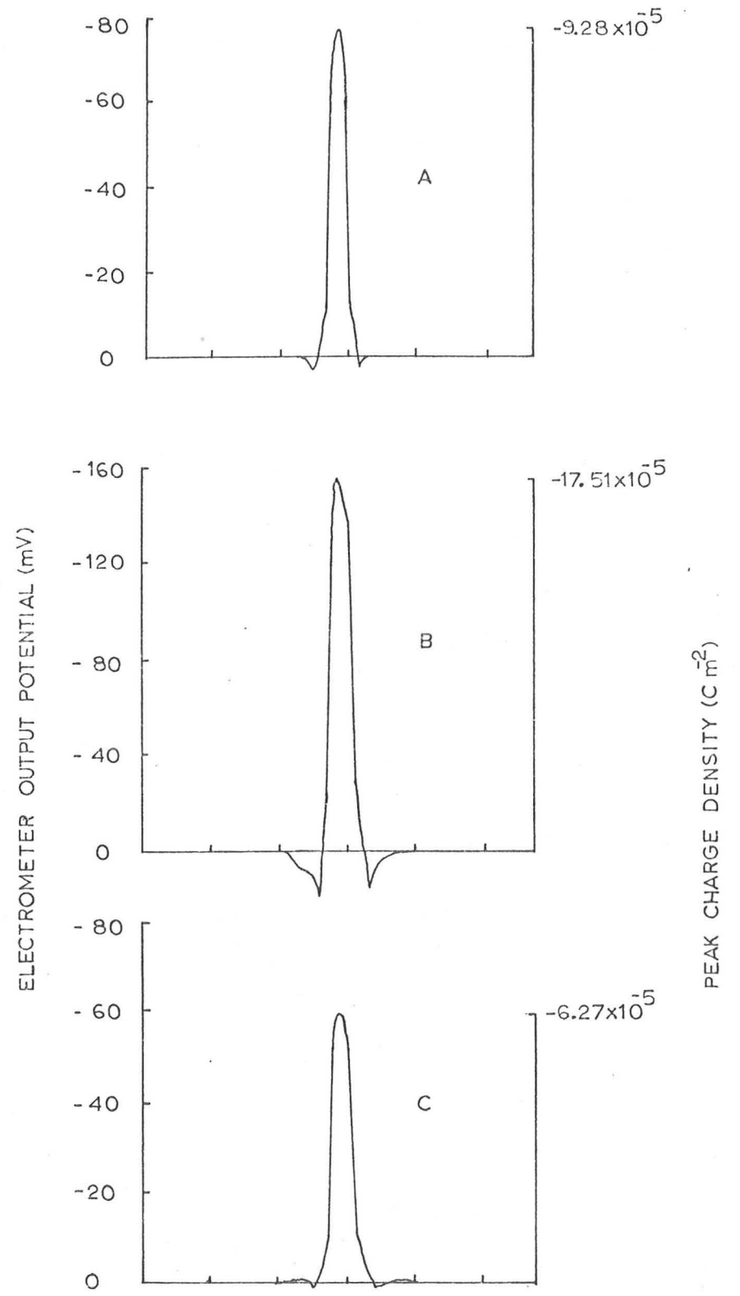

THE ABSCISSA SHOWS DISTANCE ALONG THE POLYMER SURFACE IN 5mm LENGTHS.
g = 0.127mm

FIG. 18 CHARGE DISTRIBUTIONS CORRESPONDING TO THE MATERIALS IN TABLE 4

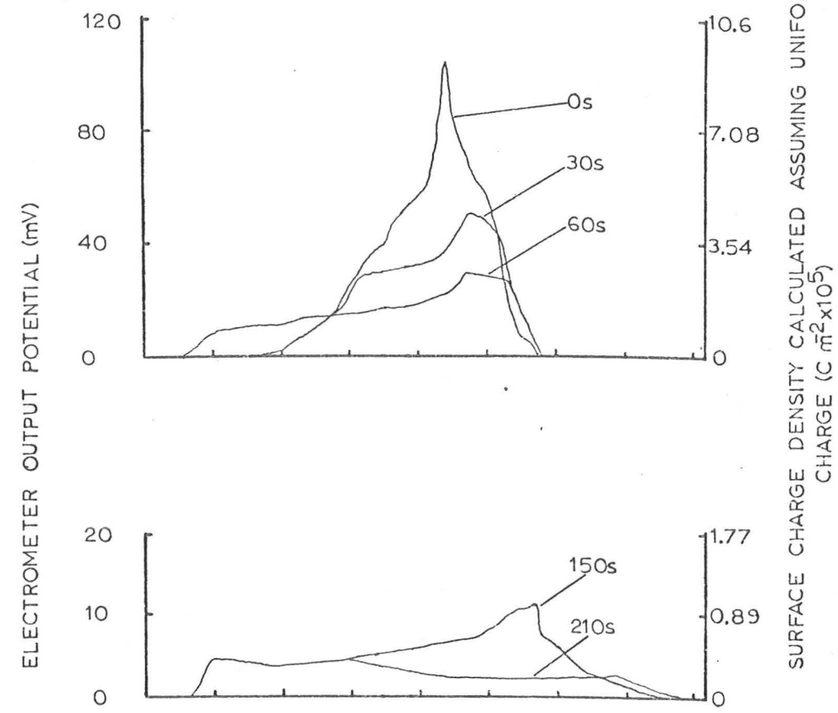

THE CHARGE LEVEL WAS BELOW THE INSTRUMENT SENSITIVITY AFTER 390s

THE IONISATION GAUGE WAS ACTIVATED AT t=0

THE ABSCISSA SHOWS DISTANCE ALONG THE POLYMER SURFACE IN 5mm LENGTHS

CONTACT SPHERE:-19.1mm DIAMETER ALUMINIUM

DIELECTRIC:-3mm THICK PMMA

ROLLING CONTACT NORMAL FORCE:-9.1N

GAS PRESSURE BELOW 10^{-4} TORR

g= 0.127 mm

FIG. 19 CHARGE DECAY CAUSED BY THE IONISATION PRESSURE MEASUREMENT GAUGE

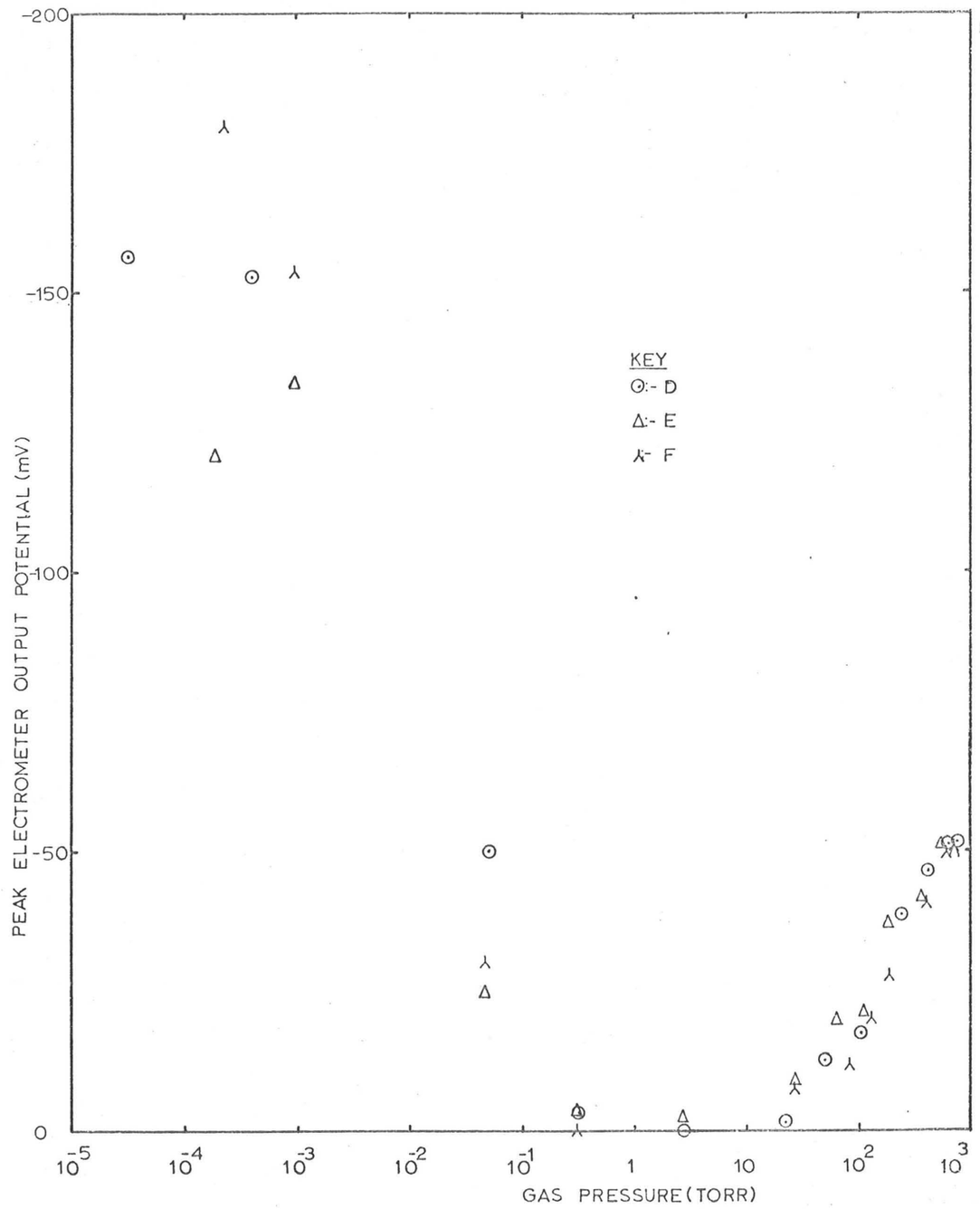

g= 0.127 mm

FIG. 20 THE INFLUENCE OF GAS PRESSURE ON THE PEAK ELECTROMETER OUTPUT POTENTIAL CORRESPONDING TO THE PEAK CHARGE REGION (THE CODE LETTERS REFER TO TABLE 6)

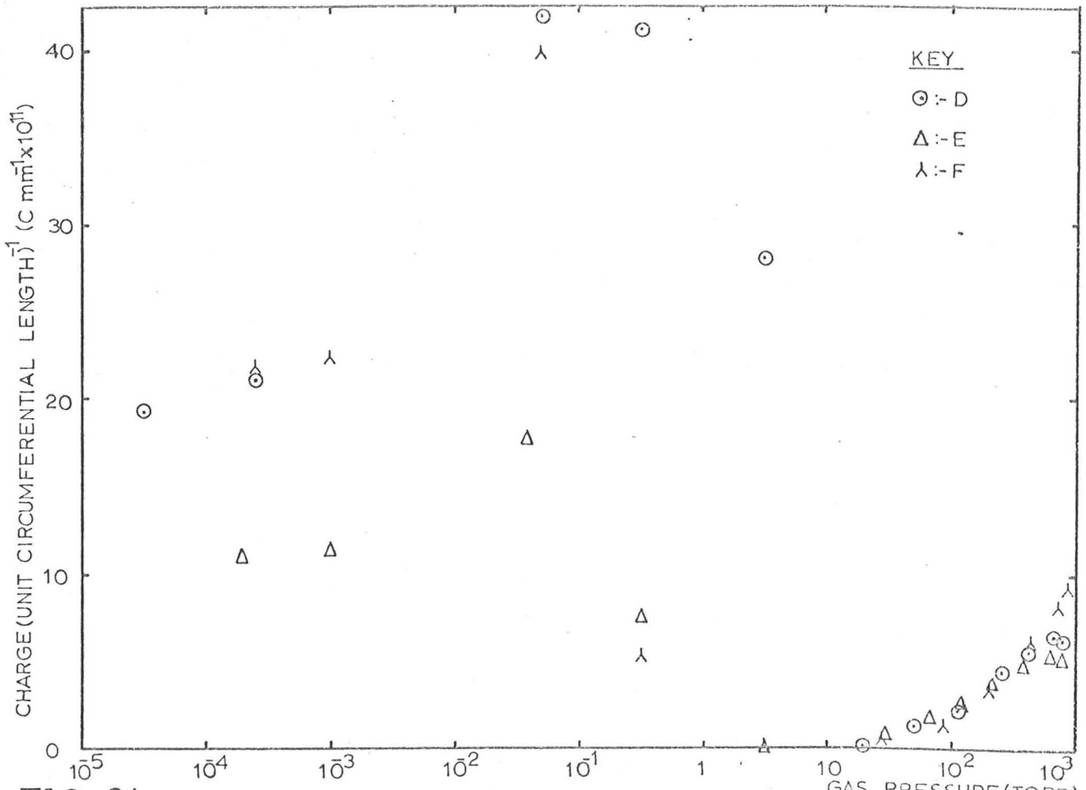

FIG. 21 THE INFLUENCE OF GAS PRESSURE ON THE SPHERE CHARGE (UNIT CIRCUMFERENTIAL LENGTH)$^{-1}$ AFTER 6 TURNTABLE REVOLUTIONS (THE CODE LETTERS REFER TO TABLE 6)

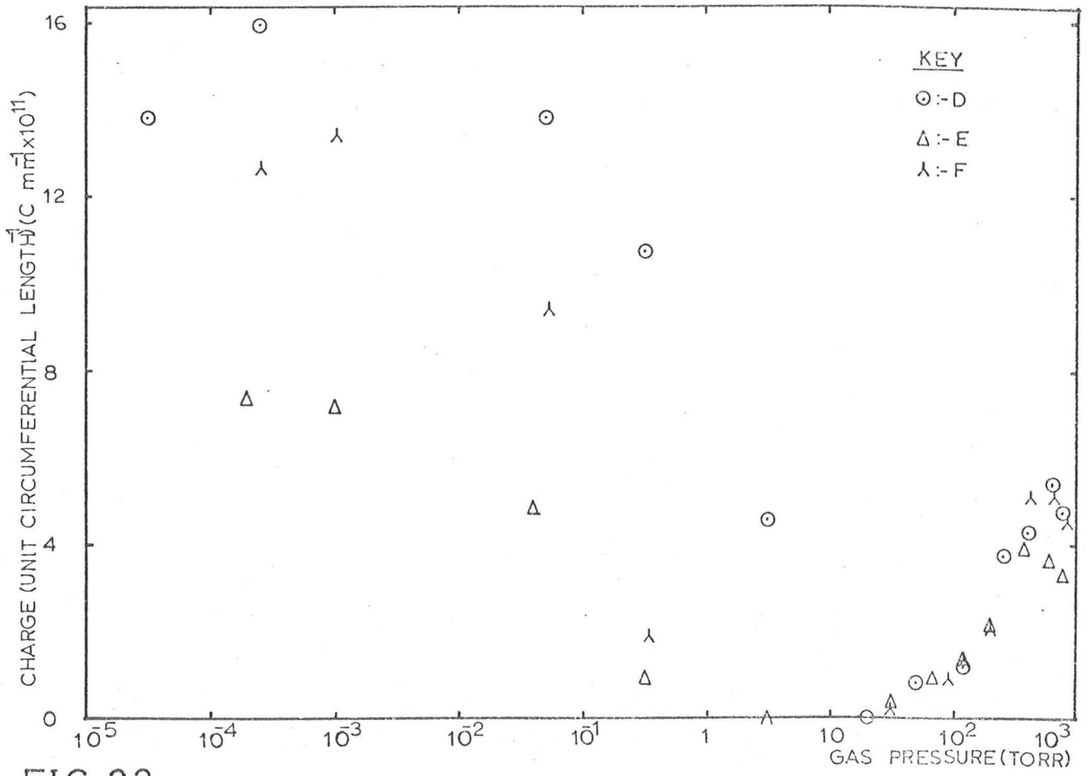

FIG. 22 THE INFLUENCE OF GAS PRESSURE ON THE SPHERE CHARGE (UNIT CIRCUMFERENTIAL LENGTH)$^{-1}$ AFTER 1 TURNTABLE REVOLUTION (THE CODE LETTERS REFER TO TABLE 6)

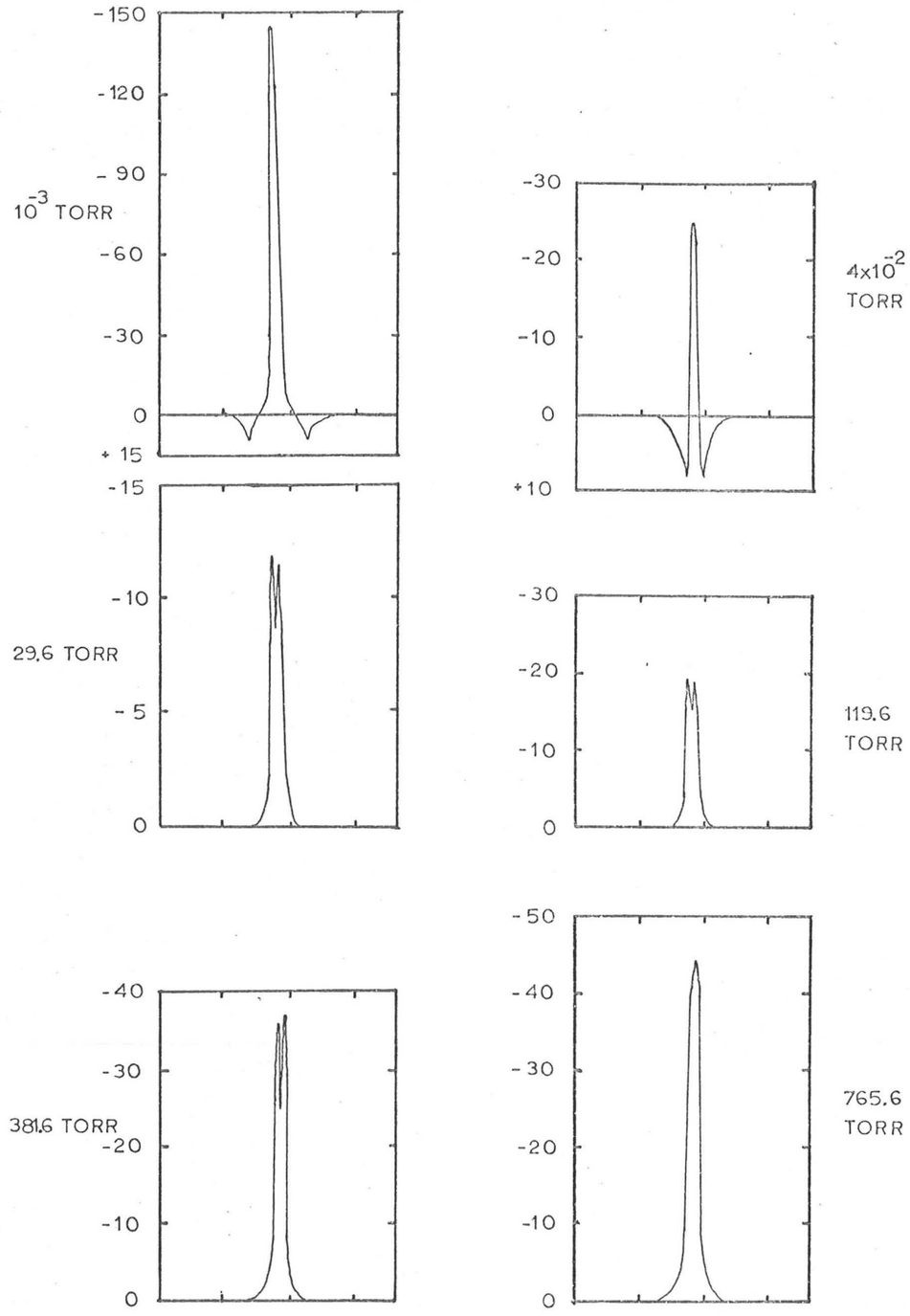

THE ABSCISSA SHOWS DISTANCE ALONG THE POLYMER SURFACE IN 5 mm LENGTHS

THE ORDINATE SHOWS THE ELECTROMETER OUTPUT POTENTIAL (mV). 1mV OF THE PEAK POTENTIAL $=1.2 \times 10^{6}$ C m^{-2} SURFACE CHARGE DENSITY FOR k=0.36.
g= 0.127 mm

FIG. 23 RADIAL CHARGE SCANS AT VARIOUS GAS PRESSURES FOR SAMPLE E IN TABLE 6

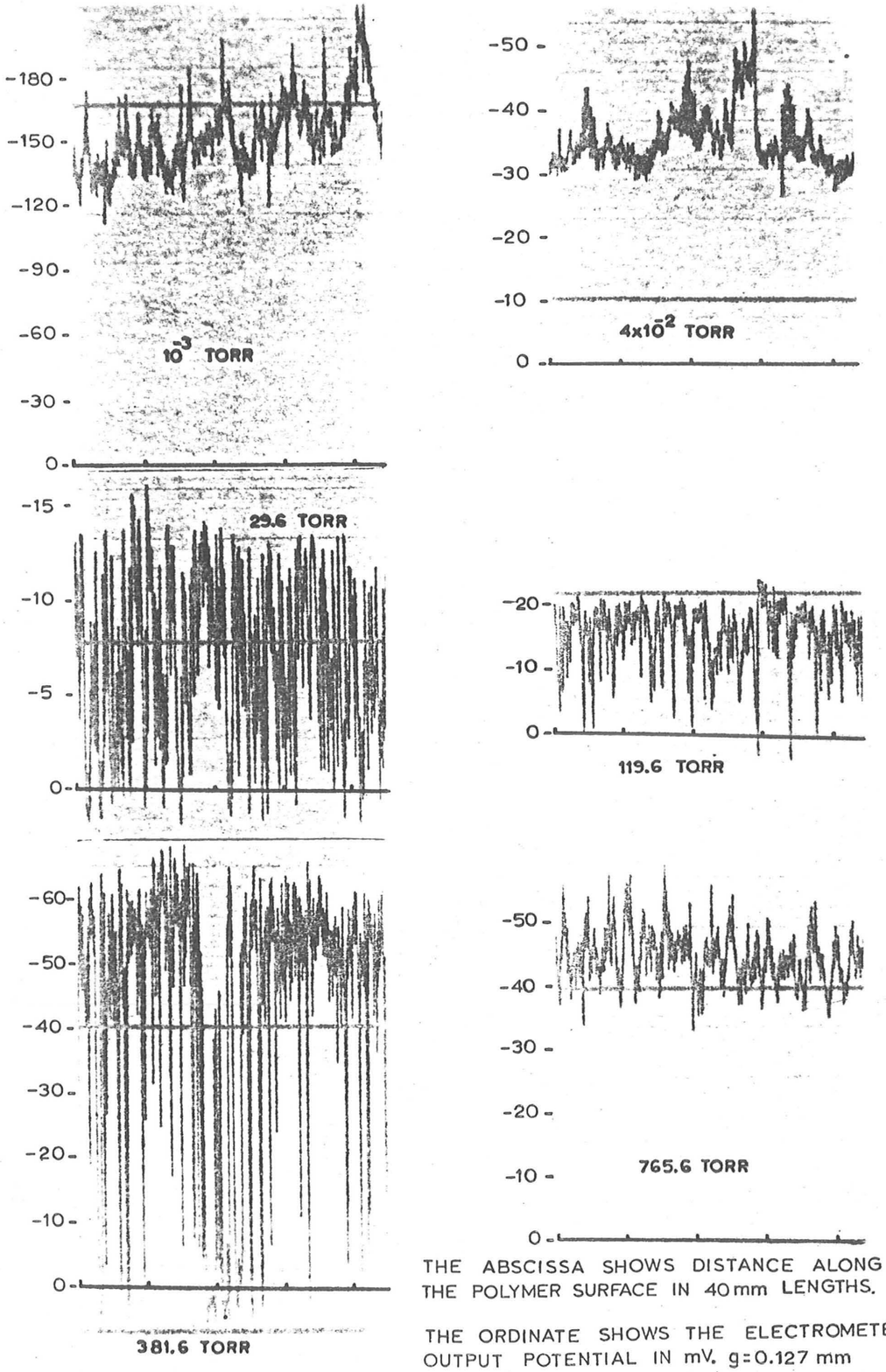

THE ABSCISSA SHOWS DISTANCE ALONG THE POLYMER SURFACE IN 40 mm LENGTHS.

THE ORDINATE SHOWS THE ELECTROMETER OUTPUT POTENTIAL IN mV. g=0.127 mm

FIG. 24 CIRCULAR CHARGE SCANS AT VARIOUS GAS PRESSURES FOR SAMPLE E IN TABLE 6

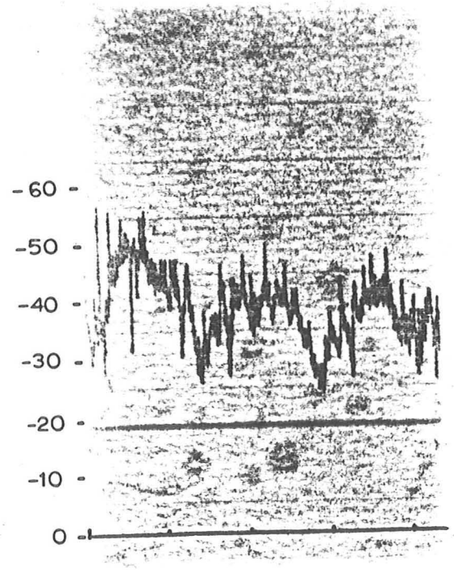

D

F

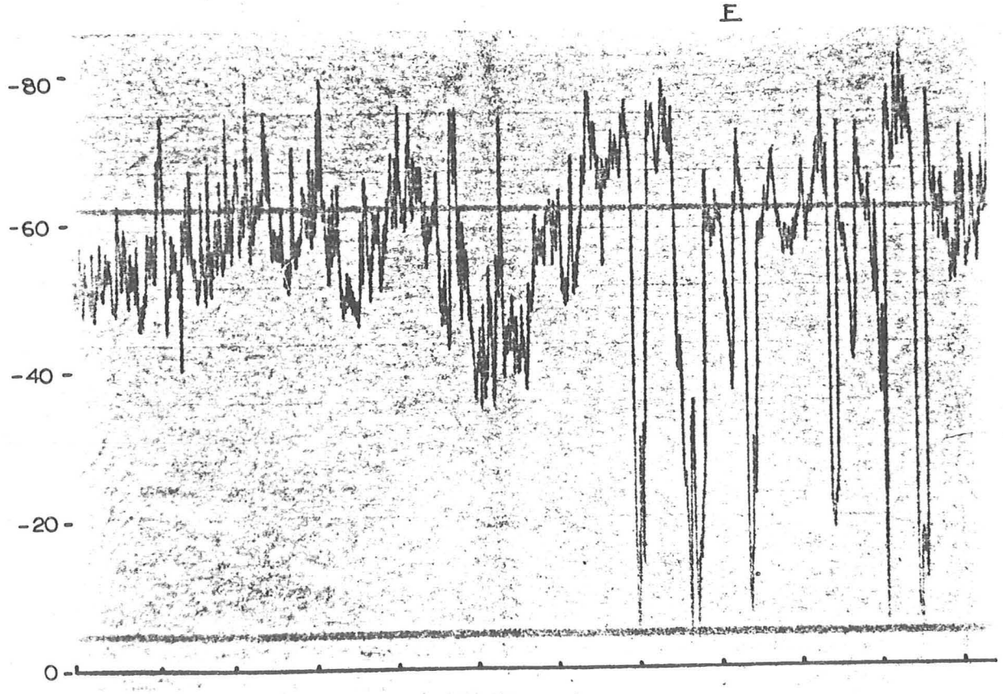

THE ABSCISSA SHOWS DISTANCE ALONG THE POLYMER SURFACE IN 40 mm LENGTHS.

THE ORDINATE SHOWS THE ELECTROMETER OUTPUT POTENTIAL IN mV.
g = 0.127 mm

FIG. 25 CIRCULAR CHARGE SCANS FOR MATERIALS D AND F OF TABLE 6, AT ATMOSPHERIC PRESSURE

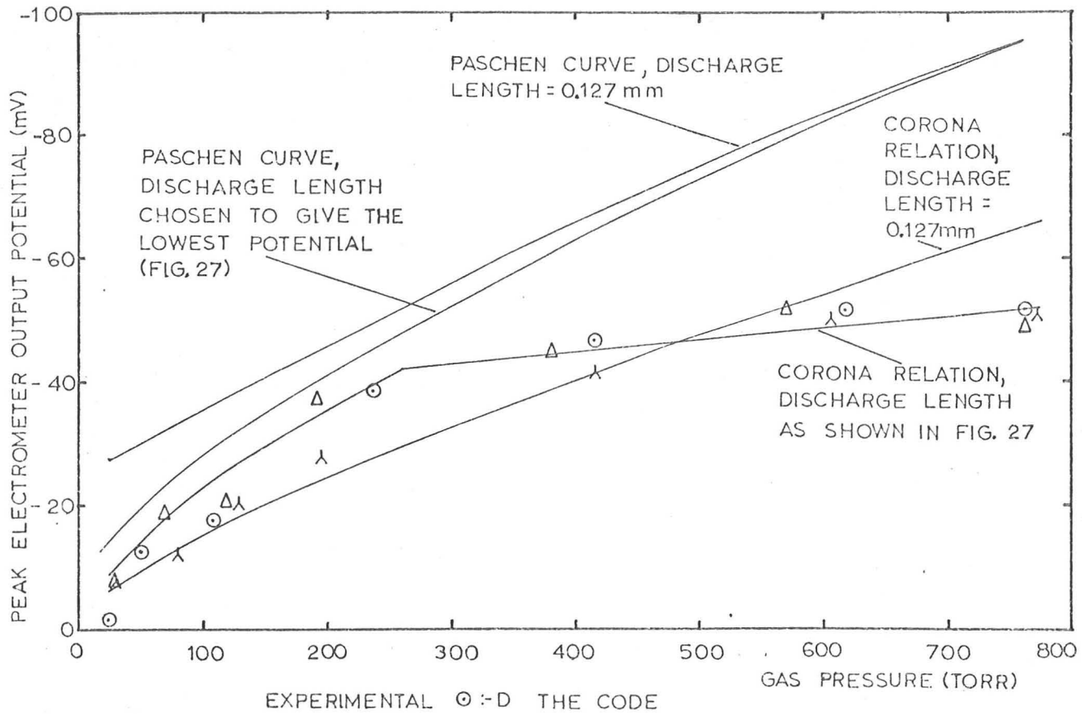

FOR POLYPROPYLENE $\sigma = 1.16 \times 10^{-3} V_{mg}$ C m^{-2} (k = 0.5).

g = 0.127mm

FIG. 26 COMPARISON BETWEEN THE PREDICTED AND OBSERVED PEAK ELECTROMETER OUTPUT POTENTIAL AS A FUNCTION OF GAS PRESSURE

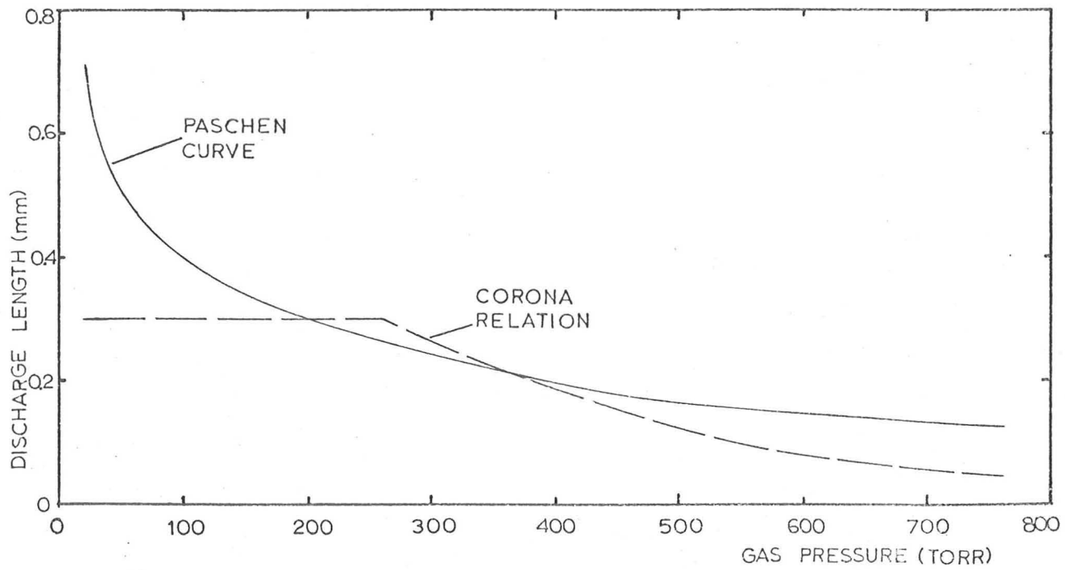

FIG. 27 ESTIMATED DISCHARGE LENGTH FROM THE CORONA RELATION AND PASCHEN CURVE, AS A FUNCTION OF GAS PRESSURE

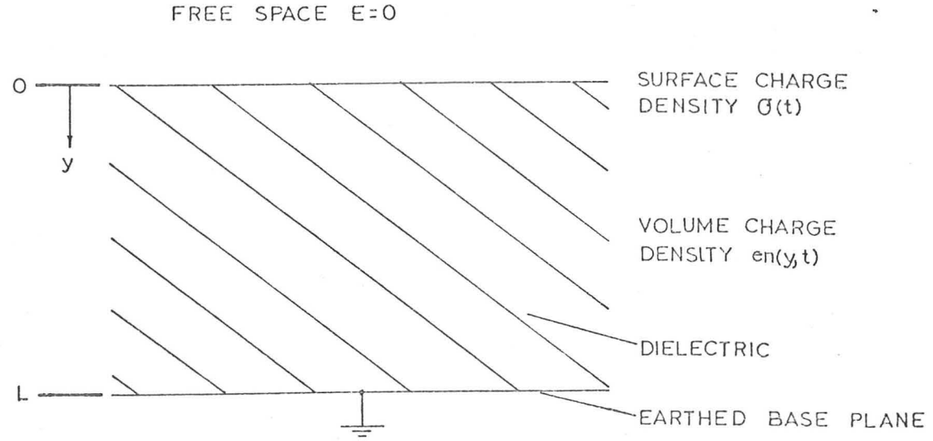

a. PHYSICAL ARRANGEMENT FOR THE CHARGE DECAY ANALYSIS PROPOSED BY WINTLE[91]

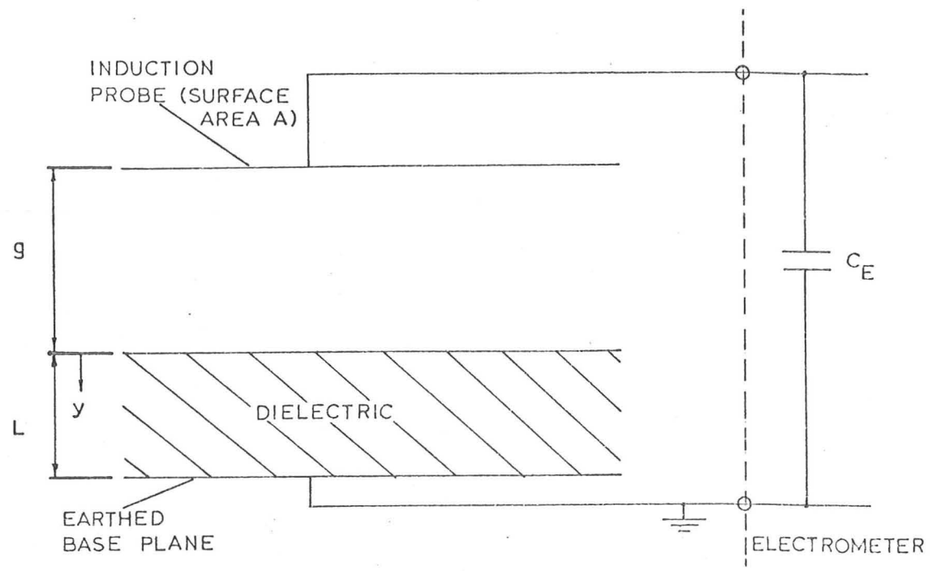

b. PHYSICAL ARRANGEMENT FOR VOLUME CHARGE MEASUREMENT ANALYSED BY WINTLE[116]

FIG. 28

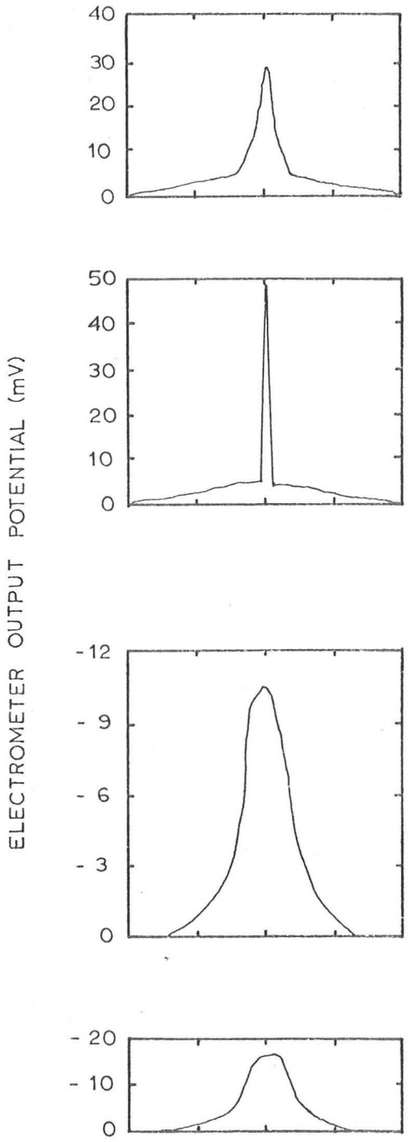

NYLON 66 G
90s AFTER CONTACT WAS TERMINATED

NYLON 66 H
120s AFTER CONTACT WAS TERMINATED

VITON® I
120s AFTER CONTACT WAS TERMINATED

VITON® J
75s AFTER CONTACT WAS TERMINATED

THE ABSCISSA SHOWS DISTANCE ALONG THE POLYMER SURFACE IN 5mm LENGTHS

g= 0.127 mm , L=3mm

FIG. 29 RADIAL CHARGE SCANS DURING THE CHARGE DECAY MEASUREMENTS. THE CODE LETTERS REFER TO TABLE 7

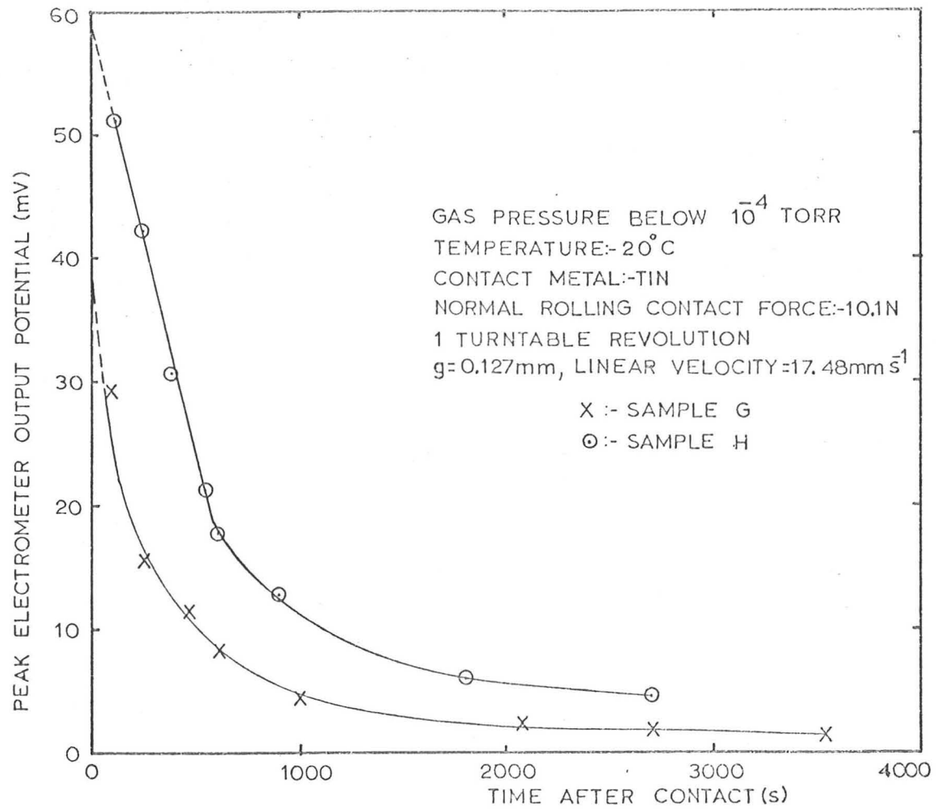

a. NYLON 66

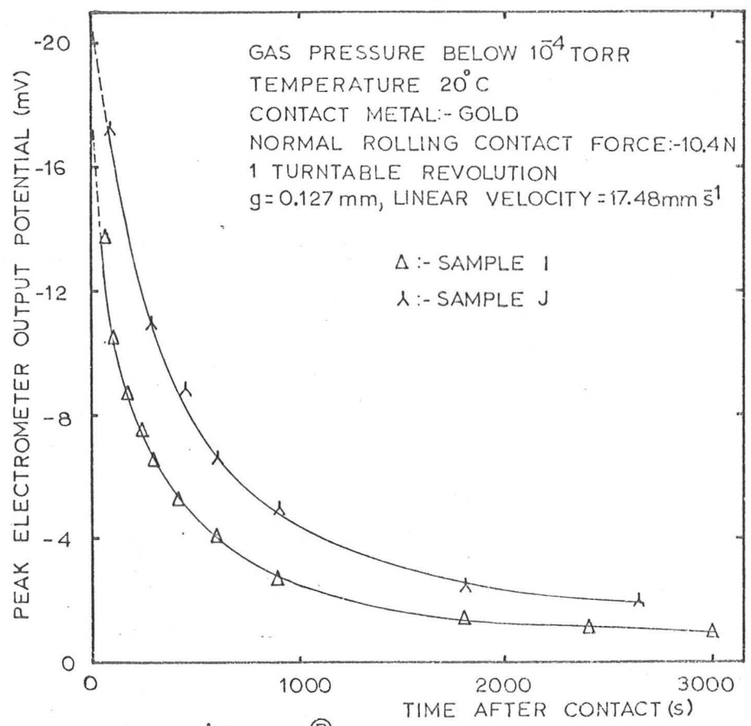

b. VITON®

FIG. 30 CHARGE DECAY ON NYLON 66 AND VITON®. THE CODE LETTERS REFER TO TABLE 7

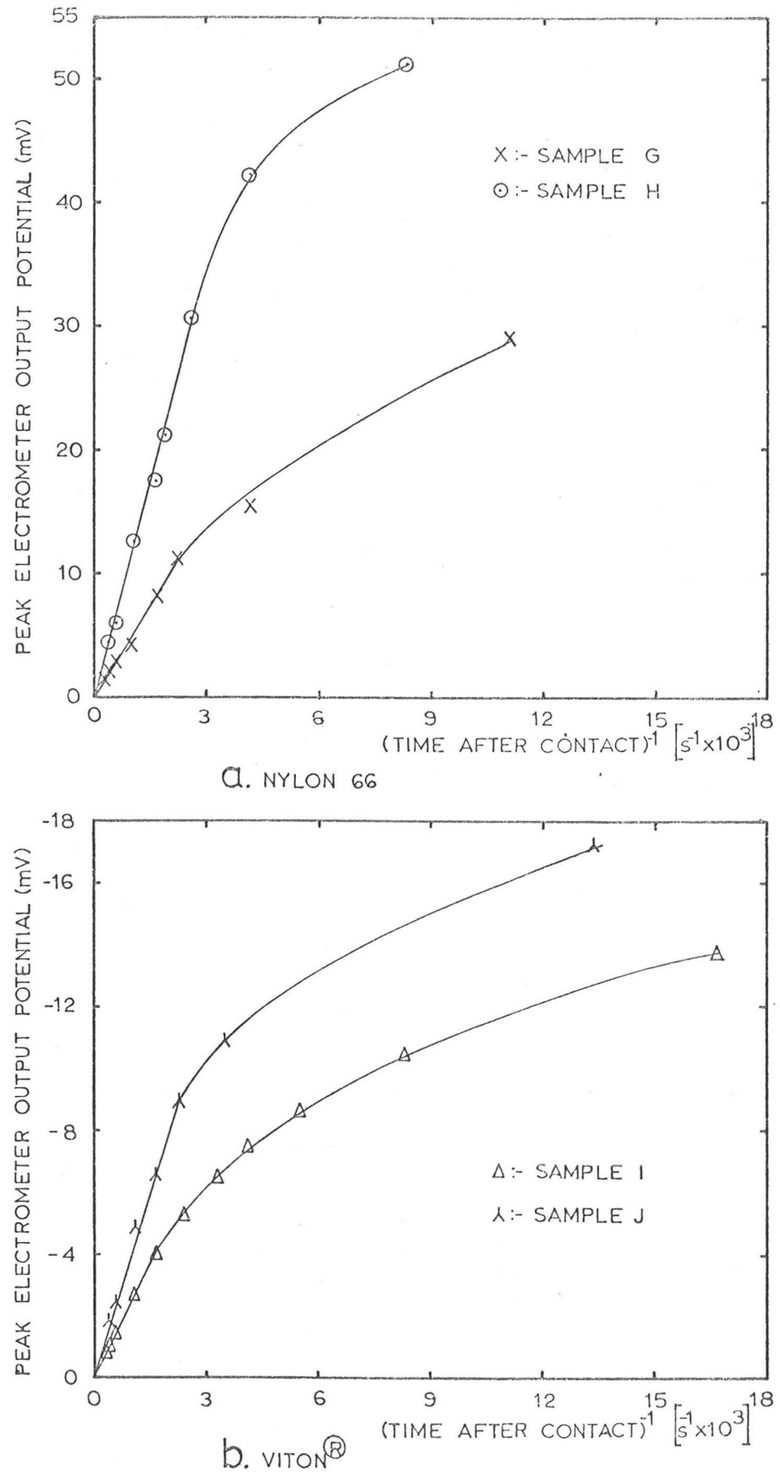

FIG. 31 THE PEAK ELECTROMETER POTENTIAL PLOTTED AGAINST THE RECIPROCAL OF TIME, FOR NYLON 66 AND VITON®. THE RESULTS ARE THOSE OF FIG.30 AND THE CODE LETTERS REFER TO TABLE 7

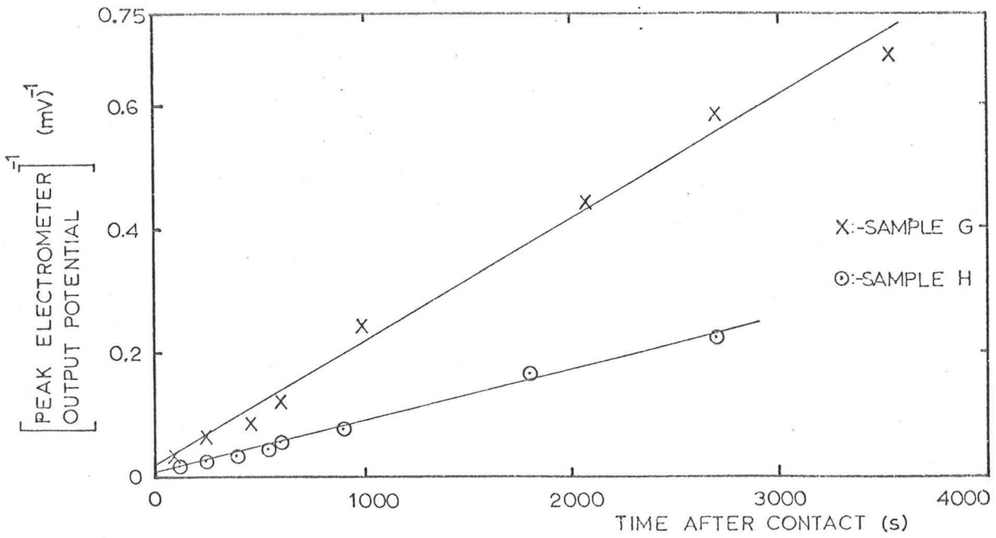

a. NYLON 66

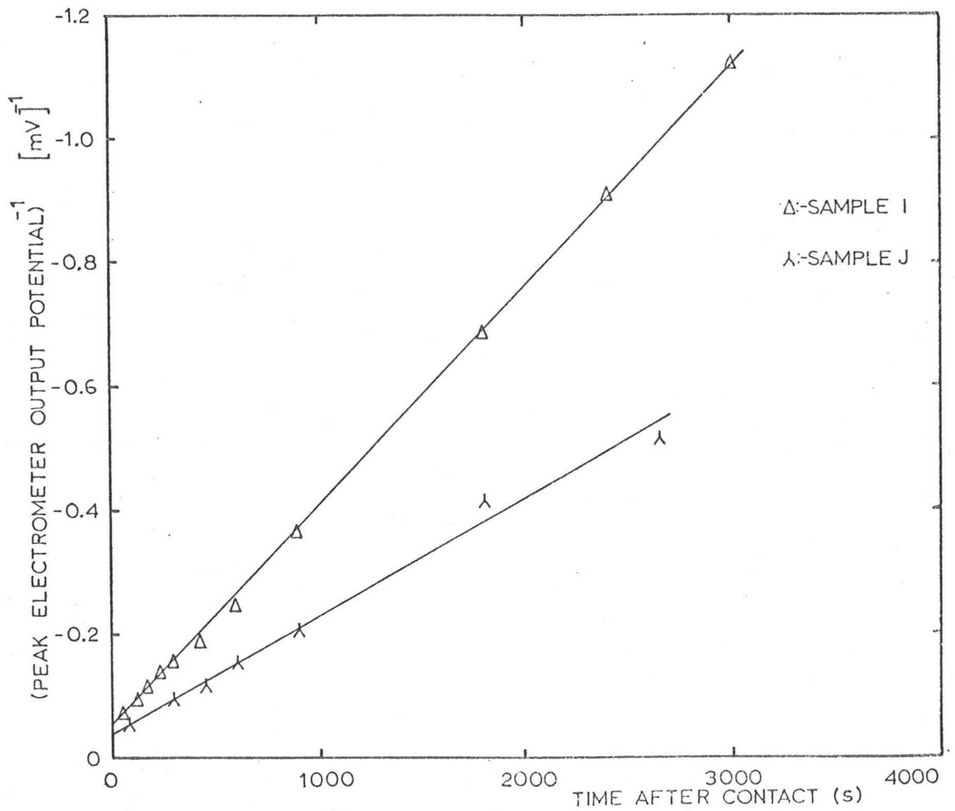

b. VITON®

FIG. 32 THE RECIPROCAL OF THE PEAK ELECTROMETER POTENTIAL PLOTTED AGAINST TIME, FOR NYLON 66 AND VITON®. THE RESULTS ARE THOSE OF FIG. 30 AND THE CODE LETTERS REFER TO TABLE 7

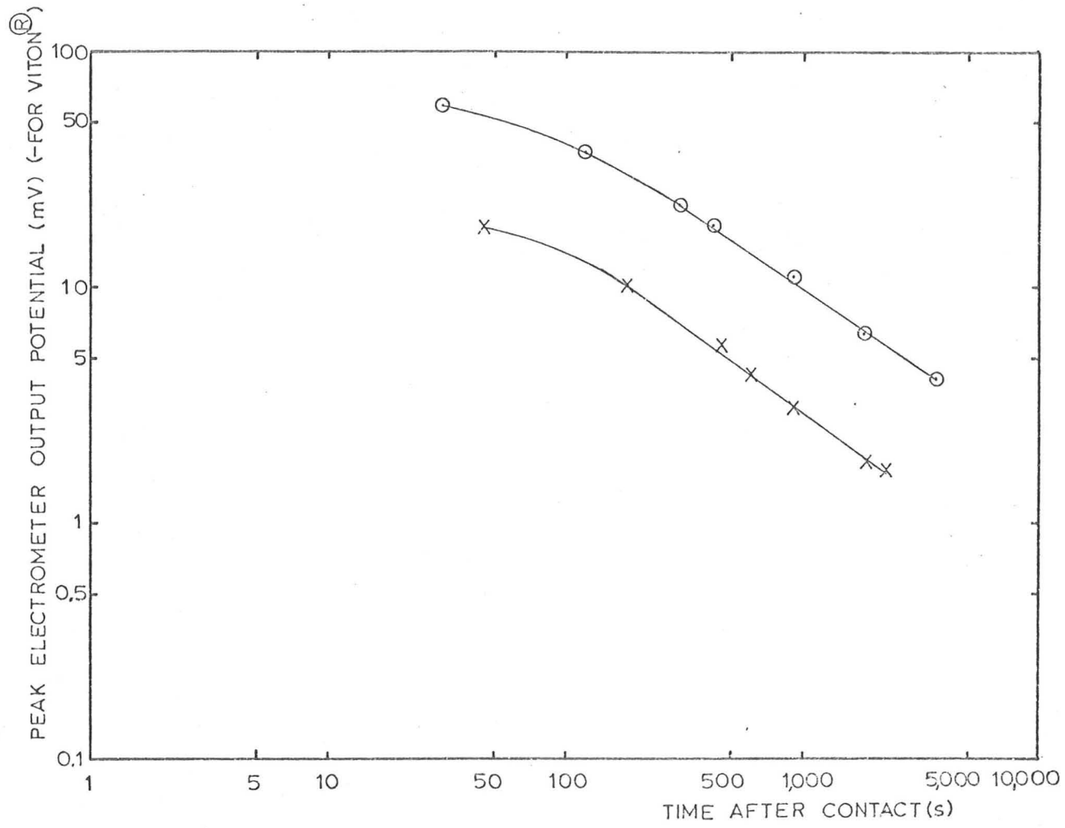

TIME AFTER CONTACT(s)

THE CONTACT CONDITIONS WERE AS FOLLOWS:-

EXPTL. POINTS	MATERIAL	ROLLING CONTACT NORMAL FORCE(N)	CONTACT METAL	LINEAR VELOCITY (mm s^{-1})	CIRCULAR SPEED (R.P.M.)	No. OF TURNTABLE REVOLUTIONS	SIGN OF CHARGE
⊙	NYLON 66	9.9	ALUMINIUM	17.48	5.56	6	+
X	VITON®	10.4	GOLD	17.48	5.56	9	−

FIG. 33 CHARGE DECAY ON NYLON 66 AND VITON® AFTER SEVERAL TURNTABLE REVOLUTIONS

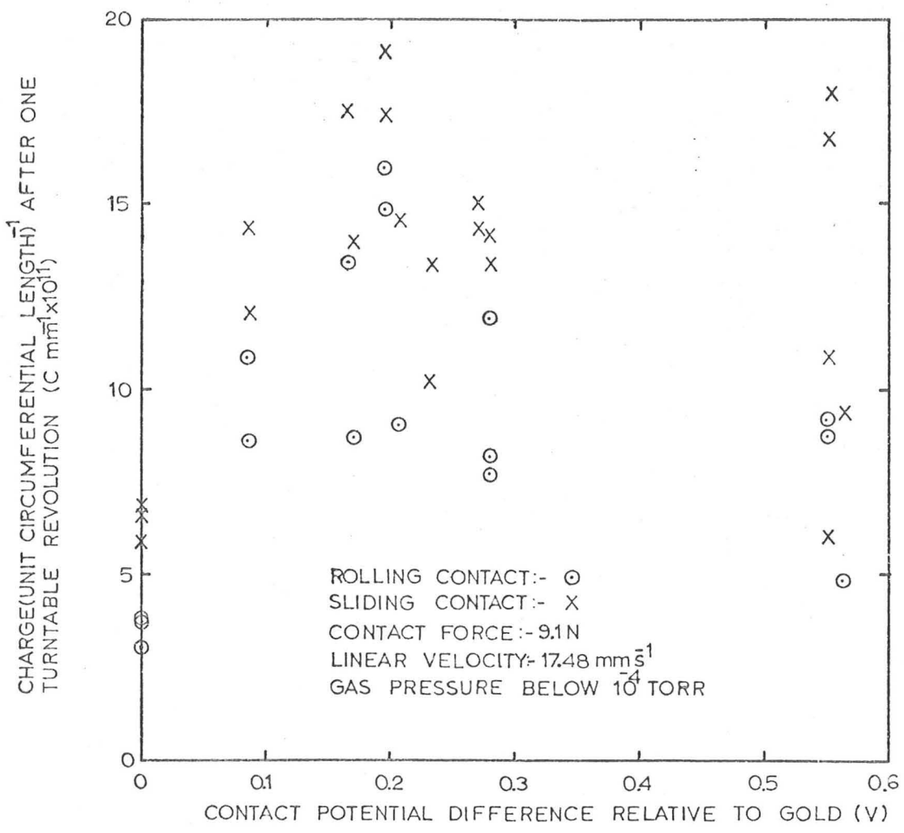

FIG. 34 THE CHARGE TRANSFERRED TO 19.1 mm DIAMETER CONTACT SPHERES PLOTTED AGAINST METAL CONTACT POTENTIAL DIFFERENCE. 3mm THICK POLYPROPYLENE DIELECTRIC

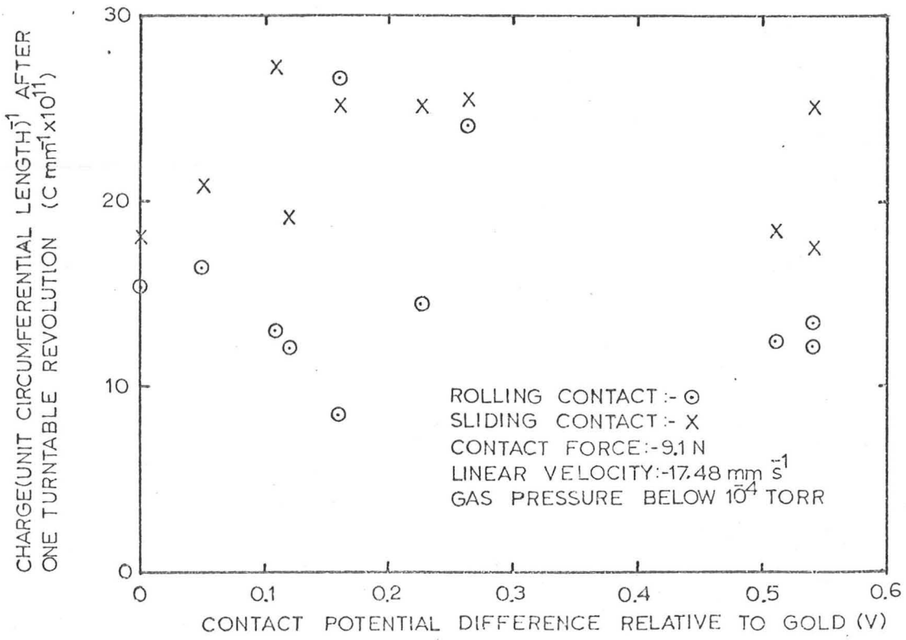

FIG. 35 THE CHARGE TRANSFERRED TO 19.1 mm DIAMETER CONTACT SPHERES PLOTTED AGAINST METAL CONTACT POTENTIAL DIFFERENCE. 3mm THICK POLYETHYLENE (L.D.) DIELECTRIC

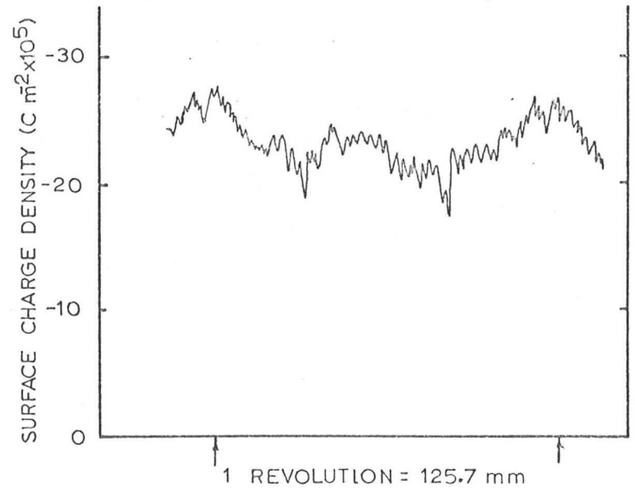

DIELECTRIC:-3mm THICK POLYPROPYLENE
CONTACT METAL:-19.1 mm DIAMETER BRASS SPHERE
SLIDING CONTACT NORMAL FORCE :-9.1 N
LINEAR VELOCITY DURING CONTACT AND SCANNING :-17.48 mm s^{-1}
GAS PRESSURE BELOW 10^{-4} TORR
g=0.127 mm

FIG. 36 A TYPICAL CIRCULAR CHARGE SCAN

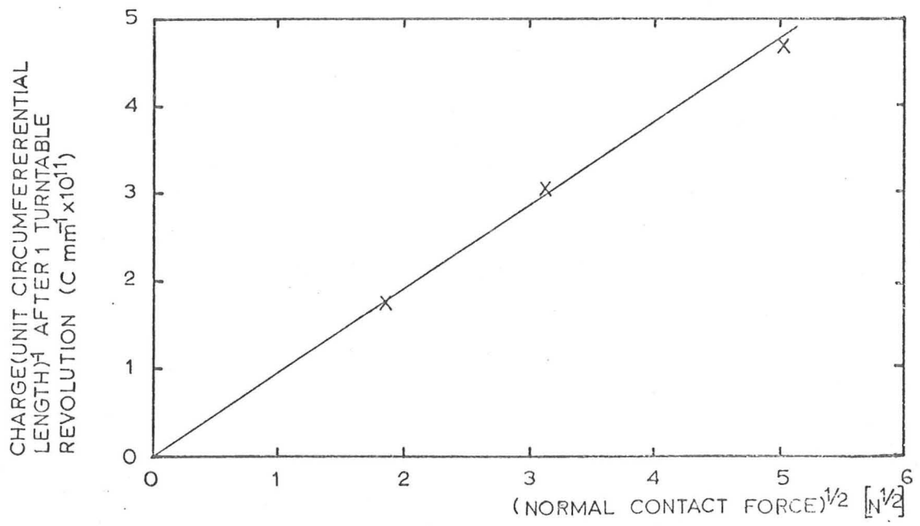

GAS PRESSURE BELOW 10^{-4} TORR
LINEAR VELOCITY :-17.48 mm s^{-1}

FIG. 37 THE CHARGE TRANSFERRED TO A 19.1 mm DIAMETER GOLD CONTACT SPHERE, AFTER ROLLING CONTACT WITH A 3mm THICK POLYPROPYLENE DIELECTRIC, PLOTTED AGAINST THE SQUARE ROOT OF THE NORMAL CONTACT FORCE

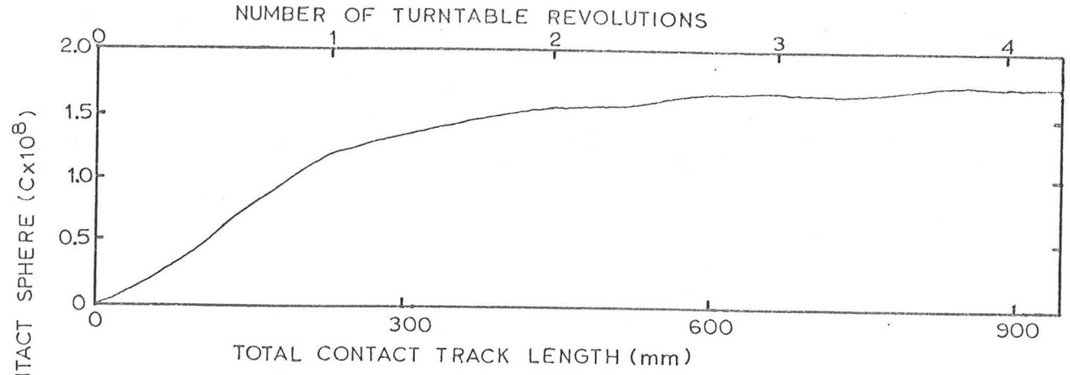

a. POLYETHYLENE(L.D.) DIELECTRIC

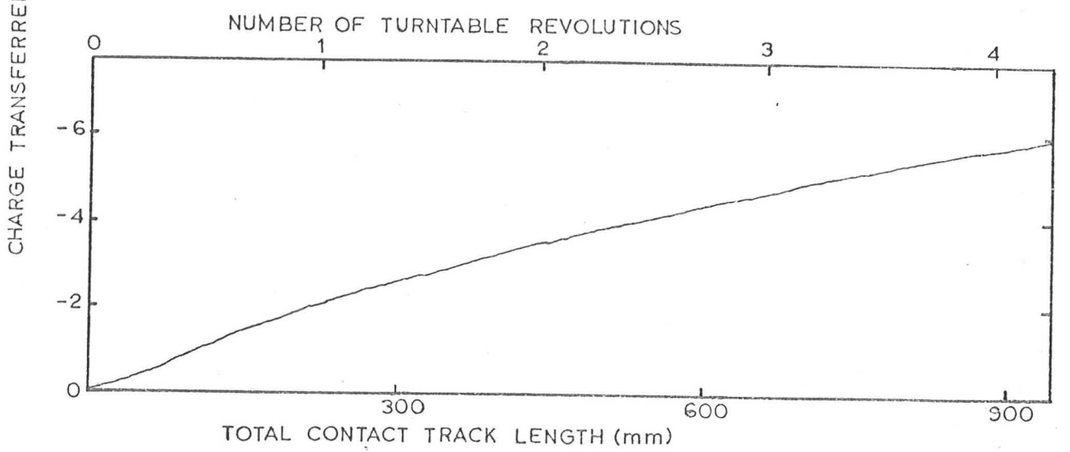

b. NYLON 66 DIELECTRIC

THE CONTACT CONDITIONS FOR BOTH POLYETHYLENE AND NYLON 66 WERE AS FOLLOWS:-

ROLLING CONTACT NORMAL FORCE :- 9.9 N
3mm THICK DIELECTRIC SPECIMEN
GAS PRESSURE BELOW 10^{-4} TORR
CONTACT METAL:- ALUMINIUM
LINEAR VELOCITY:- 36.7 mm s^{-1}

FIG. 38 THE CHARGE TRANSFERRED TO THE CONTACT SPHERE PLOTTED AGAINST THE TOTAL TRACK LENGTH

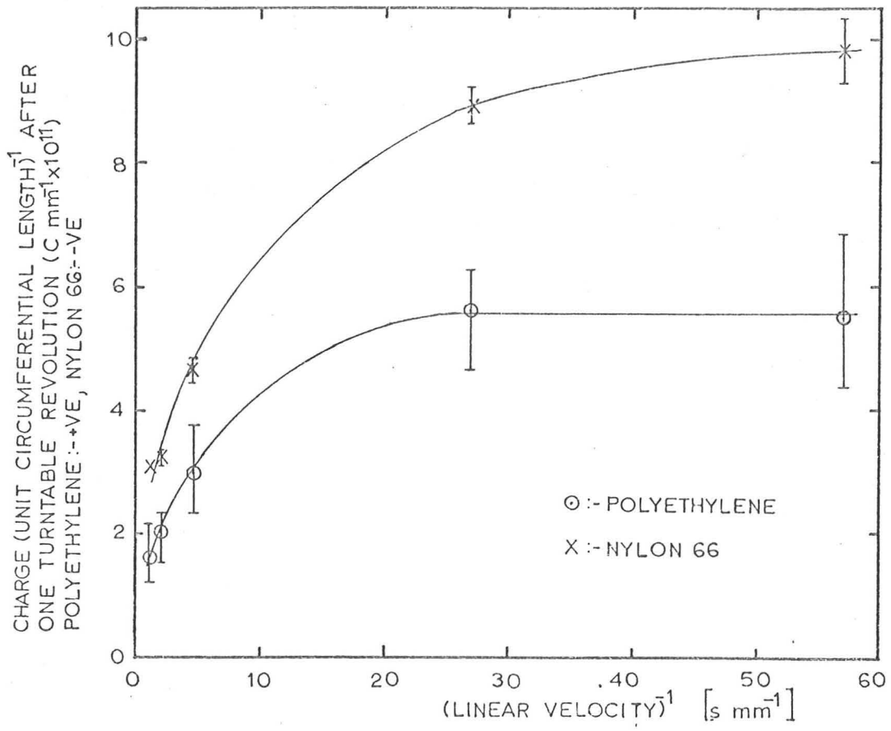

a. THE CHARGE TRANSFERRED PLOTTED AGAINST THE RECIPROCAL OF THE LINEAR VELOCITY

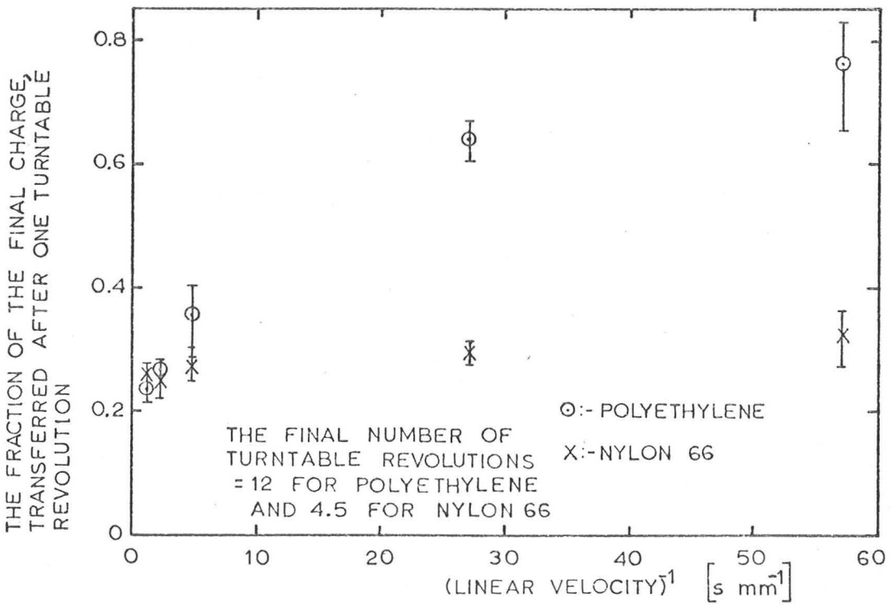

b. THE FRACTION OF THE FINAL CHARGE, TRANSFERRED AFTER ONE TURNTABLE REVOLUTION, PLOTTED AGAINST THE RECIPROCAL OF THE LINEAR VELOCITY

ALL CONTACT CONDITIONS EXCEPT FOR THE LINEAR VELOCITY ARE AS IN FIG. 38

FIG. 39

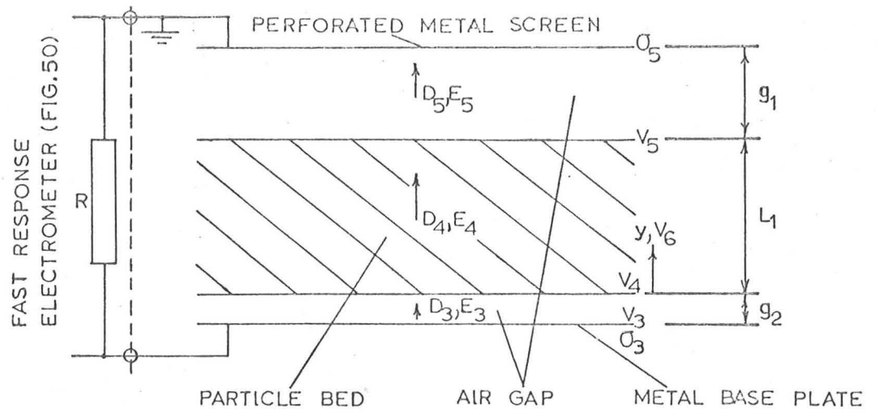

THE LENGTH $g_1 + g_2 + L_1$ REMAINS CONSTANT

FIG. 40 MEASUREMENT SYSTEM AND GEOMETRY FOR MEASUREMENT OF THE POTENTIAL INDUCED BY VIBRATED BED MOVEMENT

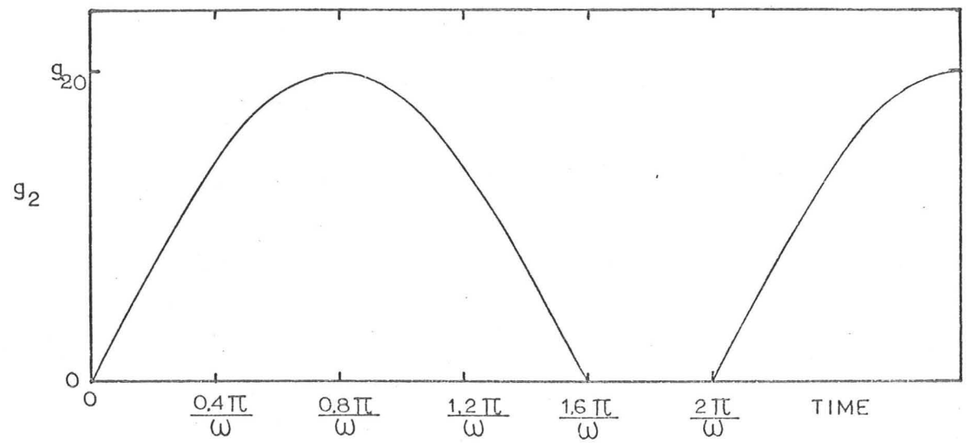

FIG. 41 THE ASSUMED AIR GAP WIDTH AT THE LOWER BED SURFACE AS A FUNCTION OF TIME, WITH $\beta = 0.8$

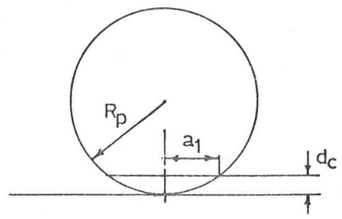

BY THE INTERSECTING CHORD THEOREM :-

$$(2R_p - d_c)d_c = a_1^2$$

THUS FOR $d_c \ll R_p$

$$A_c = \pi a_1^2 = 2\pi R_p d_c$$

FIG. 42 AREA OF THE EQUIVALENT PARALLEL PLATE CAPACITOR FOR CHARGE TRANSFER TO A PARTICLE

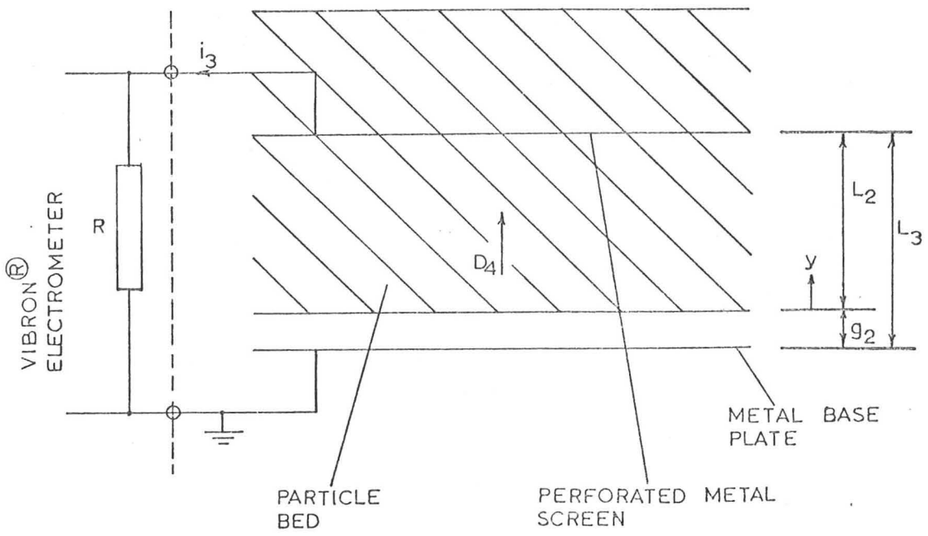

THE LENGTH $L_2 + g_2$ REMAINS CONSTANT

FIG. 43 MEASUREMENT SYSTEM AND GEOMETRY FOR MEASUREMENT OF THE CONDUCTION CURRENT

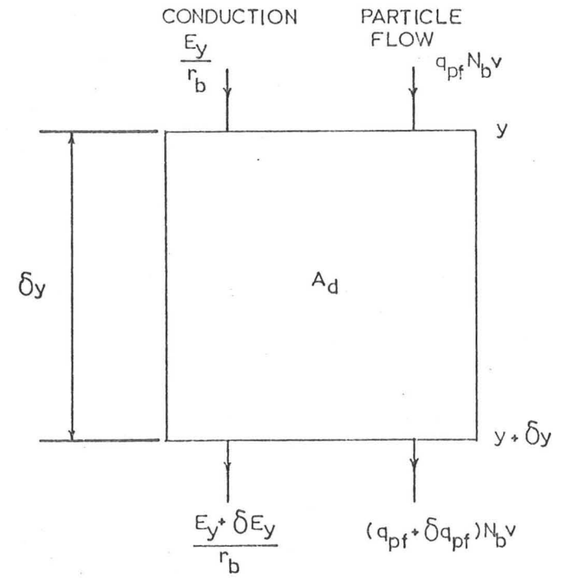

FIG. 44 DIFFERENTIAL CHARGE ELEMENT IN THE PARTICLE BED ADJACENT TO THE PERFORATED SCREEN

KEY FOR FIG. 45.

A:- Perforated screen support, 7.5mm thick perspex

B:- Perforated screen brass support rods x 2, 4BA, with an 8BA tapped hole in the lower end to allow attachment of the screen

C:- Perspex vessel, 9.5mm thick perspex walls

D:- Spring clamp outer support. Dural bar:- 9mm x 22mm x 188mm.

E:- Position sensing capacitor support rod, insulated from the capacitor plate

F:- Upper plate of position sensing capacitor, 37.5mm in diameter, 1.6mm thick

G:- Lower plate of position sensing capacitor, 50.8mm in diameter, 1.6mm thick

H:- Massive steel base

I:- Dural, spring support blocks. 73mm x 76mm x 6.4mm

J:- Spring steel leaf 38mm x 1.6mm in section

K:- Polythene capacitor disc support. 4mm thick

L:- Dural vessel base plate. 6mm thick

M:- Dural electrical screening 51mm x 1.6mm in section

N:- Wood support block

O:- Vibrator

P:- Dural connecting bar. 9mm x 22mm x 178mm

Q:- Steel vibrating table

R:- 6mm thick perspex block

S:- Dexion® support framework

T:- Particle bed

U:- Zinc coated metal perforated screen, 70mm x 19.4mm x 0.38mm, with perforations 2mm in diameter, 3mm apart, on a triangular pitch

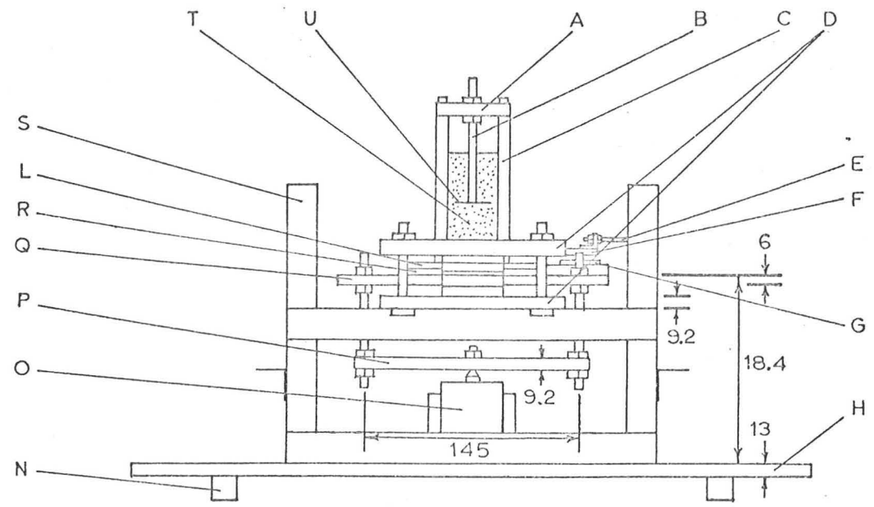

a. SIDE VIEW OF THE VIBRATION SYSTEM. THE ELECTRICAL SCREENING IS NOT SHOWN

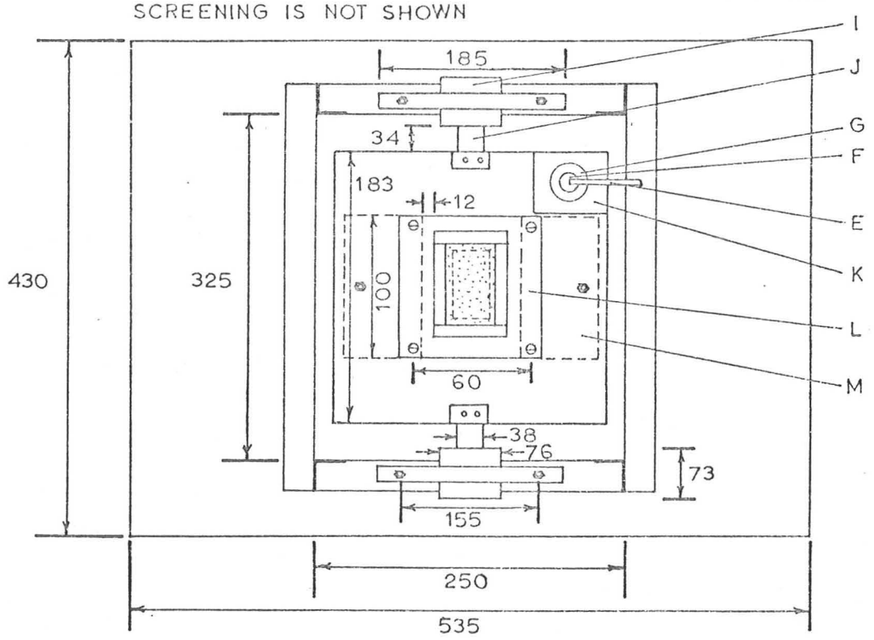

b. TOP VIEW OF THE VIBRATION SYSTEM. THE POSITIONS OF THE ELECTRICAL SCREENING AND THE PERFORATED SCREEN ARE SHOWN IN DOTTED OUTLINE

DIMENSIONS IN mm, NOT TO SCALE

FIG. 45 THE VIBRATION SYSTEM

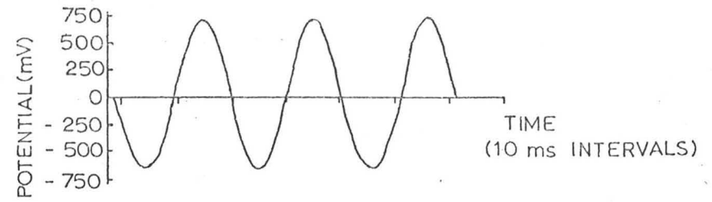

PEAK AMPLITUDE = 0.404 mm, VIBRATIONAL FREQUENCY (f) = 48 Hz

FIG. 46 THE OUTPUT POTENTIAL FROM THE TABLE DISPLACEMENT MEASUREMENT SYSTEM

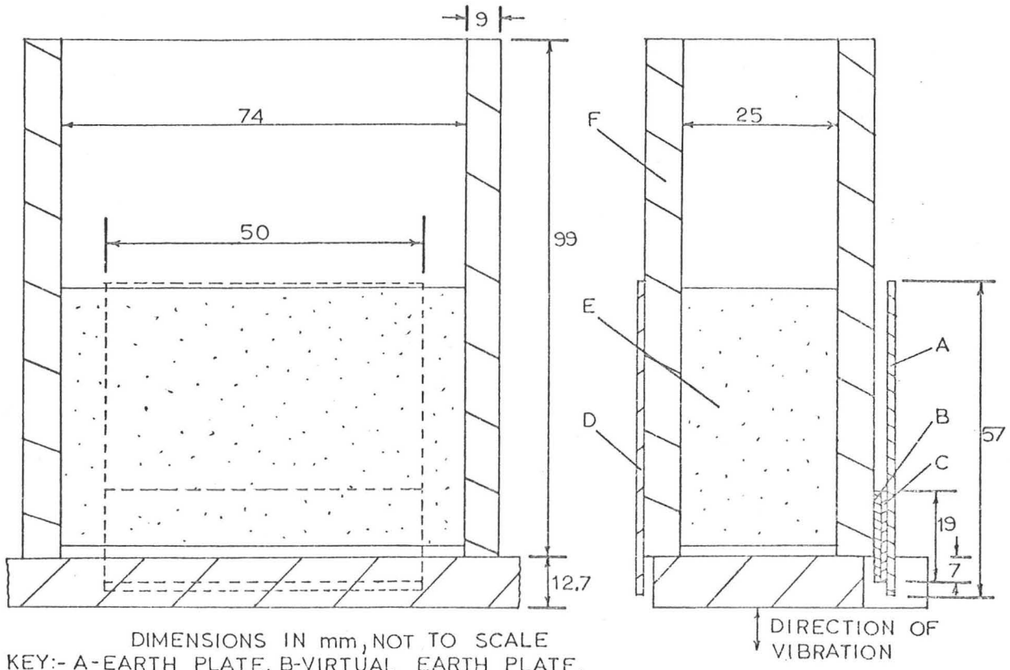

DIMENSIONS IN mm, NOT TO SCALE

KEY:- A-EARTH PLATE, B-VIRTUAL EARTH PLATE, C-PTFE INSULATION, D-PLATE MAINTAINED AT A POTENTIAL, E-PARTICLE BED, F-PERSPEX VESSEL

FIG. 47 SECTIONAL VIEW OF THE CAPACITANCE PLATE SYSTEM FOR VIBRATED BED POSITION MONITORING

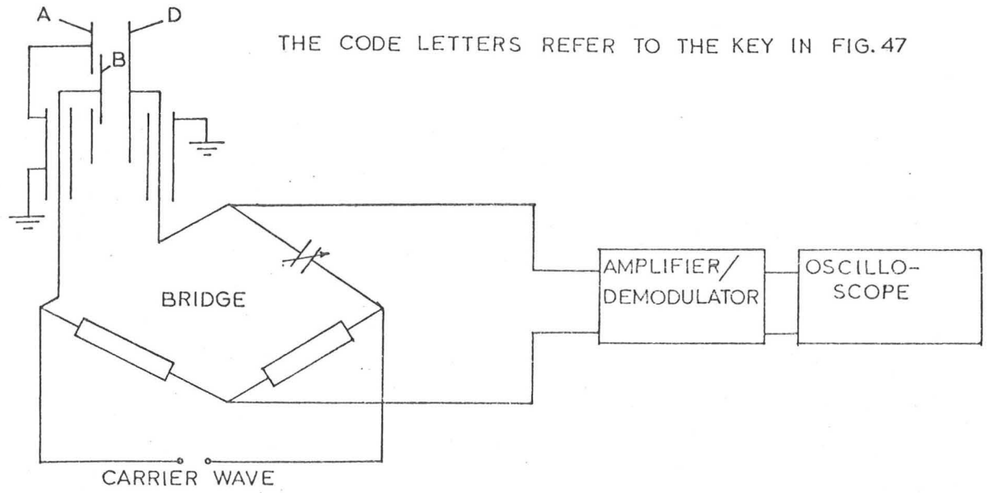

THE CODE LETTERS REFER TO THE KEY IN FIG. 47

FIG. 48 THE ELECTRONIC CIRCUIT FOR THE BED DISPLACEMENT MEASUREMENT

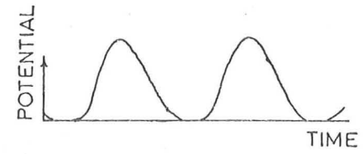

106–150 μm DIAMETER GLASS BALLOTINI, BED DEPTH = 45 mm
f = 48 Hz, y_0 = 0.524 mm, g_{20} = 0.55 mm

FIG. 49 THE OUTPUT POTENTIAL FROM THE BED DISPLACEMENT MEASUREMENT SYSTEM

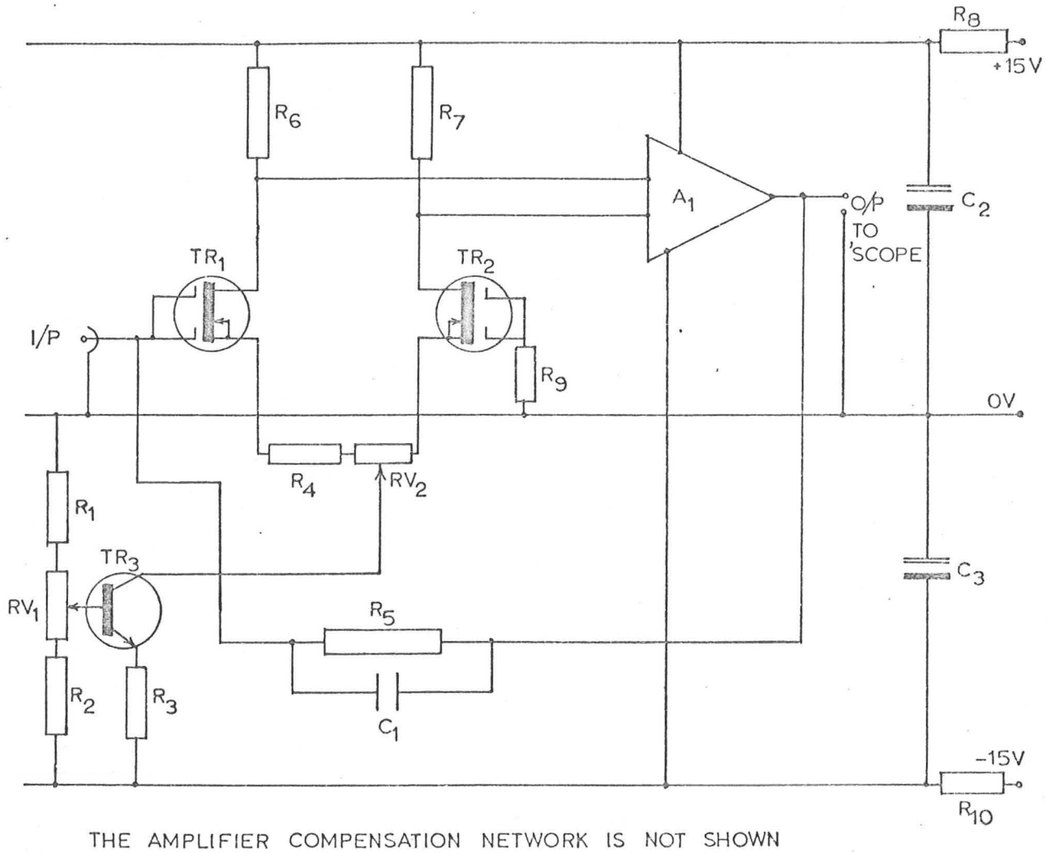

THE AMPLIFIER COMPENSATION NETWORK IS NOT SHOWN

KEY

R_1:-10kΩ R_4:-1.5 kΩ SELECTED R_7:-22 kΩ R_{10}:-470Ω C_1:-10pF TR_1:-BFS 28, A_1:-TAA 521

R_2:-1kΩ R_5:-10MΩ R_8:-470Ω RV_1:-1 kΩ C_2:-150μF TR_2:-BFS 28

R_3:-1.5kΩ R_6:-22 kΩ R_9:-100Ω RV_2:-500Ω HELIPOT C_3:-150μF TR_3:-ZT 41

FIG. 50 CIRCUIT DIAGRAM OF THE ELECTROMETER CONNECTED TO THE VIBRATED VESSEL BASE PLATE

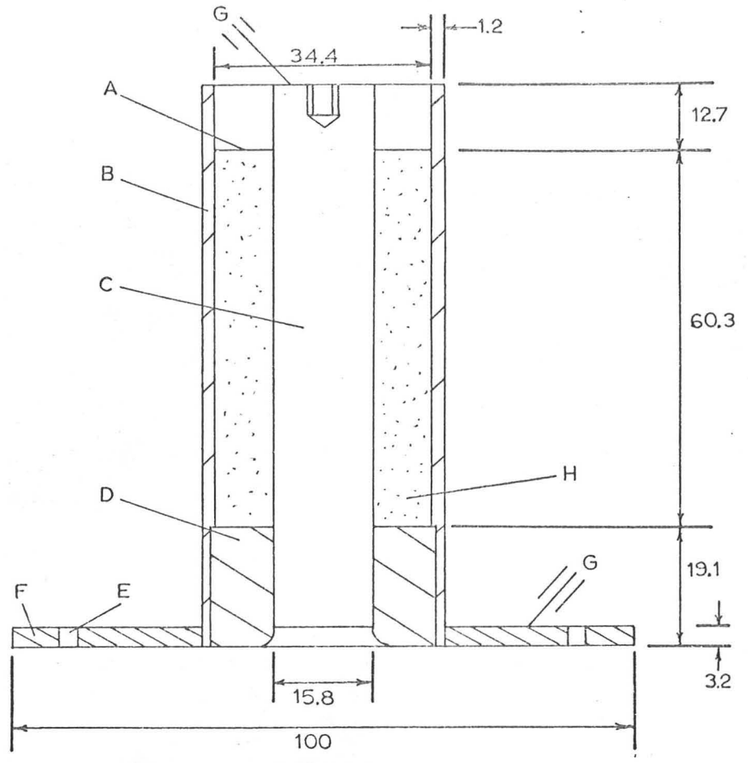

DIMENSIONS IN mm, NOT TO SCALE

KEY

A:- LINE TO WHICH THE CELL IS FILLED

B:- BRASS CYLINDER , C:- STEEL ROD

D:- PTFE BLOCK , E:- 4x2BA CLEARANCE HOLES ON AN 82.6mm PITCH CIRCLE DIAMETER

F:- BRASS DISC, G:- CONNECTION TO THE ELECTRICAL CIRCUIT

H:- PARTICULATE MATERIAL

FIG. 51 SECTIONAL VIEW OF THE RESISTIVITY MEASUREMENT CELL

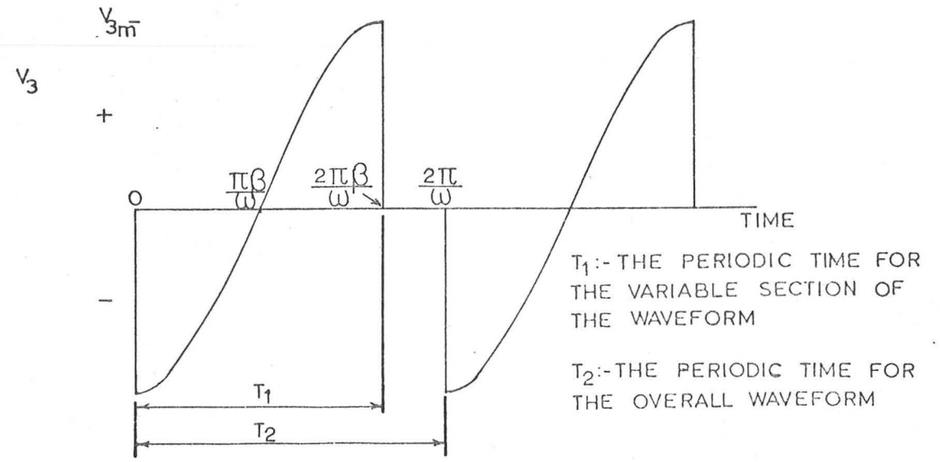

T_1:- THE PERIODIC TIME FOR THE VARIABLE SECTION OF THE WAVEFORM

T_2:- THE PERIODIC TIME FOR THE OVERALL WAVEFORM

FIG. 52 THE PREDICTED ELECTROMETER OUTPUT POTENTIAL FROM EQUATION 4.12, ALLOWING FOR AMPLIFIER INVERSION. β=0.8, AND NEGATIVE PARTICLE CHARGE IS ASSUMED

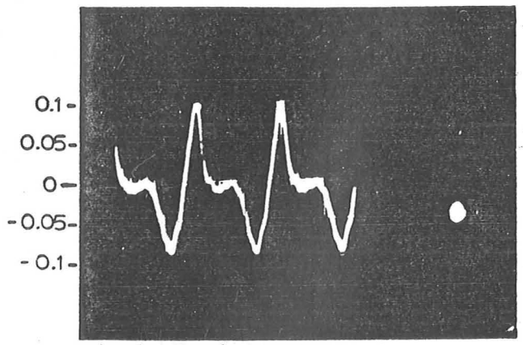

a. POLPROPYLENE PARTICLES

$\frac{\omega^2 y_0}{g_a} = 3.06$

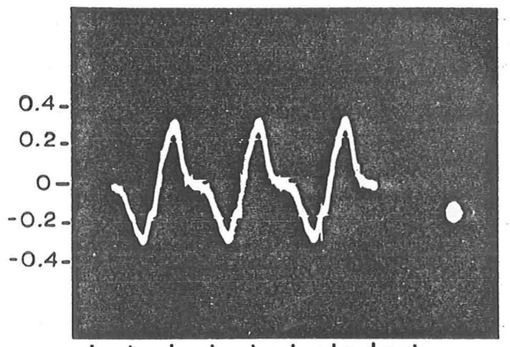

b. POLYPROPYLENE PARTICLES

$\frac{\omega^2 y_0}{g_a} = 4.86$

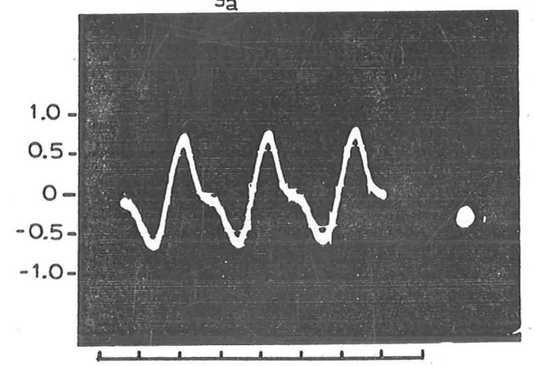

c. POLYPROPYLENE PARTICLES

$\frac{\omega^2 y_0}{g_a} = 6.95$

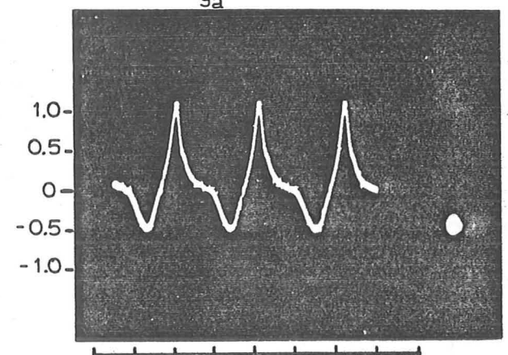

d. GLASS BALLOTINI

$\frac{\omega^2 y_0}{g_a} = 3.75$

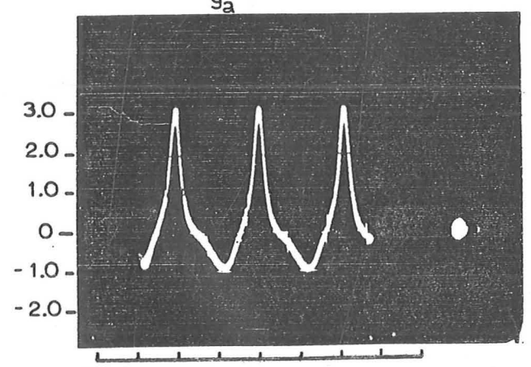

e. GLASS BALLOTINI

$\frac{\omega^2 y_0}{g_a} = 5.93$

$L_1 = 45$ mm , $f = 48$ Hz

L_3 FOR FIGS. a,b,c = 65 mm

L_3 FOR FIGS. d,e = 40 mm

THE ABSCISSA SHOWS TIME IN 10 ms INTERVALS

THE ORDINATE SHOWS THE ELECTROMETER OUTPUT POTENTIAL IN V

FIG. 53 THE POTENTIAL INDUCED IN THE VIBRATED BED SUPPORT VESSEL BASE PLATE BY POLYPROPYLENE PARTICLES AND GLASS BALLOTINI (THE SIGNAL SHOWN IS INVERTED)

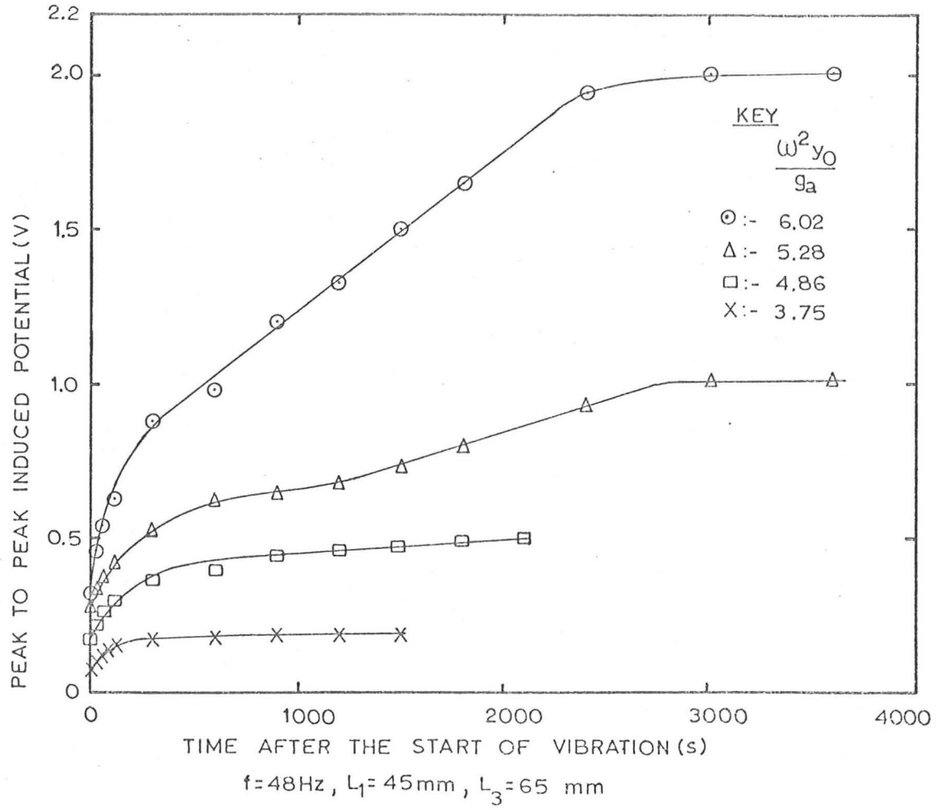

f=48Hz, L_1= 45mm, L_3=65 mm

FIG. 54 THE POTENTIAL INDUCED IN THE BASE PLATE, PLOTTED AGAINST TIME AFTER THE START OF VIBRATION FOR POLYPROPYLENE PARTICLES

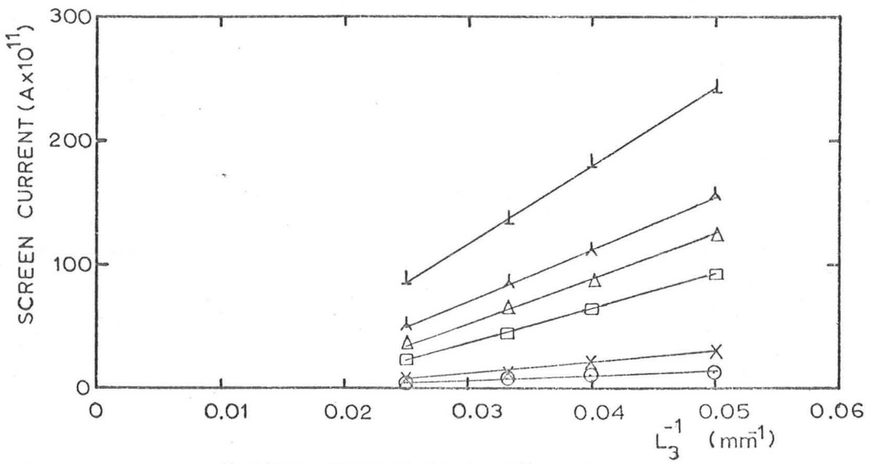

QUARTZ PARTICLES, L_1= 45mm, f = 48Hz

KEY FOR FIG.55

$\omega^2 y_0 / g_a$		$\omega^2 y_0 / g_a$	
⊥ :-	6.95	□ :-	4.86
⅄ :-	5.93	X :-	3.75
Δ :-	5.28	⊙ :-	3.06

FIG. 55 THE SCREEN CURRENT PLOTTED AGAINST THE ELECTRODE SEPARATION DISTANCE RECIPROCAL, FOR QUARTZ PARTICLES

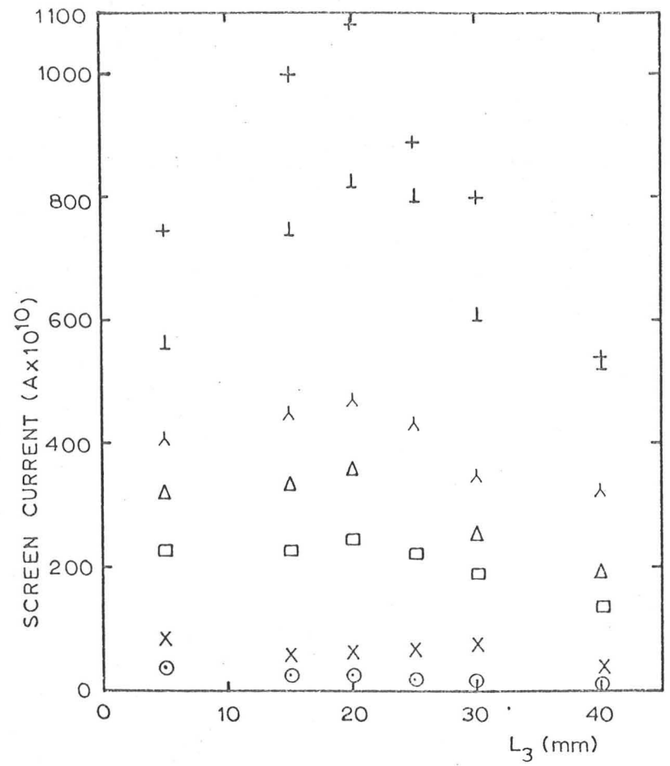

a. GLASS BALLOTINI

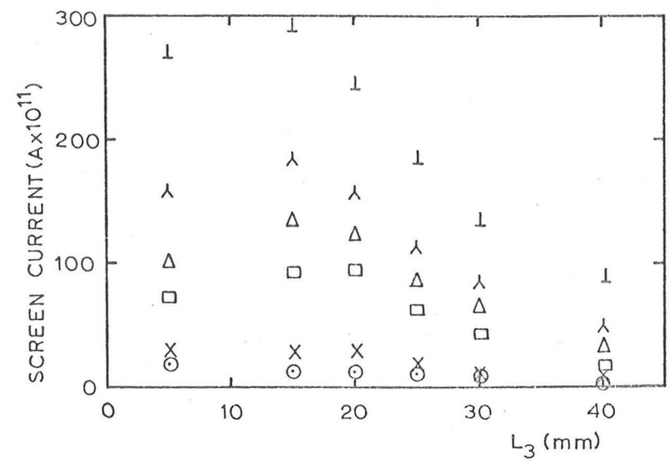

b. QUARTZ PARTICLES

KEY FOR FIG. 56

$\frac{\omega^2 y_0}{g_a}$		$\frac{\omega^2 y_0}{g_a}$	
+ :-	7.4	□ :-	4.86
⊥ :-	6.95	X :-	3.75
⅄ :-	5.93	⊙ :-	3.06
Δ :-	5.28		

f = 48 Hz, L_1 = 45 mm

FIG. 56 THE SCREEN CURRENT PLOTTED AGAINST THE ELECTRODE SEPARATION DISTANCE

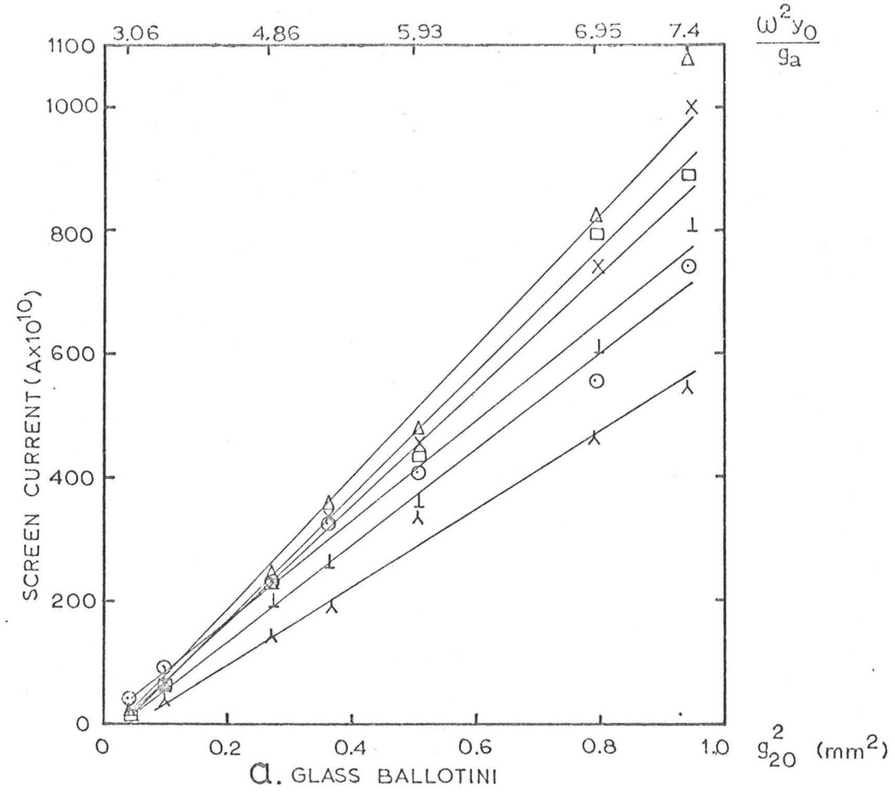

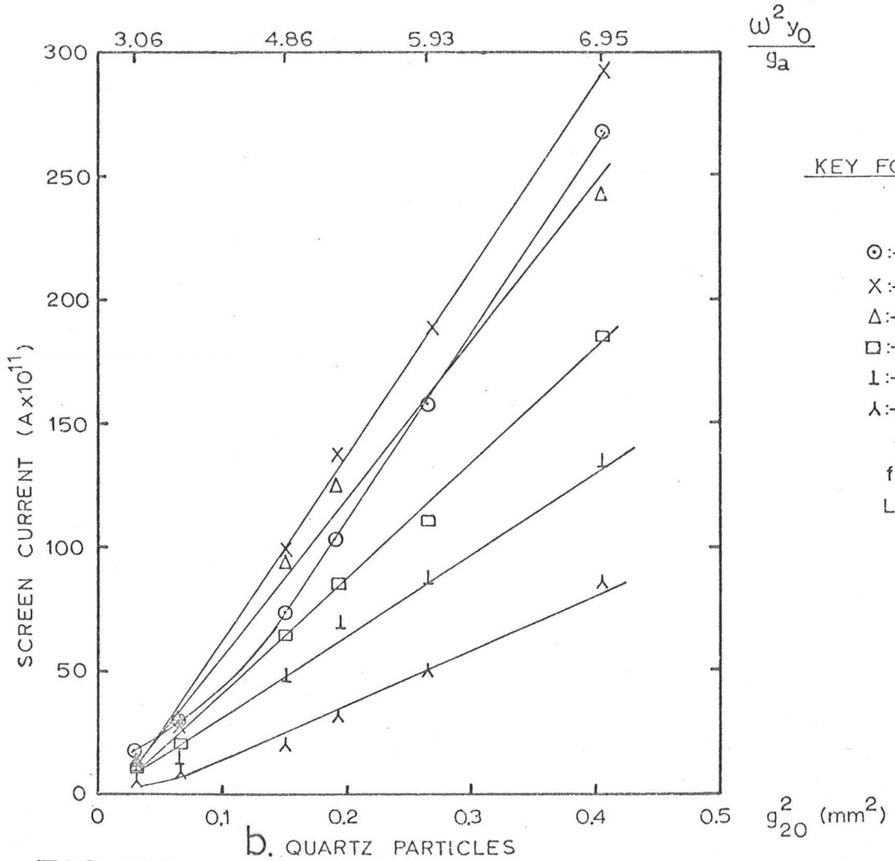

KEY FOR FIG. 57

	L_3(mm)
⊙ :-	5
X :-	15
Δ :-	20
□ :-	25
⊥ :-	30
λ :-	40

f = 48Hz
L_1 = 45 mm

FIG. 57 THE SCREEN CURRENT PLOTTED AGAINST THE MAXIMUM BED DISPLACEMENT SQUARED

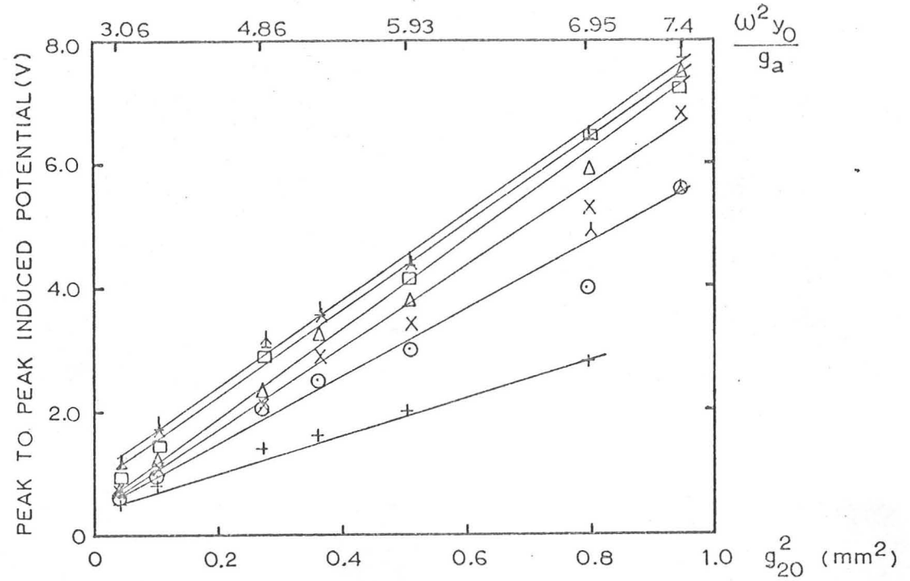

a. GLASS BALLOTINI

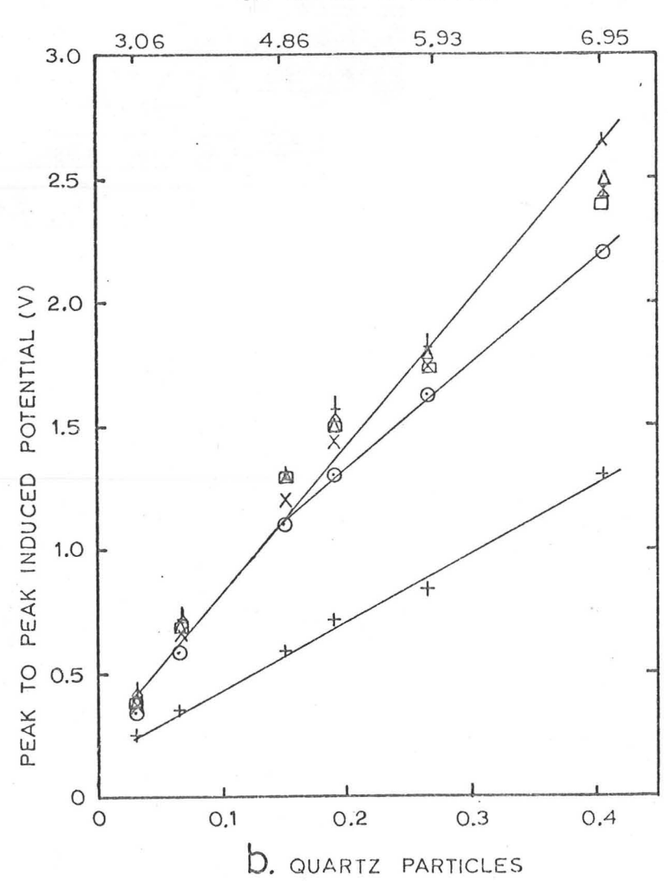

b. QUARTZ PARTICLES

KEY FOR FIG. 58

L_3 (mm)

⊙ :- 5
X :- 15
Δ :- 20
□ :- 25
⊥ :- 30
⅄ :- 40
+ :- 65

f=48Hz, L_1=45mm

FIG. 58 THE PEAK TO PEAK INDUCED POTENTIAL PLOTTED AGAINST THE PEAK BED DISPLACEMENT SQUARED

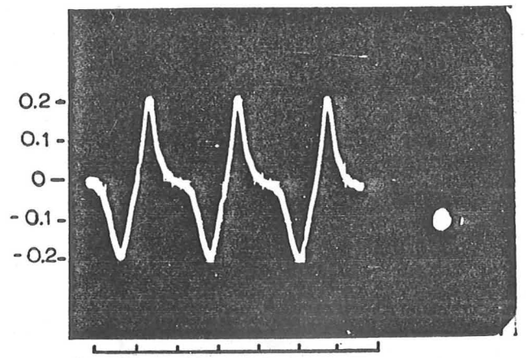

a. QUARTZ PARTICLES

$\frac{\omega^2 y_0}{g_a} = 3.06$

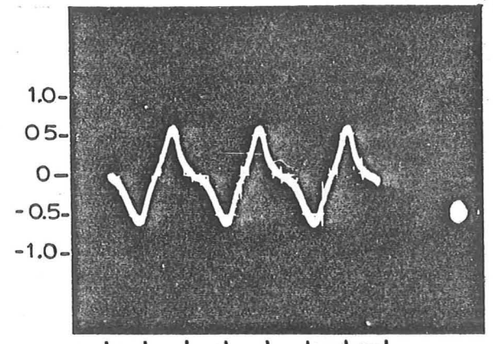

b. QUARTZ PARTICLES

$\frac{\omega^2 y_0}{g_a} = 4.86$

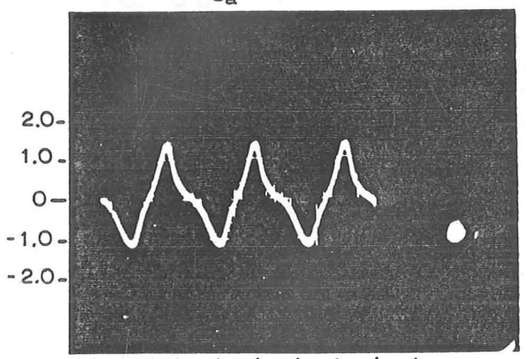

c. QUARTZ PARTICLES

$\frac{\omega^2 y_0}{g_a} = 6.95$

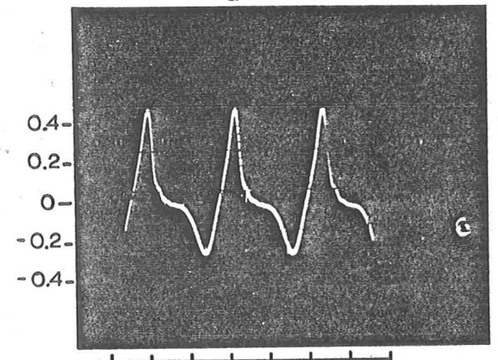

d. DIAKON® PARTICLES

$\frac{\omega^2 y_0}{g_a} = 3.06$

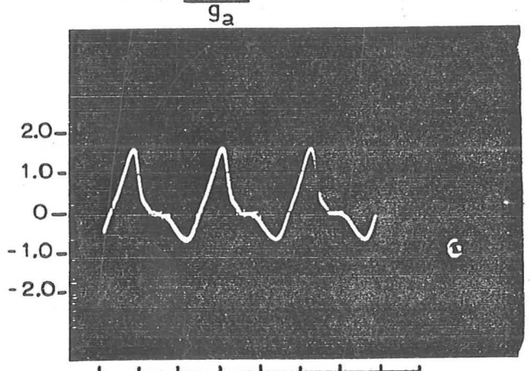

e. DIAKON® PARTICLES

$\frac{\omega^2 y_0}{g_a} = 4.86$

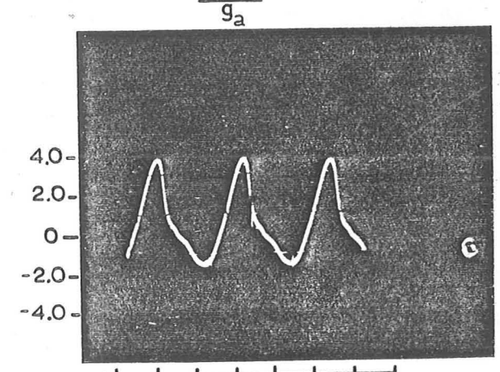

f. DIAKON® PARTICLES

$\frac{\omega^2 y_0}{g_a} = 6.95$

THE ABSCISSA SHOWS TIME IN 10 ms INTERVALS
THE ORDINATE SHOWS THE ELECTROMETER OUTPUT POTENTIAL IN V
$L_1 = 45$ mm , $L_3 = 40$ mm , f = 48 Hz

FIG. 59 THE POTENTIAL INDUCED IN THE VIBRATED BED SUPPORT VESSEL BASE PLATE BY QUARTZ AND DIAKON® PARTICLES (THE SIGNAL SHOWN IS INVERTED)

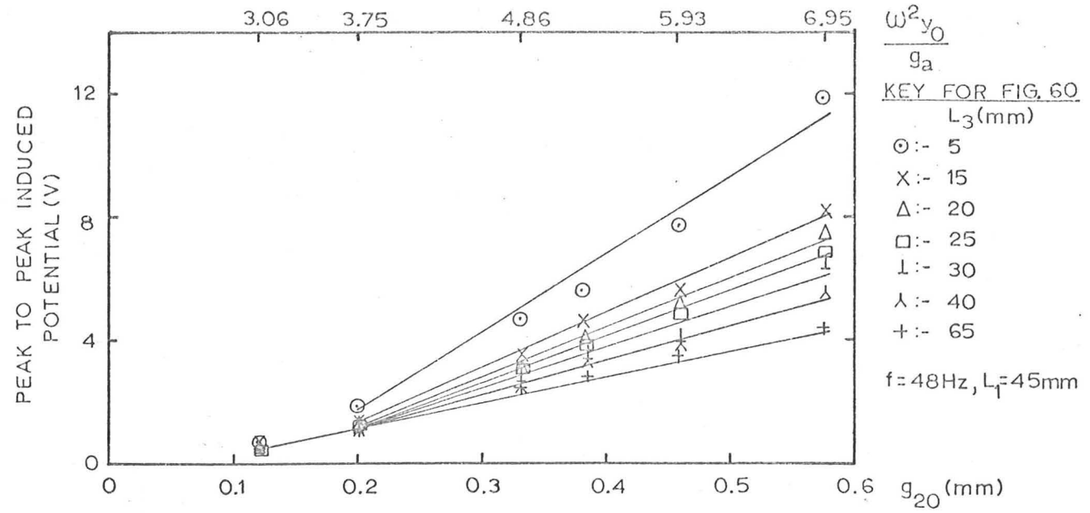

FIG. 60 THE PEAK TO PEAK INDUCED POTENTIAL PLOTTED AGAINST THE PEAK BED DISPLACEMENT FOR DIAKON® PARTICLES. THE POTENTIALS ARE THE STABLE VALUES AFTER SEVERAL MINUTES OF VIBRATION

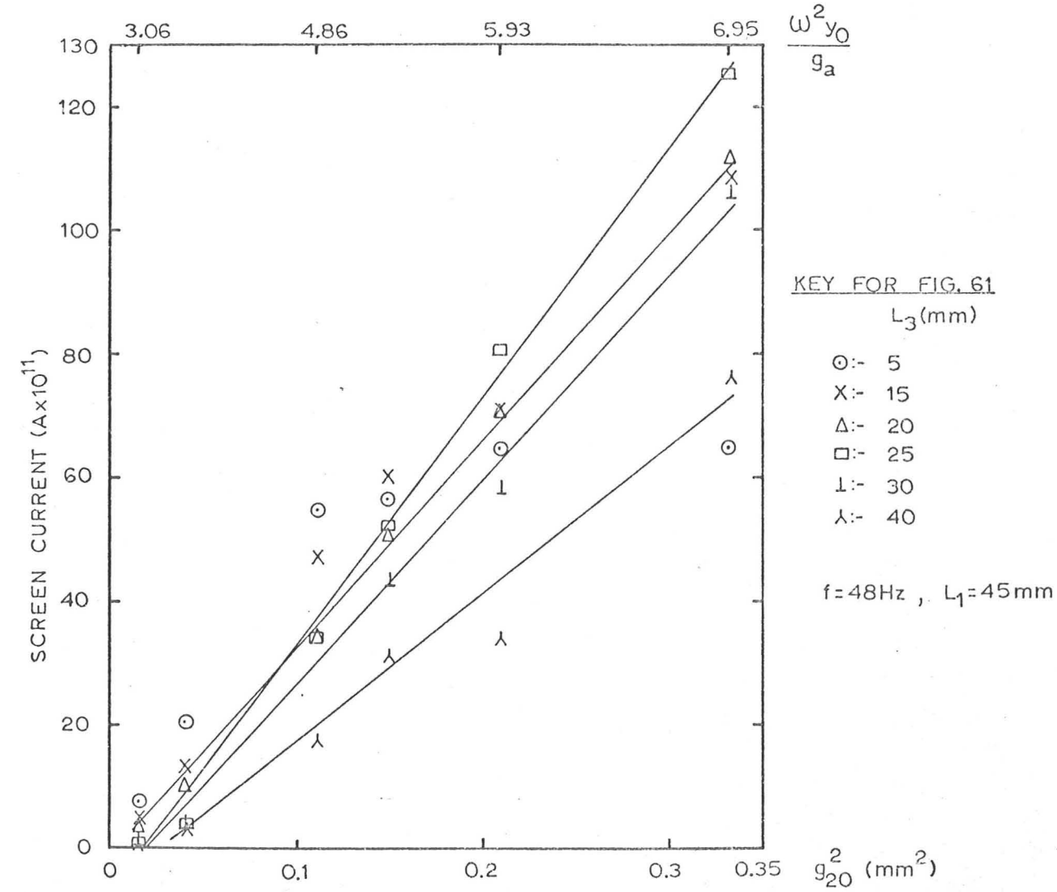

FIG. 61 THE STABLE SCREEN CURRENT AFTER SEVERAL MINUTES OF VIBRATION, PLOTTED AGAINST THE PEAK BED DISPLACEMENT SQUARED FOR DIAKON® PARTICLES

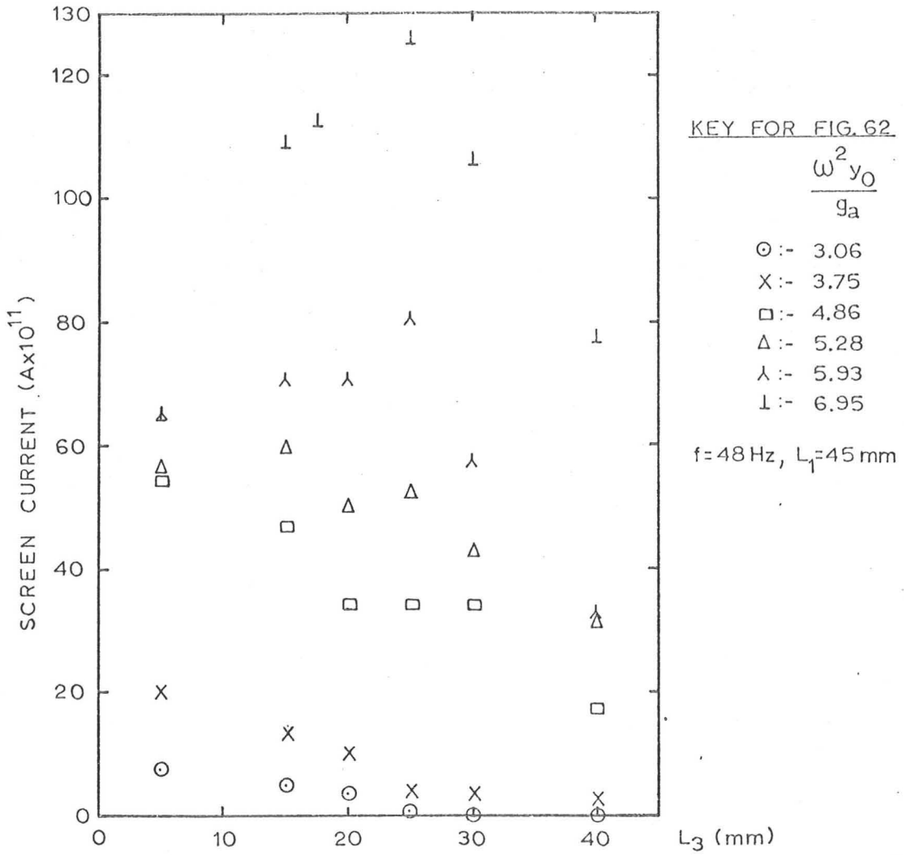

FIG. 62 THE STABLE SCREEN CURRENT AFTER SEVERAL MINUTES OF VIBRATION, PLOTTED AGAINST THE ELECTRODE SEPARATION DISTANCE FOR DIAKON® PARTICLES

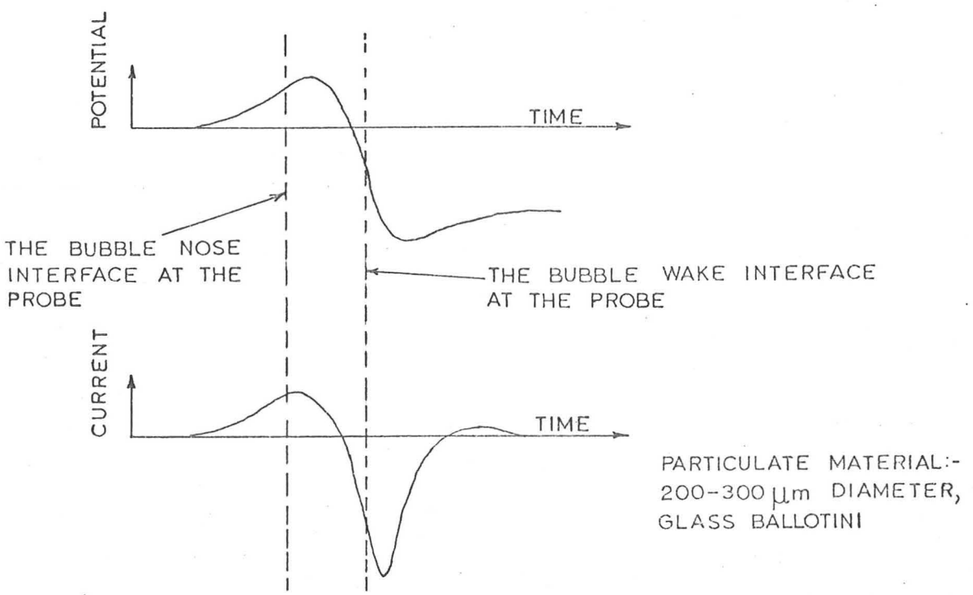

FIG. 63 THE POTENTIAL OF, AND THE CURRENT FROM, A PROBE EMBEDDED IN THE WALL OF A FLUIDISED BED, DUE TO THE PASSAGE OF A BUBBLE. THE MEASUREMENTS ARE REPORTED BY BOLAND[179]

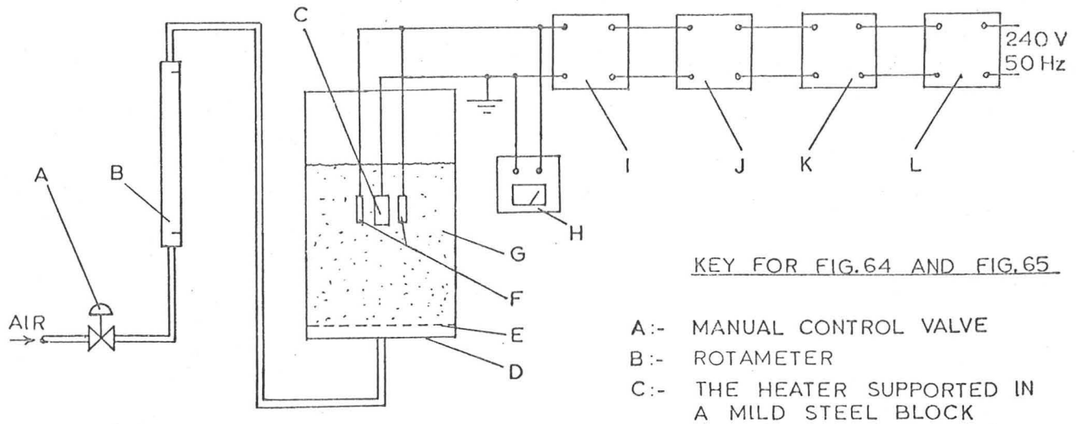

FIG. 64 SCHEMATIC DIAGRAM OF THE FLUIDISED BED HEAT TRANSFER SYSTEM

KEY FOR FIG. 64 AND FIG. 65

A :- MANUAL CONTROL VALVE
B :- ROTAMETER
C :- THE HEATER SUPPORTED IN A MILD STEEL BLOCK
D :- PERSPEX COLUMN, 146.5 mm INTERNAL DIAMETER
E :- GAUZE GAS DISTRIBUTOR
F :- BRASS ELECTRIC FIELD PLATES COVERED WITH EPOXY RESIN
G :- PARTICLE BED
H :- ELECTROSTATIC VOLTMETER
I :- HIGH POTENTIAL TRANSFORMER
J :- TRANSFORMER
K :- AMPLIFIER
L :- OSCILLATOR
M :- PERSPEX SUPPORT RODS

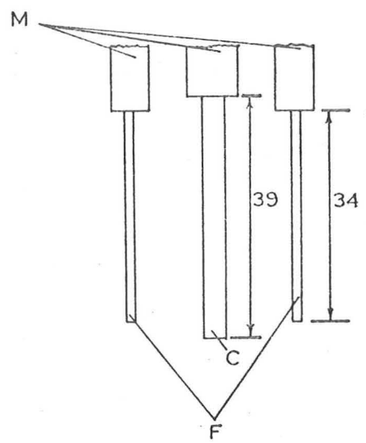

SIDE VIEW OF THE HEATER ASSEMBLY

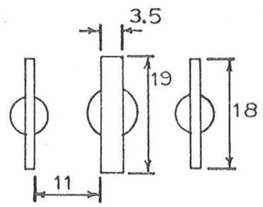

END VIEW OF THE HEATER ASSEMBLY

DIMENSIONS IN mm, NOT TO SCALE

FIG. 65 THE HEATER ASSEMBLY USED IN THE FLUIDISED BED HEAT TRANSFER STUDIES

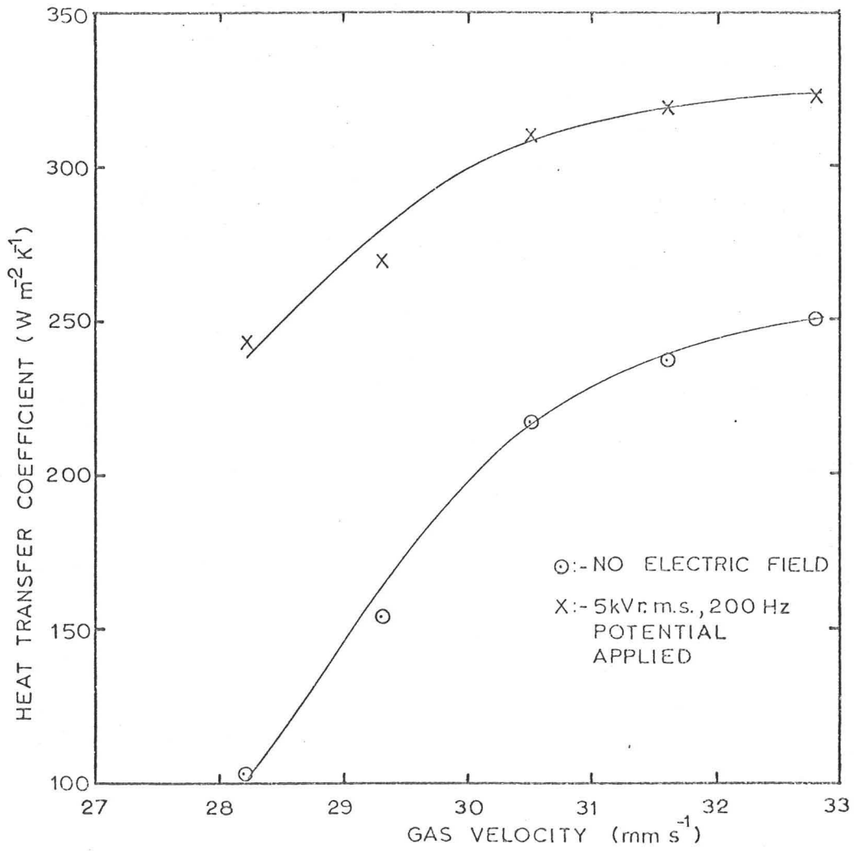

FIG. 66 THE HEAT TRANSFER COEFFICIENT PLOTTED AGAINST THE GAS VELOCITY, BOTH WITH AND WITHOUT AN APPLIED ELECTRIC FIELD

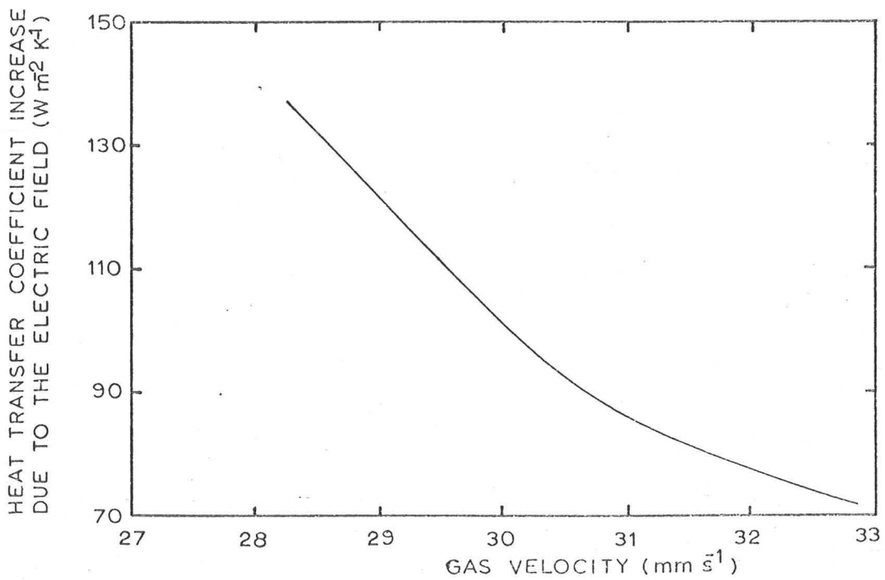

FIG. 67 THE INCREASE IN THE HEAT TRANSFER COEFFICIENT DUE TO APPLICATION OF AN ELECTRIC FIELD (RESULTS OF FIG. 66), PLOTTED AGAINST THE GAS VELOCITY

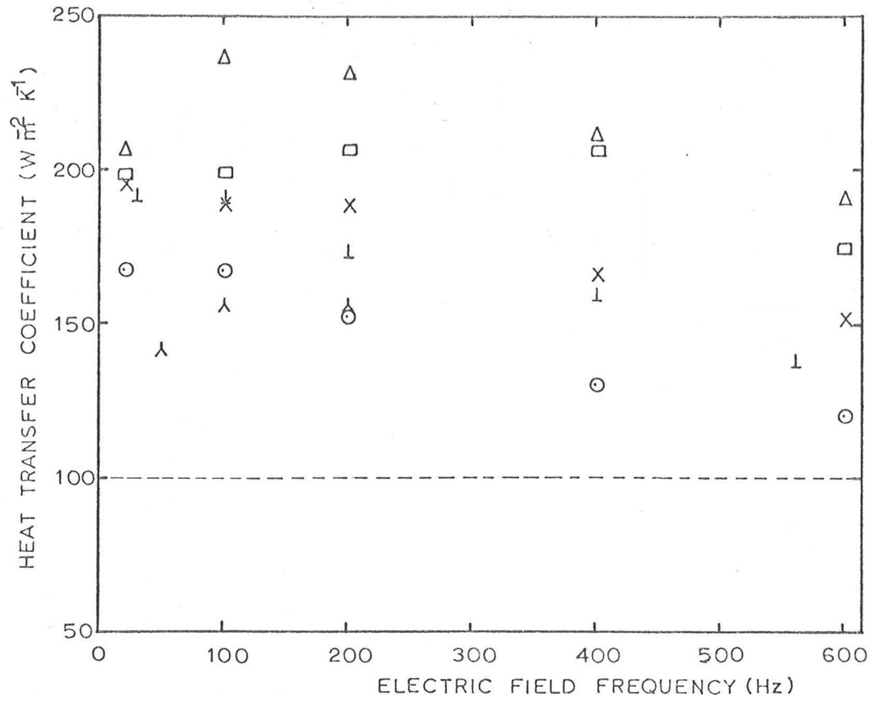

a. GAS VELOCITY = 28.2 mm s⁻¹

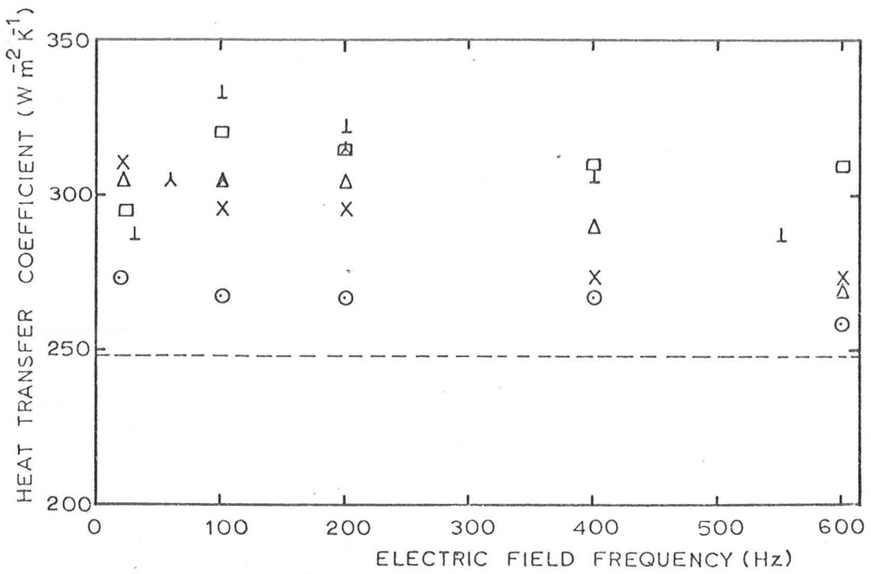

b. GAS VELOCITY = 32.8 mm s⁻¹

FIG. 68 THE HEAT TRANSFER COEFFICIENT PLOTTED AGAINST THE ELECTRIC FIELD FREQUENCY

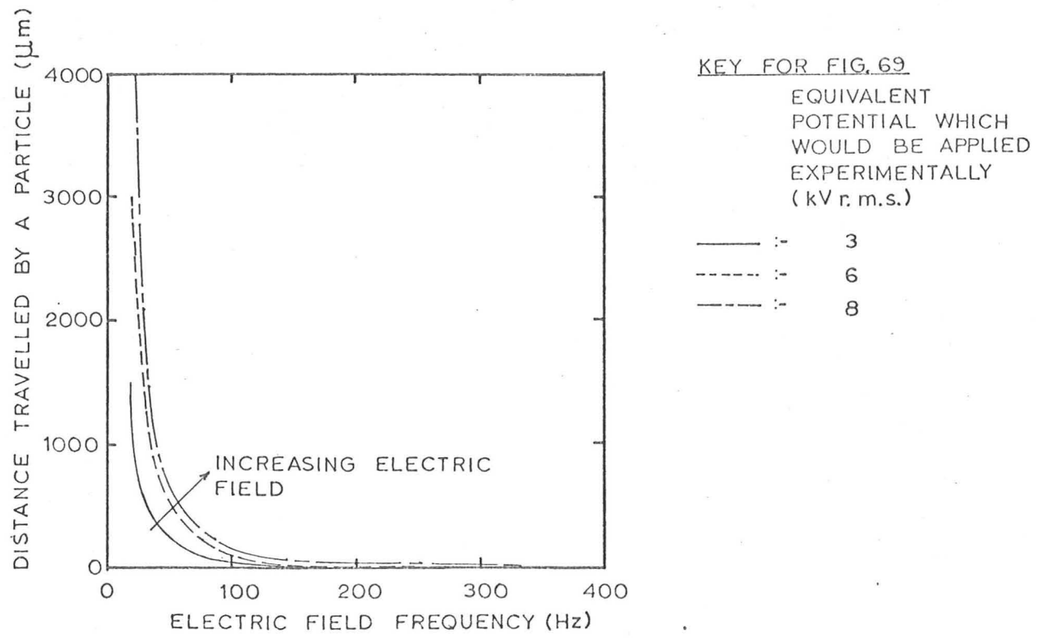

FIG. 69 THE MAXIMUM OSCILLATORY DISPLACEMENT FOR A DIAKON® PARTICLE WITH A CHARGE OF 2.45×10^{-13} C, CALCULATED FROM EQUATION 6.5 ASSUMING A PARTICLE DIAMETER OF 240 μm, AND A PARTICLE DENSITY OF 1100 kg m^{-3}

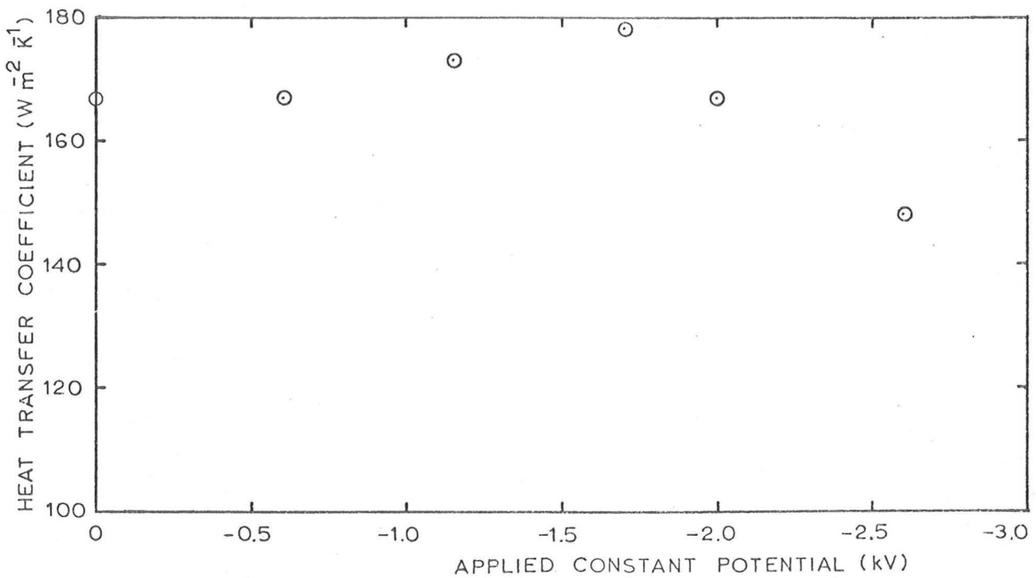

FIG. 70 THE HEAT TRANSFER COEFFICIENT PLOTTED AGAINST THE APPLIED CONSTANT POTENTIAL, FOR A GAS VELOCITY OF 28.2 mm s^{-1} AND NO APPLIED ALTERNATING POTENTIAL

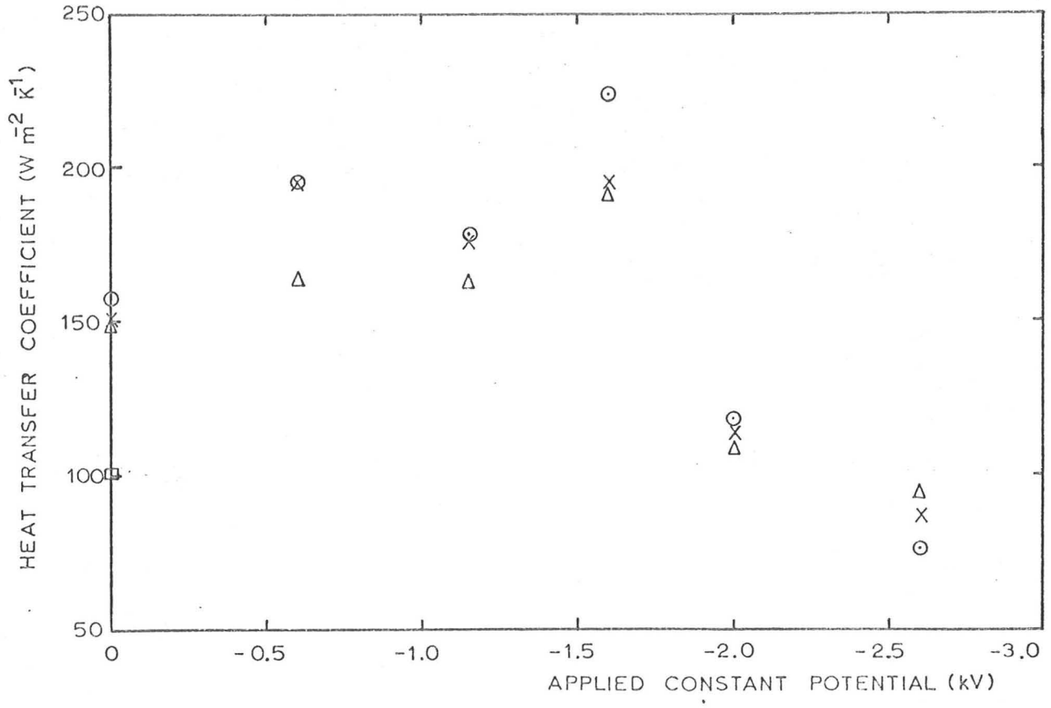

a. GAS VELOCITY = 28.2 mm s⁻¹

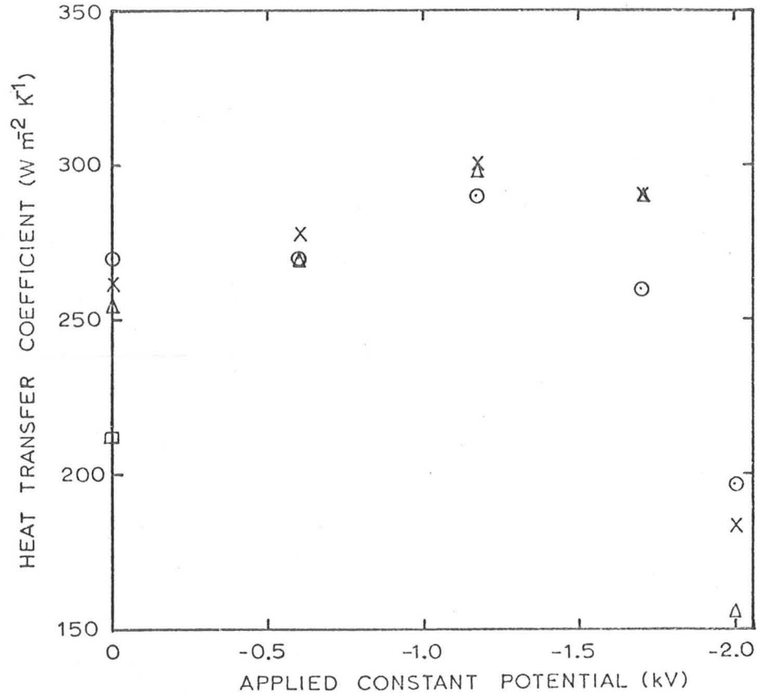

b. GAS VELOCITY = 32.8 mm s⁻¹

KEY FOR FIG 71

	APPLIED ALTERNATING POTENTIAL (kV r. m. s.)
□:-	0
⊙:-	4.0
X:-	5.5
Δ:-	7.0

FREQUENCY = 200 Hz

FIG. 71 THE HEAT TRANSFER COEFFICIENT PLOTTED AGAINST THE APPLIED CONSTANT POTENTIAL

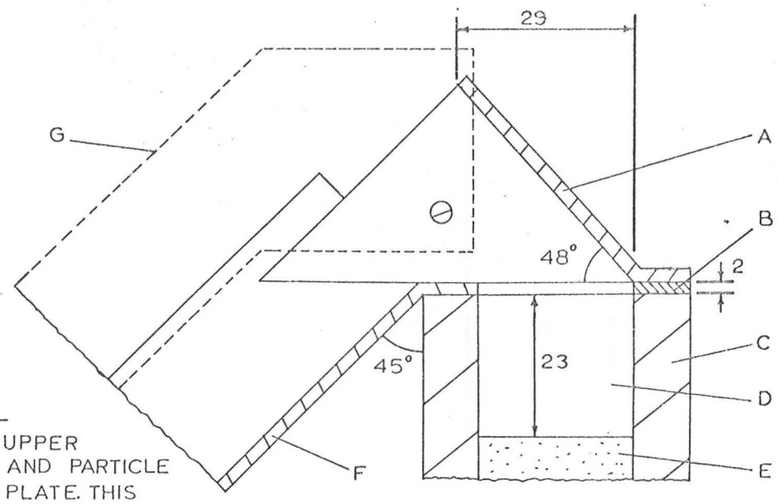

KEY FOR FIG. 72

A :- THE DURAL UPPER ELECTRODE AND PARTICLE DEFLECTOR PLATE. THIS COVERED THE ENTIRE BED SURFACE

B :- DURAL SPACER

C :- PERSPEX VESSEL WALL (THE VESSEL DIMENSIONS ARE SHOWN IN FIG. 47)

D :- FREEBOARD

E :- PARTICLE BED

F :- DURAL COLLECTION CHUTE

G :- DURAL, COLLECTION CHUTE COVER. THE POSITION WHICH THE COVER OCCUPIED IS SHOWN BY DOTTED LINES

FIG. 72 SCHEMATIC SECTIONAL DIAGRAM OF THE ELECTROSTATIC SEPARATION DEVICE. (DIMENSIONS IN mm, NOT TO SCALE)

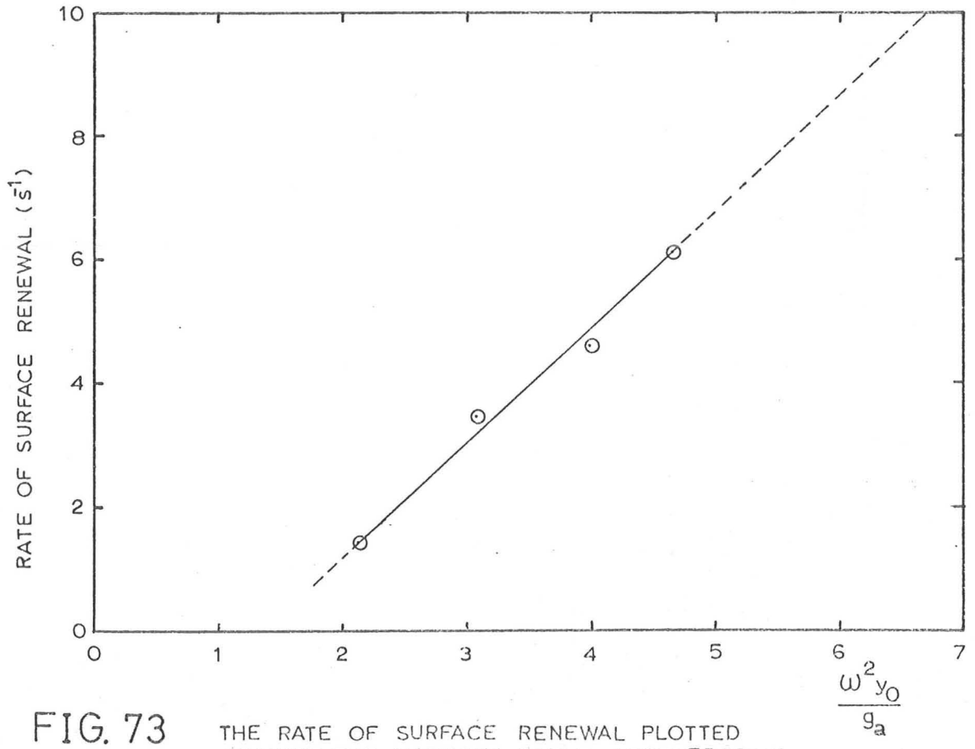

FIG. 73 THE RATE OF SURFACE RENEWAL PLOTTED AGAINST THE MAXIMUM TABLE ACCELERATION

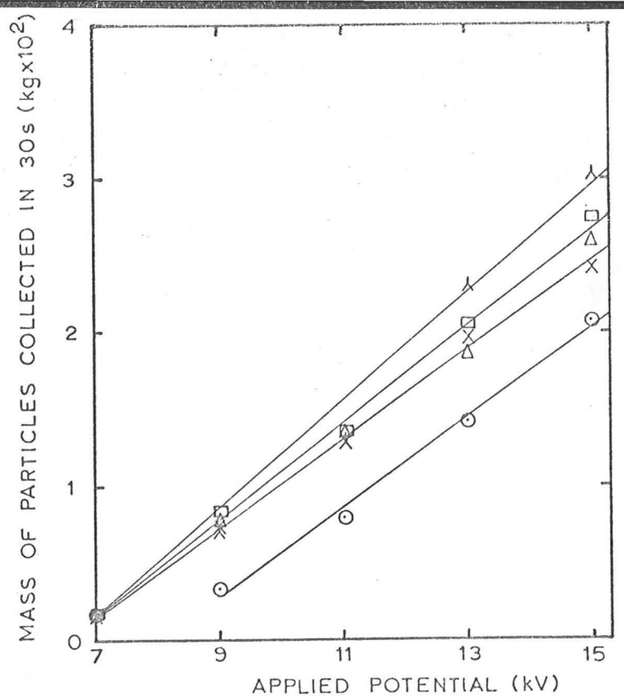

KEY FOR FIG.74

$\frac{\omega^2 y_0}{g_a}$

⊙ :- 0
X :- 2.14
Δ :- 2.6
□ :- 3.06
⅄ :- 3.99

FIG. 74 THE MASS OF 106–150 μm DIAMETER GLASS BALLOTINI COLLECTED IN 30s, PLOTTED AGAINST THE APPLIED POTENTIAL

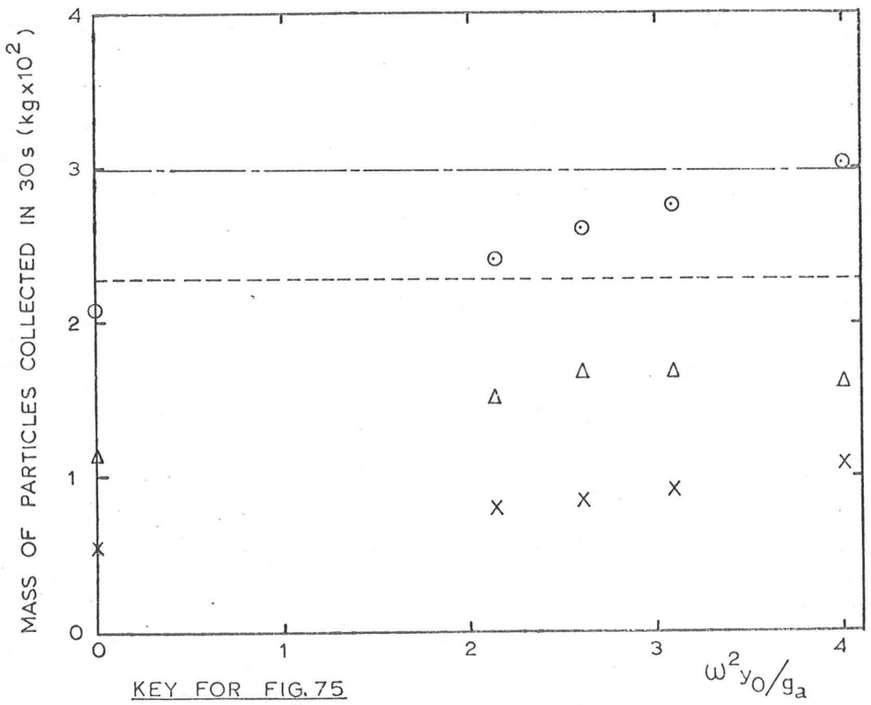

KEY FOR FIG. 75

MATERIAL	EXPERIMENTAL RESULTS	THEORETICAL PREDICTION
106-150 μm DIAMETER GLASS BALLOTINI	⊙	——·—·——
106-150 μm DIAMETER QUARTZ	X	——·—·——
104-250 μm DIAMETER IRON SHOT	Δ	----------

FIG. 75 THE MASS OF PARTICLES COLLECTED IN 30s, PLOTTED AGAINST THE MAXIMUM TABLE ACCELERATION, FOR AN APPLIED POTENTIAL OF 15 kV

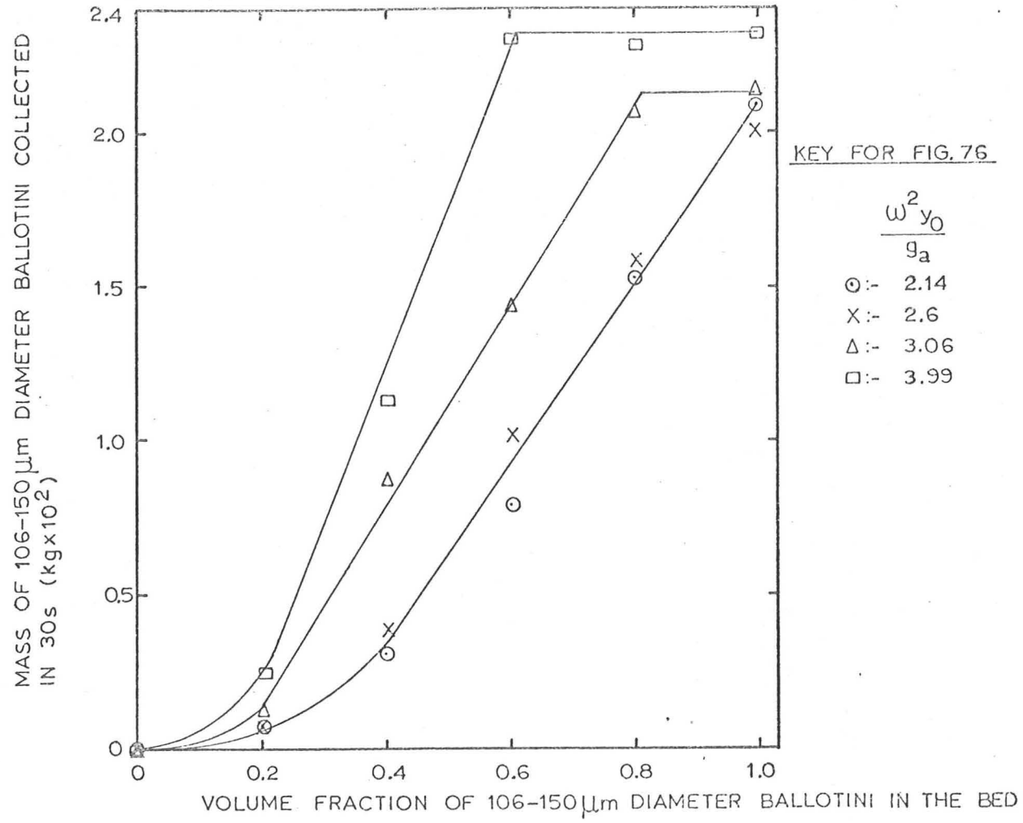

FIG. 76 THE MASS OF 106-150 μm DIAMETER GLASS BALLOTINI, SEPARATED FROM A MIXTURE CONTAINING ALSO 300-599 μm DIAMETER GLASS BALLOTINI, PLOTTED AGAINST THE 106-150 μm DIAMETER BALLOTINI INITIAL BED VOLUME FRACTION

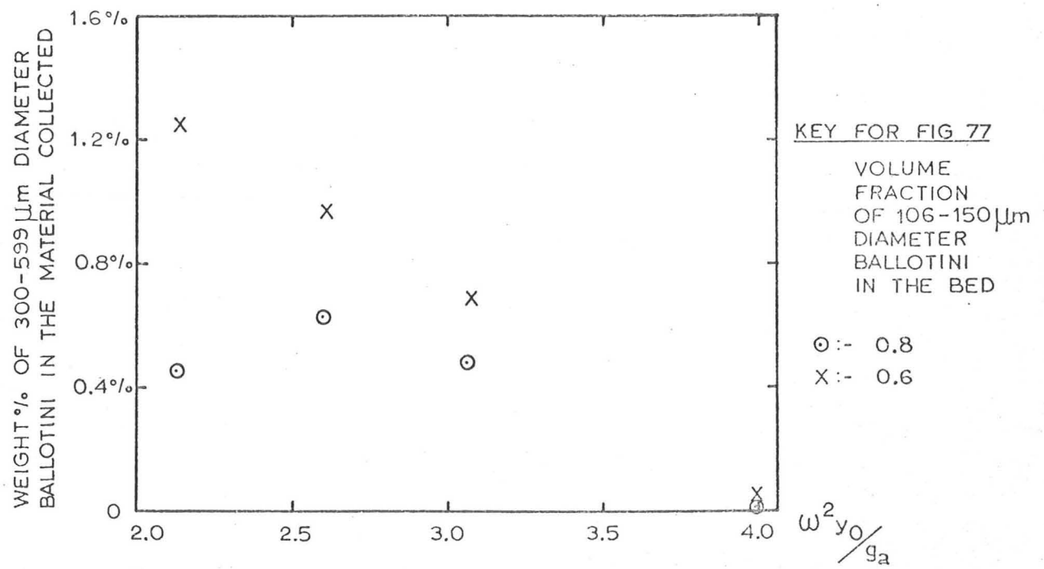

FIG. 77 PERCENTAGE BY WEIGHT OF THE 300-599 μm DIAMETER BALLOTINI IN THE MATERIAL COLLECTED AFTER 30 s APPLICATION OF 15 kV POTENTIAL, PLOTTED AGAINST THE MAXIMUM TABLE ACCELERATION. THE MASS OF 106-150 μm DIAMETER BALLOTINI COLLECTED FOR THE CORRESPONDING CONDITIONS IS SHOWN IN FIG. 76